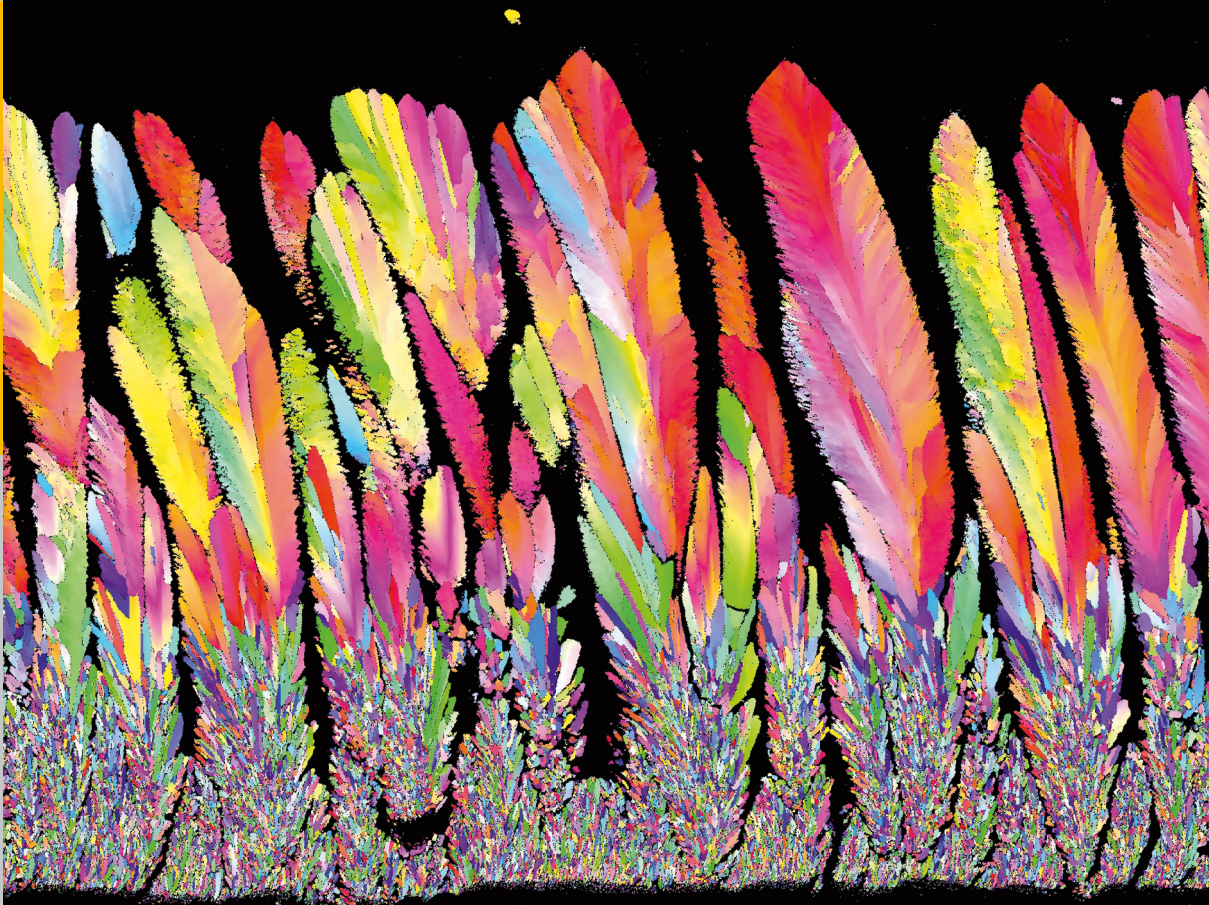


Deposition Mechanisms of Thermal Barrier Coatings (TBCs) Manufactured by Plasma Spray-Physical Vapor Deposition (PS-PVD)

Wenting He



Member of the Helmholtz Association

Energie & Umwelt /
Energy & Environment
Band / Volume 398
ISBN 978-3-95806-275-7

 **JÜLICH**
FORSCHUNGSZENTRUM

Forschungszentrum Jülich GmbH
Institute of Energy and Climate Research
Materials Synthesis and Processing (IEK-1)

Deposition Mechanisms of Thermal Barrier Coatings (TBCs) Manufactured by Plasma Spray-Physical Vapor Deposition (PS-PVD)

Wenting He

Schriften des Forschungszentrums Jülich
Reihe Energie & Umwelt / Energy & Environment

Band / Volume 398

ISSN 1866-1793

ISBN 978-3-95806-275-7

Bibliographic information published by the Deutsche Nationalbibliothek.
The Deutsche Nationalbibliothek lists this publication in the Deutsche
Nationalbibliografie; detailed bibliographic data are available in the
Internet at <http://dnb.d-nb.de>.

Publisher and
Distributor: Forschungszentrum Jülich GmbH
Zentralbibliothek
52425 Jülich
Tel: +49 2461 61-5368
Fax: +49 2461 61-6103
Email: zb-publikation@fz-juelich.de
www.fz-juelich.de/zb

Cover Design: Grafische Medien, Forschungszentrum Jülich GmbH

Printer: Grafische Medien, Forschungszentrum Jülich GmbH

Copyright: Forschungszentrum Jülich 2017

Schriften des Forschungszentrums Jülich
Reihe Energie & Umwelt / Energy & Environment, Band / Volume 398

D 294 (Diss., Bochum, Univ., 2017)

ISSN 1866-1793
ISBN 978-3-95806-275-7

The complete volume is freely available on the Internet on the Jülicher Open Access Server (JuSER)
at www.fz-juelich.de/zb/openaccess.



This is an Open Access publication distributed under the terms of the [Creative Commons Attribution License 4.0](https://creativecommons.org/licenses/by/4.0/),
which permits unrestricted use, distribution, and reproduction in any medium, provided the original work is properly cited.

Abstract

Plasma spray-physical vapor deposition (PS-PVD) is a promising technology to produce columnar structured ceramic thermal barrier coatings with excellent performance at high deposition rates. In the PS-PVD process, major fractions of the feedstock powder can be evaporated so that coatings are deposited mainly from the vapor phase similar to electron beam-physical vapor deposition (EB-PVD). But, unlike conventional PVD processes, the interaction between plasma flow and vapor species in combination with the higher chamber pressure makes non-line of sight deposition possible to deposit coatings on shadowed parts of the substrate. The different processing parameters can definitely affect the coating growth mechanisms in PS-PVD. However, their relations to deposition mechanisms which are significant for coating development are still not very clear and relevant reports are limited.

In this work, the characteristics of plasma jets generated in the PS-PVD process by standard plasma gases, Ar, He and H₂, have been studied by optical emission spectroscopy. Abel inversion was introduced to reconstruct the spatial characteristics. In the central area of the plasma jet, the ionization of Ar was found to be one of the reasons for low emission of atomic Ar. The excitation temperature of Ar was calculated by the Boltzmann plot method. Its value decreased from the center to the edge of the plasma jet. Applying the same method, a spurious high excitation temperature of He was obtained, which could be caused by the strong deviation from local thermal equilibrium of He. The addition of H₂ into plasma gases leads to a lower excitation temperature, however a higher substrate temperature due to the high thermal conductivity induced by the dissociation of H₂. A loading effect is exerted by the feedstock powder on the plasma jet, which was found to reduce the average excitation temperature considerably by more than 700 K in the Ar/He jet.

This characterization of plasma jets under PS-PVD conditions was an important basis for the following studies of the columnar structured YSZ coatings. They were investigated with respect to the powder feeding rate, the agglomeration of feedstock, deposition rate, substrate surface temperature, vapor incidence angle, and flow condition. With increasing powder feeding rate, the efficiency of heat transfer from plasma to the powder declined gradually followed by a lower evaporation rate of the feedstock. Hence, a moderate powder feeding rate and agglomeration of feedstock by organic binder should be used in PS-PVD to achieve effective feedstock evaporation and thus vapor deposition. The observation on initial deposits indicates that faceted crystals are deposited from vapor phase. Based on electron backscatter diffraction

investigations, the coating growth process can be roughly divided into three stages: equiaxed growth, competitive growth, and preferential growth. The equiaxed crystals were generally found to grow in the beginning of coating deposition due to a high nucleation rate induced by large undercooling effect. The mechanisms of the preferential growth were explained by the competition between diffusion and shadowing, referring to deposition parameters: deposition rate, substrate temperature, and vapor incidence angle. In the end, a concept of boundary-layer was introduced to discuss the influence of the flow conditions in the boundary-layer and the possibility of cluster deposition. The cauliflower structure deposited in the later period of the coating process where substrate temperature was rather high was suspected to be due to changes of the flow conditions.

Kurzfassung

Plasma spray-physical vapor deposition (PS-PVD) ist eine vielversprechende Technologie für die Herstellung kolumnar strukturierter, leistungsfähiger keramischer Wärmedämmschichten bei hohen Abscheideraten. Im PS-PVD-Prozess werden große Teile des pulverförmigen Vorstufenmaterials verdampft, so dass die Schichten ähnlich wie beim Electron beam-physical vapor deposition (EB-PVD) überwiegend aus der Dampfphase abgeschieden werden. Im Gegensatz zu solch konventionellen PVD-Prozessen ist der PS-PVD-Prozess jedoch nicht auf die Beschichtung entlang von Sichtlinien beschränkt, was in der strömungsmechanischen Wechselwirkung des Vorstufenmaterials mit dem Plasma sowie dem vergleichsweise höheren Kammerdruck begründet ist. So können auch Hinterschneidungen und abgeschattete Bereiche von Substraten beschichtet werden. Die für das Aufwachsen der Schicht bestimmenden Mechanismen sind von den Prozessparametern abhängig. Jedoch sind die genauen Zusammenhänge, soweit sie für die Schichtabscheidung signifikant sind, noch weitgehend unklar; entsprechende Literatur ist bislang kaum verfügbar.

In dieser Arbeit wurden die Eigenschaften des standardmäßig aus Ar, He und H₂ zusammengesetzten Plasmastrahls im PS-PVD-Prozess mit Hilfe der optischen Emissions-Spektroskopie untersucht. Dabei wurde die Abel-Inversion eingesetzt, um die räumliche Verteilung der Charakteristiken zu rekonstruieren. Es zeigte sich, dass die Emission von neutralem Ar im zentralen Bereich des Strahls aufgrund des hohen Ionisationsgrades relativ gering ist. Weiterhin wurden die Anregungstemperaturen des Ars mithilfe von Boltzmann-Graphen bestimmt. Die Werte zeigten von der Mitte zu den Rändern hin eine abnehmende Tendenz. Für He ergaben sich hier scheinbar hohe Anregungstemperaturen, was auf starke Abweichungen vom lokalen thermodynamischen Gleichgewicht zurückgeführt werden kann. Die Zugabe von H₂ zum Plasmagas führte zu einer Absenkung der Anregungstemperaturen, dabei stiegen jedoch die Substrat-Oberflächentemperaturen aufgrund der hohen Wärmeleitfähigkeit infolge der Dissoziation des H₂ an. Durch die Injektion von pulverförmigem Vorstufenmaterial kam es zu einem Beladungseffekt im Plasmastrahl, so dass die Temperaturen im Ar/He-Strahl um bis zu 700 K niedriger lagen.

Diese Charakterisierung des Plasmastrahls unter PS-PVD-Bedingungen war eine wichtige Grundlage für die weitere Untersuchung des Aufwachsens kolumnarer Strukturen aus Yttriumoxid-stabilisierten Zirkoniumdioxid. Dabei wurden die Einflüsse der Vorstufen-Förderrate, der Agglomerationsstärke des Pulvers, der Abscheiderate, der Oberflächentemperatur der Substrate, des Einfallswinkels sowie der

Strömungsverhältnisse berücksichtigt. Mit zunehmender Vorstufenförderrate nahm die Effizienz des Wärmeübertrags vom Plasma auf das Pulver schrittweise ab, was eine Reduzierung des verdampften Anteils der Vorstufe zur Folge hatte. Somit erscheint eine moderate Vorstufen-Förderrate sowie eine angepasste Agglomerationsstärke in der Vorstufe mittels organischen Binders vorteilhaft, um eine möglichst effektive Verdampfung der Vorstufe zu erreichen. Die aus der Dampfphase anfänglich abgeschiedenen Schichten zeigten charakteristische facettierte Kristallite. Die mittels Elektronenrückstreubeugung gewonnenen Ergebnisse zeigten, dass das Aufwachsen der Schichten in drei Stadien eingeteilt werden kann: Gleichachsiges Wachstum, konkurrierendes Wachstum und bevorzugtes Wachstum. Die gleichachsigen Kristallite traten im Allgemeinen infolge hoher Keimbildungsraten durch starke Unterkühlung zu Beginn der Abscheidung auf. Das bevorzugte Wachstum konnte durch den Einfluss von Diffusion und Abschattung je nach Abscheiderate, Substrat-Oberflächentemperaturen und Einfallswinkels erklärt werden. Schließlich wurde das Modell einer Grenzschicht entwickelt, um den Einfluss der Strömung sowie einer möglichen Abscheidung von Clustern zu erörtern. Die Abscheidung von Blumenkohl-ähnlichen Strukturen bei fortgeschrittener Abscheidung und recht hohen Substrat-Oberflächentemperaturen wurde auf örtlich variierende Strömungseinflüsse zurückgeführt.

Abbreviations

APS	Atmospheric Plasma Spray
BC	Bond Coat
BSE	Back-Scattered Electron
CEA	Chemical Equilibrium with Applications
CFD	Computational Fluid Dynamics
CL	Cathodoluminescence
CMAS	Calcium-Magnesium-Alumino-Silicate
CMCs	Ceramic Matrix Composites
CVD	Chemical Vapor Deposition
EBCs	Environmental Barrier Coating
EBSD	Electron Back-Scattered Diffraction
EB-PVD	Electron Beam-Physical Vapor Deposition
EDX	Energy Dispersive X-Ray Analysis
HVOF	High Velocity Oxy-Fuel
IPF	Inverse Pole Figure
IQ	Image Quality
LPPS	Low Pressure Plasma Spray
LTE	Local Thermal Equilibrium
NASA	National Aeronautics and Space Administration
N.A.	Not Applicable
ND	Normal Direction
OES	Optical Emission Spectroscopy
PECVD	Plasma Enhanced Chemical Vapor Deposition
PFR	Powder Feeding Rate
pLTE	partially Local Thermal Equilibrium
PSD	Particle Size Distribution
PS-PVD	Plasma Spray-Physical Vapor Deposition
RD	Rolling direction
SE	Secondary Electron
SEM	Scanning Electron Microscopy
SLPM	Standard Litter Per Minute
SPS	Suspension Plasma Spray
SZM	Structure Zone Model
TBCs	Thermal Barrier Coatings
TC	Texture Coefficient
TCN	Theory of Charged Nanoparticles

TD	Transverse Direction
TEM	Transmission Electron Microscopy
TGO	Thermally Grown Oxide
VIA	Vapor Incidence Angle
VLPPS	Very Low Pressure Plasma Spray
VPA	Vapor Phase Aluminizing
VPS	Vacuum Plasma Spray
XRD	X-Ray Diffraction
YSZ	Yttria-Stabilized Zirconia

Symbols

A	Pre-exponential kinetic parameter
A_{jk}	Transition probability
A_n	Unknown amplitudes
c	Velocity of light
c	Cubic phase
c_p	Specific heat capacity
$c/a\sqrt{2}$	Tetragonality
D	Diffusion rate
d	Spacing between diffracting planes
d_0	Mean nucleation distance
d_{10}, d_{50}, d_{90}	Diameters below 10%, 50%, and 90 % of the total volume
E_a	Activation energy for a process
E_d	Energy barrier for diffusion
E_j	Energy of the excited level j
E_λ	Energy emitted from a target
$E_{b\lambda}$	Energy emitted from an ideal black body
$E_{r\lambda}$	Energy received by pyrometer
F	Total influence coefficient
f	Fluorite
ΔG^*	Nucleation energy
g_j	Statistical weight of the excited level j
h	Plank constant
I_{jk}	Absolute intensity of a spectral line emitted by the plasma due to the transition from an excited state j to a lower energy state k
$I(y)$	Laterally measured intensity
k_B	Boltzmann constant

k	Rate of a process
L	Emission source depth
m	Monoclinic phase
N	Nucleation rate
N_l	Lower frequency limit
N_u	Upper frequency limit
n	Any integer
n_s	Equilibrium concentration of monomer
n_0	Concentration of monomer
n_{tot}	Density of emitting atoms/ions
R or r	Radius
R_{CW}	Ratio of coating weight
R_{IA}	Ratio of the integral area value
Re	Reynolds number
S	Supersaturation ratio
T	Absolute temperature
T_{exc}	Excitation temperature
$T_{exc}(r)$	Localized excitation temperature
$T_{exc}^{(A)}$	Average excitation temperature
T_m	Melting temperature
T_s	Substrate temperature
T_r	Temperature measured by pyrometer
t	Transformable tetragonal phase
t'	Non-transformable tetragonal phase
u_∞	Velocity of the free flow
v_0	Monomer volume
Z	Partition function
ε	Emissivity in thermal radiation
$\varepsilon(r)$	Local emission intensity
γ	Surface energy
λ	Wavelength
λ_{jk}	Wavelength of the emission due to the transition from an excited state j to a lower energy state k
μ	Dynamic viscosity
ν	Kinematic viscosity of the fluid
ρ	Density
θ	Incident angle of the X-ray

Contents

Chapter 1 Introduction and Objectives.....	1
Chapter 2 Background and Current Knowledge	3
2.1 Thermal barrier coating system	3
2.1.1 The structure of TBCs	4
2.1.2 Ceramic materials for topcoats.....	7
2.1.3 Manufacturing methods of topcoats	11
2.2 Plasma spray-physical vapor deposition	20
2.2.1 Plasma characteristics and interaction with feedstock in PS-PVD.....	21
2.2.2 Microstructures, properties and performance of TBCs by PS-PVD.....	24
2.3 Mechanisms of coating deposition out of vapor phase.....	27
2.3.1 Atomic (or molecular) deposition.....	28
2.3.2 Cluster deposition.....	34
2.3.3 Current knowledge about growth mechanisms of PS-PVD coatings	39
2.4 Summary	41
Chapter 3 Applied Methods and Materials.....	43
3.1 Plasma diagnostics: optical emission spectroscopy.....	43
3.1.1 Boltzmann plot method	43
3.1.2 Abel inversion	46
3.2 Materials.....	49
3.2.1 Feedstocks	49
3.2.2 Substrates.....	51
3.3 Spraying process.....	52
3.3.1 Coating deposition: spraying parameters	52
3.3.2 Substrate temperature measured by thermocouple and pyrometer.....	53
3.4 Characterization of the coatings	55
3.4.1 Microscopy	55
3.4.2 Standard X-ray diffraction and pole figure.....	56
3.4.3 Electron back-scatter diffraction	58
Chapter 4 Plasma Jet Characterization	61
4.1 Local emission intensity profiles.....	62

4.2 Temperatures	66
4.2.1 Excitation temperature profiles.....	66
4.2.2 Substrate temperatures.....	67
4.3 Concentration profiles of Ar and He.....	69
4.4 Interaction of plasma and powder feedstock	71
4.4.1 Effect of powder loading	71
4.4.2 Vapor density estimated by spectroscopy.....	72
4.5 Summary.....	74
Chapter 5 Deposition Mechanisms of Columnar Structured YSZ Coatings	75
5.1 The influence of feedstock powder.....	76
5.1.1 Powder feeding rate	76
5.1.2 Particle size and agglomeration	82
5.2 Deposition perpendicular to the axis of the plasma jet.....	86
5.2.1 Coatings deposited at different spray distances without torch swing	86
5.2.2 Coatings deposited with torch swing	97
5.3 Deposition parallel to the axis of the plasma jet.....	102
5.3.1 Coatings deposited on different substrate locations.....	102
5.3.2 Coatings deposited at high powder feeding rate.....	112
5.4 Potential growth mechanisms	116
5.4.1 Equiaxed growth.....	117
5.4.2 Preferential growth	120
5.4.3 Effects of the boundary-layer on growth	128
5.5 Summary.....	133
Chapter 6 Conclusions and Outlook	135
Reference	139
Appendix.....	153
Academic Contributions during Ph.D. Research	160
Acknowledgements.....	161

Chapter 1 Introduction and Objectives

Nowadays, thermal barrier coatings (TBCs) are essential for gas turbine engines to protect the metallic substrates from high-temperatures and corrosive attacks. The use of TBCs in conjunction with air cooling prolongs the lifetime of the components in the hot sections of gas turbines. It also offers the opportunity of increasing the inlet gas temperature, and consequently, of improving the efficiency of the gas turbine [1]. Yttria-stabilized zirconia (YSZ) is one of the most widely used materials for TBCs owing to its low thermal conductivity, high fracture toughness, and relatively high coefficient of thermal expansion [2]. In the past decades, the two main methods for manufacturing YSZ-TBCs have been atmospheric plasma spray (APS) and electron beam physical vapor deposition (EB-PVD). Typical APS coatings have a laminar structure formed by solidification of liquid droplets, consisting of layered splats and pores and cracks in-between. Different from APS coatings, EB-PVD coatings are columnar structured. Accordingly, thermal mismatch between the ceramic topcoat and metallic substrates is better accommodated by the in-plane compliance of columnar structures. However, the merits of EB-PVD coatings are gained at the expense of high thermal conductivity and high production cost.

Plasma spray physical vapor deposition (PS-PVD) has emerged to evaporate ceramic feedstock by plasma and to form EB-PVD like columnar structured YSZ-TBCs. In the PS-PVD process, the considerably low operating pressure of 50~200 Pa leads to an extend plasma jet more than 2 m in length and up to 0.4 m in diameter [3], which enables to form uniform coatings in large areas. The columnar structured TBCs produced by PS-PVD have shown improved thermal cycling lifetimes more than two times higher than conventional APS TBCs [4], good erosion resistance [5], and relatively low thermal conductivity [6]. In addition, the interaction of plasma gas and deposit species in combination with the high chamber pressure (compared with PVD) makes non-line of sight deposition possible to coat complex geometries. Up to now, the deposition mechanisms in PS-PVD are not very clear and relevant reports are limited. A structure zone model (SZM) similar to SZM of magnetron sputtered coatings [7] was reported and highlighted the effects of shadowing and diffusion in PS-PVD similar to conventional PVD [8]. Notwithstanding, some phenomena found in PS-PVD still need to be explained, for example, columnar and dense coatings were found in different regions of a sample [8]. Besides, those deposition mechanisms which are significant for

coating elaboration are unknown so that a comprehensive understanding of the process is still missing and is urgent to know. Therefore, the objectives of this work are to investigate the deposition mechanisms of TBCs manufactured by PS-PVD. It will establish the dependence of microstructures as well as crystallographic textures of the columnar structured YSZ coatings on the processing conditions: on one hand, plasma jet characteristics and its interaction with feedstock; on the other hand, vapor incidence angle (VIA), substrate temperature (T_s), deposition rate and flow conditions.

- **Structure of this thesis**

Chapter 2 gives a general introduction to TBC systems, a summary of the current knowledge of PS-PVD, and a literature review about possible mechanisms of coating deposition out of vapor phase. Chapter 3 describes the theoretical and experimental methods used in the present work, including plasma diagnostics, materials and deposition conditions, as well as characterization of the coatings. Chapter 4 and Chapter 5 comprise the results and their discussion. Excitation temperatures and constituent concentration profiles of the plasma jet under PS-PVD conditions, along with powder loading effects will be discussed in Chapter 4. The influence of powder feedstock related to powder feeding rate, particle size and agglomeration will be presented in the first section of chapter 5. The following two sections of Chapter 5 will show the microstructures and crystallographic textures of the coatings deposited at different VIAs (different orientations of the substrate related to the axis of the plasma jet). Then, the deposition mechanisms with respect to the growth process of columnar PS-PVD coatings in a sequence of equiaxed growth and preferential growth will be discussed. In the end, a concept of boundary-layer will be introduced to discuss the influence of the flow conditions in the boundary-layer and the possibility of cluster deposition. In Chapter 6, conclusions of this work and outlook will be given.

Chapter 2 Background and Current Knowledge

Thermal barrier coatings (TBCs) are highly advanced refractory materials systems and usually applied on the hottest components of gas turbine engines used to propel aircraft or to generate electricity. Fig. 2.1 shows the internal structure of an aviation engine, where an aircraft gets propulsion force and mechanical power to propel it. The air first comes into the compressor. After compression, air enters a combustion chamber into which fuel is injected and the resulting products of the combustion expand and drive the turbine. The efficiency of a gas turbine is related to the pressure ratio between the air inlet and outlet according to the Brayton Cycle [9] and to the gas temperature within the turbine [10]. To further increase the efficiency of gas turbines, one of the ways is to increase the gas temperature, which will definitely rely on the use of TBCs.

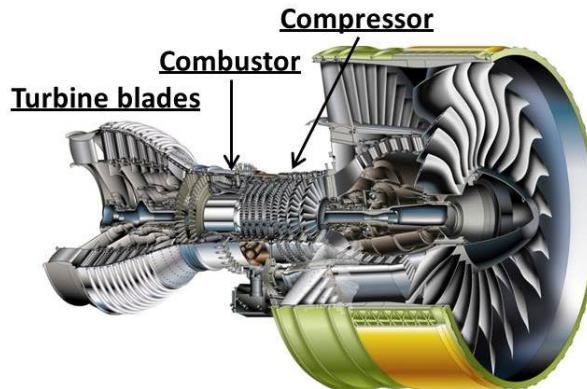


Fig. 2.1 Cutaway view of the Engine Alliance GP7200 aircraft engine; adapted from [1]

2.1 Thermal barrier coating system

TBCs were first successfully applied to turbine section components in the earlier 1960s. In the mid-1970s, a two-layer TBC consisting of a porous APS YSZ coating on a NiCrAlY bondcoat was first tested successfully on a turbine blade at National aeronautics and space administration's (NASA) [11]. By the 1980s they had entered into revenue service in the turbine section of certain commercial gas turbine engines [12]. TBCs, having a complex structure comprising metal and ceramic multilayers, prevent hot components of gas turbines from the hot gas stream to enhance

2.1 Thermal barrier coating system

the durability of turbine blades and energy efficiency of the engines [13]. As illustrated in Fig. 2.2, up to now, the use of TBCs along with internal cooling of the underlying super-alloy component, provide major reductions in the surface temperature up to 400 K of the super-alloy [1]. Therefore, TBCs are a crucial technique because the gas temperature is higher than the maximum endurable temperature of the underlying super-alloy and any failure of the TBCs could endanger the engine. Moreover, because of the interaction between the underlying super-alloy and the top ceramic layer, it is essential to consider TBCs as a complex, interrelated, and evolving material system [1].

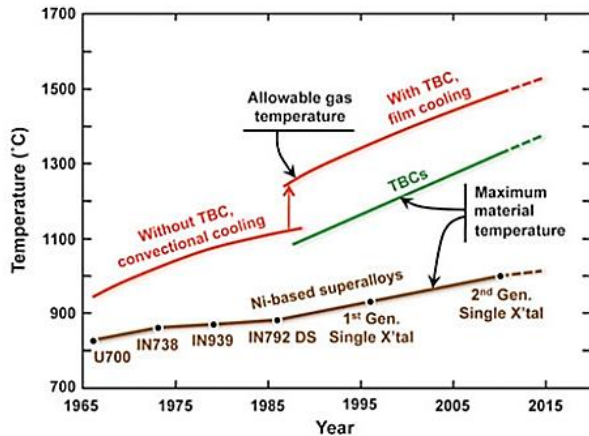


Fig. 2.2 Progression of temperature capabilities of Ni-based superalloys and thermal-barrier coating (TBC) materials over the past 50 years [1]

2.1.1 The structure of TBCs

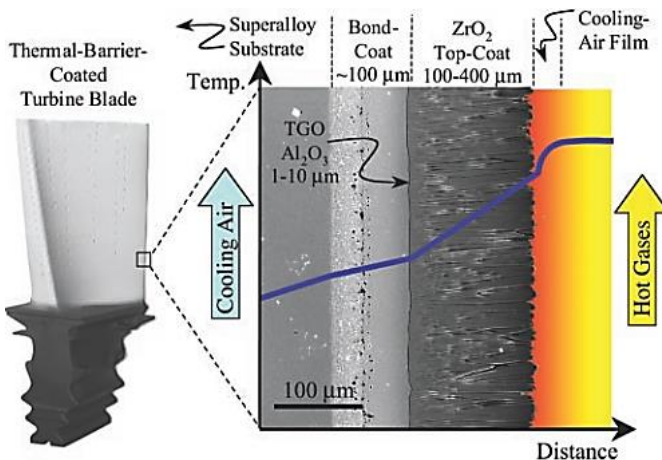


Fig. 2.3 Cross-sectional scanning electron micrograph (SEM) of an electron beam-physical vapor deposited TBC, superimposed onto a schematic diagram showing the temperature reduction provided by the TBC [13].

As shown in Fig. 2.3, a typical thermal barrier coating system on a super-alloy substrate contains three sublayers: metallic bondcoat (BC), ceramic topcoat, and the thermally grown oxide (TGO) growing between the BC and the topcoat during operation.

- **Substrates**

Generally, high-temperature-resistant Ni-based superalloys are now utilized as the substrates, which are air-cooled from the inside through internal hollow channels. Ni-based superalloys are complex alloys with various microstructural features that contribute to their mechanical properties [14]. These features include grain size, size and distribution of γ' -phase, carbide- and boride-phase content, and grain-boundary morphology. The super-alloy component is casted in single-crystal or poly-crystalline forms. In a polycrystal Ni-alloy, the grain size and grain boundaries are the most important issues because the grain boundaries are sites for damage accumulation and fast diffusion at high temperatures and thus greatly influence strength, creep, and fatigue crack initiation [15]. Thus, the blades in the early stages of the turbine (hotter) are nowadays typically single crystals, whereas the blades in the later (cooler) stages of the turbine are fabricated from equiaxed alloys [16]. The γ' is an intermetallic phase based on $\text{Ni}_3(\text{Al}, \text{Ti}, \text{Ta})$ phase, coherent with the matrix (γ phase) of the superalloy to strengthen the alloy matrix [17]. Carbides and borides are beneficial to wrought processed nickel-based super-alloy turbine discs. They improve grain boundary performance during creep through grain boundary sliding resistance [14]. The superalloy contains as many as 5 to 12 additional elements that are added for the enhancement of specific properties such as high-temperature strength, ductility, oxidation resistance, hot-corrosion resistance, and castability [18]. At the high temperature of operation, diffusion of high relative concentration elements occurs between superalloy substrate and bondcoat, which can reduce the specific properties of the superalloy.

Besides, it seems to exist an intrinsic, and not easily surmountable, limit for high-temperature applications of metallic materials [19]. However, the development of a new generation of gas turbines for higher combustion temperatures requires new materials that can withstand temperatures of up to 1500 °C for several thousand hours. Ceramic matrix composites (CMCs) were reported to show extremely promising properties for use in higher performance turbine engines [19]. CMCs are generally fabricated at high temperature, thermal mismatch between components has a very important influence on CMC performance because of limited matrix ductility [20]. Environmental barrier coatings (EBCs) are required to prevent CMCs from accelerated

oxidation and volatilization due to exposure to steam in high temperature combustion environments [21]. In addition, some key technologies, such as the processing of ceramic matrix composites, improving the required properties with the available reinforcements, and the establishment of a design method and the development of non-destructive evaluation techniques, require further development before CMCs can be used widely in service [22, 23].

- **Bondcoat and thermally grown oxide**

On the top of the substrate, a metallic BC is deposited, which on one hand accomplishes a better bonding with the topcoat and on the other hand prevents the substrate from oxidation [24]. Metallic alloys like diffusion aluminides [25] and MCrAlY-type (M= Ni, Co, Fe) coatings or combinations are most widely used for mitigating degradation in harsh environments. The diffusion aluminide coatings are based on β -NiAl phase and MCrAlY coatings are based on a mixture of β -NiAl, γ -fcc solid solution, and γ' -Ni₃Al phases.

Diffusion aluminides is often made by inexpensive pack cementation. More advanced processes include vapor phase aluminizing (VPA) and chemical vapor deposition (CVD). The latter one is used especially when there is a need to coat also the internals of components [26]. MCrAlY coatings are manufactured by thermal spray methods, such as, low pressure plasma spray (LPPS), high velocity oxy-fuel (HVOF), and can also be deposited by EB-PVD [27].

At elevated temperature, the oxidation of the BC results in the formation of a TGO at the interface of BC and topcoat, which mainly is α -Al₂O₃. This thin TGO acts as a diffusion barrier to suppress formation of other detrimental oxides, thus protecting the substrate from further oxidation and improving the durability of TBC system [28]. A pre-oxidation treatment in low-pressure oxygen environments can suppress the formation of the detrimental oxides by promoting the formation of an Al₂O₃ layer at the ceramic topcoat/bond coat interface [29]. It is also reported to increase the durability of EB-PVD coatings because pre-oxidation forms a thin α -Al₂O₃ layer on the BC [30]. Standard MCrAlY coatings have high content of Al (8-12 wt.%) which selectively oxidizes to insure formation of a continuous Al₂O₃ layer during high temperature oxidation. Also, a significant amount of Cr (18-22 wt.%) can be added to the coatings for high temperature corrosion resistance and promoting formation of a continuous Al₂O₃ layer at lower Al concentrations [31]. Yttrium as a reactive element (Y \leq 1 wt.%) promotes TGO adhesion by tying up impurities like sulfur in the coating [32]. In the

meanwhile, the BC and superalloy substrate try to reach chemical equilibrium and form interdiffusion zones. This bi-directional diffusion results in the loss of protective elements [33], like Al, and is a main degradation mechanism for the MCrAlY coatings. Therefore, many other elements additions, such as Si, Ti, La, Ce, Hf, Pt, etc., were also studied to reduce the β -NiAl to γ/γ' -Ni₃Al phase transformation rate during thermal cycling, reduce the TGO growth rate and improve resistance to delamination of TBCs, and/or improve resistance to hot corrosion [34-36].

- **Topcoats**

The topcoat provides the thermal insulation and is typically made from ceramic materials, such as the frequently-used yttria-stabilized-zirconia (YSZ) in which metastable tetragonal YSZ is used for TBCs. It was first reported at room temperature and termed “ceramic steels” in 1975 [37]. Up to now, two main methods used for TBC topcoat deposition are (i) atmospheric plasma-spray (APS) and (ii) electron beam physical-vapor deposition (EB-PVD). The former one was first brought into application at the NASA Lewis research center [11]. The latter one was developed at Pratt & Whitney in the late 1970s [38]. The columnar structured YSZ coating shown in Fig. 2.3 is made by EB-PVD. It imparts the TBCs superior strain tolerance because they can separate at high temperatures, accommodating thermal expansion mismatch stresses [39]. The main work of this study is about the topcoat, so the detailed knowledge about topcoats will be summarized below.

2.1.2 Ceramic materials for topcoats

Considering the extremely harsh operating environment of TBCs, the requirements for materials are: i) high melting point, ii) low thermal conductivity, iii) good high temperature phase stability, iv) chemical inertness, v) high sintering resistance, and vi) similar coefficient of thermal expansion to the metallic substrate.

- **YSZ**

In principle, zirconia (ZrO₂) could be used in TBCs because it has a high melting point up to 2700°C, low thermal conductivity and high resistance to chemical reaction. However, zirconia also has its drawbacks. A phase transformation between monoclinic phase (m) and tetragonal phase (t) happens during heating up (1180 °C) and cooling down (950 °C) along with a volume shrinkage or expansion (4–6 %) and the associated cracking would have a detrimental effect on coating life. To solve this problem, some stabilizers are added to avoid the transformation, such as magnesia (MgO), calcia

2.1 Thermal barrier coating system

(CaO), and yttria (Y_2O_3). The problem with ZrO_2 -MgO and ZrO_2 -CaO is related to "destabilization" from the cubic fluorite (f- ZrO_2) phase that is observed in the as-sprayed material to the monoclinic (m- ZrO_2) phase [40].

The majority of TBCs in use today are made from YSZ containing 7~8 wt.% Y_2O_3 ($\approx 7.6\sim 8.7$ mol% $YO_{1.5}$) (termed as 7-8YSZ). According to the phase diagram proposed by Scott [41], at room temperature, 7-8YSZ is metastable non-transformable tetragonal phase (t') while the high temperature phase is cubic. Between these two phases, there is a two-phase region at the temperatures of 600~2000 °C where the phase composition is a mixture of the t' and c phases. The addition of Y_2O_3 more than 8 mol% will form fully stabilized zirconia at room temperature. The structure becomes a cubic solid solution and has no phase transformation when heating from room temperature up to 2500 °C. Because of its high oxygen ion conductivity, fully stabilized YSZ is often used as oxygen sensor and electrolyte for solid oxide fuel cells [42, 43]. For TBCs, fully stabilized YSZ is not favorable because of its poor thermomechanical characteristics, e.g. low toughness.

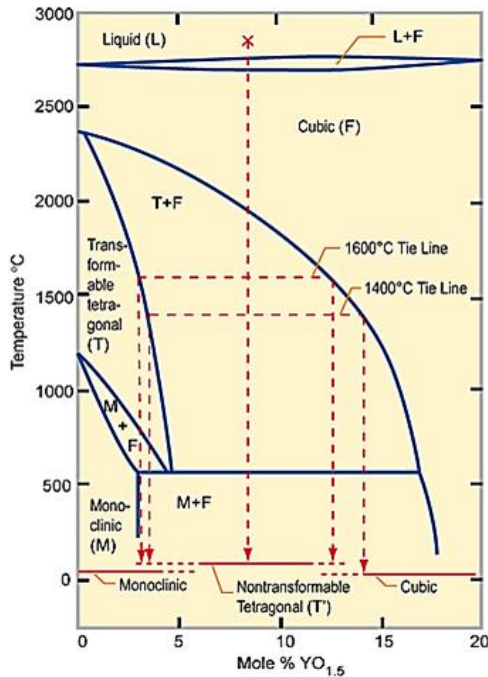


Fig. 2.4 Low yttria region of ZrO_2 - Y_2O_3 phase diagram; adapted from [44]

The phase diagram modified by Miller et al. [44] (Fig. 2.4) shows the main existence of the t phase in the range of 0-6 mol% $YO_{1.5}$. The addition of Y_2O_3 allows obtaining t'

phase up to approx. 13 mol%YO_{1.5}. The slope of the line dividing the transformable tetragonal phase (t) and t'+c is of significance. Because of heating to an elevated temperature for a long duration, t' decomposes into high yttria and low yttria containing phases. The latter (forming t phase) transforms to monoclinic phase on cooling down with a large detrimental volume change as mentioned above [24, 44, 45]. Hence, the stability of t' is important for TBCs and phase analysis can be a tool to analyze the failure of TBCs. In many research works [44-47], the region from 72° to 76° in an X-ray diffraction pattern containing peaks (004) and (220) of tetragonal phase is always used to estimate the composition of the tetragonal phase. The ratio of lattice parameters can be used to distinguish t and t' phase by determining the tetragonality that is the value of $c/a\sqrt{2}$ [48].

The YSZ possesses a suite of desirable properties that make it the material of choice for the topcoat [49]. First, YSZ has a high melting point (~2700 °C), making it suitable for high temperature application. It has one of the lowest thermal conductivities of all ceramic materials due to the high concentration of defects (oxygen vacancies, substitutional solute atoms), which scatter heat-conducting phonons [50]. YSZ has a high thermal expansion coefficient (~11-13 x10⁻⁶ K⁻¹) close to the underlying metallic layer (15~18 x10⁻⁶ K⁻¹), which helps to alleviate the stress arising from the mismatching thermal coefficients between them [24]. Finally, 7-8YSZ has been shown to have unusually high fracture toughness. The toughening in 7-8YSZ does not arise from the martensitic transformation but rather from reversible ferroelastic domain switching from one tetragonal variant to another when stressed even at high temperature [51, 52]. All of these properties make YSZ to be the most suitable material for TBCs for a long period and even now it is still the state of art for topcoat materials.

- **Alternative topcoat materials**

In order to comply with the growing demands of the improved fuel efficiency of gas turbines, high-performance materials are in need to be exploited. Until now, a number of new ceramic materials were researched to alternate the standard material YSZ, e.g. pyrochlore structured oxides A₂B₂O₇, defect cluster TBCs (zirconia doped by rare-earth cations), lanthanate hexaaluminates, and ABO₃ perovskites [24]. In comparison with 7-8YSZ, these materials have their own advantages and disadvantages as listed in Table 2.1.

2.1 Thermal barrier coating system

Table 2.1 Topcoat materials and their characteristics (Summarized based on ref. [24, 53])

Materials	Advantages	Disadvantages
7-8YSZ	<ul style="list-style-type: none"> ✓ High thermal expansion coefficient ✓ Low thermal conductivity ✓ High fracture toughness 	<ul style="list-style-type: none"> ✗ Sintering above 1200 °C ✗ Degradation of t' phase (phase transformation) ✗ Corrosion
Pyrochlores (e.g. Gd₂Zr₂O₇)	<ul style="list-style-type: none"> ✓ High thermal stability (no phase transformation up to 2000 °C) ✓ Low thermal conductivity ✓ Low sintering tendency 	<ul style="list-style-type: none"> ✗ Relatively low thermal expansion coefficient ✗ Low fracture toughness
Defect cluster materials (e.g. ZrO₂-Y₂O₃-Gd₂O₃-Yb₂O₃)	<ul style="list-style-type: none"> ✓ Low thermal conductivity ✓ High thermal stability ✓ High thermal expansion coefficient 	<ul style="list-style-type: none"> ✗ Low thermal cycling lifetime
Hexaaluminates (e.g. LaMgAl₁₁O₁₉)	<ul style="list-style-type: none"> ✓ High melting point ✓ High thermal expansion ✓ Low thermal conductivity ✓ High sintering resistance ✓ Structural stability up to 1800 °C 	<ul style="list-style-type: none"> ✗ Shrinkage caused by recrystallization
Perovskites (e.g. SrZrO₃)	<ul style="list-style-type: none"> ✓ High melting point ✓ Good cycling performance above 1250 °C 	<ul style="list-style-type: none"> ✗ Phase transformation ✗ Low fracture toughness

In comparison, TBCs made of pyrochlores and defect cluster materials have a lower thermal conductivity and relatively high thermal expansion coefficient, are the most interesting and promising alternative materials. Among pyrochlores, rare-earth doped zirconates are the most interesting materials. Wherein, Gd₂Zr₂O₇ and La₂Zr₂O₇ seem to be the most promising for TBC application due to their outstanding bulk properties compared to standard YSZ, which have a high thermal stability up to 2000 °C, a low thermal conductivity [54] and a low sintering tendency [24]. However, Gd₂Zr₂O₇ show significantly lower fracture toughness, thus a double-layer system with a first layer of YSZ and a top layer made of pyrochlore materials is needed to improve the thermal cycling lifetime [55, 56]. Although the loss of lanthania and gadolinia during spraying forming nonstoichiometric coating of non-stabilized ZrO₂ might be detrimental to the coating performance, it was found that the gadolinia evaporation is less pronounced than the lanthania evaporation [56]. Likewise, other materials also show different issues during processing and cycling lifetime test. Hence, applications of the above-mentioned materials as TBCs on real hot components still need further investigations. Also, this is the reason for continuing to use 7-8YSZ as the topcoat materials.

2.1.3 Manufacturing methods of topcoats

In the past decades, two methods APS and EB-PVD have been widely used to manufacture topcoats with different microstructures as shown in Fig. 2.5. The typical APS coating is formed by solidification of liquid droplets consisting of layered splats, pores and cracks. Completely different to APS coatings, EB-PVD coatings have a relatively homogeneous columnar structure composed of compact single columns.

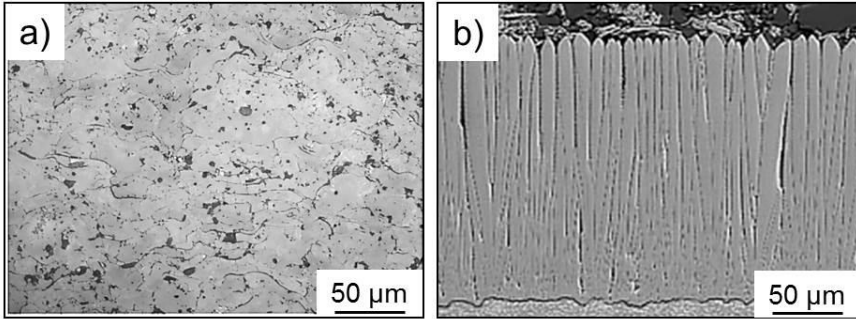


Fig. 2.5 Cross-section of YSZ coating deposited by a) APS [57] and b) EB-PVD [3]

- APS

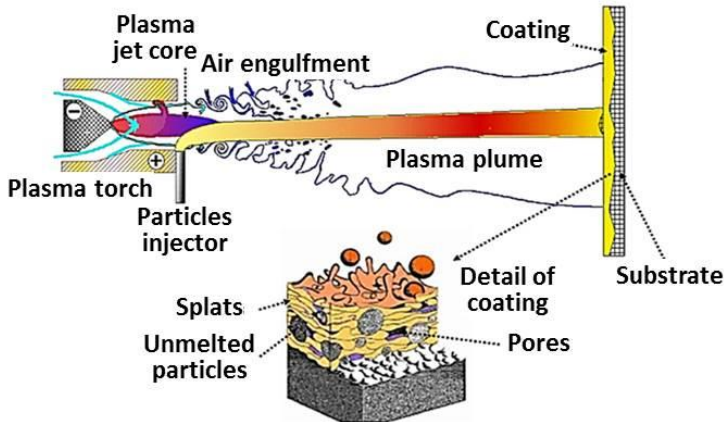


Fig. 2.6 Schematic of the different steps of the plasma spray process [58, 59]

In the APS process, the plasma gas (Ar, He or H₂) is ionized in a plasma generator to form a high-energy and high-speed plasma jet. The powder feedstock is injected in the plasma by the carrier gas, being melted and accelerated by the plasma jet to impinge on the substrate. On the substrate, the molten droplets flattened and solidified (called as splats) forming lamellar coating under atmospheric conditions. Due to the rapid solidification, the derived *t'* phase of YSZ can be formed in APS coatings. As the

2.1 Thermal barrier coating system

powder feedstock can have a size distribution between a few micrometers and more than 100 micrometers, the splats have varied thicknesses and some unmelted particles are directly incorporated in the microstructures as shown in Fig. 2.6. Thus, between these splats, globular pores, interlamellar pores, cracks in the splats are coexisting in the coating, which give the coating a wide range of properties and performance in service by controlling these defects. In general, the porosity of an APS coating varies from less than 2% to more than 20% depending on the type of powders and the spray parameters used, which contribute to the low-thermal conductivity of APS TBCs [60]. In addition, the microcracks can also determine the performance and lifetime of the coatings by affecting the thermal conductivity and mechanical properties.

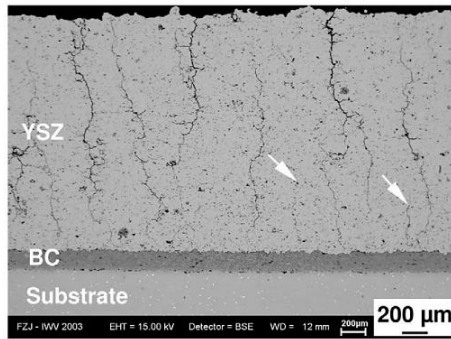


Fig. 2.7 SEM image of cross-section of TBCs with segmentation cracks [61]

To improve the efficiency of gas turbines by increasing the allowed inlet gas temperature, massive efforts have been invested to improve the thermal insulation properties of the TBCs. Thicker topcoats up to 1 mm were found to improve the thermal insulation, but reductions of adhesion and thermal shock resistance were also observed [62]. Later, topcoats with segmentation cracks were made to improve the strain tolerance of the coatings and thereby to improve the thermal shock resistance [61]. Segmentation cracks are cracks running perpendicular to the coating surface and penetrating at least half of the coating thickness as shown in Fig. 2.7. To obtain such segmentation crack, a high substrate temperature and also high powder feeding rate are needed. High liquid droplets temperature can also increase the segmentation crack density [63]. However, such coatings have higher thermal conductivity compared with porous APS coatings, and thus advanced processing methods need to be developed to increase segmentation crack density and porosity at the same time. APS coatings can provide good thermal protection, and due to advantages of low cost and higher deposition rates, it is now mostly employed for deposition of topcoats on the hot components like burner cans or combustion chambers.

- **EB-PVD**

In the EB-PVD process, a YSZ ingot is evaporated by a high energetic electron beam in a high vacuum chamber as shown in Fig. 2.8 [64], and the coating is developed by vapor condensation. By controlling power, diameter and position of electron beam, thickness and homogeneity of coating can be accurately controlled. Besides, the substrate can be heated up to a desired value being well monitored by a thermocouple, and typically controlled within ± 10 °C. Due to its line of sight deposition, the substrate has to be rotated by a controlled velocity to obtain homogeneous coating thickness and microstructures [65]. To achieve defined stoichiometric zirconia, a controlled amount of oxygen is led into the deposition chamber. Besides, the deposition parameters, such as chamber pressure, substrate temperature, rotation speed, and vapor incident angle affect the morphology and microstructure of the EB-PVD coatings.

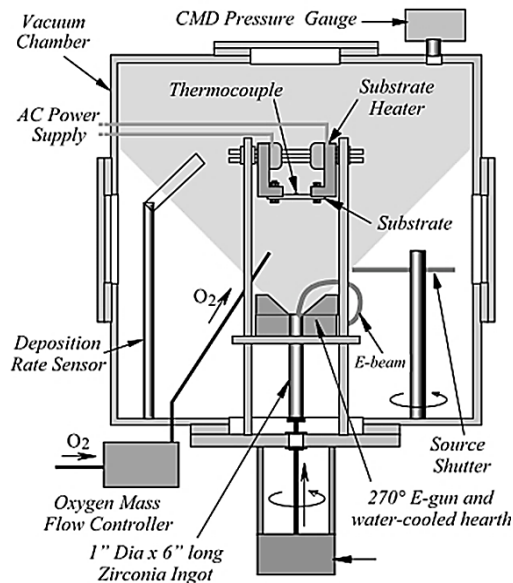


Fig. 2.8 Schematic of a EB-PVD system [64]

Because of their specific microstructure as shown in Fig. 2.5b, the columnar structured coatings possess superior strain tolerance against thermal shock compared with porous APS coatings, thus giving significant rise of the lifetime under hash cycling loading. EB-PVD is particularly favored for applications on more pretentious components, such as rotating parts like high pressure turbine blades [38]. However, this columnar structure also brings a higher thermal conductivity to EB-PVD coatings. To further optimize the thermal conductivity, improved the microstructures or alternative materials having intrinsically low thermal conductivity are required.

2.1 Thermal barrier coating system

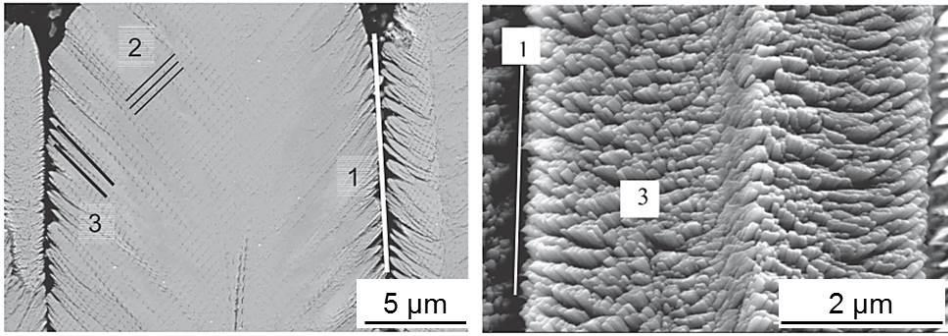


Fig. 2.9 Morphology of EB-PVD P-YSZ TBCs in polished (left) and fractured cross section (right) in as-coated condition [66]

Intensive efforts were devoted to modify the porosity of the EB-PVD coatings to reduce its thermal conductivity and to improve the lifetime [64, 67-70]. Before that, one has to understand the origin of the different microstructural features, their contribution to thermal insulation, and their changes during service. In EB-PVD coatings, three types of porosity features are well defined as shown in Fig. 2.9 [66]. Columns and inter-columnar gaps denoted as type 1 originated from macroscopic shadowing and rotation of the substrate. They contribute mainly to the strain tolerance of the TBCs. Globular and elongated spheroid type 2 pores are believed to consist mostly of closed porosity and are a consequence of rotation [71]. The last type 3 referred to as “feather arms” is a consequence of shadowing by growth steps on the column tips near the center of a column [64]. Lower thermal conductivities of EB-PVD TBCs rely mainly on type 2 and 3 intra-columnar porosity while type 1 inter-columnar porosity is less effective [72].

It was found that EB-PVD deposition at high chamber pressure (~ 1.8 Pa) and low substrate temperature (~ 970 °C) possess a low density of TBCs characterized by larger gaps between the columns and an increasing column diameter with thickness, offering a reduction of thermal conductivity [66]. The zig-zag structured EB-PVD coatings by tilted angle between vapor incidence and substrate provide a significant reduction of the thermal conductivity up to 40% as well as erosion resistance [66]. Hereafter, layered structures at a finer scale (layers of 1 μm) produced by switching the D.C. bias applied to the substrate during deposition were introduced to reduce 37–45% of the thermal conductivity while maintaining the erosion resistance [73]. Beyond improving microstructures, massive efforts were also put on the deposition of new materials, such as pyrochlores as mentioned above [74]. Since the attack by calcium-magnesium-alumino-silicate (CMAS) infiltration on TBCs was reported [75], this has caused much attention on degradation mechanism, in particular concerning

columnar structured EB-PVD coatings into which CMAS is supposed to penetrate more easily, changing the near-surface mechanical properties and enhancing the spalling tendency [76]. This also promotes the search for new materials to withstand CMAS attack.

Beside the properties, performance, and processing, the related deposition mechanisms of EB-PVD is a complicated topic, because it depends on several aspects: the deposition conditions, nucleation, surface energy, surface and volume diffusion, coating composition, and so on. In spite of this, the relationship between processing conditions and microstructure are related to the fundamental coating properties. This is undoubtedly significant for finally improvement of coating's performance. For EB-PVD, some studies have been carried out to establish and quantify the microstructure as well as crystallographic texture dependence on processing conditions, mainly vapor incidence angle (VIA), substrate temperature (T_s), chamber pressure and deposition rate. The crystallographic textures of EB-PVD YSZ coatings with respect to the processing parameters are summarized in Table 2.2.

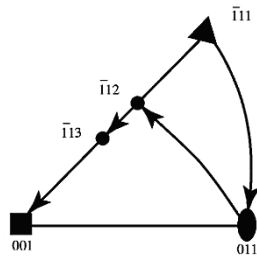


Fig. 2.10 The order of extinction of observed crystal orientations in the form of a $\{001\}$ stereographic triangle for a cubic system [77]

Fiber texture of (111) is normally found at a low substrate temperature (lower than 900 °C) while a preferred orientation (200) was dominant at high substrate temperature. Columnar grains are approximately oriented in the $\langle 100 \rangle$ direction. The VIA and substrate rotation can also affect the texture and planes such as (110), (311), and (211) are also observed [78]. Wada et al. [77] summarized the crystal orientations observed during the EB-PVD process and plotted on a standard stereographic triangle based on a $\{001\}$ pole as shown in Fig. 2.10. Arrows in this diagram connecting the two poles indicate the order of the extinction that reveals that extinction of crystals occurs from the crystal $\{111\}$ pole to $\{011\}$ pole, and moves in turn to $\{001\}$ pole.

2.1 Thermal barrier coating system

Table 2.2 Crystallographic textures of 7-8 YSZ deposited by EB-PVD

Reference	VIA	Substrate temperature (°C)	Chamber pressure (Pa)	Texture	Remarks
Unal, (1994) [71]	N.A.	1050	N.A.	(200)	
Sohn, (1994) [78]	0°	900	1.33	(111)	The temperature was chamber temperature, 100-200 K higher than substrate temperature
	20°	900		(211)	
	0°	1100		(311)	
	0°	1130		(200)	
	20°	1130		(110)	
Schulz, (1996) [79]	0° - 15°	920-1100	0.2-0.6	<100>	
	15° - 40°			<113>	
Terry, (1999) [64]	0°	900	1.3	<111>	
	45°	900		<101>	
	0° - 45°	1100		<101>	
An, (1999) [67]	N.A.	700	0.13-1.33	(111)	Texture of (111) on (111) substrate
		950-1150		(200)	
Schulz, (2000) [80]	0°	980-1050	N.A.	<113>	Stationary Stationary Rotated
	> 0°			<111><110>	
				<111>	
Heydt, (2001) [81]	0°	700-900	N.A.	(111)	Epitaxial (111) on (111) substrate
		1050		(200)	
Schulz, (2003) [65]	0°	995	1.0	(200) (220)*	Rotation mode A Rotation mode P
		935		(200)	
Wada, (2004) [77]	0°	652-748	1.0	(111)	
		845		(111)&(200)	
		938-1047		(200)	
Wada, (2005) [82]	N.A.	938		(111) (200)&(220)*	Stationary Rotation speed 10 rpm
Zhao, (2006) [83]	N.A.	1000±20	3.3-13.3	(111) (200)&(220)*	Stationary Rotation speed >1 rpm

* In-plane texture

Schulz et al. stated that in the early stage of coating growth a thin equiaxed zone of randomly orientated grains was observed [79, 80]. As shown in Fig. 2.11, the first thin layer (approximately 0.1 µm thick) adjacent to the substrate (so-called equiaxed zone) consists of equiaxed grains of about 30 nm in diameter. The selected area diffraction patterns originating from a number of crystallites clearly show that no preferred orientation exists in it. Its thickness varied from 0 µm to 0.2 µm [80]. The formation of the equiaxed zone was ruled mainly by the energy of the condensing adatoms and their charging state [80]. But in a previous study [71], high energetic vapor atoms caused by a negatively biased substrate were found to lead to an increase in thickness of the equiaxed zone from 0.2 to 2 µm, which later was testified as caused by the geometry rather than bias-voltage. Immediately after the equiaxed zone, columns start to grow

along $\langle 100 \rangle$ directions and the final symmetry appears within the first 2-5 μm [80]. The texture becomes sharp with growth of coating. This was explained by an evolutionary selection so that the structure will be dominated by grains through the thickness of the film having nearly the same “fast growth” axis, which results in a strong fiber texture of the film [65]. Fiber textures are common for PVD because the vapor flux defines a preferred growth direction vertical to the substrate surface on a stationary substrate. Beside fiber textures, a fourfold in-plane texture (220) was well known at high rotation speed of the substrate [80, 82, 83]. But loss of the fiber character was observed for high VIAs and high deposition rates [80].

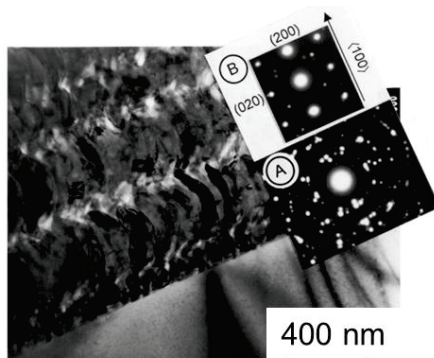


Fig. 2.11 TEM micrograph of ‘root’ area in higher magnification; inset A: selected area electron diffraction (SAED) pattern of the equiaxed zone; inset B: SAED pattern of the second layer with bent crystals. Adapted from [80]

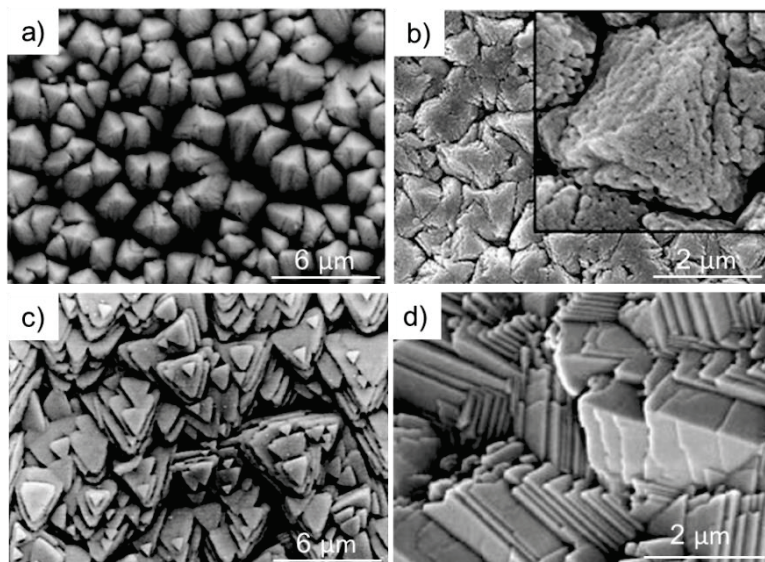


Fig. 2.12 Surface morphologies of EB-PVD coatings deposited under different conditions showing different textures: a) $\langle 001 \rangle$, b) and c) $\langle 111 \rangle$, d) $\langle 101 \rangle$. Adapted from [77], [83], [64] and [77], respectively.

The morphologies of the EB-PVD coatings vary with the textures under different deposition parameters. For example, Fig. 2.12 shows some EB-PVD coatings deposited with stationary substrate, wherein the orientation of a) is $\langle 100 \rangle$, b) and c) is $\langle 111 \rangle$, d) is $\langle 101 \rangle$. The $\langle 001 \rangle$, $\langle 111 \rangle$, and $\langle 101 \rangle$ growth directions for the columns seem to be defined by tips consisting of $\{111\}$ facets arranged as, respectively, a four-sided pyramid (Fig. 2.12a), a three-sided pyramid (Fig. 2.12b) or flat (Fig. 2.12c), and a two-sided “rooftop” (Fig. 2.12d).

- **Suspension plasma spraying**

Another thermal spray process, the so called suspension plasma spraying (SPS) is an emerging coating technology, in which the powder feedstock is dispersed in a liquid suspension before being injected into the plasma jet. Conventional APS cannot process fine-grained feedstock powders smaller than $\sim 10 \mu\text{m}$ in size because the powder must be flowable [84]. In SPS, the use of suspensions yields a higher flexibility so that even nano-scaled materials can be processed forming small molten droplets with a diameter of a few hundred nanometers to a few micrometers. This leads to much smaller splats compared to conventional APS splats [85]. Thus, advanced microstructures can be formed by SPS as shown in Fig. 2.13. Porous structure with segmentation cracks and columnar structures can be produced, which provide high strain tolerance to TBCs compared with porous APS coatings. Besides, the SPS coatings exhibit finer pores than the standard APS ones, which contribute to very low thermal conductivity of approx. 0.5 to $1 \text{ Wm}^{-1}\text{K}^{-1}$ [86].

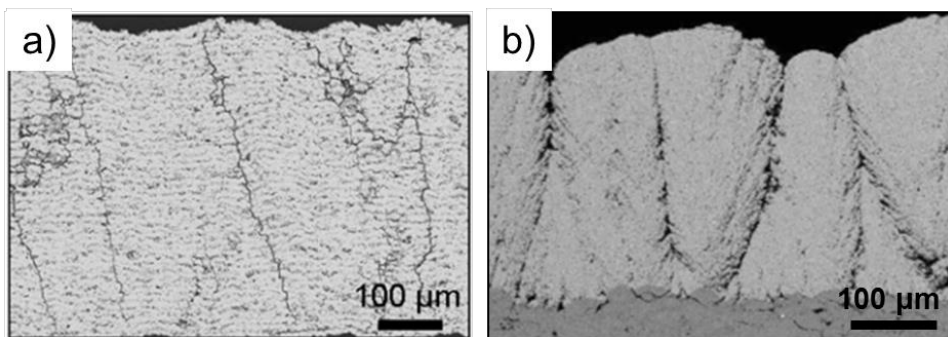


Fig. 2.13 Cross sections of SPS YSZ coatings showing a) porous structure with segmentation cracks [86] and b) columnar structure [87]

However, for tests at $1400 \text{ }^\circ\text{C}$, the lifetime of SPS YSZ coatings with segmentation cracks is still approximately 50% lower than that of standard APS YSZ coatings. This might be caused by fast sintering of YSZ at $1400 \text{ }^\circ\text{C}$ [86]. One development direction

for SPS is to modify the microstructures of SPS coatings. For example, the columnar structured TBCs (Fig. 2.13b) being in some extent similar to EB-PVD coatings, but their thermal cycling lifetime is still not been sufficiently investigated. Another development direction is to combine the microstructural benefits of SPS with new TBC materials such as zirconate pyrochlores which have lower sintering tendency than YSZ.

- **Chemical vapor deposition**

The interest in TBCs on large and complex shaped components has promoted the use of chemical vapor deposition (CVD) to deposit YSZ coatings because of its advantageous capability to coat complex surfaces uniformly with excellent conformal coverage [88] as well as to deposit EB-PVD like columnar structure. However, CVD is known to have deposition rate below $10 \mu\text{m/h}$ ($\approx 0.17 \mu\text{m/min}$). Various means, such as plasma enhanced CVD (PECVD) [89], and laser CVD [90, 91], were utilized to improve the deposition rate. Fig. 2.14 shows two examples of YSZ coatings deposited at improved growth rates by laser CVD [90]. A medium deposition rate ($3.83 \mu\text{m/min}$) along with the substrate pre-heating temperature of $750 \text{ }^\circ\text{C}$ led to a columnar microstructure with well-developed faceted tops (Fig. 2.14a) orientated along (200). By further increasing the precursor flux rate, a higher deposition rate of $11 \mu\text{m/min}$ resulted in a cone-shaped structure (Fig. 2.14b) as well as in large number of nano-pores in grains leading to a significantly smaller thermal conductivity of 0.7 W/mK . Pr auchaat et al. reported that the PECVD coatings deposited at $900 \text{ }^\circ\text{C}$ exhibited good resistance towards sintering [89]. Notwithstanding, the low deposition rate of CVD causing high costs limits its application.

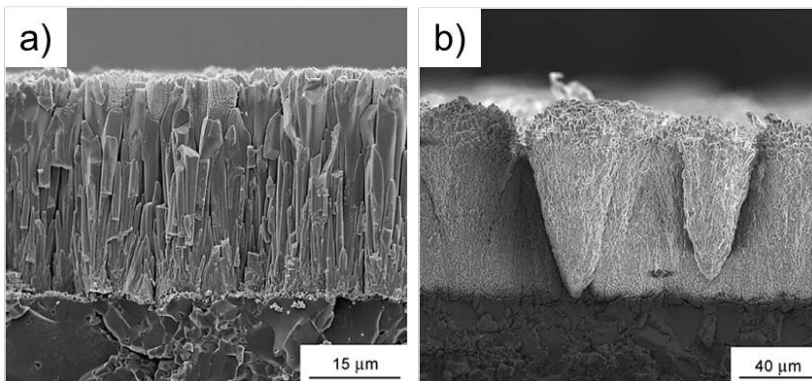


Fig. 2.14 Cross-section of an YSZ coating prepared at a deposition rate of a) $3.83 \mu\text{m/min}$ and b) $11 \mu\text{m/min}$ [90]

Besides the above mentioned processes, another way to produce finely structured coatings is to evaporate powder feedstock by plasma spraying, which leads to the subject of this work “plasma spray-physical vapor deposition (PS-PVD)”, a novel technology combining the advantages of APS and EB-PVD: cheap, fast, and good performance.

2.2 Plasma spray-physical vapor deposition

In the low-pressure plasma spraying (LPPS), formerly termed as vacuum plasma spraying (VPS), a typical pressure is 5~20 kPa. When the chamber pressure reduces to a very low level (a typical pressure of 5-200 Pa), the characteristics of plasma change compared with LPPS, leading to a jet more than 2 meters in length and a diameter ranging from 200 mm to 400 mm as shown in Fig. 2.15 [92]. Therefore, it was developed for the aim of thin and uniform coatings with large area coverage [92, 93]. Initially, the coating was mainly deposited by molten droplets forming thin and dense films, so this technique was firstly called LPPS-TF by Sulzer Metco AG (Switzerland). In 2010, Sulzer Metco AG developed the electrical input power up to 180 kW along with specific powder feedstock so that the major fraction of the powder feedstock is evaporated and the deposits mainly come from vapor phase. Thus, the process is referred to as plasma spray-physical vapor deposition (PS-PVD) [94]. Moreover, the interaction of plasma gas and feedstock vapor phase makes the non-line of sight deposition possible to deposit high quality columnar structured coatings not only on the front side of the substrate but also on the shadowed parts, which is not possible by using conventional PVD or plasma spraying [95].

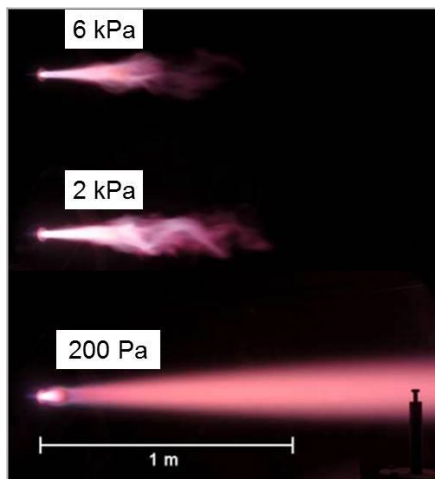


Fig. 2.15 Photos of Ar/He plasma jets at different chamber pressures [96]

2.2.1 Plasma characteristics and interaction with feedstock in PS-PVD

Similar to conventional thermal spray, in PS-PVD process, the plasma gases (commonly Ar, He, H₂ and N₂) are ignited and ionized by applying a DC current between the cathode and the nozzle shaped anode in the plasma generator. The feedstock is also injected in the nozzle. Thus, the initial interaction between plasma and feedstock occurs here. Fig. 2.16 shows a cross-section drawing of the O3CP nozzle used in PS-PVD; the powder is injected at position 1.

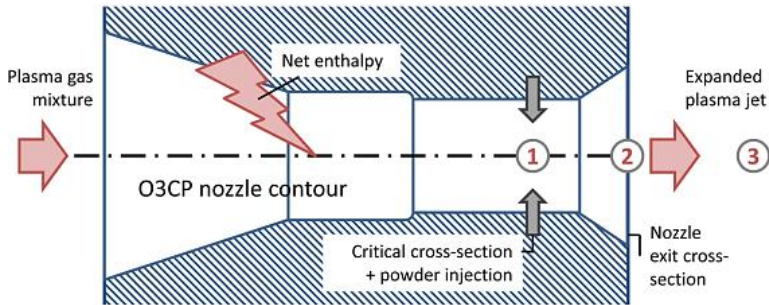


Fig. 2.16 Cross-section through the O3CP torch nozzle: the nozzle throat (position 1), the nozzle exit (position 2), and the expanded plasma jet (position 3) [97]. The cathode is not shown here.

Mauer [97] has calculated the plasma characteristics and plasma particle interactions at positions 1, 2, and 3 as shown in Fig. 2.16 by the modeling approaches developed by Chen et al. [98, 99]. For three different process parameters (the plasma gas composition and currents are indicated), the calculated temperatures (Fig. 2.17a) reveal that the Ar/He parameter provides the hottest condition. The addition of H₂ lowers the temperature due to the energy consumption for H₂ dissociation [97]. The pressures (Fig. 2.17b) at the nozzle exit are larger than the chamber pressure so that the plasma jets are underexpanded in the region very close to the nozzle exit. Then, it expands immediately after the nozzle to accommodate to the chamber pressure.

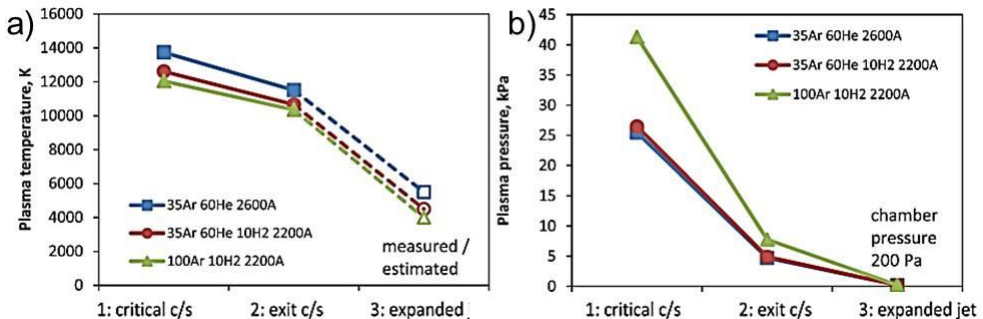


Fig. 2.17 Calculated plasma properties, a) temperatures, and b) pressures at the nozzle throat (critical c/s), nozzle exit (exit c/s), and in the expanded jet [97]

2.2 Plasma spray-physical vapor deposition

The calculated Knudsen numbers (Kn) (Fig. 2.18) for a representative particle with a diameter of $1\ \mu\text{m}$ indicate that free molecular flow conditions prevail under PS-PVD conditions because the Knudsen number is much larger than 10, in particular in the expanded jet. The Reynolds numbers of the expanded jet are in the range of 100 [100]. So the expanded plasma jet is highly laminar, and the interaction of the plasma jet with the surrounding atmosphere is weak [8]. In consequence, the plasma jet is less cooled and decelerated. Therefore, the temperature and velocity distributions in the expanded plasma jet are at a high level and more uniform compared to conventional spraying processes.

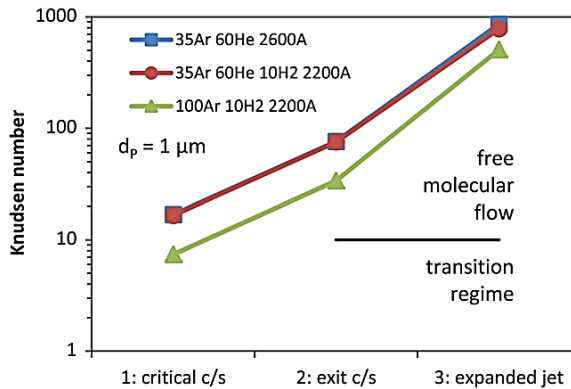


Fig. 2.18 Kn numbers calculated at the nozzle throat (critical c/s), nozzle exit (exit c/s), and in the expanded jet [97]

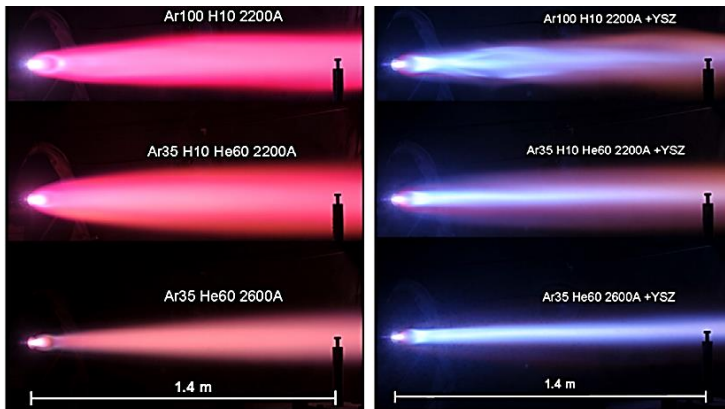


Fig. 2.19 Photographs of PS-PVD plasma jets generated by different gas compositions [92]

The photos of the plasma jets generated by the different plasma gas compositions for the three calculated cases are shown in Fig. 2.19. One can see that with He in the plasma jet, the plasma jets are well concentrated. The addition of H₂ diffuses the plasma jet resulting in a broader intensity and temperature distributions of plasma jet

while He seems to concentrate not only plasma jets but also particle plumes [92]. By assuming a linear development of the heat transfer curve between injection and nozzle exit and integration over time, the enthalpy transferred to spherical particles was estimated as plotted in Fig. 2.20. The results indicate that the enthalpy transferred to the particle in case of Ar/He parameter is sufficient to evaporate particles up to 0.92 μm in diameter. But with increasing diameter to 3 μm , it is only partially evaporated. The Ar/He/H₂ and Ar/H₂ parameters transfer less enthalpy to the particles compared to the Ar/He parameter. These calculations also suggest that the feedstock treatment along the very first trajectory segment between injector and jet expansion plays a key role [97] as further heat treatment is not to be expected in the expanded plasma jet due to the weak interaction as mentioned above.

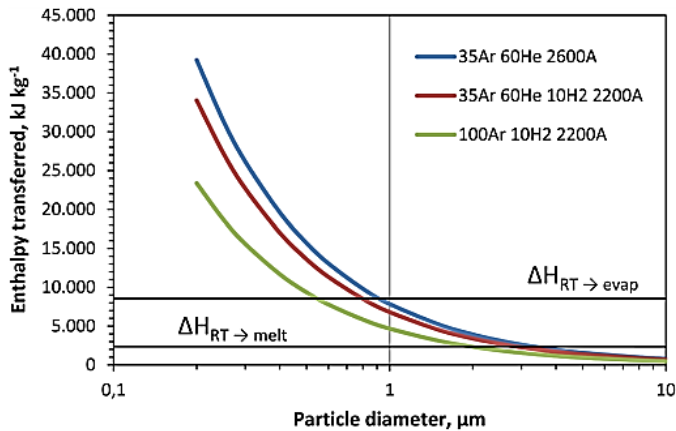


Fig. 2.20 Enthalpy transferred to spherical particles as a function of the particle diameter [97]

Computational Fluid Dynamic (CFD) simulation was also introduced to get a better understanding of the physical processes taking place inside of the nozzle [101, 102]. It was reported that applying Ar/He parameter, 57% of powder are evaporated at a powder feeding rate of 20 g/min, which confirms that significant vaporization already occurs in the torch [102]. As shown in Fig. 2.21, the highest plasma temperature is achieved at the axis of the torch in the core of plasma. The reducing of mean particle diameter describes that the powder particles are continuously evaporated in the very short initial parts of the flight trajectories.

In the chamber, the expanded plasma jets are optically thin and thus the plasma can be investigated by optical emission spectroscopy (OES). The experimental set-up and the spectrometer used as well as the evaluation of the measurements are described in ref. [103]. By Boltzmann plot method assuming a local thermodynamic equilibrium

2.2 Plasma spray-physical vapor deposition

(LTE), the excitation temperature can be calculated based on the measured intensities of observed atomic lines. Fig. 2.22 shows the electron temperatures (equal to the excitation temperature when the non-equilibrium parameter is close to unity) of Ar/He is higher than that of Ar/He/H₂ as already indicated by the temperature calculation in the nozzle. Here, the Abel inversion was not used so that the excitation temperatures are just approximation of the temperatures in the plasma jet center. Calculation about the non-equilibrium parameter found a moderate departure from LTE at chamber pressure of 200 Pa [103].

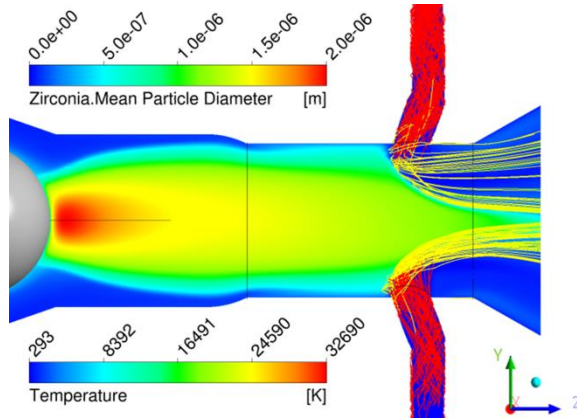


Fig. 2.21 Plasma temperature and particle tracks colored by diameter [102]

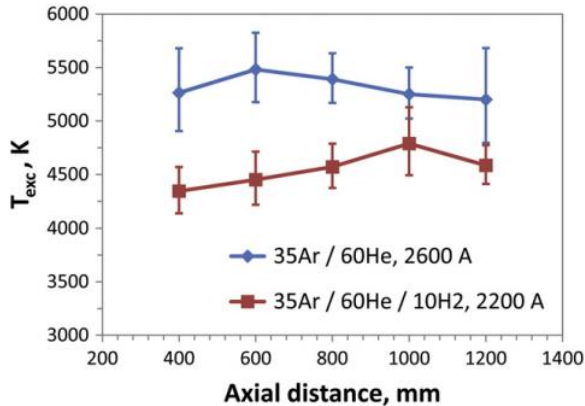


Fig. 2.22 Excitation temperatures determined for two spraying parameters in dependence on the axial distance [104]

2.2.2 Microstructures, properties and performance of TBCs by PS-PVD

Different microstructures can be obtained by controlling the parameters in PS-PVD, such as plasma gas, powder feeding rate, and input power. Examples are shown in

Fig. 2.23: 1) a purely splat deposition can be obtained by using a very high powder feed (40~80 g/min) rate and a Ar/H₂ gas composition which result in a relatively low vaporization degree; thin, dense and gas-tight coating obtained under such conditions can be used as functional layers, such as electrolyte or gas separation membranes; 2) with decreasing the powder feeding rate to 20 g/min, the vaporization degree increases and a splat/cluster/vapor hybrid deposition can be obtained; 3) when changing plasma gas composition to Ar/He, a high vaporization degree can be achieved, combined with a medium powder feeding rate 20 g/min, resulting in a columnar structured cluster/vapor deposition. TBCs which possess such kind of microstructure have high strain tolerance similar to EB-PVD coatings and thus have good thermo-mechanical fatigue performance; 4) if further decreasing the powder feeding rate to 2 g/min, a very high vaporization degree leads to an almost exclusive vapor deposition [92]. Ceramic coatings manufactured under different process conditions demonstrate the diversity of microstructural features achievable by PS-PVD.

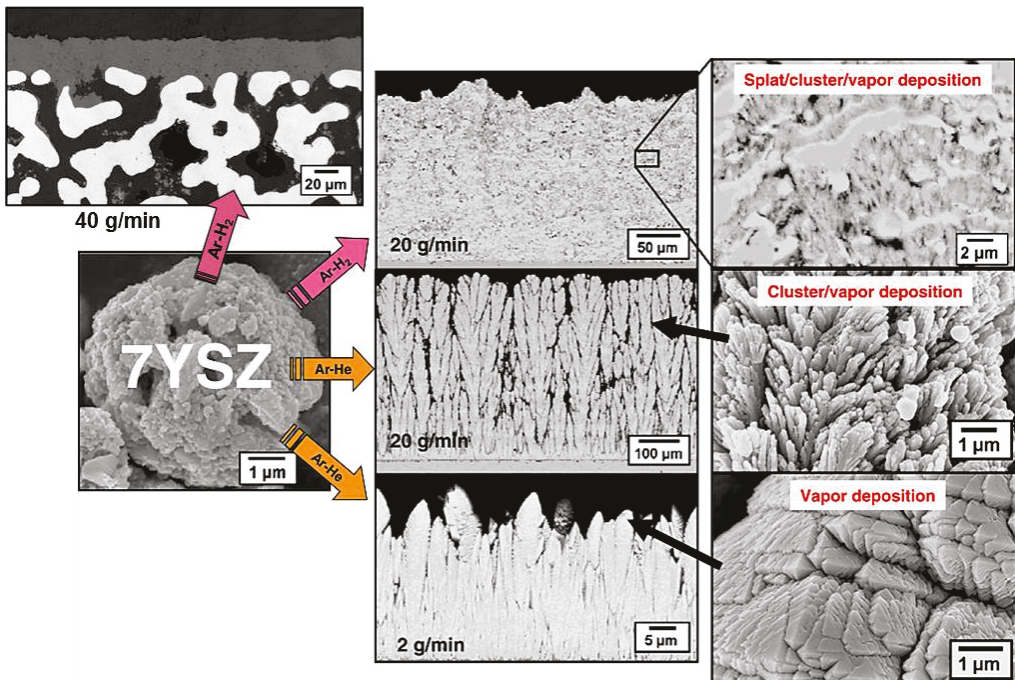


Fig. 2.23 SEM images of different YSZ coatings manufactured by PS-PVD; adapted from [92]

By addition of H₂ in the plasma gases, the microstructure becomes more compact and denser as seen in Fig. 2.24; the gaps between the columns are narrower; and the featherlike substructure is less pronounced [97]. The deposition rate (in μm/min) of Ar/He/H₂ parameter is clearly lower than that of Ar/He parameter. Measurements of the

2.2 Plasma spray-physical vapor deposition

vapor intensity by OES and calculations indicate that admixture of H_2 to the He/Ar plasma gas reduce the plasma temperature due to initial consumption and later release of dissociation energy, and therefore affect the growth and microstructure of the coatings [103]. The porosity of TBCs produced by Ar/He parameter as shown in Fig. 2.24a is typically between 25% and 30% [96, 97]. Its thermal conductivity of $1.2 \text{ Wm}^{-1}\text{K}^{-1}$ was found slightly higher than for APS coatings but lower than for EB-PVD coatings [96]. Accordingly, the coating produced by Ar/He/ H_2 parameter has a lower porosity of 10-15% and the thermal conductivity is $1.4 \text{ Wm}^{-1}\text{K}^{-1}$. However, as given in Fig. 2.25a, the room temperature erosion tests measured according to standard ASTM G 76-13 showed a strongly improved erosion resistance of PS-PVD coatings deposited with the Ar/He/ H_2 parameter (Here, it should be noted that, due to the low erosion resistance of the coatings deposited by some PS-PVD parameters, the test was continued until a color shift was observed at the TBC surface) [5]. Recently, PS-PVD coatings have shown improved thermal cycling lifetimes more than two times higher than conventionally sprayed TBCs by introducing processing steps of low deposition rate and an extended pre-oxidation [4]. In addition, it was reported that PS-PVD TBCs have sufficient resistance to CMAS corrosion attack for application on gas turbine components as they showed comparable lifetime with respect to CMAS attack under thermal cycling conditions with temperature gradients (Fig. 2.25b) [5]. Therefore, the Ar/He/ H_2 parameter is favorable for industrial applications if erosion is essential for TBCs.

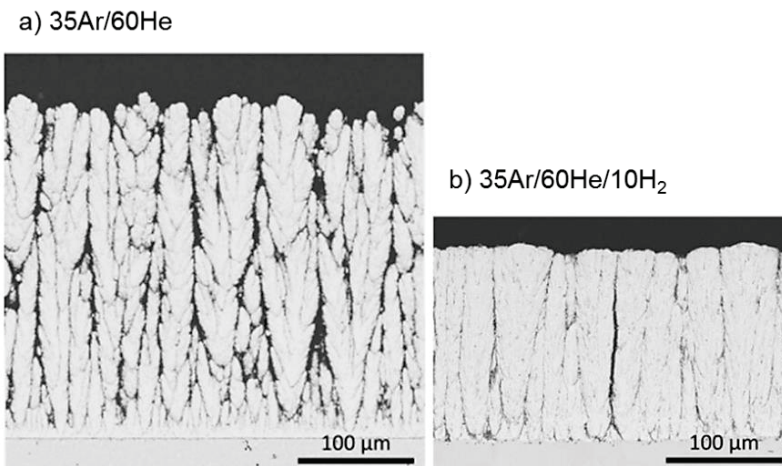


Fig. 2.24 Cross-sections of YSZ coatings manufactured by a) Ar/He jet and b) Ar/He/ H_2 jet [97]

von Niessen et al. also prepared TBCs by PS-PVD which showed good erosion resistance being lower than that of EB-PVD but higher than that of APS [6]. They also reported that the thermal conductivity of PS-PVD coating was $0.8 \text{ W/m}^1\text{K}^{-1}$ between room temperature and $1000 \text{ }^\circ\text{C}$. Gao et al. also reported a “quasi-column” coating exhibiting a low thermal conductivity of $\sim 1.15 \text{ Wm}^{-1}\text{K}^{-1}$ at $1200 \text{ }^\circ\text{C}$ due to its highest porosity ($\sim 17\%$) [105]. Such coatings have a rather low micro-hardness of 6.8 GPa , a Young's modulus of 89 GPa , and showed an average life of around 2000 cycles during flame shock testing. In conclusion, the coatings manufactured by PS-PVD combine the advantages of coatings deposited by APS and EB-PVD.

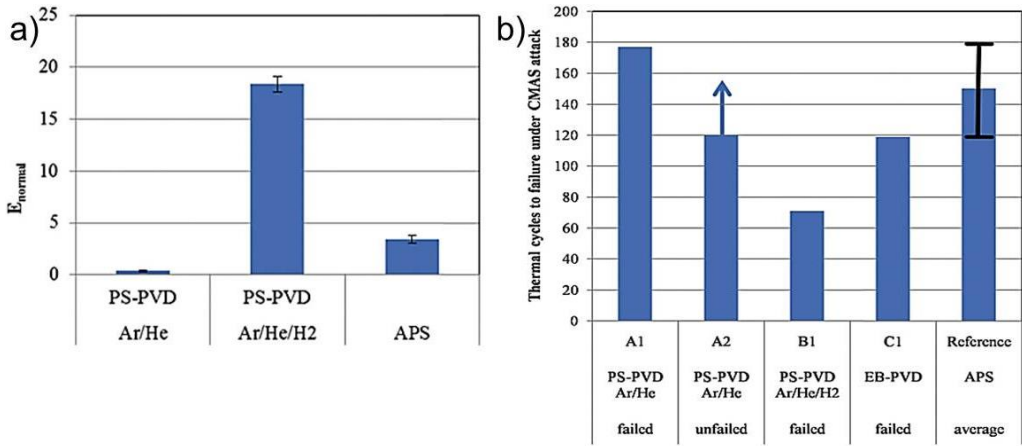


Fig. 2.25 a) Relative erosion resistances and b) Numbers of thermal cycles in burner rig tests with simultaneous CMAS attack of different coatings produced by PS-PVD, EB-PVD, and APS as reference [5]

2.3 Mechanisms of coating deposition out of vapor phase

The fabrication of coatings out of vapor phase on solid surfaces usually a) starts with impingements, adsorption, diffusion, desorption and sticking; b) initial nucleation; and c) proceeds through island growth, coalescence of islands; d) grain growth, development of a continuous structure; and e) the further coating growth as illustrated in Fig. 2.26. The precise control of the growth and thus the structures and properties of the films or coatings become possible only after understanding of the mechanisms. Thus, although film growth is a complex phenomenon, it is widely investigated. Many deposition modes have been developed to illustrate deposition mechanisms [106-108].

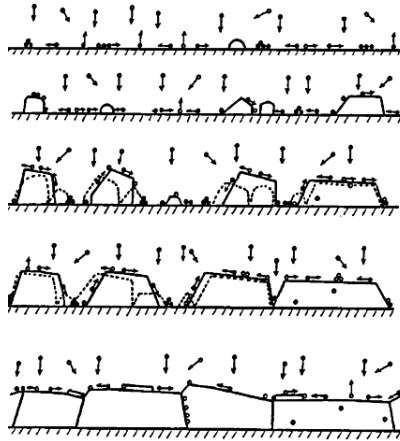


Fig. 2.26 Schematic diagram illustrating fundamental growth processes controlling microstructural evolution [109]

2.3.1 Atomic (or molecular) deposition

- **Adsorption and diffusion**

In the beginning of deposition, vapor species impinge on the substrate, after which they may immediately re-evaporate or adsorb and diffuse along the surface, and finally be trapped on the surface. To participate in these processes, the vapor species have to overcome the characteristic energy barriers, which are normally given by an Arrhenius-type exponential law: $k = A \exp(-E_a/k_B T)$; wherein, k is the rate of a process, A is a pre-exponential kinetic parameter for the process, E_a the activation energy for that particular process, k_B is the Boltzmann constant, T is the absolute temperature.

- 1) Adsorption: vapor species are attracted in a potential well. The depth of the potential well is the binding energy. For physisorption, the binding energy E_{phys} is in the order of 0.01~0.3 eV [110]. Due to the low binding energy E_{phys} , the physisorbed species is mobile and will be able to diffuse around. Sometimes, the species are stronger bonded by chemisorption with a binding energy E_{chemi} , which is typically in the order of 1~10 eV [110].
- 2) Diffusion: adsorbed species are possible to change their positions along the surface if they have enough energy to overcome the diffusion barrier E_d . This diffusion barrier for a physisorbed species $E_{d,phys}$ is typically in the order of 0.1 eV while the diffusion barrier for a chemisorbed species $E_{d,chem}$ is in the order of 0.3~2 eV [111]. These diffusion barriers are generally smaller than the binding energies. The diffusion rate D can be expressed by

$$D = D_0 \exp(-E_d/k_B T) \quad (2.1)$$

3) The sticking coefficient (S_c) is defined as the fraction of the impinging species which remains adsorbed and becomes incorporated in the coating.

As described in equation (2.1), the diffusion rate depends on diffusion barrier E_d and T . In addition, diffusion is anisotropic in both diffusion rates and mechanisms at various crystal orientations of a given material. For example, close packed surfaces such as the fcc (111) tend to have higher diffusion rates than the correspondingly more "open" faces of the same material such as fcc (100) [112]. Also, the vapor species flux can affect the diffusion and S_c because a diffusing species may be ceased by the next deposited species before it can desorb or be trapped on the surface [113].

- **Nucleation (primary nucleation)**

Three possible modes of crystal growth on surfaces are generally accepted, the 3D Volmer-Weber mode (island-by-island), the 2D Frank-van der Merwe mode (layer-by-layer), and Stranski-Krastanov mode (layer-plus-island) as illustrated in Fig. 2.27 [112].

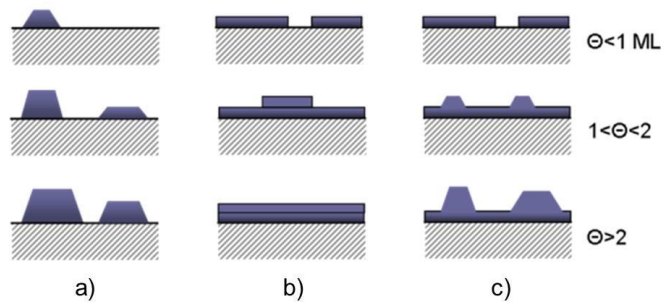


Fig. 2.27 Schematic cross-section views of the three primary modes of thin-film growth including: a) island-by-island, b) layer-by-layer, and c) layer-plus-island. Each mode is shown for several different amounts of surface coverage Θ [112].

In the island mode, small clusters of atoms are nucleated directly on the substrate surface and grow into islands of condensed phase. This happens when the atoms (or molecules) of the deposit are more strongly bound to each other than to the substrate. The layer mode happens at opposite condition if deposits are more strongly bound to the substrate. The third mode, layer plus island, is an intermediate case of the previous two modes. After forming the first (or a few) monolayer, islands are more favorable for subsequent growth which can be caused by several possible reasons, for example the lattice parameter of, or surface energy of, or molecular orientation in, the intermediate layer [106]. The nucleation of vapor phase on the substrate surface is heterogeneous nucleation, which takes place at high super-saturation (S). Thus, the growth mode is controlled not only by interface energies but also by super-saturation ratios [107].

According to classic nucleation theory, the nucleation rate N can be described by the following equation:

$$N = A \exp\left(-\frac{\Delta G^*}{k_B T}\right) \quad (2.2)$$

wherein k_B is the Boltzmann constant, A is a pre-exponential kinetic parameter, T is the absolute temperature and ΔG^* is the nucleation energy. In the approximation of spherical nuclei, the nucleation energy ΔG^* is giving by

$$\Delta G^* = \frac{16\pi v_0^2 \gamma^3}{3(k_B T)^2 \ln^2 S} \quad (2.3)$$

where γ is the surface energy, v_0 is the monomer volume, k_B is the Boltzmann constant, S is the super-saturation ratio which is defined as n_0/n_s (n_0 is the concentration (m^{-3}) of monomer, n_s is the equilibrium monomer concentration).

The formation of approx. spherical nuclei with a radius r will cost energy to create a new surface: $4\pi r^2 \gamma$. During nucleation and coating growth, the surface energy γ is changing. The surface energy γ may be seen as the energy needed to create an additional free surface per unit area. It depends on the chemical composition, the crystallographic orientation, atomic reconstruction, and so on. Due to this dependency, γ is anisotropic for most crystals. Consequently, there will be a thermodynamic driving force for nuclei, islands, grains to minimize their total surface energy by adapting the crystal shape to an energetically most stable configuration. All surfaces are crystallographic planes, and the solid shape adjustment is called faceting because crystals will be terminated with crystallographic planes (facets), and these facets are typically low-surface-energy planes. However, the shape of crystal grown from vapor condensation at a finite growth rate would also depend on the growth rate. The growth rate is anisotropic because the condensation rate is often higher on facets of high-surface-energy due to stronger binding. This kinetically determined anisotropic growth rate could lead to a crystal faceted by planes of slowest growing planes.

- **Coalescence (crystal growth)**

After primary nucleation, the next stage of coating growth is coalescence. Islands grow larger or coalescence of nuclei takes place until forming a continuous network. During coalescence, the diffusion of adatoms on the surface is the most important kinetic process in film growth. As mentioned above, the diffusion rate depends on diffusion barrier E_d and T but also on vapor species flux. In the initial stage of growth, if the vapor species flux is fixed, the value of D determines the average diffusion distance. As primary nucleation continues, this distance decreases and eventually becomes constant. Newly deposited atoms will predominantly join existing islands and effectively prevent

nucleation of new islands [114] until several islands are that large of touch each other. The transition from isolated islands to a continuous macroscopic network can be characterized by a percolation threshold thickness [107].

• Thickness growth and structure evolution

The above mentioned nucleation and coalescence mechanisms happen in the very early stage of a coating formation. Further film growth to thicker coatings and microstructure formation however are determined by four regimes: shadowing, surface diffusion, bulk diffusion and recrystallization.

- 1) *Shadowing* is a geometric interaction between roughness of growing surface and the incident angular directions of species.
- 2) *Surface diffusion* occurs if the adatoms have enough energy to overcome the diffusion energy barrier and enough time to exchange energy with the surface lattice and other adsorbed species until they are trapped at low-energy sites or crystal face.
- 3) *Bulk diffusion* happens if the adatoms diffuse in the volume of the grains.
- 4) *Recrystallization* is a process in which grains of a crystal structure are restructured and form new crystal shapes.

For most materials, the activation energy for diffusion is related to its melting temperature T_m . Thus, a simple structure zone model (SZM) only considering the substrate temperature was proposed by Movchan in 1969 [115], as shown in Fig. 2.28a. Three different structure zones can be divided by the ratio of substrate temperature to the melting temperature of the material (T_s/T_m , the so-called homogenous temperature). Afterwards, Thornton expanded the zone classification in sputtering deposition by adding another axis to account for the sputtering gas [7, 116]. At low T_s/T_m , the high Ar pressure shifts the zone transition to higher surface temperatures (illustrated in Fig. 2.28b) due to the fact that the adsorbed species limit the adatom mobility and persist to higher T_s/T_m . At high T_s/T_m , the Ar pressure has reduced influence because of decreased surface adsorption. The structural characteristics of the four zones were described as follows [117]:

- 1) *Zone 1* structure results if the adatom diffusion is insufficient to overcome the effects of shadowing. The Zone 1 consists of tapered crystals with domed tops which are separated by voided boundaries.
- 2) *Zone 2* is defined as the range of $T_s/T_m > 0.3$ where the coating growth process is dominated by adatom surface diffusion. The columnar grains tend to be highly faceted which are separated by dense intercrystalline boundaries.

- 3) *Zone T* was identified between Zones 1 and 2, consisting of a dense array of poorly defined fibrous grains without voided boundaries.
- 4) *Zone 3* is defined at $T_s/T_m > 0.5$ where bulk diffusion has a dominant influence on the final structure of the coating. It is recognized by dense grains with equiaxed or columnar shapes and twin boundaries, and by grain shapes that do not coincide with the substrate and coating surface topography.

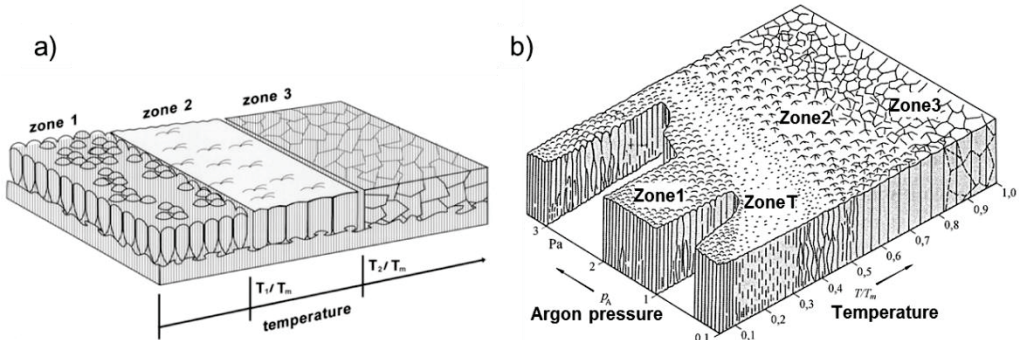


Fig. 2.28 Structure zone model: a) by Movchan [115] and b) by Thornton [7]

• Evolution of growth orientation

As the examples of EB-PVD coatings listed in Table 2.2, many coatings deposited out of vapor phase show textures. This means that the grains orientated in preferred orientations with respect to the substrate. To better understand the causes of textures, to control the textures of the coatings, and thus to obtain desired properties of coatings are of great interest. In 1962, Bauer classified the textures according to the degree of orientation [118]:

- 1) One-degree orientation means that only one crystallographic axis of most of the crystals is oriented preferentially in one direction.
- 2) Two-degree orientation means that two crystallographic axes of most of the crystals are oriented preferentially.

However, textures undergo modifications during almost all the stages of deposition. Thus, in 1967, Van der Drift [119] proposed a classification according to the stage of deposition at which they rise: orientation of nucleation, growth orientation including horizontal growth and vertical growth of the grains. The growth texture eventually leads to the textures of the coatings even that the nucleation stage is characterized by randomly orientated nuclei growing freely and uniformly. A possible mechanism proposed by Van der Drift named as evolutionary selection is based on the principle of competition between crystals: the bigger the vertical growth rate is, the greater the probability of survival will be. Hence, only the crystals with the highest component of the growth rate perpendicular to the substrate are selected, finally resulting in a

crystallographic texture. Wherein, the vertical growth rate is related to crystal orientation and the incident angle of deposits. In some extreme cases, it is possible to calculate the preferred orientations and the effect of incident angle by considering different levels of surface diffusion. Fig. 2.29 shows an example of a simulation result of the growth of a polycrystalline coating according to the model proposed by Van der Drift starting with random nuclei with infinite diffusion [120]. The evolution selection is obvious in Fig. 2.29, only those crystals with a tapered shape survive eventually.

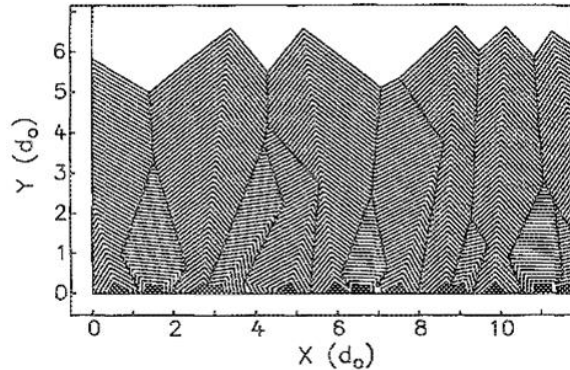


Fig. 2.29 Computer simulation of the growth of a polycrystalline diamond coating. The X and Y axes are normalized with respect to the mean nuclei distance d_0 . Adapted from [120]

Different with Van der Drift, Barna et al. [121] took the substrate temperature and impurities (some active species which are not at or beyond the required concentration for coating deposition, such as O_2 in Al thin film deposition) into consideration in details. They found the impurity whether present on the substrate surface or resulting from the evaporation source or from the residual gas, to have a great influence on coating growth. Barna classified the textures according to the origin of the textures, promoting the understanding of their evolution in coatings produced by different techniques at various parameters. The classification is as following:

- 1) Activated nucleation texture: related to the texture of the substrate
- 2) Evolutionary growth texture, including: competitive growth texture and restructuration growth texture

The evolutionary growth texture means that the evolution of texture is also along with the evolution of coating structure. Competitive growth texture takes place under relatively low temperature or relatively high impurities where the grain boundaries are immobile. Restructuration growth can be active if the grain boundaries are mobile, for example, high substrate temperature ($T_s/T_m > 0.3$) and low impurities. Thereby, he proposed a new SZM as illustrated in Fig. 2.30 [121]. At a very low level of impurity, the grain growth is not limited and the restructuration texture can develop as zone II,

see Fig. 2.30a. The grains can grow as columnar structure but the growth will be limited as impurities increase and thus grain boundary mobility decreases (zone II in Fig. 2.30b). The width of the columns will be smaller but still have restructuration texture. Further increasing impurity, competitive growth will develop due to the segregation of impurity on the grain boundary (zone T in Fig. 2.30c). At high level of impurity, the growth of crystals is limited remarkably and no evolutionary growth texture occurs. As a consequence, the coating is composed by randomly orientated small grains. In this SZM, the competitive growth texture is more or less similar to the evolutionary section model of Van der Drift. But introducing the concept of impurity makes this new SZM more universal in coating deposition out of the vapor phase.

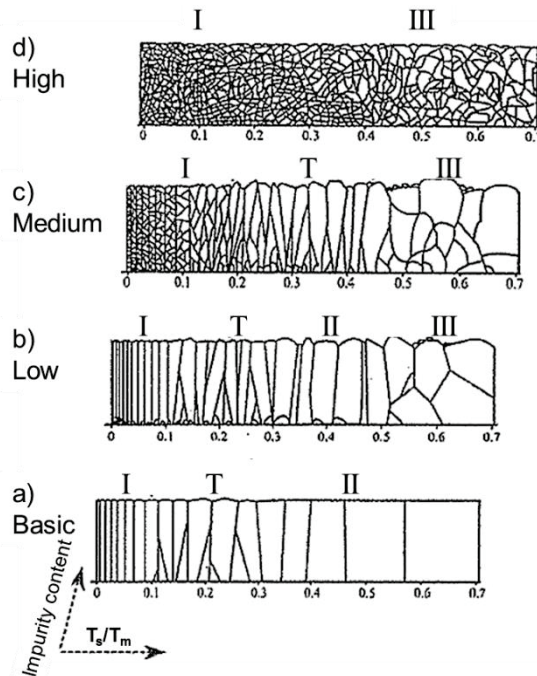


Fig. 2.30 a) Basic and real-structure zone models for b) low, c) medium, and d) high impurity concentrations [107]

2.3.2 Cluster deposition

- **Cluster beam deposition**

All the above-mentioned mechanisms in coating deposition are based on the classic vapor deposition of atomic or molecular species. As discussed before, many deposition parameters can affect the properties of thin films or coatings. Another deposition technique, so called cluster beam deposition, emerged and was proposed as a solution

to obtain coatings with desired properties. The advantages of this technology are due to the unique physical and chemical properties of clusters as well as due to the effects of the kinetic energy and chemical activity that can be achieved with charged clusters [122]. Clusters are a group of atoms or molecules containing typically from a few tens to a few thousand atoms, and they have been studied for their specific physical properties (mostly due to their large surface to volume ratio) which are size dependent and different from both the constituting atoms and the bulk material [123]. In many studies [122, 124], the clusters were formed by condensation of supersaturated vapor produced by expanding supersonic gas jets through a small nozzle into vacuum. The formation of clusters was simulated and the results confirmed that the nucleation and growth rates in metal vapors are sufficiently high to produce clusters by homogenous nucleation along the trajectories in the nozzle [122]. The size of clusters was evaluated by means of time-of-flight methods, electrostatic energy analysis [122] and transmission electron microscopy (TEM) [125-127].

Meanwhile, it was also suggested the cluster deposition mechanisms are different from atomic and molecular deposition [126]. Fig. 2.31 shows an example to compare the depositions of $Sb_{(n)}$ (n is the number of antimony molecules) by molecular beam ($n=4$) deposition and cluster ($n=1850$, 4.8 nm in diameter) deposition (the fragmentation of clusters was considered to be unlikely) [128]. The percolation threshold measured by current (indicated by the arrow in the plots in Fig. 2.31) showed that the thickness of a $Sb_{(4)}$ film is around 37 nm while that of a $Sb_{(1850)}$ film is only 2.3 nm, which means that cluster deposition can form a continuous network at a very thin thickness. The coverage of film near the threshold of the $Sb_{(4)}$ film is about 95% while that of the $Sb_{(1850)}$ film is only about 48%. It is obviously shown in the TEM images (Fig. 2.31) that the mean size of particles of the $Sb_{(4)}$ film is 200 nm, which is much larger than the 9 nm of the $Sb_{(1850)}$ film. This was interpreted by the higher mobility of the $Sb_{(4)}$ compared to the $Sb_{(1850)}$ as the mobility decreases with increasing cluster size. In case of the $Sb_{(4)}$ deposition, the nucleation process is governed by diffusion and occurs on preferential nucleation sites [127]. Owing to the low mobility of the $Sb_{(1850)}$ (cluster), the growth is entirely governed by the impinging flux (desorption and weak nucleation are negligible). Such comparison between molecular and cluster deposition is important to understand the cluster deposition mechanisms and thus to control the crystalline size due to its dependence on cluster size. For a given deposition rate, a beam of the small incident clusters allow to obtain deposits built with large particles presenting a preferential crystallographic orientation on large areas while a large incident cluster beam will produce polycrystalline films [127]. The increase of the deposition rate in

2.3 Mechanisms of coating deposition out of vapor phase

case of cluster deposition tends to promote a continuous film with small particles presenting no preferential crystallographic orientation.

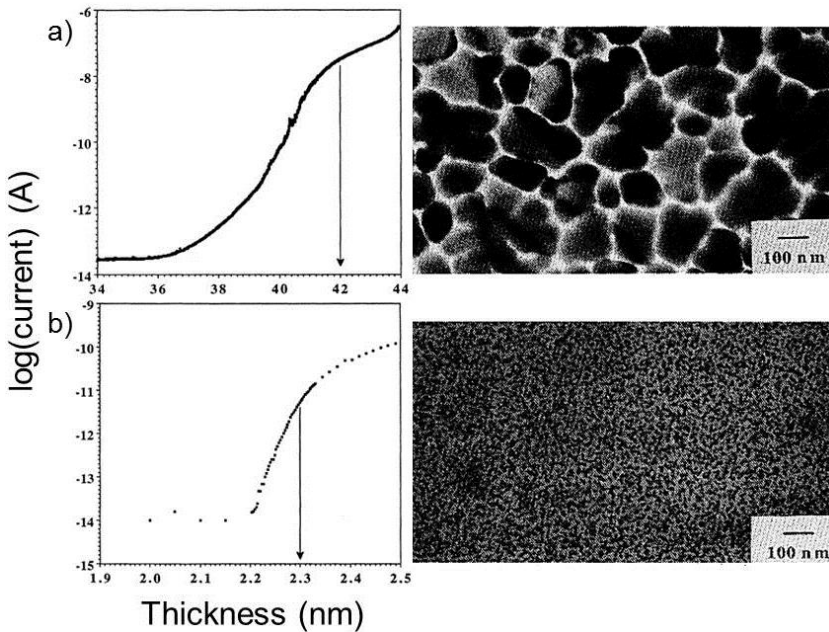


Fig. 2.31 Plots of the observed current vs. film thickness and corresponding TEM micrographs in the case of a) molecular deposition (thickness 42 nm) and b) cluster deposition (thickness 2.3 nm); TEM micrographs are corresponding to the thickness indicated by the arrows in the plots.

Adapted from [128]

Similar to atomic or molecular deposition, the substrate temperature also has an influence on the cluster deposition. This can be illustrated by the simulation of Au cluster deposition at different temperatures as shown in Fig. 2.32. The small clusters combined with high substrate temperature favored the epitaxial recrystallization of the clusters while planar defects such as twins and grain boundaries resulted from large cluster diminished at high substrate temperature gradually [129]. Besides, the impact energy of clusters was simulated from a soft touchdown at 0.1 eV/atom, over a flattening collision at 1 eV/atom, to a meteoric impact at 10 eV/atom for a $\text{Mo}_{(1043)}$ cluster on a $\text{Mo}(001)$ surface [130]. It was reported that the impact of a cluster at 10 eV/atom can create a pressure of about 100 GPa in the impact zone increasing the temperature of the cluster itself to 6607 K during the first ps after the touchdown. A porous coating is obtained with low energetic cluster impact; inversely a dense coating will be produced by high energetic cluster impact. Although the simulation results are limited in many aspects due to many assumptions, they are useful for a qualitative understanding.

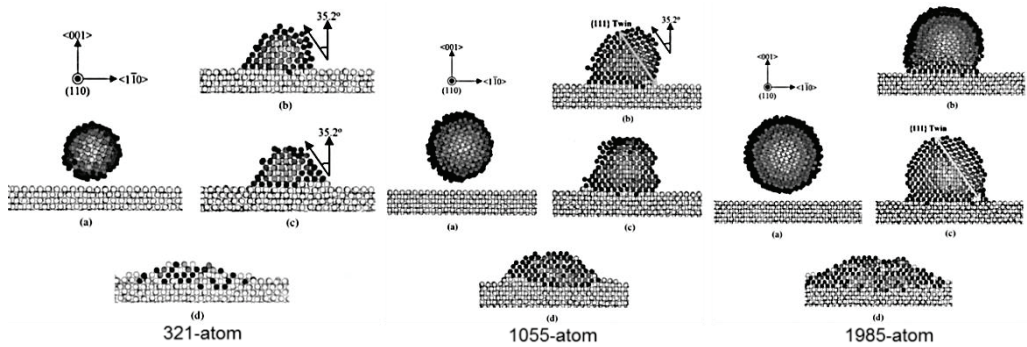


Fig. 2.32 A (110) plan view of clusters (a) before deposition and after 320 ps of deposition (b) at 300 K, (c) at 700 K (d) at 1000 K for different size of clusters: 321-atom, 1055-atom, and 1985-atom. Adapted from [129]

In addition to the intentional production of a cluster beam for deposition, clusters can form in the vapor phase under suitable conditions, such as supersaturated vapor during a fast quenching process [131]. Exclusively, atomic or molecular growth of coatings can occur if the super-saturation is low enough to inhibit the nucleation in the gas phase. However, the formation of clusters or nanoparticles was found in many CVD processes, in particular PECVD [132] where ion-induced nucleation would occur at a low nucleation barrier [133]. Besides, Girshick et al. studied in-depth nano particles created in thermal plasma processes, including calculations [134, 135] and experimental characterizations [132, 136, 137]. Either homogeneous [134] or ion-induced [138] nucleation in PECVD and thermal plasma processes is due to the cooling of high-temperature gas, which leads to the formation of supersaturated vapor. The supersaturation ratio depends on the local cooling rate and the concentration of gas phase [134]. Such particle formation and co-deposition in the coating can affect the morphologies and properties of the coatings [132, 133]. This was also reported for a gas jet assisted electron beam evaporation process in which the increase of vapor phase nucleation of YSZ clusters coincides with a transition from a (200) textured columnar morphology to a nano-granular structure with no texture and a very high nano scopic porosity volume fraction [139].

- **Theory of charged nanoparticles**

Despite the generation of clusters or nano particles in CVD has been detected experimentally, that it is not sufficient to say that the coatings and nanostructures are mainly built up by clusters or nano particles because they are invisible during deposition. Hwang et al. proposed a new mechanism, so called “theory of charged nanoparticles” (TCN), to distinguish from the conventional atomic or molecular

2.3 Mechanisms of coating deposition out of vapor phase

deposition [140]. TCN was first introduced in 1996 to interpret the well-known puzzling phenomena of simultaneous diamond deposition and graphite etching during diamond CVD using the C-H system [141]. The evolution of graphitic soot and diamond on the iron and the silicon substrates, respectively, can be approached based on the charged cluster model [141]. The understanding of crystal growth by nano-sized clusters is based on a concept of “magic size” proposed by Fujita [142]. The “magic size” is the transitional cluster size between fast-diffusion and slow-diffusion properties. He determined the magic size for an embedded ZrO_2 cluster (formed in amorphous AlO_3 - ZrO_2 composites) to be approx. 6 nm at room temperature [142] while for the isolated state it was expected to be approx. 12 nm [143]. When the clusters are smaller than the magic size, clusters are likely able to orient on the growing surface. Conversely, they might tend to retain their own orientation if they are larger than the magic size leading to nano structures.

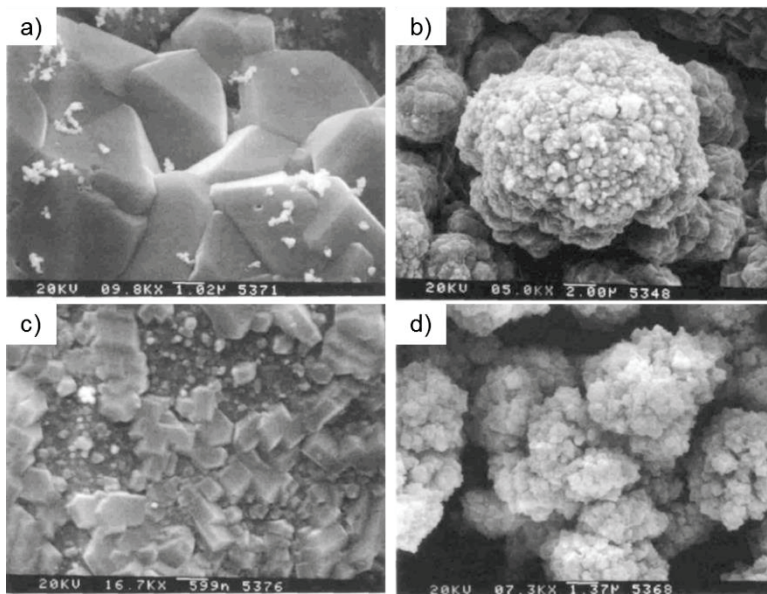


Fig. 2.33 SEM images of YSZ coatings deposited by thermal CVD: a) $T_{ZrCl_4} = 450$ °C, NiO substrate, b) $T_{ZrCl_4} = 250$ °C, NiO substrate, c) $T_{ZrCl_4} = 320$ °C, quartz substrate and d) $T_{ZrCl_4} = 320$ °C, NiO substrate. Adapted from [144]

Later, Jeon and Hwang et al. found two remarkably different microstructures: well-faceted crystal and cauliflower-shaped structures. They were formed in the deposition of YSZ by thermal CVD process depending on evaporation temperature of precursor as well as the conductivity of the substrate [144]. The SEM images in Fig. 2.33 show the different microstructures of YSZ coatings: at low evaporation temperature of $ZrCl_4$, a cauliflower structure was produced (Fig. 2.33b); with

increasing evaporation temperature, the growth rate of coating decreased and crystals with well-developed facets were evolved (Fig. 2.33a). At the same condition, a cauliflower structure was formed on more conductive substrates while well-developed facets were developed on quartz substrates. This evolution of microstructure was interpreted by the TCN concluding that high evaporation temperatures produce high ion densities resulting in small charged clusters. This is responsible for the low growth rate and the crystals with well-developed facets. Inversely, cauliflower structures are obtained at high deposition rate. Furthermore, they observed individual zirconia clusters with a size of about 8 nm by TEM. In addition to this, enhanced electric current was detected during deposition in the reactor by the increasing evaporation temperature [143]. Comparing the energy barriers of secondary nucleation (nucleation on existing crystals) and that of growth, the evolution of the cauliflower structures is difficult to explain by the conventional atomic or molecular unit crystal growth [145]. By conventional atomic or molecular deposition, the cauliflower structure should result from a very high three-dimensional nucleation on the growing surface. But the super-saturation for surface roughening (crystal growth) is expected to be much lower than that for 3-D nucleation on the surface leading to cauliflower structure. Thus, they suggested that the nanostructure or cauliflower structure could be one of the microstructural criteria that distinguish between the atomic unit and the cluster unit deposition [143, 145].

2.3.3 Current knowledge about growth mechanisms of PS-PVD coatings

Mauer et al. [8] mainly classified the deposition mechanisms in PS-PVD into three types: 1) shadowing, 2) adsorption, nucleation and growth (surface diffusion), and 3) bulk diffusion (recrystallization). It was suggested that shadowing is the main reason for the coating of tapered columns with dome tops as shown in Fig. 2.34a. As mentioned before, in this case, diffusion is insufficient to overcome the shadowing effect so that the crystals are not faceted. In the case of sufficient surface diffusion, atomic species are adsorbed and initial nuclei are formed on the substrate surface. This normally takes place at sufficiently high substrate temperatures and low deposition rates. The adatoms have enough time and energy to exchange energy with the surface lattice and other adsorbed species to form crystal facets. This kind of deposition can result in compact columnar coatings with faceted surfaces as seen in Fig. 2.34c. These two mechanisms may occur at the same time, which leads to a transitional region between shadowing and surface diffusion where the columns are still coarse and tapered but the gaps between columns start to be filled and the tips of columns become faceted as the Fig. 2.34b. Its XRD pattern indicated preferential growth orientations of

2.3 Mechanisms of coating deposition out of vapor phase

(002) and (110). The structure zone model for magnetron sputtered coatings proposed by Thornton [116] was transferred to PS-PVD to illustrate coating characterizations as given in Fig. 2.35. By calculating the homologous temperatures and molar deposition rates, experiments with different materials are considered in the same diagram. The experiment results correspond well with the characteristics of PS-PVD coatings formed by shadowing, surface diffusion as described above [8].

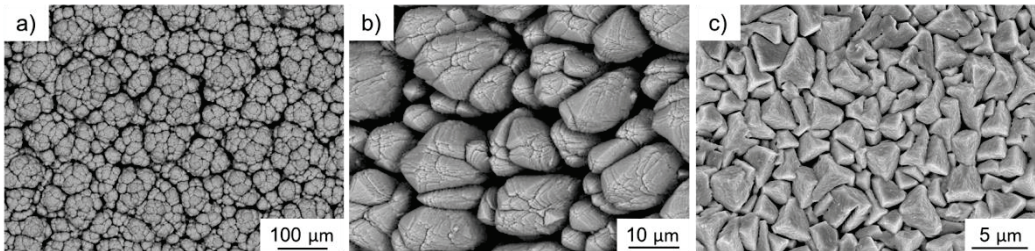


Fig. 2.34 SEM images of YSZ coatings prepared by PS-PVD under different conditions: a) shadowing dominates, c) sufficient diffusion, and b) is between a) and c) [8]

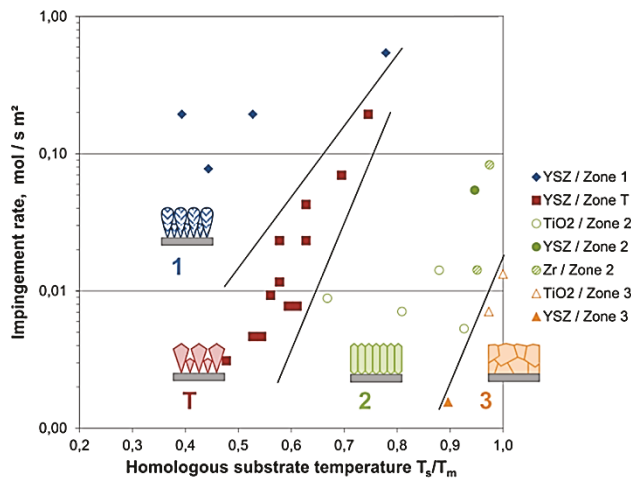


Fig. 2.35 PS-PVD structure zone model [8]

Recently, Gao et al. proposed three deposition mechanism models based on the PS-PVD dense coating, hybrid coating, and columnar coating deposited at different distances of 450 mm, 550 mm and 1000 mm, respectively [146]. They stated that at short spray distance the dense coating is deposited mainly from melted droplets while at long spray distance major fraction of deposits come from the vapor phase, which means the plasma would have continuous heating effect on the feedstock during the very long flight time to the substrate. This conclusion is contradictory to our findings that particle heating in the plasma jet is reduced due to the low plasma density [8].

Zhang et al. introduced mechanisms of heterogeneous nucleation at spray distance of 950 mm and homogeneous nucleation with increasing distance to 2200 mm [147].

Furthermore, it is noteworthy that fiber textures are very common for EB-PVD coatings as summarized in Table 2.2. By contrast, TBCs made by standard PS-PVD parameters and having typical microstructures as shown in Fig. 2.24 don't have preferential growth orientation. Reports about the texture of PS-PVD coatings are still hardly available. Besides, it was reported that different microstructures were obtained in the center (Fig. 2.36a) and at the edge regions (Fig. 2.36b) of plasma jet at short spray distance (300 mm) when a relatively high powder feeding rate (20 g/min) was utilized [148]. A similar phenomenon was reported by Li et al. [149]. All of these phenomena suggest that the microstructures of PS-PVD coatings can be affected by the interaction between the plasma flow and the substrate surface and thus the deposition mechanisms in PS-PVD is not the same as in the common PVD process even in the case that the deposits source is mainly vapor phase.

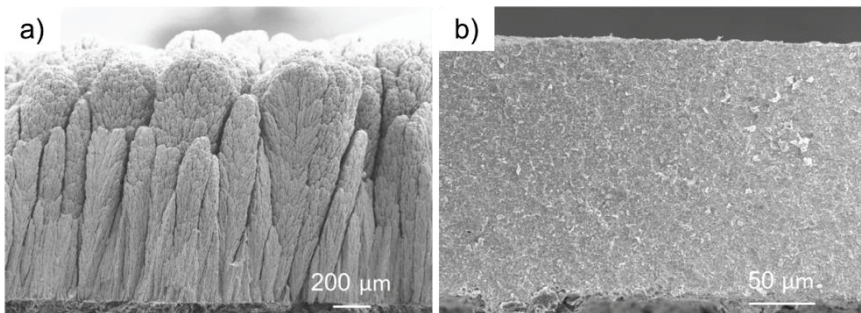


Fig. 2.36 Fracture surfaces of YSZ coatings made by PS-PVD (20 g/min, 300 mm): a) columnar structure formed in the center of plasma jet, and b) dense structure formed at 40 mm distance from center [8]

2.4 Summary

Comparing with other deposition technologies, TBCs produced by PS-PVD have shown several advantages: advanced columnar structure similar to EB-PVD TBCs, considerably higher deposition rate, low thermal conductivity, improved erosion resistance, excellent thermal cycling lifetime, and sufficient resistance to CMAS attack. In addition, the diverse spraying parameters in the PS-PVD enable to obtain multi-functional coatings. The deposition mechanisms which are significant for coating elaboration are major subjects to get a comprehensive understanding of the process. However, up to now, the deposition mechanisms in PS-PVD are not very clear and relevant reports are limited. Therefore, experimental investigations and calculations on

2.4 Summary

interaction between the plasma gases and feedstock, as well as coating growth process are still required.

Table 2.3 Typical deposition conditions for different vapor phase deposition technologies

	Chamber pressure (Pa)	Substrate temperature (K)	Deposition rate ($\mu\text{m/h}$)	Coating texture	Reference
PS-PVD	200	~ 1300	up to 1500	--	[150]
EB-PVD	~ 1	~ 1300	240~600	textured	[38]
Laser CVD	930	1025	230~660	textured to non-textured	[91]
PECVD	106	973~1173	100~250	textured	[89]

Table 2.3 summarizes some typical deposition conditions for TBCs in deposition technologies out of vapor phase. In general, PS-PVD is PVD-like, since no chemical reaction occurs during deposition. But it has some similarities with the CVD process, for example, the chamber pressure of PS-PVD is comparable with that of CVD, which is higher than that in the PVD process. This leads to the interaction between process gas and deposit species, which makes non-line of sight deposition possible in PS-PVD. The similarities of deposition conditions between PS-PVD and other technologies suggest that the above-mentioned deposition mechanisms, either atomic deposition or cluster deposition, are supposed to occur in the PS-PVD process. In addition, the PS-PVD process has a high deposition rate compared with other PVD or CVD technologies, which might lead to different deposition mechanisms. In this work, the deposition mechanisms will be discussed regarding to the microstructures and textures of the PS-PVD coatings produced under different deposition conditions.

Chapter 3 Applied Methods and Materials

3.1 Plasma diagnostics: optical emission spectroscopy

The plasma jet was characterized by an optical emission spectroscope (Aryelle 200, Laser Technik Berlin, Germany). Plasma emission was collected through a borosilicate glass window and an achromatic lens, transferred by an optical fiber to the 50 μm entrance slit of the spectrometer and detected by a 1024x1024 pixels CCD array. The system is equipped with an Echelle grating, and the spectral resolution obtained is 15.9-31.8 pm [103]. The scanning wavelength range is 381-786 nm, which was calibrated by a standard Hg lamp. In this study, OES was not only used to determine the properties of plasma jet but also the vapor species and their concentrations in the plasma jet. The parameters used for plasma jet characterization are given in Table 3.1. Besides, the exposure time for the OES measurement was 400 ms. According to ref. [151], the fluctuations frequency of the voltage spectra peaks are in the range of 4 kHz to 11 kHz. In other words, it is in a time scale of 0.25 ms to 0.1 ms. Thus, the fluctuations in the plasma jet should not affect the measured intensities.

Table 3.1 Plasma parameters for OES diagnostics

Parameters	A-200	A-1000	B-200
Plasma gases	Ar 35slpm / He 60slpm		Ar 35slpm / He 60slpm / H ₂ 10slpm
Current	2750 A		2200 A
Net power	~ 60 kW		
Carrier gas	2 x16 slpm		
Chamber pressure	200 Pa	1000 Pa	200 Pa
Spray distance	1000 mm		
Powder feeding rate	0 ~ 18 g/min		6.9 g/min

slpm: standard liter per minute

3.1.1 Boltzmann plot method

The Boltzmann plot method is valid for local thermal equilibrium (LTE) or partial local thermal equilibrium (pLTE) conditions [152]. By applying the Boltzmann distribution,

3.1 Plasma diagnostics: optical emission spectroscopy

the absolute intensity I_{jk} of a spectral line emitted by the plasma due to the transition from an excited state j to a lower energy state k is

$$I_{jk} = \frac{Lhc}{4\pi\lambda_{jk}} A_{jk} n_{tot} \frac{g_j}{Z} e^{\left(\frac{-E_j}{k_B T_{exc}}\right)} \quad (3.1)$$

wherein, L is the emission source depth, h is the Planck constant, c is the velocity of light, A_{jk} is the transition probability, n_{tot} is the density of emitting atoms/ions, g_j is the statistical weight of the excited level j , λ_{jk} is the wavelength of the emission, Z is the partition function, E_j is the energy of the excited level j , k_B is the Boltzmann constant, and T_{exc} is the excitation temperature. If a series of emission lines (for one atomic specie and ionization level) of transitions to a lower energy level k are measured, a linear plot is obtained with $\ln\left(\frac{I_{jk}\lambda_{jk}}{g_j A_{jk}}\right)$ as a linear function of E_j as shown by equation (3.2). The excitation temperature T_{exc} is yielded from the slope.

$$\ln\left(\frac{I_{jk}\lambda_{jk}}{g_j A_{jk}}\right) = \frac{-1}{k_B T_{exc}} E_j + C, C = \ln\left(\frac{Lhc n}{4\pi Z}\right) \quad (3.2)$$

The left side of this equation is called atomic-state distribution function (ASDF). Wherein, λ_{jk} , A_{jk} , g_j and E_j can be retrieved e.g. from NIST Atomic Spectra Database [153]. I_{jk} were directly taken from the peak value of the emission lines in the measured spectrograms.

However, laboratory plasma jets are seldom in LTE. Two situations of departure from LTE can be observed considering the density of the low lying levels relative to the density that they would have if they were in equilibrium with the upper lying levels [154]. As illustrated in Fig. 3.1, depending on the conditions, the lower energy levels are overpopulated (in a so-called ionizing plasma) or underpopulated (in a recombining plasma) with respect to the Saha-Boltzmann population distribution [155].

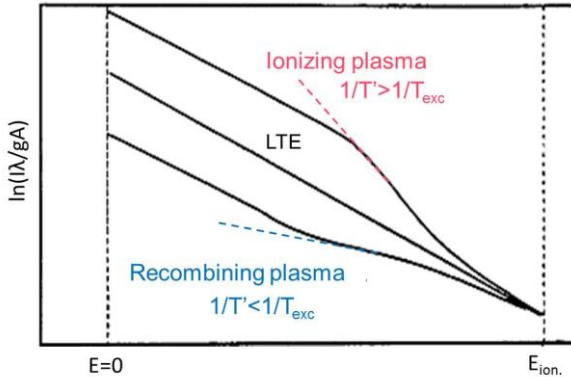


Fig. 3.1 ASDF for an LTE and for pLTE plasmas in recombining and ionizing equilibrium; adapted from [156]

Under PS-PVD conditions, where the expanding plasma jet in a chamber is at a pressure of few tens of Pascals, deviations from LTE occur because the electron density (n_e) decreases (the rate of electron energy loss per unit volume is proportional to n_e) [157]. Due to the reduction of energy exchange by collisions, the electron temperature T_e can be higher than that of heavy species T_h [158]. Only the higher energy levels can be in pLTE and therefore represent the correct excitation temperature [156]. Besides, it was found that He plasmas exhibit strong deviations even in such situations where a comparable Ar plasma is close to equilibrium [159], thus Ar neutral lines (Ar I) are used to calculate the excitation temperature in the Ar/He jet as well as in the Ar/He/H₂ jet.

All of the intensities of the emission lines were measured by OES at spray distance of 1000 mm. In the example of a Boltzmann plot (Fig. 3.2), fifteen neutral (Ar I) lines are plotted (the spectroscopic data for the 15 Ar lines are listed in Table 3.2), but four points of low energy level transitions (4p - 4s) were discarded because they are not aligned linearly with the other 11 higher energy level transitions (4d, 5d, 6s, 6d - 4p). The reason is the deviation from LTE as mentioned above. The measured intensities of the 11 Ar I emission lines have mean absolute percentage deviations from two repeated measurements of 4%~8% in the radial range of 130 mm.

Table 3.2 Ar (I) lines used in determining the excitation temperature through Boltzmann plot

λ (nm)	I_{jk} (a.u.)	A_{jk} (s ⁻¹)	g_j	$\ln(I\lambda/gA)$	E_j (eV)	Trans.
549.5874	743.6	1.69E+06	9	-3.61679	15.32	6d - 4p
555.8702	483.5	1.42E+06	5	-3.27402	15.13	5d - 4p
603.2127	1879.6	2.46E+06	9	-2.97181	15.13	5d - 4p
641.6307	817.7	1.16E+06	5	-2.40286	14.84	6s - 4p
687.1289	1541.2	2.78E+06	3	-2.06374	14.71	4d - 4p
693.7664	602.2	3.08E+06	1	-1.99772	14.69	4d - 4p
703.0251	1780.6	2.67E+06	5	-2.36693	14.84	6s - 4p
720.6980	562.5	2.48E+06	3	-2.90977	15.02	6s - 4p
735.3293	847.2	9.60E+05	7	-2.37834	14.78	4d - 4p
737.2118	2342.2	1.90E+06	9	-2.29287	14.75	4d - 4p
743.5368	574.1	9.00E+05	5	-2.35537	14.84	6s - 4p
696.5431	28791.1	6.39E+06	3	0.04509	13.33	4p - 4s
714.7042	1777	6.25E+05	3	-0.38957	13.28	4p - 4s
738.398	56332	8.47E+06	5	-0.01798	13.30	4p - 4s
751.4652	44592.5	4.02E+07	1	-0.18203	13.27	4p - 4s

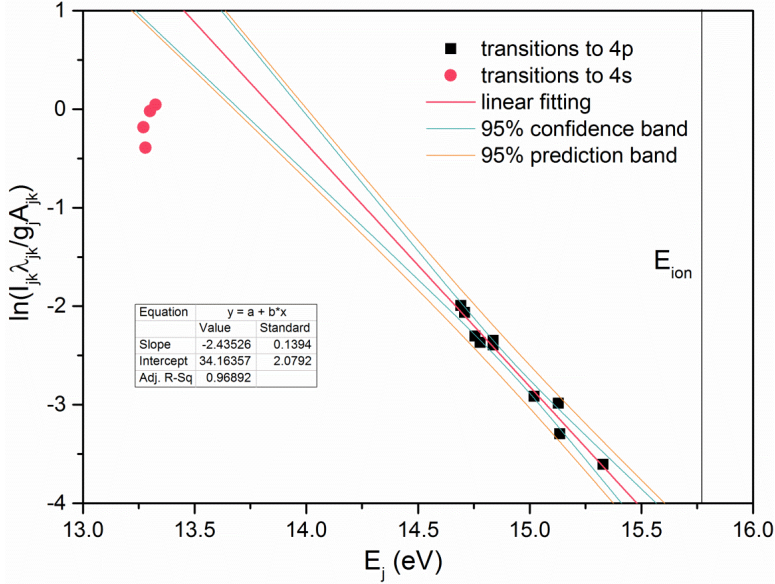


Fig. 3.2 Example of Boltzmann plot for Ar I spectral lines under condition A-200 (Ar/He jet, 200 Pa)

3.1.2 Abel inversion

Fig. 3.3 shows a photograph of the plasma jet under condition A-200 and its pseudo-color image, which shows that the plasma jet is axial symmetric. The photo was taken by Nikon D300S with an exposure time of 1/6400 s and an aperture of 4.5. A scale plate was drawn at spray distance of 1000 mm, which illustrates an approximate radius of 130 mm for the cross section of the plasma jet.

As illustrated in Fig. 3.4, the laterally measured intensity $I(y)$ at the measurement distance y_k contains the local emission intensity $\varepsilon(r)$ of all the plasma radial positions along the line of measurement (from $-x_0$ to x_0), given as equation (3.3):

$$I(y) = \int_{-x_0}^{x_0} \varepsilon(r) dx = 2 \int_0^{x_0} \varepsilon(r) dx \quad (3.3)$$

The substitution $x = \sqrt{r^2 - y^2}$ is then introduced into equation (3.3) yielding the Abel transforms of the function $\varepsilon(r)$ by equation (3.4):

$$I(y) = 2 \int_y^R \frac{\varepsilon(r)}{\sqrt{r^2 - y^2}} r dr \quad (3.4)$$

The calculated temperature depending on the $I(y)$ is therefore called the average excitation temperature $T_{exc}^{(A)}$. In order to know the local excitation temperature $T_{exc}(r)$, an

Abel inversion [160] has to be used to reconstruct the radial $\varepsilon(r)$ from the measured $I(y)$ in equation (3.4) by equation (3.5):

$$\varepsilon(r) = -\frac{1}{\pi} \int_r^R \frac{\frac{dI(y)}{dy}}{\sqrt{y^2 - r^2}} dy \quad (3.5)$$

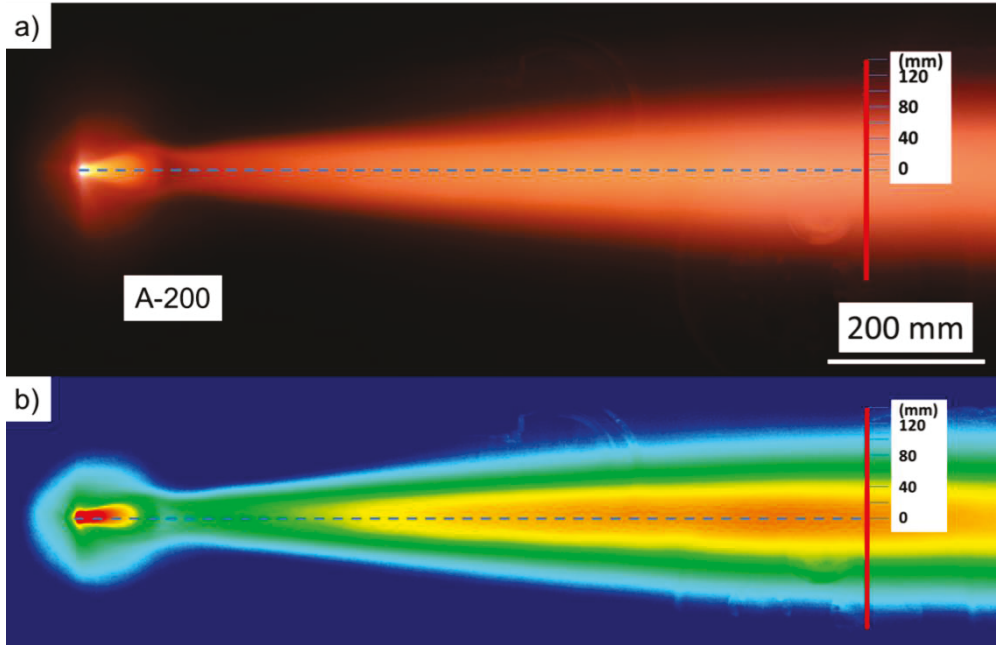


Fig. 3.3 a) Photograph of the plasma jet under condition A-200 (Ar/He jet, 200 Pa), and b) a pseudo-color image transformed from the photo

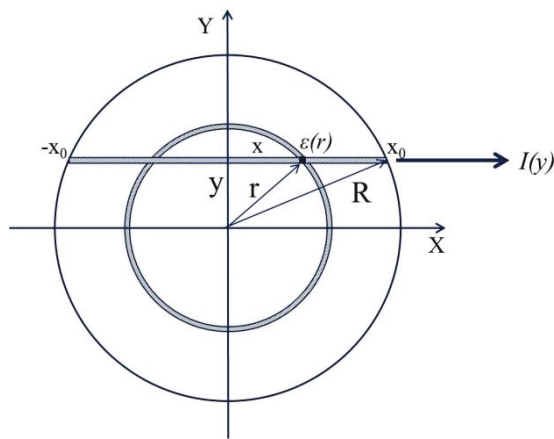


Fig. 3.4 Schematic illustration of Abel inversion in a plane perpendicular to the axis of the plasma jet

The photos of the plasma jets and the measured intensity distributions through the whole plasma jets under different conditions were published in ref. [92]. They show that the intensity distributions are axisymmetric indicating the reliability of the Abel inversion. Therefore, in this work, only half of the intensity distributions will be presented. As the Abel inversion amplifies the noise in the raw data as well as requires the intensity to fall to zero at the plasma edge, it is better to reduce the noise before data processing. It was found that polynomial fitting can be used to partially filter out noise in the raw data [161]. Therefore, before Abel inversion, the laterally measured intensity profiles were fitted by polynomials.

Because the measured $I(y)$ is not given analytically but in discrete data points, both the differentiation and the integration in equation (3.5) cannot be performed directly. There are many different methods to perform Abel inversion to reconstruct a density distribution from a measured line-integral. Pretzler et al. proposed the Fourier method [162] to perform the calculation in one single step. Comparing different reconstruction techniques by the methods of error propagation, Fourier method shows the best results because it also works as a low-pass filter [163]. In the Fourier method, the unknown distribution $\varepsilon(r)$ is expanded in a series similar to a Fourier-series:

$$\varepsilon(r) = \sum_{n=N_l}^{N_u} A_n \varepsilon_n(r) \quad (3.6)$$

with unknown amplitudes A_n , where $\varepsilon_n(r)$ is a set of cosine-functions, e.g.

$$\varepsilon_0(r) = 1, \varepsilon_n(r) = 1 - (-1)^n \cos(n\pi \frac{r}{R}) \quad (n \geq 1) \quad (3.7)$$

Following equation (3.4), the Abel transform of equation (3.6) has the form:

$$i(y) = 2 \sum_{n=N_l}^{N_u} A_n \int_y^R \frac{\varepsilon_n(r)}{\sqrt{r^2 - y^2}} r dr \quad (3.8)$$

where $i(y)$ denotes a lateral intensity fitted by a set of cosine-functions.

$$\text{The integrals } I_n(y) = \int_y^R \frac{\varepsilon_n(r)}{\sqrt{r^2 - y^2}} r dr \quad (3.9)$$

cannot be solved analytically but calculated numerically. The amplitudes A_n are still unknown, but applying equation (3.8) to be the least squares fitted to the measured data $I(y)$ at each point y_k , one obtains:

$$\sum_{k=1}^K (i(y_k) - I(y_k))^2 \rightarrow \text{Min.} \quad (3.10)$$

The insertion of equation (3.8) into equation (3.10) followed by analytical differentiation with respect to the unknown amplitudes A_n leads to

$$2 \sum_{n=N_l}^{N_u} (A_n \sum_{k=1}^K (I_n(y_k) I_m(y_k))) = \sum_{k=1}^K (I(y_k) I_m(y_k)) \quad (\forall m: N_l \leq m \leq N_u) \quad (3.11)$$

Evaluation of equation (3.11) yields the amplitudes A_n , which are inserted into equation (3.6) producing the reconstructed $\varepsilon(r)$.

The Abel inversion process was done by Matlab R2016a. The implementation of Abel inversion in Matlab was directly downloaded from the website of MathWorks, which was shared by Killer [164]. In this Matlab code, a reconstructed profile $\varepsilon(r)$ can be obtained by input the measured data points $I(y)$, radius R of plasma jet and upper frequency limit N_u . Following this method, the numerical inversion can be used as a noise filter by choosing the lower and upper frequency limits N_l and N_u in equation (3.10). Besides, N_l was set to 1, so N_u defines the number of cosine expansions. Choosing a high value of N_u would give more potential features of measured intensity while a low value of N_u results in a low-pass filtering effect reducing noise. Therefore, in this study, the value of N_u was set 10 to achieve an efficient low-pass filtering because the reconstruction is almost entirely determined by the low-frequency components.

3.2 Materials

3.2.1 Feedstocks

In this study, the ceramic top coats were produced by two different yttria stabilized zirconia (YSZ) powder batches, M6700 and TZ-5Y, holding different morphologies as shown in Fig. 3.5. Their name and manufacturer information are given Table 3.3.

Table 3.3 Information of feedstock

Name	Internal code	Materials	Yttria content	Particle size (μm)			Manufacturer
				d_{10}	d_{50}	d_{90}	
M6700	YSZ 372M	7YSZ	7 wt.% (= 7.6 mol% $\text{YO}_{1.5}$)	7	12	19	Oerlikon Metco
TZ-5Y	--	5YSZ	5 mol% (= 9.5 mol% $\text{YO}_{1.5}$)	37	61	101	Tosoh Co.
Amdry 386	BCM 319M	CoNiCrAlY	--	15	24	36	Oerlikon Metco

The feedstock, M6700, is the standard powder for PS-PVD to deposit columnar structured TBCs. The particles are agglomerated by an organic binder from many nano-sized primary particles as spherical shapes to obtain a good flowability during powder injection. The particles fragment instantaneously when they are heated after entering the hot plasma flow above the critical evaporation temperature of the organic

3.2 Materials

binder (approx. 600 K). The powder is not a pre-alloyed YSZ but composed of monoclinic ZrO_2 and 7 wt.% of cubic Y_2O_3 , which is determined by XRD of M6700 as shown in Fig. 3.5. Some distinguishable peaks belonging to monoclinic ZrO_2 and cubic Y_2O_3 are marked. The TZ-5Y feedstock is also agglomerated from many nano-sized primary particles, but the binder between them is very easy to be destroyed during powder injection causing clogging. Different with M6700, TZ-5Y is pre-alloyed YSZ containing 96% tetragonal YSZ and 4% monoclinic zirconia in mass fraction determined by Rietveld analysis of the XRD pattern.

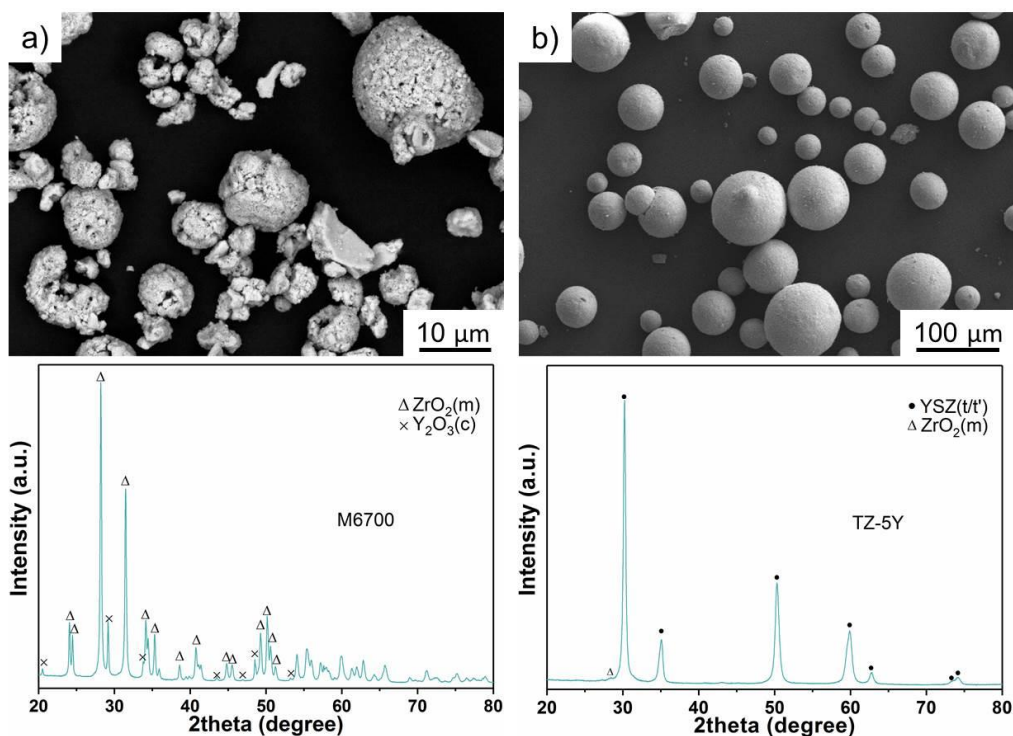


Fig. 3.5 SEM (SE) images of a) M6700 and b) TZ-5Y and corresponding XRD patterns

The particle size distributions (PSD) of the feedstocks were measured by Laser diffraction analysis (LA-950-V2, Horiba Ltd., Japan). It is based on the Fraunhofer diffraction theory stating that the particle size is directly proportional to the intensity of light scattered by a particle and inversely proportional to the angle of the laser beam [165]. Two optical models are commonly used to calculate PSD, the Fraunhofer diffraction model and the Mie theory, and the former one was used here. The obtained PSD is illustrated by the relationship of particle diameter and volume fraction or expressed as d_{10} , d_{50} , and d_{90} indicating the diameters below 10%, 50%, and 90 % of the total volume, respectively, as given in Table 3.3.

3.2.2 Substrates

The substrates used in this study were stainless steel (VA), Inconel 738, and graphite. For Inconel 738, a bond coat (BC) with 250 μm or 280 μm thickness was coated by VPS before applying TBCs. The surfaces of VA and BC were polished by silicon carbide #1200 abrasive papers in a grinding machine (Saphir 550, ATM, Germany). After polishing, the thickness of BC was around 100 μm with a roughness as given in Table 3.4. Then, the substrates were cleaned with ethanol in an ultrasonic bath for 3 minutes.

Table 3.4 Information of substrates

Name	Material	Preparation	Roughness (R_a)
VA	Stainless steel	polished	$\approx 0.03\text{--}0.05 \mu\text{m}$
IN&BC	Inconel 738 & CoNiCrAlY	polished	$\approx 0.03\text{--}0.05 \mu\text{m}$
Graphite	Graphite	polished	$\approx 1.5 \mu\text{m}$

The roughness of the substrates was measured by Perthometer (M2, Mahr, Germany). A stylus moves over the sample and scans a line profile. Various statistical roughness values such as R_a , R_q , R_z . (mean, square, average roughness) can be obtained.

In most cases, substrate temperature (T_s) was measured by infrared pyrometer (IR-AP 3CG, Chino, Japan). The pyrometer is a monochromatic narrow wavelength band radiation thermometer employing Ge as detecting element, and can measure temperatures in a range of 500 $^{\circ}\text{C}$ to 1500 $^{\circ}\text{C}$ at a measuring wavelength of 1.6 μm and a measuring area of approx. 10 mm^2 .

Two special substrate geometries for aims of investigation on the effects of boundary layer were designed to be perpendicular or parallel to the plasma axis as illustrated in Fig. 3.6. In both cases, the torch and the substrate did not move, therefore graphite was utilized as substrate material to avoid overheating of metallic substrate. The T_s was monitored by Type K thermocouple inserted in the substrate. The T_1 and T_2 in Fig. 3.6a and the A, B, and C in Fig. 3.6b indicate the positions of these thermocouples.

3.3 Spraying process

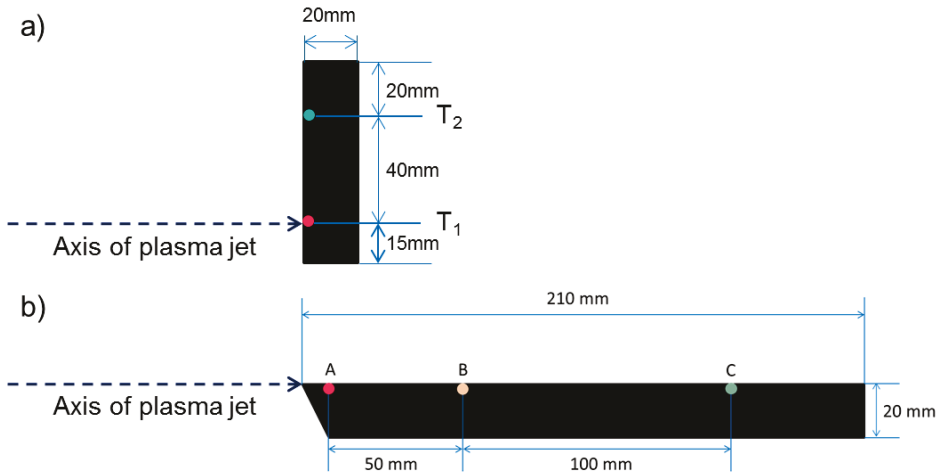


Fig. 3.6 Schematic lateral view of positions of substrates and thermocouples: a) perpendicular to plasma axis, b) parallel to plasma axis. T₁ and T₂ in a) and A, B, and C in b) indicate the positions of these thermocouples.

3.3 Spraying process

3.3.1 Coating deposition: spraying parameters

The coating processes were carried out in an Oerlikon (formerly Sulzer) Metco Multicoat system, which can achieve a low working pressure of 200 Pa and the input power of 180 kW using an O3CP torch. To produce columnar structured TBCs, two kinds of spraying parameters classified based on the plasma gases along with other parameters are given in Table 3.5. In some cases of Ar/He plasma jet, the torch did not swing. The substrates in all of the coating processes were fixed without any rotation. Carrier gases of 2x16 slpm Ar were used in all tests. Detailed spraying parameters applied for the samples in this work are summarized in Table A1 in the appendix.

Table 3.5 Spraying parameters for coating deposition

Conditions	A-1	A-2	B
Plasma gases	Ar 35 slpm / He 60 slpm		Ar 35 slpm / He 60 slpm / H ₂ 10 slpm
Current	2600 A or 2750 A		2200 A
Swing angle of torch	0°	±7°	±7°
Swing speed of torch	0	30 mm/s	30 mm/s
Spray distances	400 ~ 1000 mm		
Powder feeding rates	0 ~ 18 g/min		

slpm: standard liter per minute

3.3.2 Substrate temperature measured by thermocouple and pyrometer

The theoretical principle of a monochromatic radiation thermometer is the Planck's radiation law for an ideal black body:

$$E_{b\lambda} = \frac{C_1 \lambda^{-5}}{e^{\frac{C_2}{\lambda T}} - 1} \quad (3.12)$$

wherein, $C_1=2hc^2=3.7415 \times 10^8 \text{ Wcm}^{-2}\mu\text{m}^4$, $C_2=hc/k=1.43879 \times 10^4 \mu\text{m K}$, and λ (μm) is the radiation wavelength; T (K) is the absolute temperature. The amount of thermal energy emitted by a given object is directly related to its temperature, wavelength, and other factors such as surface quality, transparency, reflectivity, absorptivity, etc. Thus, the energy emitted from a real target E_λ is only part of $E_{b\lambda}$, that is $E_\lambda = \varepsilon E_{b\lambda}$. The emissivity coefficient ε is the ratio between the actual energy emitted from a target and that of an ideal blackbody emitter. While in the real engineering application, the energy received by the pyrometer also can be influenced by the reflected energy, ambient atmosphere, measurement distance, angle of observation, and so on. Therefore, the energy received by the pyrometer can be formulated as $E_{r\lambda}=FE_{b\lambda}$. Here, F is the total influence coefficient and it is proportional to ε . As a result, the relationship between temperature (T_r) read from the pyrometer and the real temperature of the target can be simply described by equation (3.13):

$$\frac{C_1 \lambda^{-5}}{e^{\lambda T_r} - 1} = F \frac{C_1 \lambda^{-5}}{e^{\lambda T} - 1} \quad (3.13)$$

Therefore, one can obtain:

$$T_r = \frac{C_2 T}{\lambda T \ln(e^{\frac{C_2}{\lambda T}} - 1) + F} \approx \frac{C_2 T}{C_2 - \lambda T \ln(F)} \quad (3.14)$$

$$F = e^{\frac{C_2(T_r - T)}{\lambda T T_r}} \quad (3.15)$$

In order to check the deviation of the pyrometer, a thermocouple was fixed deeply into the back side of graphite substrate (almost a perfect black body material) to ensure a good thermal conductivity between the thermocouple and the substrate. At the same time, pyrometer was measuring the front surface of the substrate. Fig. 3.7 shows the temperature measured by thermocouple (set as T) and pyrometer (set as T_r) and F calculated by equation (3.15). The emissivity was set to 0.66 in the pyrometer but the real emissivity of graphite substrate may be around or higher than 0.9, which results in a lower reading of temperature.

3.3 Spraying process

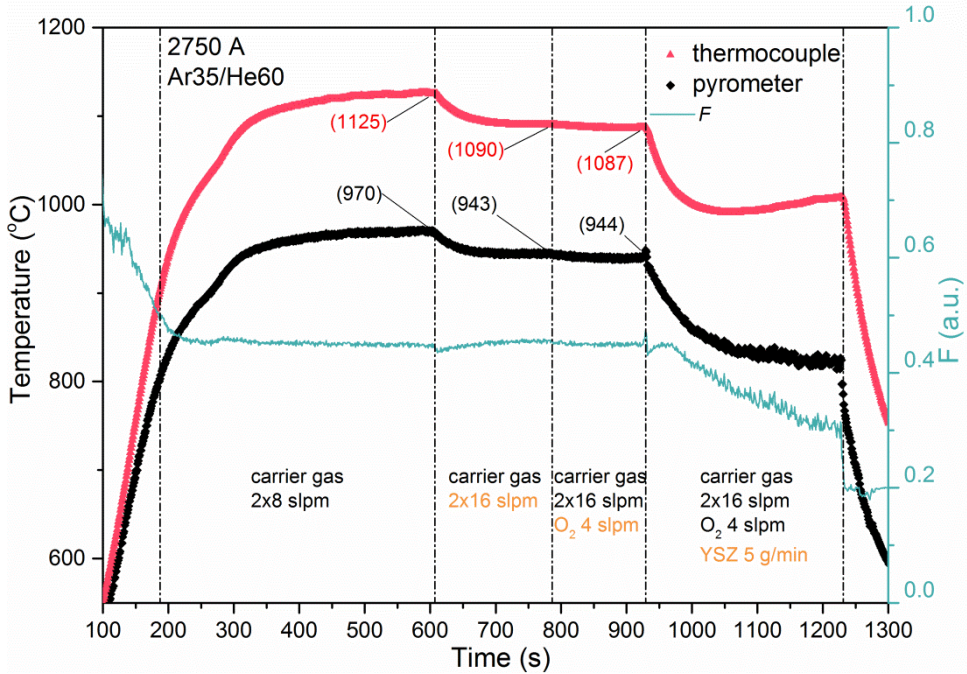


Fig. 3.7 Substrate temperature measured by thermocouple and pyrometer and the estimated total influence coefficient during spraying

In the beginning, the carrier gas started with 2x8 slpm and the current was increased step by step. After the current reached to 2750 A, the temperature increased and finally approached a balanced value. The temperatures, T and T_r , both dropped about 33 K in account of leading double amount of carrier gas 2x16 slpm. Introducing of 4 slpm oxygen did not cause any apparent temperature variation and the calculated F value kept rather constant. Graphite with oxygen will react at high temperature and form CO and CO₂. The absorbing wavelength of CO is around 4.5 μm and that of CO₂ is around 4.3 μm . And essentially O₂ is transparent to IR. Thus, the gases CO, CO₂ and O₂ should not have any influence on pyrometer temperature measurements. After feeding powder into the chamber, the temperatures decreased gradually and the calculated F value diminished little by little as well. One reason is the temperature reducing of the plasma due to the powder loading effect (will be discussed in chapter 4). The other reason is assumed to be the emissivity change of target surface due to build-up of the thermal barrier coating. As the coating grew, the surface became rougher while the internal porosity increased. As the microstructure of columnar structured YSZ coating, the high degree of scattering is likely associated with the high density of scattering defects (pores and fine feather-like microstructures [93]). Thus, at the later period of coating growth process, T started to

increase but T_r kept fluctuating at a rather constant value. This comparison shows that temperature was well monitored by pyrometer but the deviation of approx. 150 K caused by emissivity variation was found.

3.4 Characterization of the coatings

3.4.1 Microscopy

To observe the microstructures of the highly porous PS-PVD ceramic coatings by cross-sectioning, such samples must be embedded in a low-viscosity epoxy resin to stabilize the coatings for further preparation. The mounting system consists of a resin and a hardener (Struers ApS, Denmark or Cloeren technology GmbH, Germany). After embedding, samples are ground with silicon carbide (SiC) abrasive papers of the grain size 400 to 1200 in grinding machine (Saphir 550, ATM, Germany) with setting force of 20 N and speed of 150 rpm. Then samples were polished in a Minimet polishing machine (Buehler, Germany) on a perforated chemical fiber cloth with diamond or SiO₂ suspensions of 3, 1 and 0.5 μm .

The morphologies and microstructures of the coatings were investigated by a TM3000 tabletop scanning electron microscope (SEM) (Hitachi High-Technologies in Europe, Germany) and an Ultra 55 SEM (ZEISS, Germany) for different magnification. The former one was used for low magnification, in which only back-scattered electron (BSE) images can be obtained. The latter one is equipped with both secondary electron (SE) and BSE imaging modes to obtain topographic and compositional contrast at high magnification. In addition, an Energy dispersive X-ray spectroscopy (EDX) detector (type INCAEnergy355) is equipped in Ultra 55 for the elemental analysis or chemical characterization. In addition, the Ultra 55 has a detector for the evaluation of cathodoluminescence (CL). The bombardment of a luminescent material with high energy electrons can initiate the emission of photons by raising electrons from the valence band into the conduction band, creating a gap. When an electron and a gap recombine, the electron returns to its ground state energy level and it is possible for a photon to be emitted [167]. It is found that the monoclinic phase, either occurring on grain boundaries or formed by deformation, appears strongly luminescent at a specific wavelength, whereas in cubic or tetragonal material grain boundaries appear dark [168]. Therefore, CL was used to detect monoclinic phase as well as its spatial distribution in PS-PVD coatings.

3.4.2 Standard X-ray diffraction and pole figure

Standard X-ray diffraction (XRD, D4, Endeavor-Bruker AXS GmbH, Germany) was carried out to determine phase composition and crystal structure of the coatings and the powder feedstock. When the X-ray radiation penetrates solid materials, it can be scattered by crystal planes producing arrays of spherical waves. X-rays are used to produce the diffraction pattern because their wavelength λ is typically the same order of magnitude (1-100 Å) as the spacing d between planes in the crystal. Although these waves extinguish one another in most directions through destructive interference, they add constructively in a few specific directions, determined by Bragg law [169]:

$$2d \sin \theta = n\lambda \quad (3.16)$$

Here, d is the spacing between diffracting planes, θ is the incident angle, n is any integer, and λ is the wavelength of the X-ray radiation.

In standard XRD, the Cu-K $_{\alpha}$ X-ray radiation is generated at a voltage of 40 kV and a current of 40 mA. The position of the sample is fixed while the development of 2θ from 10° to 140° was controlled by the incident angle of X-ray with a 2θ step size of 0.02° and step time of 0.75 or 2 s, respectively. The small step size was used for Rietveld refinement by using a least squares approach to refine a theoretical line profile until it matches the measured profile [170], which can quantify the phase composition and lattice parameters as well as allow qualifying preferred orientations.

The stability domains of the different tetragonal forms of YSZ versus the ratio of their cell parameters are represented in Fig. 3.8. If the ratios $c/a\sqrt{2}$ (so-called tetragonality) are < 1.010 , the coating is verified to consist of t' phase. The changes of lattice parameters can be used to estimate the yttria content within tetragonal phases as described by Scott [41] and then modified by Ilavsky [171] as:

$$YO_{1.5} (\text{mol}\%) = \frac{1.0225 - \frac{c}{\sqrt{2}a}}{0.0016} \quad (3.17)$$

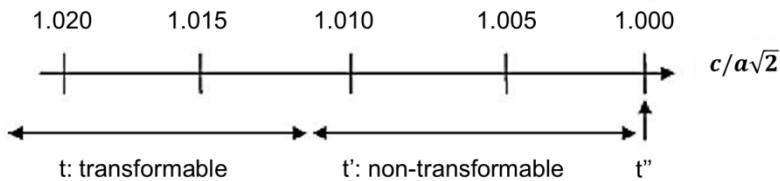


Fig. 3.8 The tetragonal forms of yttria stabilized zirconia [48]

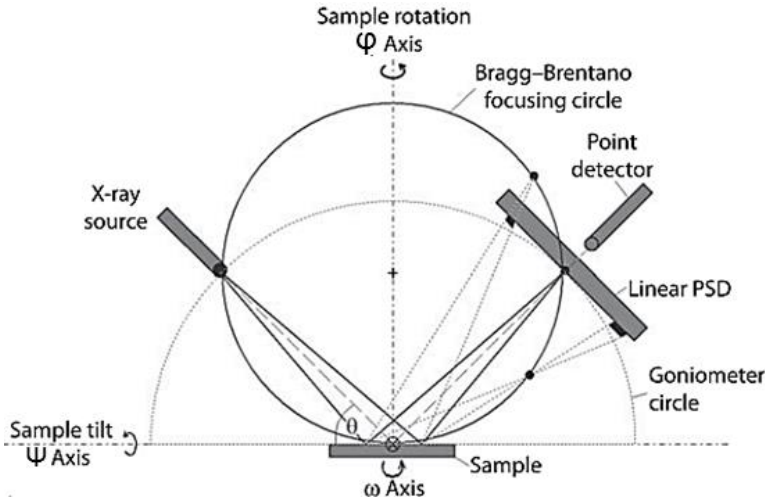


Fig. 3.9 A configuration of pole figure measurements [172]

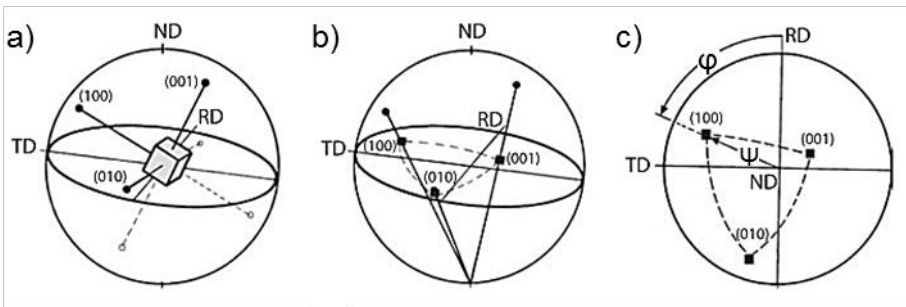


Fig. 3.10 Presentation of the {100} poles of a cubic crystal in the stereographic projection: a) crystal in the unit sphere; b) projection of the {100} poles onto the equator plane; c) {100} pole figure and definition of the pole figure angles ψ and ϕ for the (100) pole [172]

Pole figure measurements were conducted on the coating surface by X-ray diffraction (Empyrean, PANalytical GmbH, Germany). A pole figure is a two-dimensional stereographic projection in which the positions and intensities of specific crystallographic orientations are plotted in relation to the specimen geometry [172]. It was performed to determine the variation in degree of crystal orientation as well as in-plane orientation on a macro-scale. Fig. 3.9 shows the configuration of the pole figure measurement, the incident angle of the X-ray radiation was fixed so that 2θ is defined while the sample was rotated and tilted. By measuring the intensity of a Bragg diffraction peak over almost a full hemisphere, the distribution of the intensity is obtained and displayed on a stereographic projection. The tilting angle ψ describes the azimuth of the pole, where $\psi = 0^\circ$ is the north pole of the unit sphere, and the rotating angle ϕ characterizes the rotation of the pole around the polar axis, starting from a specified reference direction. To characterize the crystallographic orientation of the

crystal, the angles ψ and ϕ has to be determined with respect to an external reference, such as, the specimen coordinate system as shown in Fig. 3.10: the normal direction (ND), the rolling direction (RD), and less frequently the transverse direction (TD) of a rolled steel specimen. In the measurement, the angle ψ was varied from 0° to 85° , and the angle ϕ was 360° with a step size of 5° for both rotation and tilting.

3.4.3 Electron back-scatter diffraction

Electron back-scatter diffraction (EBSD) is a scanning electron microscope (SEM) based technique that gives crystallographic information in a micro-scale along with the microstructure in a crystal sample, such as grain size and boundary, global or local texture, phase identification and distribution. A schematic Kikuchi pattern formation in SEM-based EBSD is shown in Fig. 3.11.

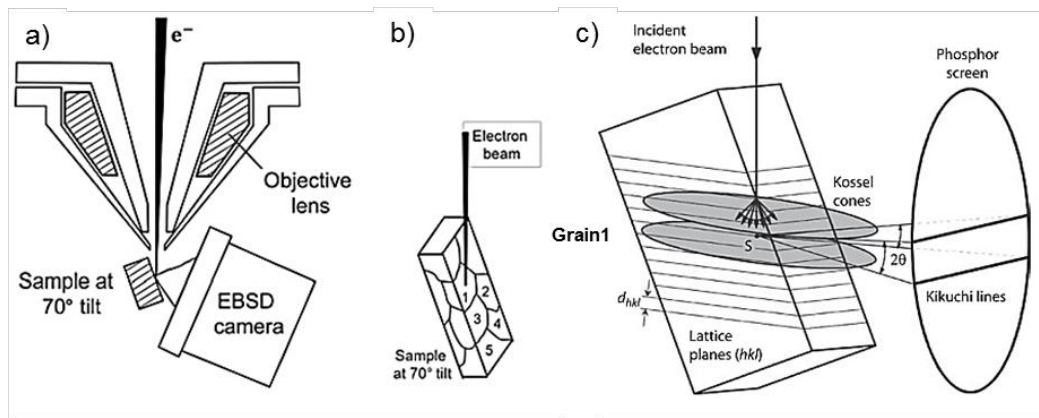


Fig. 3.11 Schematic of Kikuchi pattern formation in SEM-based EBSD technique:
a) SEM-EBSD set-up [173]; b) incidence of electron beam on a polycrystalline material [173];
c) origin of Kikuchi lines from the EBSD [172]

The electron beam impacts on the interesting point of the 70° tilted sample and a fraction of electrons are scattered in-elastically by the atoms in the sample and forming a divergent source of electrons with a small loss of energy. Some of these electrons are incident on crystal planes and diffracted at an angle θ satisfying the Bragg law (equation 3. 15) forming a pair of large-angle Kossel cones so that the projections of these cones on the phosphor screen appear as a pair of parallel lines termed Kikuchi bands, and therefore each Kikuchi band can be indexed by the Miller indices of the diffracting crystal plane which formed it [174]. The intersections of the Kikuchi bands correspond to zone axes in the crystal. Then, an automated indexing procedure based on Hough transformation [175] is carried out by the software to calculate the positions

of the Kikuchi bands and the angles between the detected bands to find the best fit solution. Then, the orientation matrix is calculated.

The EBSD was performed cooperatively at the RWTH Aachen Gemeinschaftslabor für Elektronenmikroskopie (GFE). At GFE, a JSM-7000F SEM is equipped with a “Hikari” EBSD camera (Ametek-EDAX) operating under an acceleration voltage of 20 kV and a probe current approx. 30 nA with a step size of 100 nm and a step size of 200 nm for thicker coatings, respectively. In our analyses, image quality (IQ) maps, orientation maps (also called as inverse pole figure maps (IPF)), and color-coded grain size distribution maps are mainly used. The IQ is a metric describing the quality of a diffraction pattern [176]. The orientation map is the calculated orientation matrix, which was indexed with three different pole figures. For example, cubic lattice symmetry is normally indexed with {001}, {011}, and {111} to observe the main crystallite orientations. Grains in EBSD are areas of measurement points, for which the same orientation is found. In case that the grain size is smaller than the excitation volume of the electron beam, the IQ would be poor due to the overlapping of different EBSD patterns. The interaction volume is asymmetrical in EBSD because the sample was 70° tilted. The estimated actual resolution with a step size of 100 nm is approx. 50-100 nm along the tilt axis (roughly aligned with the thickness direction of the coating); and 150-300 nm perpendicular to the tilt axis (the direction parallel to the substrate surface).

Chapter 4 Plasma Jet Characterization

In the PS-PVD process, the major fraction of the injected powder is transformed into vapor phase. As a consequence, the diagnostics based on the thermal emission of solid or liquid particles, for example by the DPV-2000, are not applicable. OES however can be used to determine the properties of the plasma jet [177-181] and was also introduced to characterize the injected material in thermal spray processes such as the VPS/LPPS [182]. In PS-PVD, the plasma gases can be different, such as Ar, He, H₂, and N₂ [95] or mixtures of them. The composition of the plasma gas has a significant influence on the microstructures of the PS-PVD coatings [93, 97, 103, 148, 183]. In earlier studies, the typical plasma characteristics of the PS-PVD process and the impact on the coating properties were investigated by OES [103, 184]. However, the calculation of the excitation temperature was based on the integral intensity through the line of measurement of OES and the assumption of (partial) local thermal equilibrium (LTE or pLTE). Due to the expansion of the plasma jet at low chamber pressure, the concentrations of all species are reduced, also the one of electrons. Therefore, the LTE conditions are not satisfied due to the fast diffusion of electrons at the plasma fringes. So the influence of the deviation from LTE and its effect on the calculation of excitation temperature should be taken into consideration in order to obtain a more accurate description of the plasma jet. Moreover, the addition of H₂ as a secondary plasma gas results in a broadened plasma jet [92] as well as in more compact columnar coating microstructure [97]. The microstructures of the coatings were found to be related to the samples' positions in the plasma jet [8, 149], and preferred growth orientations of columnar structured coatings were shown dependent on the substrate temperature [102].

In this chapter, two different PS-PVD jets composed of Ar/He and Ar/He/H₂ were investigated. Abel inversion was introduced to reconstruct the spatial characteristics of the plasma jet including the excitation temperatures along the radial direction and the distribution of atomic Ar and He in the Ar/He jet. The deviation from LTE and its effect on the calculation of excitation temperature by different emission lines of Ar and He is discussed. Besides, the influences of addition of H₂ as a secondary plasma gas on the temperature profiles of the plasma jet and the substrate temperature were analyzed. Furthermore, the effect of feedstock powder loading was investigated with respect to the reduction of the temperatures of the plasma jet.

4.1 Local emission intensity profiles

In order to compare the intensities at different chamber pressures, the intensities were normalized. Examples for measured raw data and polynomial fits of Ar I (neutral Ar) and Ar II (single ionized Ar) lines under conditions A-200 (Ar/He jet, 200 Pa) and A-1000 (Ar/He jet, 1000 Pa) are given in Fig. 4.1. Under the same conditions, all the measured intensity profiles of Ar lines at different wavelengths have a similar shape as shown in Fig. 4.1. The highest measured intensity of Ar I line at chamber pressure of 200 Pa is achieved at approx. $y = 40$ mm while that of Ar II line is near the center of the plasma jet, which means that Ar is ionized in the center of the plasma jet. Since the measured intensity $I(y)$ corresponds to the integration along the line of measurement, one can speculate that in the center of the plasma jet the concentration of neutral Ar must be low. As drawn in Fig. 4.1, a dashed line describing the 5% level of the normalized value is plotted to give a more reliable description of the radial jet extension where the values approach zero.

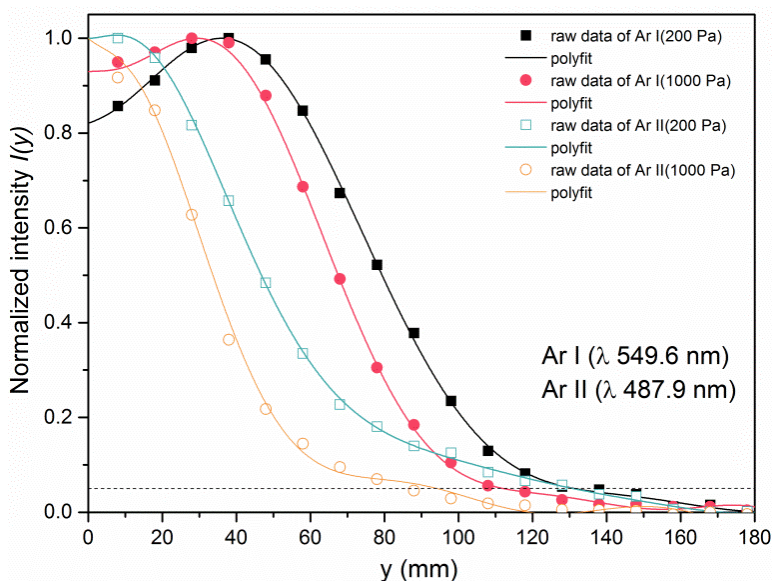


Fig. 4.1 Radial profiles of normalized measured $I(y)$ of Ar I line (549.6 nm) and Ar II line (487.9 nm) under conditions A-200 (Ar/He jet, 200 Pa) and A-1000 (Ar/He jet, 1000 Pa). The raw data points are the experimentally measured $I(y)$ and the lines are polynomial fits of raw data. The dashed line describes the 5% level of the normalized $I(y)$.

Fig. 4.2 gives the reconstructed $\varepsilon(r)$ profiles from the measured $I(y)$ (Fig. 4.1) with $N_u=10$ in the Matlab script of Abel inversion. At a chamber pressure of 200 Pa, in the center of plasma jet ($r=0$ mm), the $\varepsilon(r)$ of Ar I results slightly negative. It should be noted that with increasing N_u , this feature of negative $\varepsilon(r)$ doesn't change. The slightly

negative values in the center of the jet are not reasonable in a physical sense but only in a mathematical sense. One of the most possible reasons is the error in determining the position of the central point. This error happens because it is very difficult in practice to pinpoint the exact central point of the energy distribution curve. An estimation of this error revealed that the central point error must be kept under 1.0% of the plasma diameter or within 0.2 mm when using a 20 mm plasma diameter to keep measurement error values below 5% of the real emitted energy at a specific point [185]. There could be some other reasons, for example, that the assumption of thin plasma which is optically transparent is not fulfilled ideally. Nevertheless, a reconstruction from the obtained $\varepsilon(r)$ to $I'(y)$ (by numerical integration $I'(y) = \int_{-x_0}^{x_0} \varepsilon(r) dx$ with $x = \sqrt{r^2 - y^2}$) confirmed that the reconstructed $I'(y)$ has only 5% average deviations from the measured $I(y)$, which means that the Abel inversion algorithm works well and the error in the alignment was relatively small.

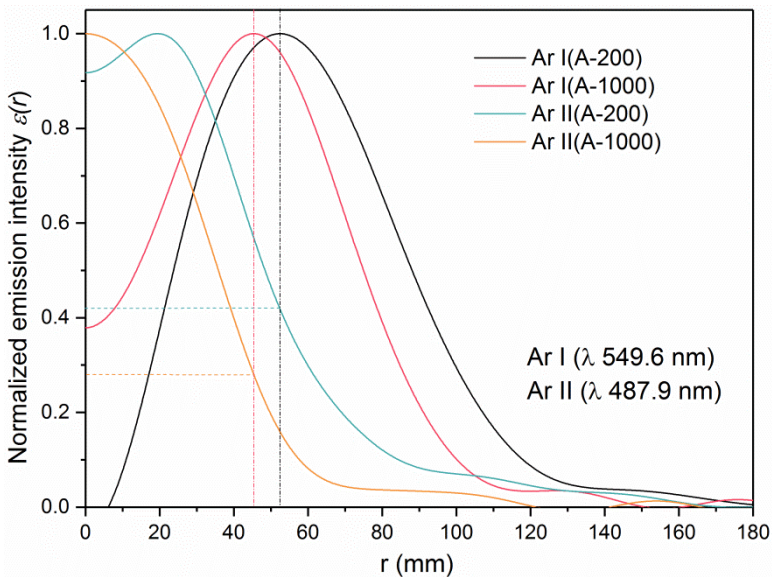


Fig. 4.2 Radial profiles of the reconstructed $\varepsilon(r)$ of Ar I line (549.6 nm) and Ar II line (487.9 nm) under conditions A-200 (Ar/He jet, 200 Pa) and A-1000 (Ar/He jet, 1000 Pa). The dashed lines describe the radii where the $\varepsilon(r)$ of Ar I line reaches the maximum value and the corresponding $\varepsilon(r)$ of Ar II line.

One should have in mind that the emission intensity is positively proportional to the concentration of the species and exponential to the temperature. Such low values $\varepsilon(r=0 \text{ mm})$ in the center of plasma jet might be caused, on one hand by the low concentration of neutral Ar due to ionization of Ar. On the other hand, the measurement error as mentioned above could also lead to slightly negative values in the center [186].

4.1 Local emission intensity profiles

When the chamber pressure increased to 1000 Pa, the relative $\varepsilon(r=0 \text{ mm})$ is much higher which could be due to the relatively enhance concentration of neutral Ar. As indicated in ref. [187], when increasing the radius in a pure Ar plasma, the $\varepsilon(r)$ of the ionic line is expected to reach its minimum value at the approximate radius where the emission of the atomic line has its maximum. However, as shown in Fig. 4.2, at chamber pressure 200 Pa, the Ar II line still has around 42% relative intensity, which means that the low concentration of neutral Ar is not the only reason but the addition of He into Ar plasma has an influence on the distribution of ionic and neutral Ar in the center of plasma jet.

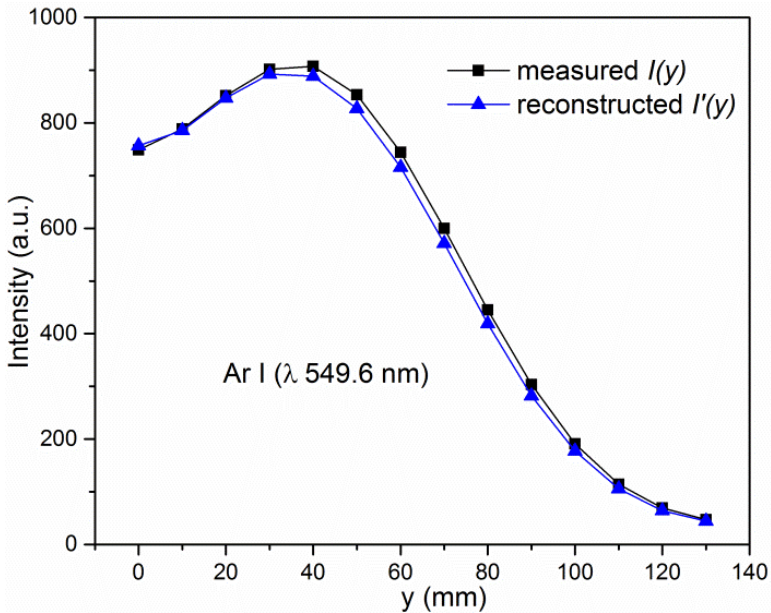


Fig. 4.3 A comparison between the measured $I(y)$ and the reconstructed $I'(y)$ for Ar I line (549.6 nm)

When H_2 was added to the plasma gases at pressure of 200 Pa, the measured intensities of all lines were much lower than those in the Ar/He jet. Both the measured intensities $I(y)$ and the reconstructed $\varepsilon(r)$ of the Ar I line ($\lambda = 549.6 \text{ nm}$) approach zero at a radius of approx. 90 mm (Fig. 4.4). Although the $\varepsilon(r=0 \text{ mm})$ of the Ar I line has a lower value as shown in Fig. 4.4, its relative value is not as low as under condition A-200 (Fig. 4.2). The possible reasons are lower ionization degrees of Ar and lower plasma jet temperatures under this condition. However, as seen in Fig. 4.5, both the measured intensities $I(y)$ and the reconstructed $\varepsilon(r)$ of the H_2 line ($H_\beta 486.1 \text{ nm}$) drop to 5% level of the maximum value at a rather large radius approx. of 160 mm, which is obviously the reason for the broader plasma jet appearance under condition B-200 (Ar/He/ H_2 jet,

200 Pa) compared to condition A-200 (Ar/He jet, 200 Pa) as the photos shown in Fig. 2.19 (from ref. [92]).

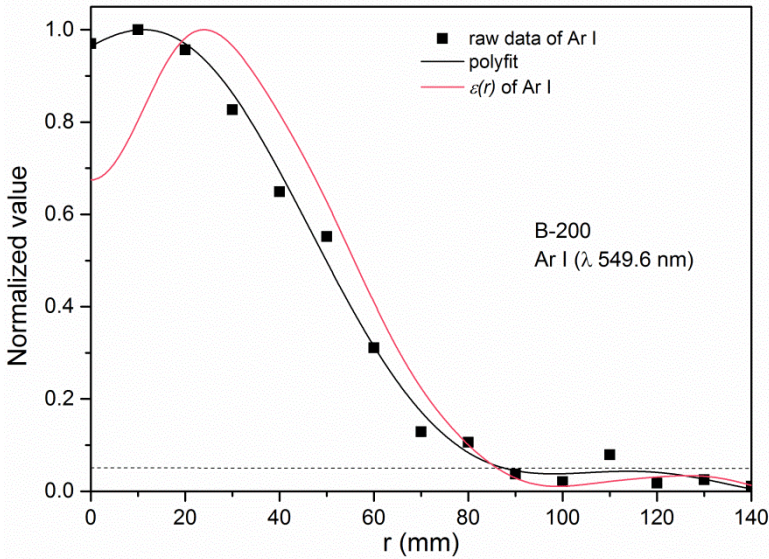


Fig. 4.4 Radial profile of measured $I(y)$, polynomial fits of raw data and the reconstructed $\varepsilon(r)$ of Ar I line (549.6 nm) under condition B-200 (Ar/He/H₂ jet, 200 Pa). The dashed line describes the 5% level of the normalized value.

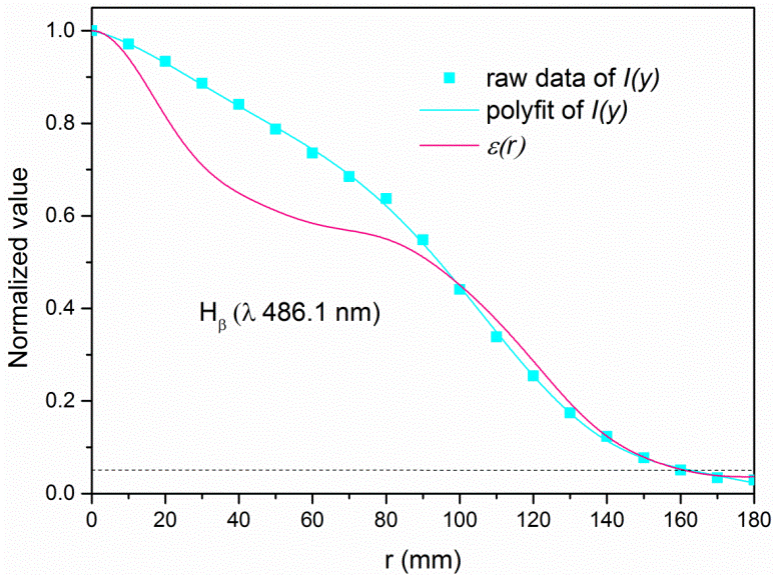


Fig. 4.5 Radial profile of measured intensities $I(y)$, polynomial fits of raw data and the reconstructed $\varepsilon(r)$ of H_β line (486.1 nm) under condition B-200 (Ar/He/H₂ jet, 200 Pa). The dashed line describes the 5% level of the normalized value.

4.2 Temperatures

4.2.1 Excitation temperature profiles

Since the reconstructed $\varepsilon(r)$ profiles of Ar I lines drop to 5% of the maximum value at $r = 130$ mm, 110 mm and 90 mm under conditions A-200, A-1000 and B-200, respectively, the errors in the temperature calculations beyond these radii become quite large; therefore, the T_{exc} profiles were calculated only up to these radii. The local excitation temperature $T_{exc}(r)$ can be obtained from the slope of a linear Boltzmann plot by replacing $I(y)$ with $\varepsilon(r)$ in equation (3.2). Under condition A-200, due to the very low emission of Ar I lines in the center of plasma (seen in Fig. 4.2), it is not possible to apply the Boltzmann plot method to calculate the local excitation temperature $T_{exc}(r)$ anymore because of the large uncertainty. But beyond a radius of 15 mm, the enhanceive emission intensities indicate the increasing amount of neutral Ar. Therefore, the $T_{exc}(r)$ profiles of Ar under condition A-200 were calculated starting from $r = 15$ mm.

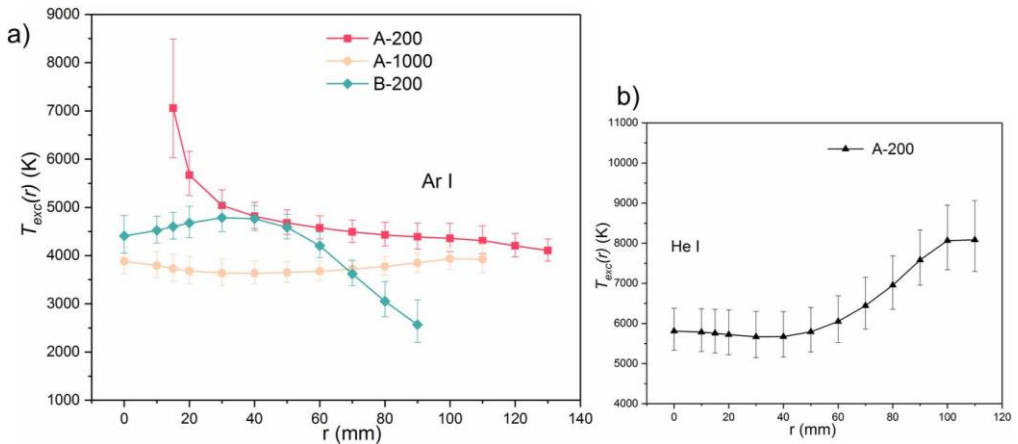


Fig. 4.6 a) Development of the excitation temperatures along the radial direction of plasma jet under condition A-200 (Ar/He jet, 200 Pa), A-1000 (Ar/He jet, 1000 Pa) and B-200 (Ar/He/H₂ jet, 200 Pa); b) Calculated temperatures by He lines along the radial direction of plasma jet under condition A-200 (Ar/He jet, 200 Pa)

Under condition A-200, $T_{exc}(r=15 \text{ mm})$ is about 7000 K and $T_{exc}(r>15 \text{ mm})$ decreases along the radial direction as given in Fig. 4.6a. When the chamber pressure increases to 1000 Pa, the calculated temperature $T_{exc}(r)$ for condition A-1000 is much lower than that at 200 Pa. The $T_{exc}(r)$ for A-1000 decreased by 250 K from $r = 0$ mm to $r = 40$ mm and then slightly increased along the radial direction. This apparently increasing temperature at the outer fringe of the plasma jet is unreasonable. A straight line may be obtained in the Boltzmann plot even when non-pLTE levels are included, thus leading

to spurious excitation temperatures [156]. In the case of a recombining plasma, the underpopulation of low energy levels leads to a higher excitation temperature. In other words, at the periphery of plasma jet, all chosen levels are probably not in LTE so that the obtained T_{exc} becomes spuriously high. The same phenomenon can be also found when the temperature was calculated with neutral He (He I) lines. Seven He I lines were chosen as ref. [103] to calculate the excitation temperature. As shown in Fig. 4.6b, the calculated excitation temperature of He dropped slightly and then increased dramatically along the radial direction until reaching the outer fringe where it stopped to increase. The possible reason could be that, in the outer fringe region, the density of electrons is not sufficient to sustain LTE, in particular for He typically exhibiting strong deviations from LTE as mentioned before. Therefore, under condition B-200 (Ar/He/H₂ jet, 200 Pa), the excitation temperature was also calculated by Ar I lines as under condition A-200 and the temperature profile is given in Fig. 4.6a. It is obvious that, compared with Ar/He jet, the Ar/He/H₂ jet has lower $T_{exc}(r)$ and is only similar at radii of 40 and 50 mm. The $T_{exc}(r)$ starts to drop very fast at $r > 50$ mm and down to $T_{exc}(r=90 \text{ mm}) = 2500 \text{ K}$.

4.2.2 Substrate temperatures

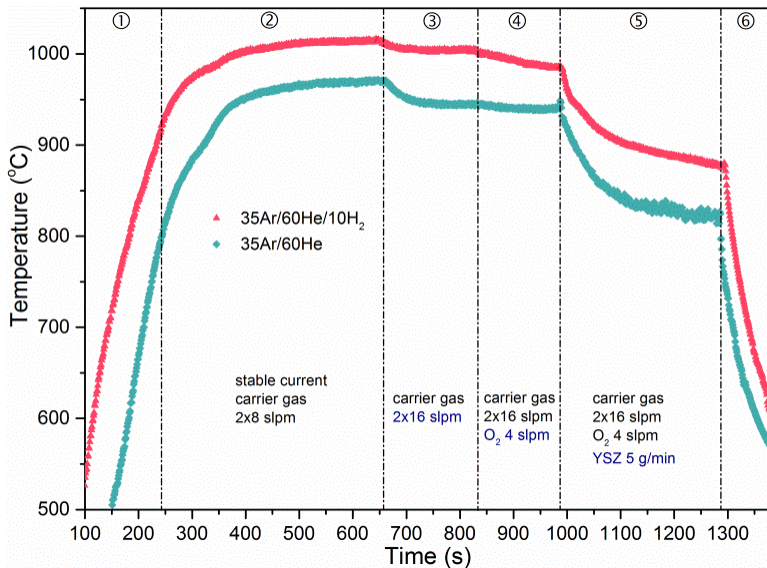


Fig. 4.7 Substrate temperatures under conditions A-200 (Ar/He jet, 200 Pa, green curve) and B-200 (Ar/He/H₂ jet, 200 Pa, red curve)

As the substrate temperature (T_s) has a major influence on the microstructure of the coatings made by thin film deposition [7], T_s was recorded continuously by pyrometer

4.2 Temperatures

at different stages through the whole coating process at a spray distance of 1000 mm. The results are given in Fig. 4.7. In the first stage of the experiment, the current was adjusted approaching to the appropriate current step by step so that T_s kept increasing. After the currents became stable, T_s reached a maximum value and then kept rather constant. In the third stage, the carrier gas was changed from 2x8 slpm to 2x16 slpm, which led to a slight T_s drop under both conditions. One reason could be that adding of carrier gas reduced the plasma jet temperature and thus the substrate temperature decreased. Later, after T_s was stable again, O_2 (4 slpm) was led into the chamber, which did not cause any apparent temperature variation. After feeding powder into the chamber, the temperatures decrease gradually. One reason is that the powder absorbed energy from the plasma (loading effect of powder feedstock will be discussed later). Another reason is assumed to be the emissivity change of target surface due to coating formation (see Fig. 3.7 and analyses in section 3.3.2). As the coating grows, the surface becomes rougher while the internal porosity increases.

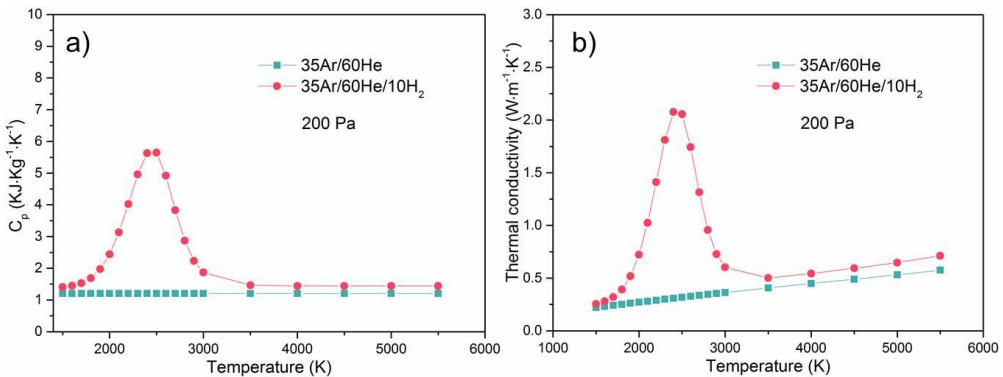


Fig. 4.8 Calculated a) specific heat capacity (c_p) and b) thermal conductivity profiles under conditions A-200 (Ar/He jet, 200 Pa) and B-200 (Ar/He/H₂ jet, 200 Pa)

The overall T_s under condition B-200 (Ar/He/H₂ jet, 200 Pa) was about 50 K higher than that under condition A-200 (Ar/He jet, 200 Pa). According to Fig. 4.6a in section 4.2, the T_{exc} of Ar/He jet at 200 Pa was higher. The reason for this unusual phenomenon could be caused by the high thermal conductivity of H₂ in the temperature range of 2000 K to 5000 K for atmospheric pressure due to the dissociation of H₂ as presented in ref. [188]. Thus, the specific heat capacity (c_p) and thermal conductivity under chemical equilibrium were calculated by NASA Chemical Equilibrium with Applications (CEA) software assigning discrete temperatures and the chamber pressure of 200 Pa [189, 190]. As shown in Fig. 4.8a, the peak of c_p in the temperature range of 2000 to 3000 K in the Ar/He/H₂ jet is due to the dissociation of H₂. The dissociation energy is consumed without contributing to an increase of the temperature. This could

be one reason that the Ar/He/H₂ jet has a relatively low excitation temperature compared to the Ar/He jet. Similarly, the dissociation of H₂ increases the reaction thermal conductivity (Fig. 4.8b) in the Ar/He/H₂ jet. In comparison, in the range of calculated $T_{exc}(r)$, the thermal conductivity of the Ar/He/H₂ jet is higher than that of the Ar/He jet, especially around 2500 K. As a result, a higher heat transfer coefficient is expected leading to high T_s under condition B-200.

4.3 Concentration profiles of Ar and He

Considering that He is prone to serious deviations from LTE at the fringe region of the PS-PVD jet, the calculation of concentration profiles becomes quite complicated. In this section, a rough but simple method is discussed to estimate the constituent concentration profiles in Ar/He plasma jet.

Assuming LTE condition in PS-PVD, the excited states can still be illustrated by a Boltzmann distribution. As the intercept of equation (3.2), $C = \ln\left(\frac{Lhc n_{tot}(r)}{4\pi Z}\right)$, is related to n_{tot} , the ratio between atomic Ar and He in the plasma can be calculated according to equation (4.1) at every given radius:

$$\frac{n_{tot}(Ar)}{n_{tot}(He)} = \frac{\exp(C(Ar)) Z(Ar)}{\exp(C(He)) Z(He)} \quad (4.1)$$

wherein, $C(Ar)$ and $C(He)$ can be obtained from the intercept of Boltzmann plots. The values of the partition functions $Z(Ar)$ and $Z(He)$ are retrieved from NIST Atomic Spectra Database [153], in which the element and its ionization stage have to be specified as well as temperature for the partition function. In the case of Ar I and He I, both $Z(Ar)$ and $Z(He)$ are almost equal to unity in the temperature range of 0.1 eV (1160.5 K) to 1 eV (11605 K). Therefore, equation (4.1) can be simplified as:

$$\frac{n_{tot}(Ar)}{n_{tot}(He)} = \frac{\exp(C(Ar))}{\exp(C(He))} \quad (4.2)$$

Using this approach, the $n_{tot}(Ar)/n_{tot}(He)$ ratio can be determined along the radial direction. As seen in Fig. 4.9, the increasing $n_{tot}(Ar)/n_{tot}(He)$ ratio with increasing r indicates that in the center of plasma jet the main constitute is atomic He while atomic Ar prevails mainly at the periphery of He flow. However, it should be noted that the under-population of low energy levels leads to higher spurious excitation temperatures (as discussed in section 4.2.1) as well as to smaller values of C , especially for He. Thus, the calculated results in Fig. 4.9 could be higher than the real ratio of $n_{tot}(Ar)/n_{tot}(He)$ especially at the outer fringe region where $T_{exc}(r)$ of He shows spurious high values as

4.3 Concentration profiles of Ar and He

mentioned in Fig. 4.6b. But the increasing tendency of $n_{tot}(Ar)/n_{tot}(He)$ should be correct. The input ratio of Ar and He is $35/60 \approx 0.58$ as indicated by the dashed line in Fig. 4.9. When the chamber pressure increased from 200 Pa to 1000 Pa, the plasma jet became shorter and narrower. Hence, the calculated $n_{tot}(Ar)/n_{tot}(He)$ values reach this input ratio at a smaller radius. The uncertainty of the ratio of concentration in Fig. 4.9 is estimated by calculating the ratios in equation (4.2) with the standard errors of $C(Ar)$ and $C(He)$ of the linear fit. Here, it is assumed that the absence of LTE affects the fitting quality. The uncertainty actually increases from the center region to the outer fringe region of the plasma jet. Because the values in Fig. 4.9 are given in “log” format, the increasing tendency is not very evident in the diagram.

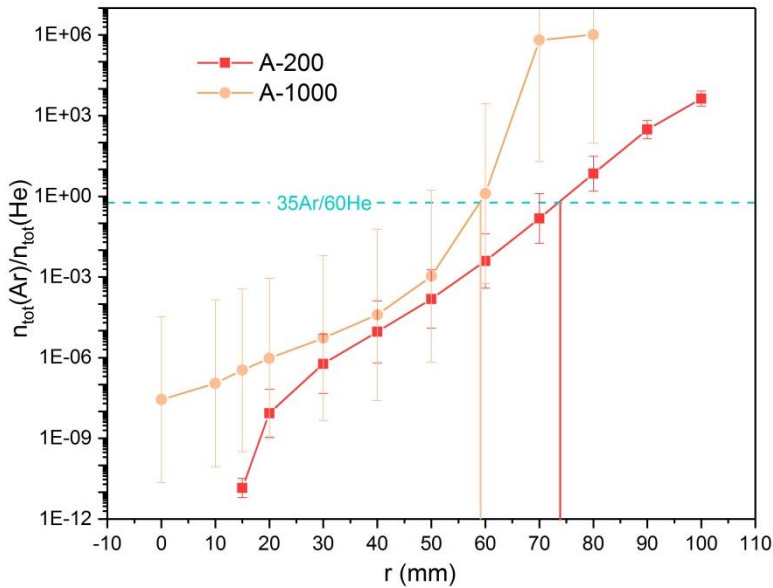


Fig. 4.9 Ratio of concentration between atomic Ar and atomic He under conditions A-200 (Ar/He jet, 200 Pa) and A-1000 (Ar/He jet, 1000 Pa)

Besides, as mentioned in section 4.1, in the center of plasma jet, Ar is mainly ionized so that $\varepsilon(r)$ of atomic Ar is low. However, the ionization of Ar is obviously not the only reason for the low $\varepsilon(r)$ of neutral Ar, as the demixing of Ar and He can be the other reason. The demixing of Ar and He in atmospheric-pressure free-burning arcs has been investigated by A. B. Murphy, who found that demixing almost always has a large influence on arc composition and He concentrates in the center of Ar-He arc [191]. In an Ar-He arc, the three categorical demixing processes (mole fraction (partial pressure gradient), frictional force, thermal diffusion) can contribute to the increase of the He mass fraction in the regions at higher temperatures. Under PS-PVD conditions, the plasma is very thin and therefore the influence of fractional forces caused by collisional

interactions might be small. However, in the center region of the plasma jet, Ar is ionized but He is not ionized due to its high ionization energy. This will cause a concentration gradient leading to an increase in the mass fraction of He in the high-temperature region. Besides, according to the $T_{exc}(r)$ of Ar (see Fig. 4.6a in section 4.2.1), a temperature gradient is present along the radial direction of plasma jet. Thus, the mole fraction gradients caused by ionization of Ar as well as by thermal diffusion could lead to an increase of un-ionized and light He in the center (high-temperature) region of the plasma jet.

4.4 Interaction of plasma and powder feedstock

4.4.1 Effect of powder loading

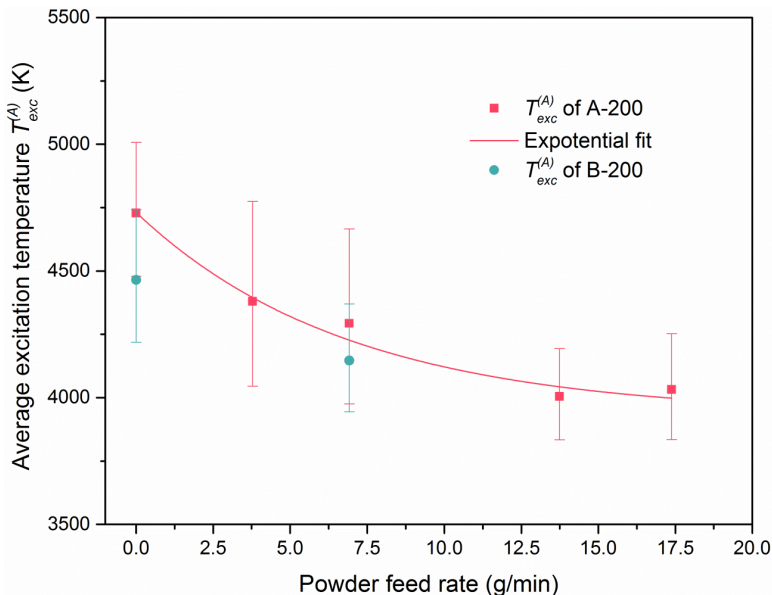


Fig. 4.10 Variation of average excitation temperatures $T_{exc}^{(A)}$ of Ar determined for different powder feeding rates under conditions A-200 (Ar/He jet, 200 Pa) and B-200 (Ar/He/H₂ jet, 200 Pa).

Although a more accurate excitation temperature can be obtained by introducing Abel inversion, the laborious data processing of Abel inversion complicates the application of OES. Hence, the measured integral $I(y)$ is more favored to estimate the average excitation temperature $T_{exc}^{(A)}$ of a plasma jet in engineering applications. In particular, with the injection of powder, the vapor species from evaporated feedstock powder has an influence on general plasma properties such as a cooling effect [192]. Therefore, with the injection of feedstock into the plasma, $T_{exc}^{(A)}$ of Ar at PFR were calculated based

on the measured $I(y=0 \text{ mm})$ by applying the Boltzmann plot method without Abel inversion. An alternative method proposed in ref. [193] to calculate axial plasma temperatures without Abel inversion was also employed. However, the results show that the axial temperature was approx. 100 K higher than the corresponding $T_{exc}^{(A)}$, but lower than the $T_{exc}(0)$ obtained by Abel inversion. The possible reason might be that the LTE is not satisfied. Thus, the uncorrected $T_{exc}^{(A)}$ were considered to be representative of an average jet temperature.

As shown in Fig. 4.10, under condition A-200, when the powder was introduced with a small rate of 3.8 g/min into the plasma jet, the powder loading effect was found as $T_{exc}^{(A)}$ reduced by 360 K. With increasing PFR, $T_{exc}^{(A)}$ decreases degressively and approaches 4000 K. In addition, $T_{exc}^{(A)}$ at a PFR of 13.7 g/min is more or less the same as that at a PFR of 16.4 g/min. This means the efficiency of energy transfer between plasma and powder is likely to reach its threshold at around PFR of 13.7 g/min. The same powder loading effect can be found under condition B-200 as well. In this case, only one PFR 6.9 g/min was tested, which led to about 320 K drop of $T_{exc}^{(A)}$. It was reported that two mechanisms are involved in the cooling effect of metal vapor in the plasma for a fixed input power. The first one is the increase of radiation powder losses leading directly to the cooling while the second one is related to the increase of the electrical conductivity which tends to enhance the conduction radius of the plasma due to the low ionization potential of the metal and then decrease the temperature in the hottest region [192]. But the importance of these effects depends on the current density and on the nature of the gas.

4.4.2 Vapor density estimated by spectroscopy

The reconstructed local emission intensities of $\varepsilon(r)$ after Abel inversion of the Zr I line (422.7 nm, relatively isolated and no significant self-absorption) at different PFR are given in Fig. 4.11. The overall emission intensity enhances as the PFR increases from 3.8 to 16.4 g/min. On one hand, one should note that $\varepsilon(r)$ is proportional to n_{tot} (density) and an exponential function of T_{exc} . On the other hand, as mentioned above, the injection of powder has a loading effect on T_{exc} in the plasma jet. Therefore, the increasing $\varepsilon(r)$ means that the density of vapor species in the plasma jet augments. However, it is noteworthy that $T_{exc}^{(A)}$ as well as the emission intensity profiles of the Zr I line at PFR of 13.7 and 16.4 g/min are nearly the same. In other words, the n_{tot} (density) of Zr in case of PFRs of 13.7 g/min and 16.4 g/min should be at the same order of

magnitude. This suggests a further increase of PFR above 13.7 g/min could not enhance the vapor density in the plasma jet.

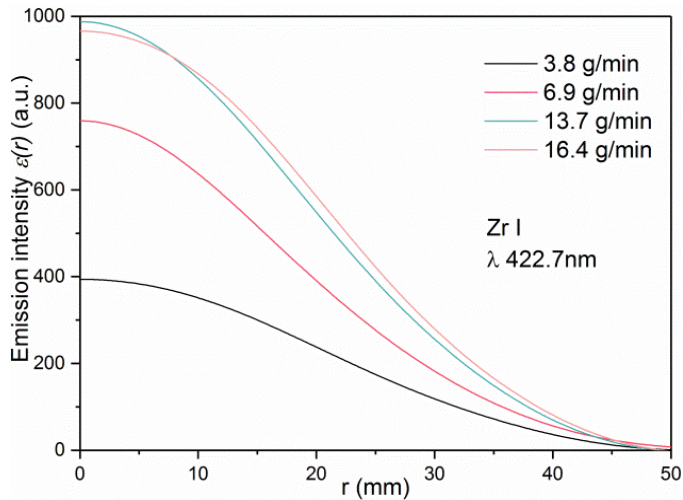


Fig. 4.11 The reconstructed $\varepsilon(r)$ profiles of Zr I (422.7 nm) at different PFRs under condition A-200 (Ar/He jet, 200 Pa)

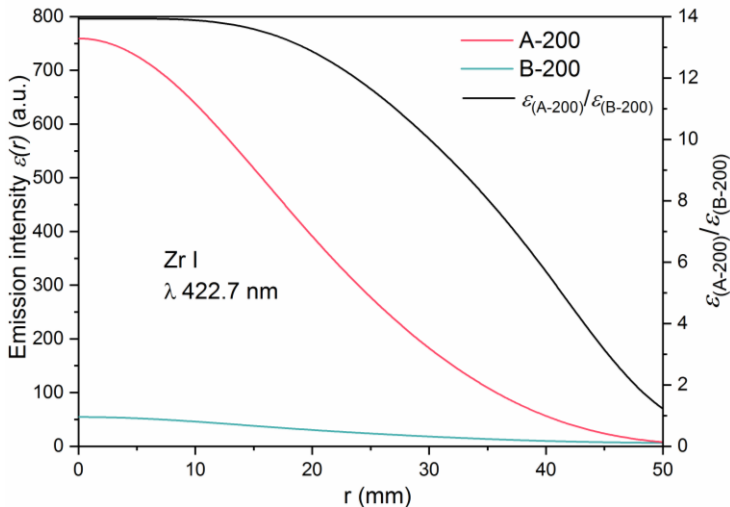


Fig. 4.12 The reconstructed $\varepsilon(r)$ profiles of the Zr I line (422.7 nm) under conditions A-200 (Ar/He jet, 200 Pa) and B-200 (Ar/He/H₂ jet, 200 Pa). The black curve is the $\varepsilon(r)$ ratio between these two conditions.

As mentioned in section 2.2.2 (Fig. 2.24), the addition of H₂ in the Ar/He plasma results in a lower deposition rate. The calculation of interaction between plasma and powder feedstock in the nozzle has implied that the Ar/He/H₂ parameter transferred less enthalpy to the particles [97], which might attenuate the evaporation rate and thus result

in lower vapor density. Due to lack of information about the emission lines of Zr I, it's not possible to quantify the vapor density in the plasma jet. Here, the emission intensities of the Zr I line for PFR of 6.9 g/min obtained under conditions A-200 and B-200 are shown in Fig. 4.12. The ratio of $\varepsilon_{(A-200)}/\varepsilon_{(B-200)}$ in the radius range is larger than 1 and up to 14. One can estimate that in the case of A-200 (Ar/He jet) the vapor density is likely higher and therefore the deposition rate increases.

4.5 Summary

In this chapter, the characteristics of Ar/He and Ar/He/H₂ plasma jet under PS-PVD conditions were investigated by OES. The main conclusions are as follows:

- Abel inversion was introduced to obtain the local distribution of emission intensity. Thus, it became possible to determine the development of the excitation temperatures calculated by the Boltzmann plot method along the radial direction of the plasma jet. From the center to the edge of the plasma jet, the local excitation temperature $T_{exc}(r)$ of Ar decreases gradually. He was found to deviate from LTE even where Ar is still in LTE, which leads to apparently higher excitation temperatures at the fringe of the plasma jet.
- A robust and simple method was proposed to estimate concentration profiles of atomic Ar/He in the plasma jet. In the central region, the ionization of Ar is one of the reasons for the very low ratio between atomic Ar and He $n_{tot}(Ar)/n_{tot}(He)$; other reasons could be demixing effects.
- The addition of H₂ into the plasma gas reduces the excitation temperature in the plasma jet but leading to a relatively high substrate temperature (approx. 50 K) due to the high thermal conductivity induced by the dissociation of H₂ in the temperature range of 2000 K to 3000 K.
- The injection of feedstock powder into the plasma jet results in a decrease of the jet temperature, however the overall average jet temperatures still remained above 4000 K. The energy transfer between plasma and feedstock can reach a threshold when increasing the PFR. Increase of PFR beyond 13.7 g/min was found probably not to improve the vapor density in the plasma jet.

Chapter 5 Deposition Mechanisms of Columnar Structured YSZ Coatings

In the PS-PVD process, the coatings can be deposited from a source of vapor phase similar to EB-PVD. But in contrast to EB-PVD, the interaction between plasma flow and vapor species makes the non-line of sight deposition possible to deposit coatings on shadowed parts of the substrate [8]. Besides, it was reported that different microstructures are obtained in the center and at the edge regions of the plasma jet at a short spray distance (300 mm) [148, 149], which suggests that the microstructures of PS-PVD coatings can be affected by the interaction between the plasma flow and the substrate surface.

The deposition rate of EB-PVD for TBCs is 4-10 $\mu\text{m}/\text{min}$ [38]. While in PS-PVD, a standard parameter to produce columnar structured TBCs is 14.5 $\mu\text{m}/\text{min}$ [4]. Without moving the plasma torch and the substrate, the deposition rate in PS-PVD can be 5-10 times higher than that in EB-PVD [93, 102]. To compare the microstructures of columnar structured TBCs produced by EB-PVD and PS-PVD, the former one consists of a relatively homogeneous columnar structure composed of compact single columns [65, 194] while the latter one shows tapered columns consisting of many fine needles with a high defect density and a high amount of internal porosity [6]. Additionally, EB-PVD coatings are commonly textured as summarized in Table 2.2. On the contrary, there are hardly reports about textures of PS-PVD coatings. Therefore, it is supposed that the deposition mechanisms in PS-PVD are not the same as in EB-PVD although both of them are deposited out of the vapor phase.

In this chapter, the deposition of columnar structured YSZ coatings is investigated according to the agglomeration of feedstock, the powder feeding rate (PFR), deposition rate, substrate temperature (T_s), vapor incidence angle (VIA) and flow condition. The microstructural and crystallographic characteristics of the coatings are investigated by means of SEM, XRD, and EBSD. In the end, the potential deposition mechanisms of columnar structured PS-PVD coatings are discussed. A concept of boundary-layer was introduced and the influence of the flow conditions in the boundary-layer and the possibility of cluster deposition are discussed.

5.1 The influence of feedstock powder

5.1.1 Powder feeding rate

In section 4.4.2, the vapor densities at different PFRs were estimated by OES with the reconstructed $\varepsilon(r)$ profiles of a Zr I line (see Fig. 4.12). To semi-quantify the relationship between vapor density in the plasma and the amount of vapor deposits in the coating, the four PFRs used in the OES measurements were taken into spraying tests with parameter A-1 (see Table 3.5). The sample holder was also made as a mask so that only the front side of the substrate was exposed to the plasma jet to collect deposits on the front side. The plasma torch and the substrate were stationary in the whole process. The diameter of substrate exposed to the plasma jet was about 26 mm. Then, the samples were weighted before and after spraying so that the coating weights could be calculated as listed in Table 5.1. The coating deposited with the lowest PFR (3.8 g/min) was taken as a reference to calculate the ratios of the integral area values (denoted as R_{CW}) deposited at different PFRs. The results are listed in Table 5.1.

Table 5.1 Summary of calculations

Test	A-5	B-10	C-20	D-30
Rotation speed of the powder hoppers (2x)	5%	10%	20%	30%
Powder feeding rate (g/min)	3.8	6.9	13.7	16.4
Coating weight (g)	0.2441	0.5229	0.9062	1.3025
R_{CW}	1	2.14	3.71	5.34
Integral area (a.u.)	4808.55	8975.18	11879.68	11837.15
R_{IA}	1	1.87	2.47	2.46

Furthermore, based on the emission profiles of the Zr I line (Fig. 4.12), the integral area values of emission for radius ($r = 13$ mm) are calculated by gadget integration in OriginPro 9, and an example is given in Fig. 5.1. Similar to the calculation of coating weight ratio, the integral area values and their ratios to the reference case are calculated and listed in Table 5.1 as well. Assuming the feedstock powder was completely evaporated at the PFR of 3.8 g/min and ignoring the possible effect of temperature, the ratios of the integral area values (denoted as R_{IA}) can be estimation for the vapor concentration ratios in the plasma jet. For a better comparison, the results are plotted in Fig. 5.2.

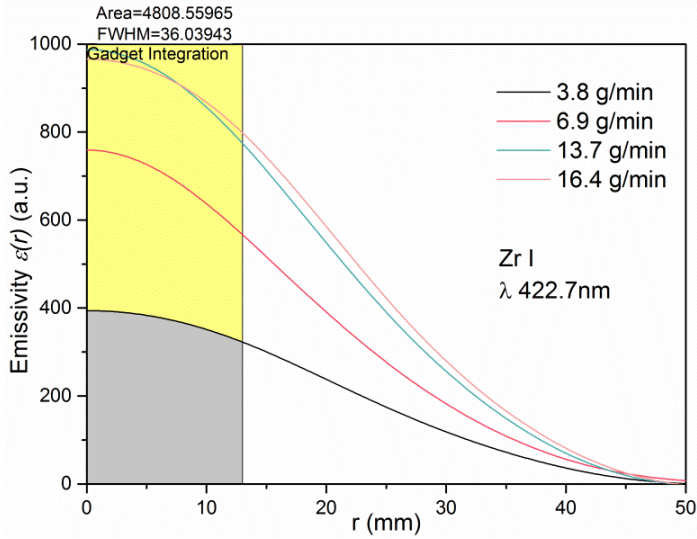


Fig. 5.1 Example of integration of $\varepsilon(r)$ along the radius at powder feeding rate of 3.8 g/min

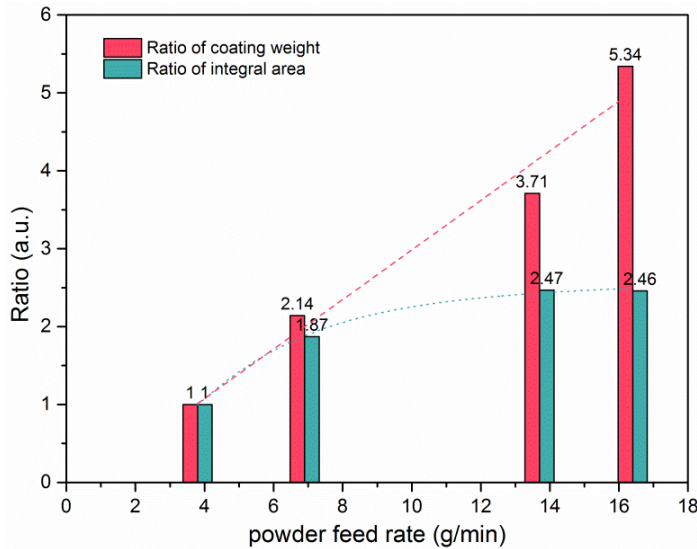


Fig. 5.2 Comparison of coating weight and integral area at different powder feeding rates; the dashed lines are only a guide for eyes.

With increasing PFRs, the R_{CW} increases rather linearly while the R_{IA} has a slow upward tendency. This can be interpreted as that the coatings are not only deposited by vapor phase, in particular, at high PFRs of 13.7 and 16.4 g/min. Fig. 5.3 shows the development of the coating thickness with the sample radius. It is obvious that the coatings have maximum thickness in the center of the sample. Besides, one can see that the thickness of coating D-30 (16.4 g/min) is higher than that of coating C-20

5.1 The influence of feedstock powder

(13.7 g/min). However, the R_{LA} of these two tests are almost the same. This means that at high PFR there must be a fraction of deposits not originating from vapor phase.

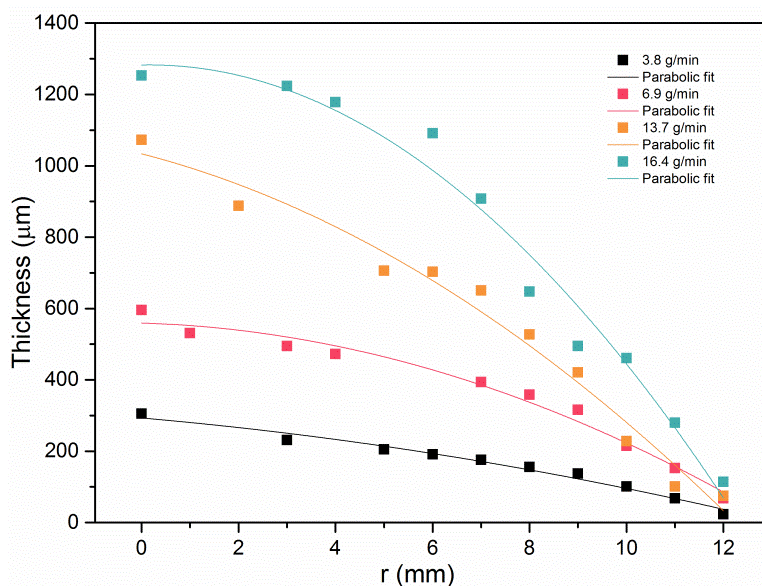


Fig. 5.3 Estimated coating thickness vs. sample radius for coatings deposited at different powder feeding rates

Fig. 5.4 shows the surface morphologies of coatings deposited at different PFRs. With the lowest PFR of 3.8 g/min, pyramidal shaped column tops composed of four-sided facets were developed (Fig. 5.4a). This pyramidal shaped column tops are similar to that in the EB-PVD coating as shown in Fig. 2.12a, in which the tip is along crystal orientation $c<001>$. But, the column tips in this coating do not grow along a same direction with respect to the substrate surface normal (this can be seen in the SEM images with low resolution shown in Fig. A2 in the appendix), thus the preferred orientation of this coating is not distinctive in the XRD pattern (Fig. 5.5). Besides, according to Rietveld analyses (summarized in Table 5.2), this coating shows mainly tetragonal phase, which indicates the powder feedstock was evaporated so that the deposition of vapor mixture of zirconia and yttria leads to partially stabilized tetragonal (t or t') phase. In addition, a small amount of ZrC formed caused due to the interaction between deposits and the graphite substrate [195]. As increasing the PFR to 6.9 g/min, the well-developed pyramidal top became less clear instead of smaller facets, which has been observed in previous work [96]. The main phase of this coating is tetragonal phase deposited from vapor phase; but it also contains a small amount of monoclinic (m) phase and the possible reason will be discussed later.

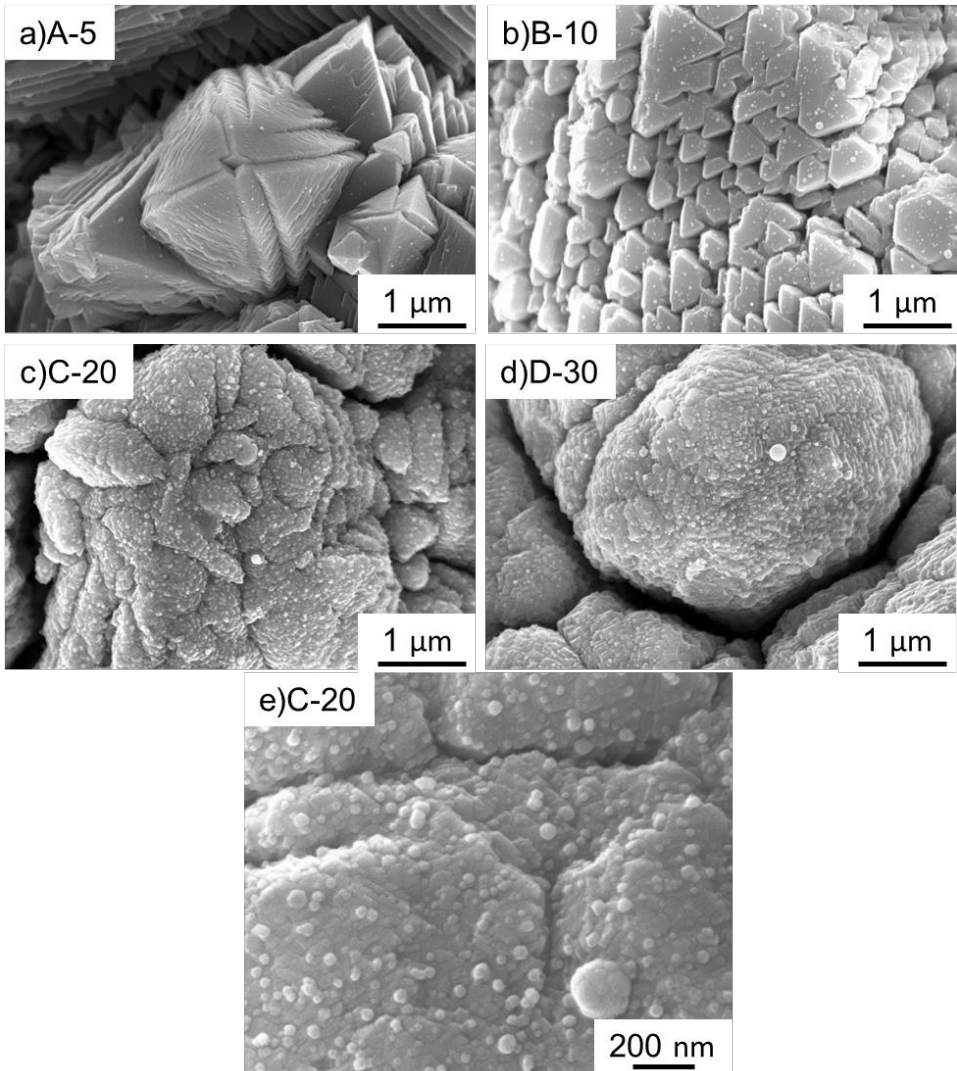


Fig. 5.4 SEM (SE) images of coating surfaces deposited at PFRs: a) 3.8 g/min, b) 6.9 g/min, c) 13.7 g/min and d) 16.4 g/min; and e) is the high magnification of image c

Further increasing the PFR to 13.7 g/min, the morphology of the column top (Fig. 5.4c) did not exhibit faceted structure anymore. In the meanwhile, the amount of monoclinic phase increased to approx. 40%, which is also observed in the coating deposited by 16.4 g/min. Considering that R_{CW} of these two coatings are much higher than their R_{LA} along with a large amount of m phase, one can deduce that there might be unevaporated feedstock particles incorporated in the coatings. Because the feedstock powder was an agglomeration of m zirconia and cubic (c) yttria (not pre-alloyed yttria stabilized zirconia), the m phase can originate from those unevaporated feedstock particles which

5.1 The influence of feedstock powder

were unstabilized and thus transformed to m phase on cooling. The high magnification SEM image of the coating (Fig. 5.4e) deposited at relatively high PFR shows their surfaces are composed by many nanoparticles in a size range of 20-60 nm being even smaller than the primary nanoparticles in the feedstock powder (Fig. 5.7b). Such nanoparticles could be formed by un-evaporated particles or solidification of nano-sized droplets. In addition, all of these coatings have no strong texture.

Table 5.2 Rietveld analyses of coatings deposited by different powder feeding rates

Powder feeding rate (g/min)	Lattice parameters of t phase		$c/a\sqrt{2}$	Mass fraction of m ZrO_2	Crystallite size (nm)		Mass fraction of Zr_3O	Texture
	a (Å)	c (Å)			t	m		
3.8	3.612(1)	5.172(3)	1.013	--	~144	--	--	textured
6.9	3.62(8)	5.18(2)	1.012	~10(2)%	~17	~12	--	textured
13.7	3.62(3)	5.20(7)	1.016	~40%	~7	~13	~15%	--
16.4	3.62(2)	5.18(5)	1.012	~37%	~7	~13	~12%	--

Furthermore, the peaks in the XRD patterns (Fig. 5.5) became broader with increasing PFR, which might be caused by the decreasing crystallite size or micro-strain in the crystal (indicated by peak shifts). According to Rietveld analysis, the estimation of crystallite size shows a declined tendency as increasing PFR, but the crystallite size analyses are limited due to the micro-strain in the coatings.

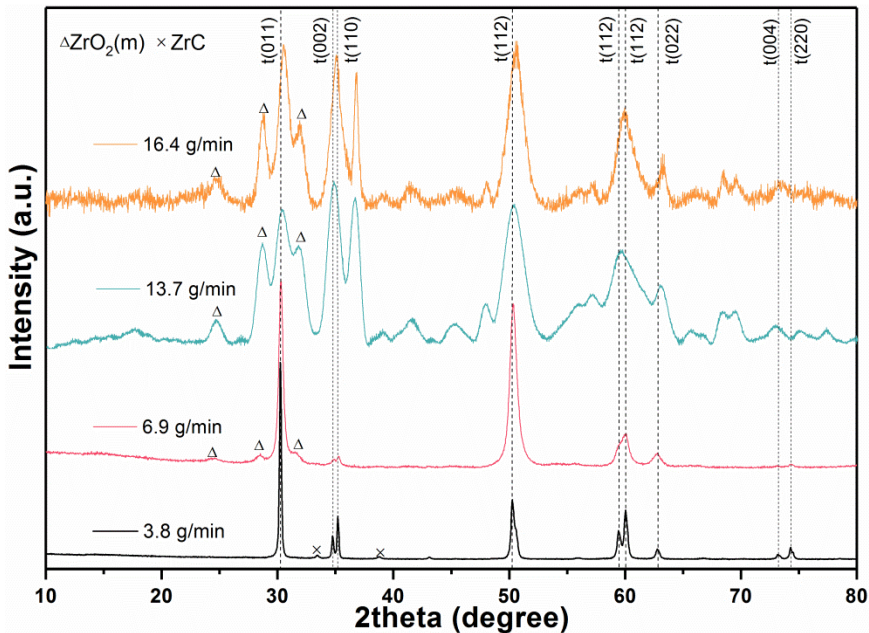


Fig. 5.5 XRD patterns of coatings deposited at different powder feeding rates

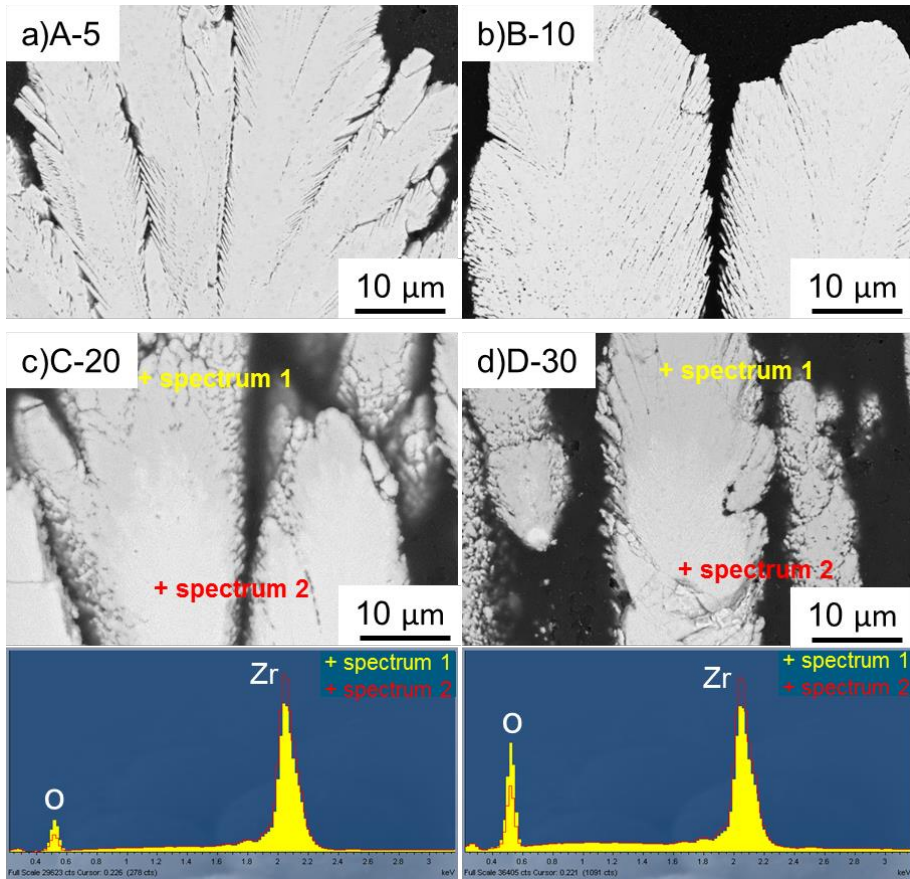


Fig. 5.6 SEM (BSE) images of cross-sections of coatings deposited at different powder feeding rates: a) 3.8 g/min, b) 6.9 g/min, c) 13.7 and d) 16.4 g/min and EDX comparison in coating C-20 and D-30

The feather-like needles (as observed in ref. [8, 96]) are clearly visible in the cross-sections of the coatings A-5 and B-10 deposited at lower PFRs. Such feather-like needles are like the feather arms in EB-PVD coatings as described in Fig. 2.9. This indicates that the deposition at low PFRs are mainly from vapor condensation. In contrast, the coatings deposited by higher PFRs (Fig. 5.6c and d) do not show such feather-like microstructures anymore, and the interior of the columns is denser. Besides, nano particles are obvious even in the cross-section. In comparison, the coatings deposited at higher PFR are not only built up by vapor phase but also by nano particles. It was found that the luminescence properties of the m phase zirconia are much more intensive at a specific wavelength than that of the partially stabilized tetragonal or the fully stabilized c phase [167]. However, the cathodoluminescence (CL) micrographs of these coatings do not show obvious luminescence, which means that the m phase as found in XRD cannot be detected with this method. The spatial resolution of CL is in

the range of 1 μm [167] but also dependent on the resolution of the SEM. One possible reason is that the grain size of the m phase is smaller than the resolution of the CL in the SEM, thus it is unlikely to be detected. A slight contrast was found in SEM images (BSE) of coatings C-20 and D-30 (Fig. 5.6), and EDX analyses indicate the contrast is due to different ratios of Zr and O. The O content in the surface area of the column is slightly higher than that in the inner area. Since this phase contrast is only found on the surface areas of the coatings, it might result from O in the chamber diffusing into the coatings after spraying.

5.1.2 Particle size and agglomeration

Initially, the tests were designed to spray in a very short time (about 2 s), swinging the plasma torch over the substrate only for one cycle. Since the fundamental purpose of this experiment was to study the deposition out of the vapor phase, the spraying at relatively low PFR 2x10% (≈ 6.9 g/min) and parameter A-2 as given in Table 3.5 were used to obtain higher ratio of vapor concentration as well as a considerable deposition rate (as indicated in section 5.1.1). In this case, the standard feedstock powder M6700 was used.

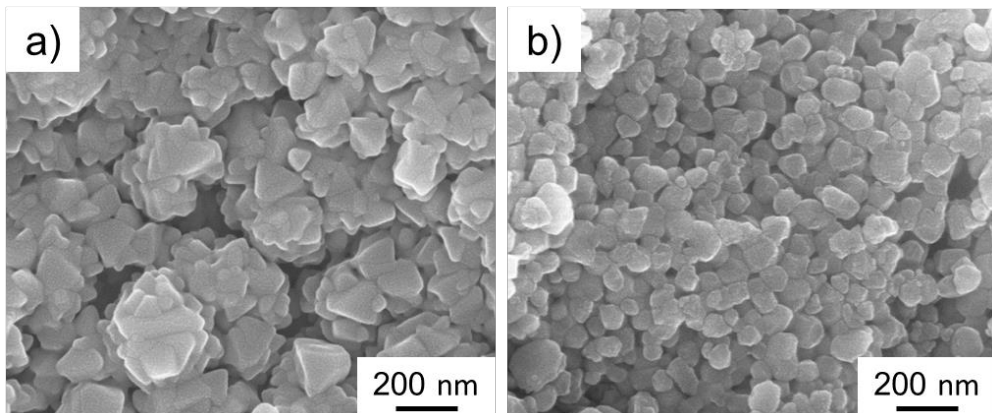


Fig. 5.7 SEM (SE) images of a) surface structures of deposits (magnification of Fig. 5.8d) and b) primary particles in the feedstock powder M6700

It was found that the main deposits were some small faceted crystal grains as shown in Fig. 5.7a. The well-regulated structures of these grains are quite different with the irregular primary particles in the feedstock (Fig. 5.7b) as well as the nano particles shown in Fig. 5.4e. It is suggested that such deposits are from vapor phase and the formation mechanism will be discussed in the following parts of this chapter.

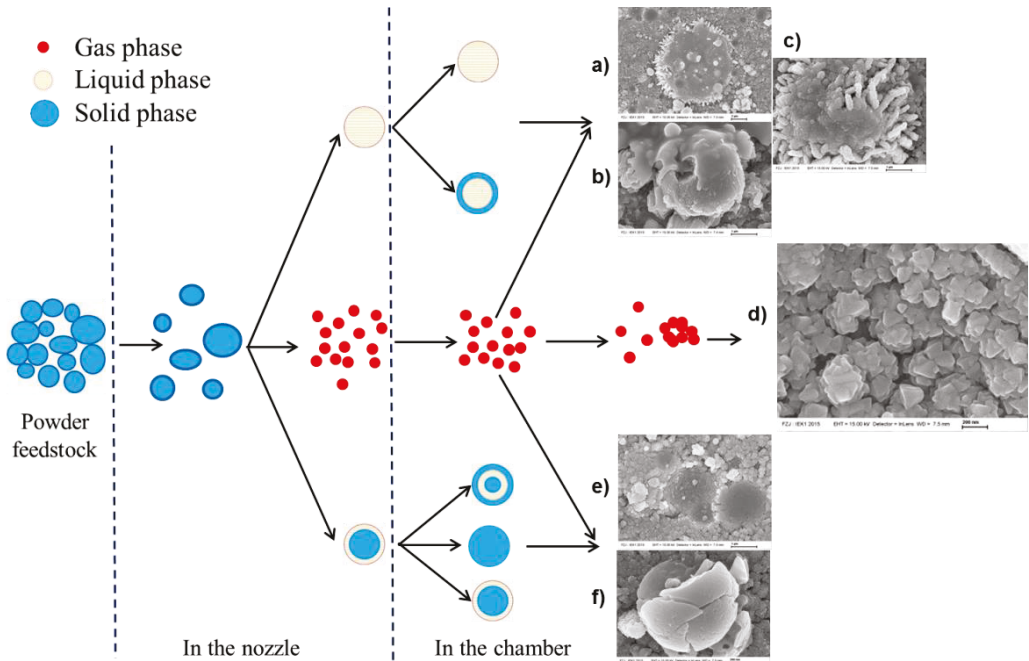


Fig. 5.8 Illustration of possible melting and evaporation of feedstock occurring in the nozzle and during flight in plasma jet and corresponding microstructures. SEM (SE) images a) to f) are the corresponding deposits and the magnifications are shown in Fig. A1 in the appendix.

Besides, some other microstructures were observed as shown in Fig. 5.8, such as micron-sized spherical particles (Fig. 5.8b and f), splats (Fig. 5.8a, b, and c) and concave pits (Fig. 5.8e). Magnifications of Fig. 5.8a-f are presented in Fig. A1 in the appendix. These microstructures illustrate that the major fraction of powder was evaporated but still a small fraction of powder is un-evaporated (probably melted or partially melted as schematically illustrated in Fig. 5.8). The possible reasons could be that the de-agglomeration of feedstock in the nozzle was not complete or the feedstock does not reach the core of the plasma. Hence, the energy transfer from plasma to feedstock particles is insufficient to evaporate them. The calculation in ref. [97] indicates that only particles size smaller than $1\ \mu\text{m}$ can be evaporated by the spraying parameters applied here. When these un-evaporated particles arrive on the substrate, splats and large particles, and concave pits caused by impingement will be incorporated in the deposits from vapor phase. Since the concentration of these deposits from un-evaporated particles accounts only for a very small proportion, their influence on vapor deposition is not considered in the following sections of this study.

As known from above, a small fraction of the feedstock M6700 was not evaporated. So it was tried to coat alternatively with TZ-5Y to further improve the evaporation rate. In

5.1 The influence of feedstock powder

contrast to M6700, TZ-5Y is not agglomerated by the organic binder. The raw TZ-5Y powder was verified to be non-feedable after feeding tests because it caused clogging in the feeding system. The reason was due to the weak agglomeration between the primary nano-particles. As indicated by the PSD of TZ-5Y given in Table 5.3, the micro-particle powder TZ-5Y might be destroyed forming submicro-particle and nano-particles during powder feeding since the d_{90} of TZ-5Y was reduced to 1 μm only after 3 min ultrasonic treatment.

Table 5.3 Particle size distributions of TZ-5Y after calcination in comparison with M6700

Name-sintering T (°C)	Ultrasonic 0min			Ultrasonic 3min		
	d_{10} (μm)	d_{50} (μm)	d_{90} (μm)	d_{10} (μm)	d_{50} (μm)	d_{90} (μm)
TZ-5Y	37.0	60.9	101.3	0.5	0.7	1.0
TZ-5Y-500	36.5	60.4	94.6	0.5	0.8	59.1
TZ-5Y-650	36.1	57.1	86.5	0.4	18.9	63.0
TZ-5Y-800	36.4	64.1	106.8	35.2	63.6	107.5
M6700	6.6	11.5	19.0	6.1	10.8	18.4

Hence, calcinations at different temperatures were carried out to enhance the agglomeration between the primary nano particles on one hand to improve the possibility of feeding powder TZ-5Y; on the other hand, the agglomeration should be not too strong to ensure fragmentation after injection into the nozzle. As the PSD listed in Table 5.3, calcination at 500 °C and 650 °C didn't really inhibit the production of nano particles but powder feeding tests were successful and no clogging occurred. However, a phenomenon which is described as spitting happened after 2 minutes spraying of TZ-5Y-500. This is assumed to result from the weak agglomeration of TZ-5Y-500 and thus intensive evaporation. Spitting refers to a phenomenon that molten or re-condensed powder adheres and accumulates on the inside wall of the injection nozzles causing deflection of the plasma jet and undesired deposits in coatings, therefore it leads to a decrease in the quality of coatings. In comparison with powder M6700, after 3 min ultrasonic treatment, the PSD of powder calcined at 800 °C (TZ-5Y-800) kept unchanged and thus was chosen to reduce the risk of spitting. For this powder, the parameter A-1 and a similar PFR ($2 \times 10\% \approx 7 \text{ g/min}$) were used to spray at distances of 400 and 1000 mm. Because of the high T_s , graphite was utilized as the substrate material.

Seen from the image in Fig. 5.9a, a coating was hardly formed on the substrate even after 5 minutes' spraying at 1000 mm. In the SEM image, the morphology of this

coating seems like fragments of powder particles, not column-like. The coating sprayed at 400 mm has covered the substrate completely due to the high substrate temperature and the morphology looks column-like. However, the tops of the columns are not faceted as found in the coating deposited with powder M6700 (Fig. 5.4b). No matter at which spray distance, plenty of splats and some fine particles (Fig. 5.9c) like sintered fragments of feedstock were found in the coatings instead of faceted grains as shown in Fig. 5.7a. This means that a large fraction of this powder was not evaporated.

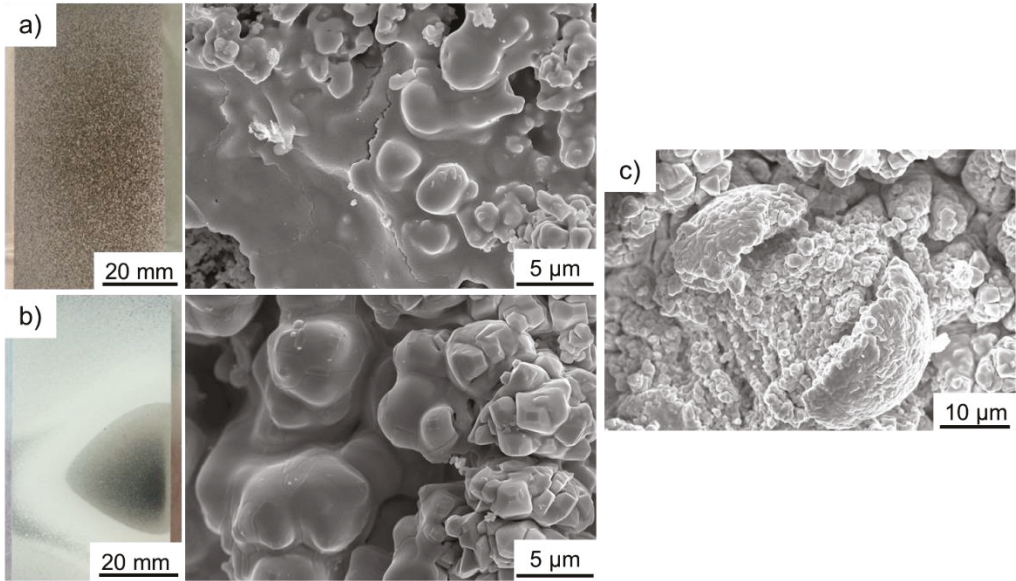


Fig. 5.9 Photos and corresponding SEM (SE) images of coating made of TZ-5Y-800 coated at spray distance: a) 1000 mm ($T_s \sim 1400$ °C); b) and c) 400 mm ($T_s > 1500$ °C)

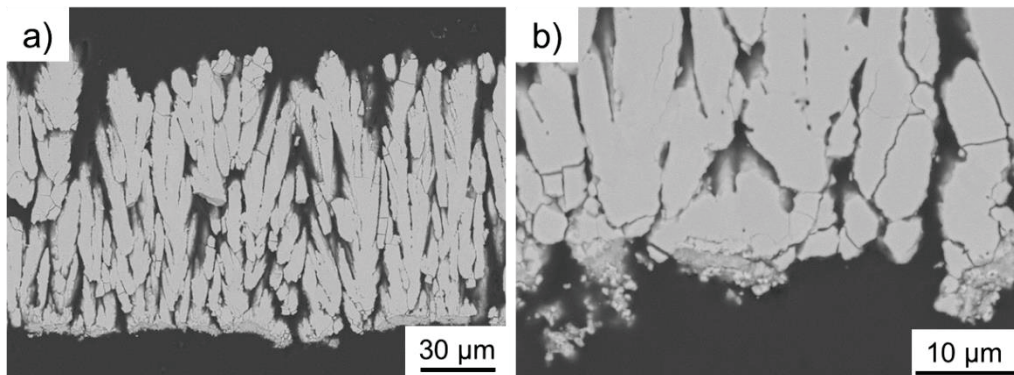


Fig. 5.10 Cross-sections (SEM (BSE) images) of coatings sprayed with TZ-5Y-800 at 400 mm

The cross-section (seen in Fig. 5.10a) of the coating sprayed at 400 mm shows columnar structure but the interior of the columns is dense rather than showing feathery-like needles or pores and cracks. This coating is likely formed at a higher melting degree compared with APS coating and at a lower evaporation rate compared with PS-PVD coating produced by powder M6700. Due to lack of interior fine structures (pores and needles as shown in Fig. 2.9 and Fig. 5.6a), this coating would have relatively high thermal conductivity which is undesired for TBCs. In conclusion, it is difficult to use TZ-5Y powder for deposition of desired columnar structured TBCs by PS-PVD and agglomeration by organic binder like M6700 is a much better way of powder preparation.

5.2 Deposition perpendicular to the axis of the plasma jet

In this section, the coating growth in the case of the axis of the plasma jet perpendicular to the substrate is investigated. Here, the average VIA is defined as 0° from the substrate normal. Under such condition, in a small region on the substrate surface, the plasma jet is stagnated or changed the direction of velocity and flows over the substrate similar to the plane stagnation-point flow [196]. On one hand, the prompt reduction of the plasma flow velocity could actually increase the pressure. On the other hand, the huge temperature difference between the hot plasma jet and the cool substrate is possible to cause undercooling of the vaporized feedstock. Both can lead to the formation of super-saturated vapor and thus promote nucleation and condensation of the vapor phase.

5.2.1 Coatings deposited at different spray distances without torch swing

The influence of spray distances along with substrate temperatures and vapor densities will be presented in this section. As discussed in section 5.1.1, a moderate PFR ($2 \times 10\% \approx 6.9$ g/min) was applied here to investigate vapor deposition in PS-PVD. The coatings were deposited on the designed substrate as shown in Fig. 3.6a with parameter A-1 given in Table 3.5. Other parameters are listed in Table 5.4 and the positions of substrates are shown in Fig. 5.11. Only in test A-1000, two thermocouples were inserted in the substrate to monitor the substrate temperatures at two different positions T_1 and T_2 as illustrated in Fig. 3.6a. In test B-700 and C-400, the substrate temperatures were monitored by a pyrometer. Because the substrate and the plasma torch were stationary, graphite was utilized as the substrate material to avoid overheating.

Table 5.4 Spraying parameters

Test	A-1000	B-700	C-400
Spray distance (mm)	1000	700	400
Spray duration (min)	5	3	2
Temperature (°C)	1350	1450	> 1500

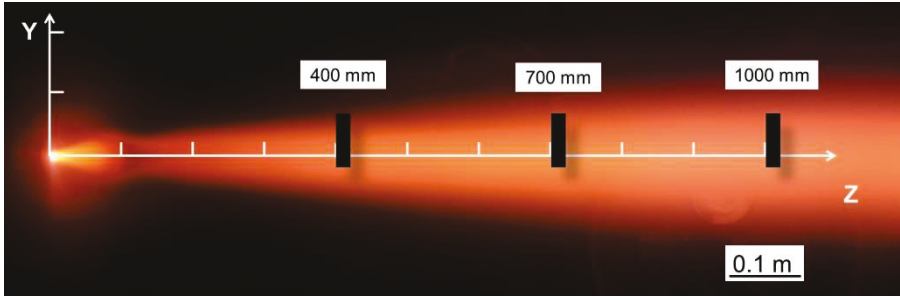


Fig. 5.11 Schematic illustration of substrate positions in the plasma jet (the lateral view)

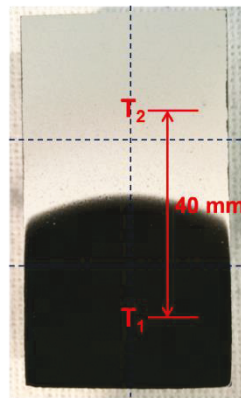


Fig. 5.12 Photograph of as-sprayed sample in test A-1000 (the front surface): T_1 and T_2 are the corresponding positions of the thermocouples. During coating process, the position T_1 was opposite to the Z axis of the plasma jet.

Fig. 5.12 shows the front surfaces of the as-sprayed coating in the test A-1000. It is visible that deposition of black YSZ takes place in the center area of the plasma jet. This phenomenon was also found in previous work [96], which is preliminarily determined as the reduction of ZrO_2 [197] although 4 slpm oxygen flow was led into the chamber during coating. But this black coating would be oxidized in service environment and no influence on coating properties was observed yet. The sample was cut into 6 pieces for localized investigations. Coatings deposited at positions T_1 and T_2 corresponding to the positions from the center of the plasma jet to the edge will be presented here and were referred to as coating 1000- T_1 and 1000- T_2 , respectively.

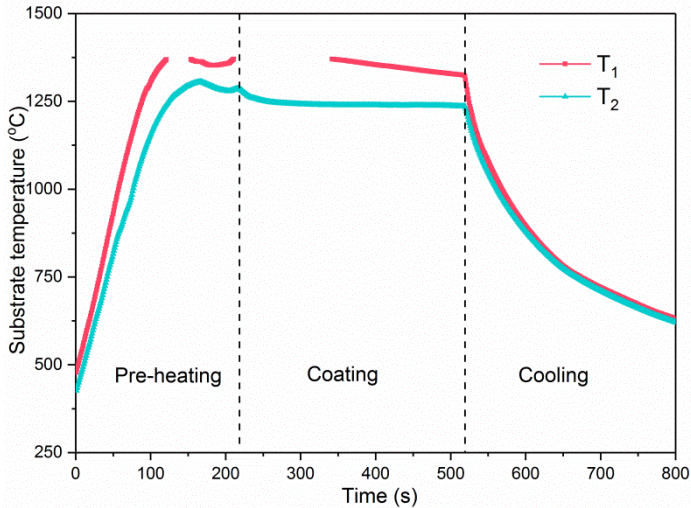


Fig. 5.13 Substrate temperatures measured by type-K thermocouples in test A-1000

The T_s measurement results are given in Fig. 5.13. The data loss of T_1 was caused by the high substrate temperature, which was beyond the measuring range (1370 °C) of type-K thermocouple. Before coating, the substrate was pre-heated by the plasma. During pre-heating, if only the heat transfer from plasma to the substrate is considered, $T_1 > T_2$ means that substrate temperature and plasma temperature in the center of plasma jet are higher than that at the edge, which is consistent with the calculated plasma temperatures in section 4.2.1. The temperature drop during preheating is caused by current adjustment. On coating onset, T_2 decreases slightly and then keeps constant. T_1 keeps reducing until the end of coating due to the formation of thick thermal barrier coating (It could also be due to degradation of the thermocouple). The result basically illustrates: T_1 (1324 °C =1597 K) is higher than T_2 (1235 °C =1508 K). The ratio between T_s and melting point of zirconia (T_m is 2715 °C =2988 K), T_s/T_m , is between 0.5~0.55.

- **Microstructures**

Columnar structured coatings were successfully deposited on the whole substrate. Fig. 5.14 shows the fracture surfaces of the coatings formed at spray distances of 400, 700, and 1000 mm. The coating 1000- T_1 (Fig. 5.14A1) was deposited in the center of the plasma jet, a typical column starts to grow up first along the normal direction of the substrate and then branches into many finer columns. At the edge of the plasma jet, the coating 1000- T_2 (Fig. 5.14A2) has a limited thickness and the columns show relatively uniform diameter.

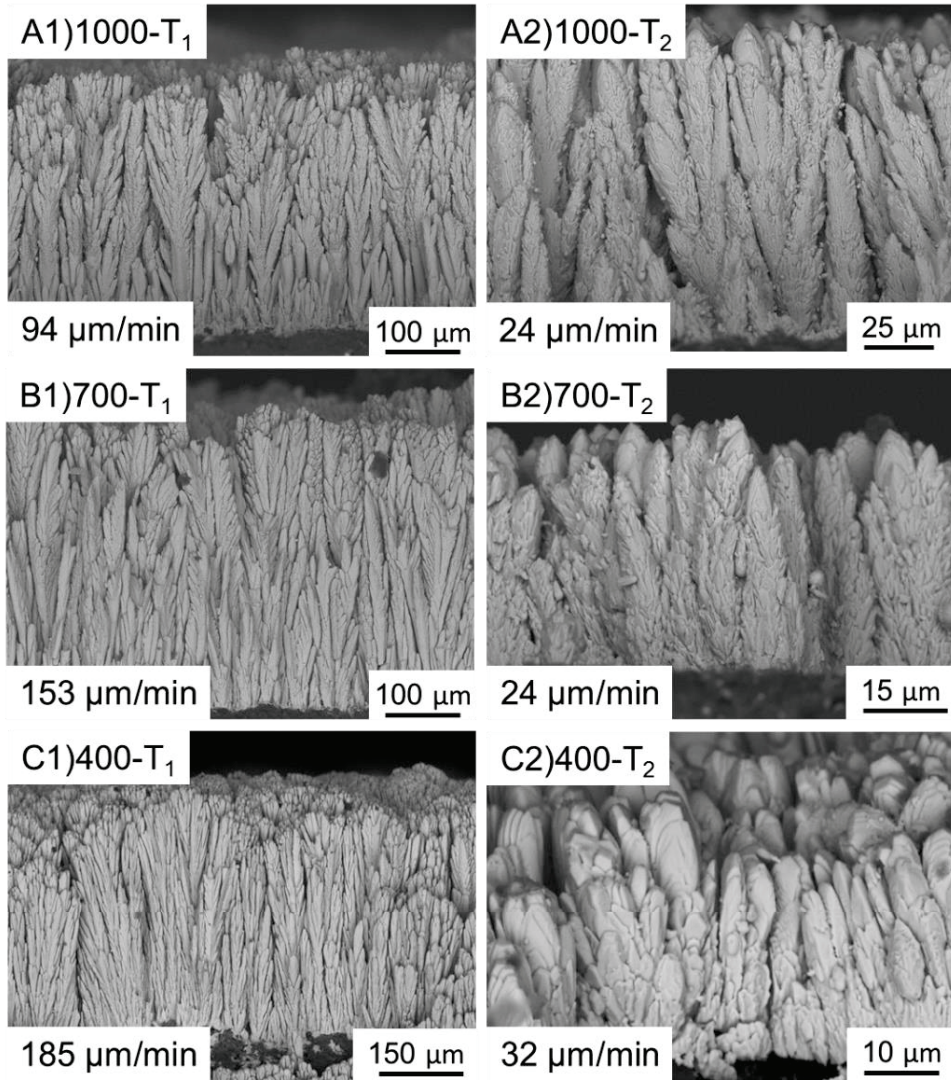


Fig. 5.14 SEM (BSE) images of fracture surfaces: A1), B1), C1) and A2), B2), C2) are corresponding to position T_1 and T_2 in test A-1000, test B-700, and test C-400, respectively.

The higher deposition rate in the center of the plasma jet demonstrates that the deposited species are concentrated around the axis of the plasma jet. This is more pronounced for the coatings deposited at shorter spray distances. In the test C-400, the substrate was very close to the torch, the deposition rate of coating 400- T_1 is about double of that of coating 1000- T_1 . At the edge of plasma jet, the deposition rates have little difference only. This illustrates the distribution of deposit species is divergent from the torch to downstream locations of the plasma jet.

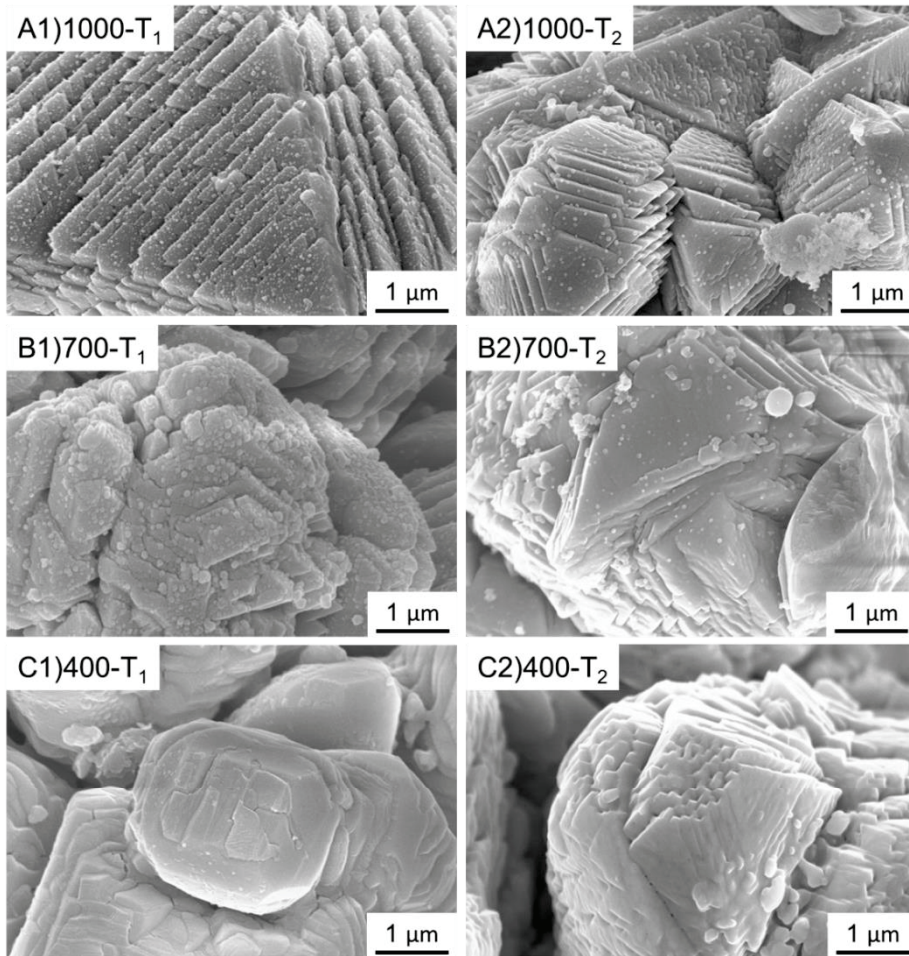


Fig. 5.15 SEM (SE) images of column tops: A1), B1), C1) and A2), B2), C2) are corresponding to position T₁ and T₂ in test A-1000, test B-700, and test C-400, respectively.

The SEM images in Fig. 5.15 give the top views of the coatings. It is obvious that the coatings sprayed at 1000 mm (Fig. 5.15A1 and A2) are faceted as observed in Fig. 5.4b. Such faceted structure can be found in coatings 700-T₂, 700-T₁, and 400-T₂ but the sharpness of facets decreases gradually. Moreover, a substantial amount of nanoparticles (even smaller than 20 nm) can be seen on the surfaces of the coatings deposited at 1000 and 700 mm. The coatings formed at 400 mm have relatively flat tops. The different microstructures of the coatings signify different crystal growth processes due to different spray distances followed by the variation of substrate temperatures and deposition rates (or the concentration of deposits). But it is also possible that the microstructures are affected by sintering effect due to high temperature.

- Crystallographic evaluations

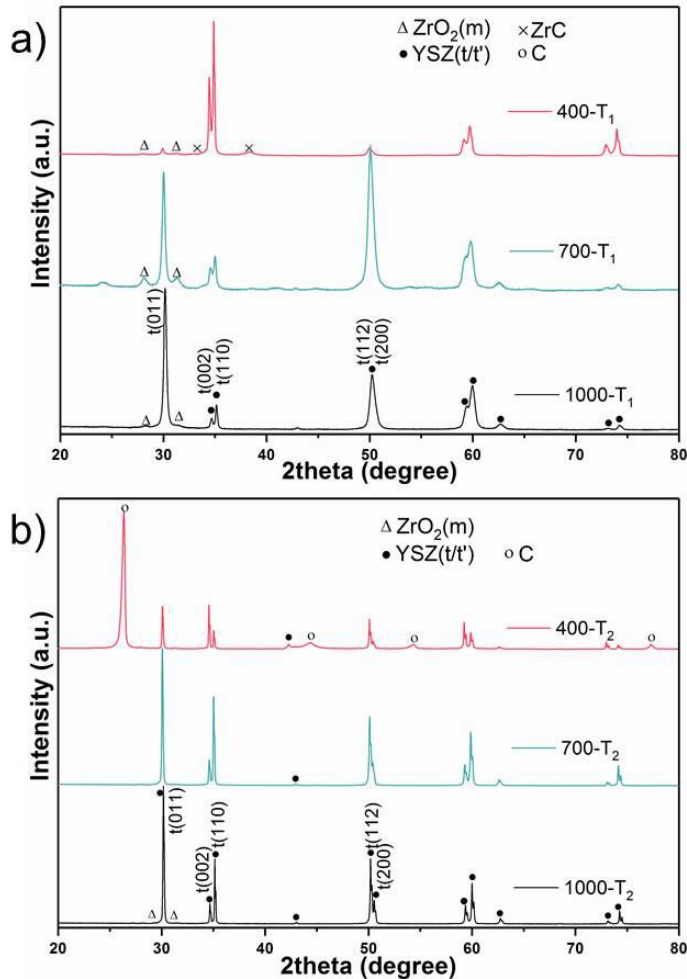


Fig. 5.16 XRD patterns of coatings: a) coatings deposited in the center; b) coatings deposited at 40 mm distant from the center

XRD was carried out to determine the phase compositions, crystal structures and preferred orientation of the coatings. The XRD patterns in Fig. 5.16 show that the main phase of all as-sprayed coatings is tetragonal YSZ, which gives evidence that major fraction of powder feedstock was evaporated so that the deposition of a vapor mixture of zirconia and yttria leads to a tetragonal phase. But a small amount of monoclinic phase also exists in the coating as discussed in section 5.1.1. Furthermore, in Fig. 2.21, the particle tracks in the nozzle illustrate that some particles do not reach the core of plasma and could still keep their particle sizes at the exit of the torch [102]. This kind of particles is difficult to be evaporated in the plasma jet, so they can directly solidify and incorporate in the coating. In addition, a small amount of ZrC formed in the coating

400-T₁ due to the extremely high temperature [195]. In coating 400-T₂, some peaks belonging to graphite are strong. This is caused by partial exfoliation of the coating, which makes the substrate material graphite to be detectable by XRD. Moreover, the yttria content in the tetragonal phase can be estimated according to equation (3.17), and the results are given in Table 5.5. The yttria content in the feedstock powder obtained from the chemical analysis is about 7 wt.% Y₂O₃ (= 7.6 YO_{1.5} mol%). As one can see from Table 5.5, the calculated yttria content in tetragonal phase of the as-sprayed coatings is less than 7 mol%YO_{1.5}, lower than the yttria content in the feedstock. Furthermore, preferred orientations of crystallographic planes (002) and (110) are indicated in some of these coatings by Rietveld analyses. But according to the XRD patterns (Fig. 5.16), only intensities of the peaks for planes (002) and (110) in coating 400-T₁ are stronger than that of plane (011).

Table 5.5 Rietveld analyses of the coatings

Coating	Lattice parameters		$c/a\sqrt{2}$ (±0.0005)	YO _{1.5} (mol%) (±0.3)	Mass fraction of m phase	Preferred orientations
	a (Å)	c (Å)				
1000-T ₁	3.612(1)	5.173(1)	1.013	6.13	~5%	--
1000-T ₂	3.609(1)	5.172(1)	1.013	5.72	~3%	(110)
700-T ₁	3.614(1)	5.174(1)	1.012	6.35	10%~20%	(112)
700-T ₂	3.610(1)	5.169(1)	1.012	6.27	<3%	(002) (110)
400-T ₁	3.613(1)	5.170(1)	1.012	6.67	~5%	(002) (110)
400-T ₂	3.609(1)	5.173(1)	1.014	5.60	~2%	(002) (110)
400-T _b	3.614(1)	5.165(1)	1.011	7.46	0	--

The coating 400-T_b will be presented later.

For polycrystalline materials, the relative prominence of the preferred orientation (hkl) with respect to the other observed reflections can be expressed in terms of unnormalized texture coefficient (TC) [198], as follows:

$$TC(hkl) = \frac{I(hkl)/I_0(hkl)}{\sum_N I(hkl)/I_0(hkl)} \quad (5.1)$$

wherein, $I_0(hkl)$ and $I(hkl)$ are the standard XRD intensity of the ZrO₂ powder and the measure XRD intensity, respectively, and N is the number of crystal planes. Here, eight major reflection planes were taken into consideration, thus powder-like reflections have $TC(hkl) = 0.125$. While samples ideally orientated along one direction would have $TC(hkl) = 1$. The considered crystal planes and calculated TCs were listed in Table A2 in the appendix.

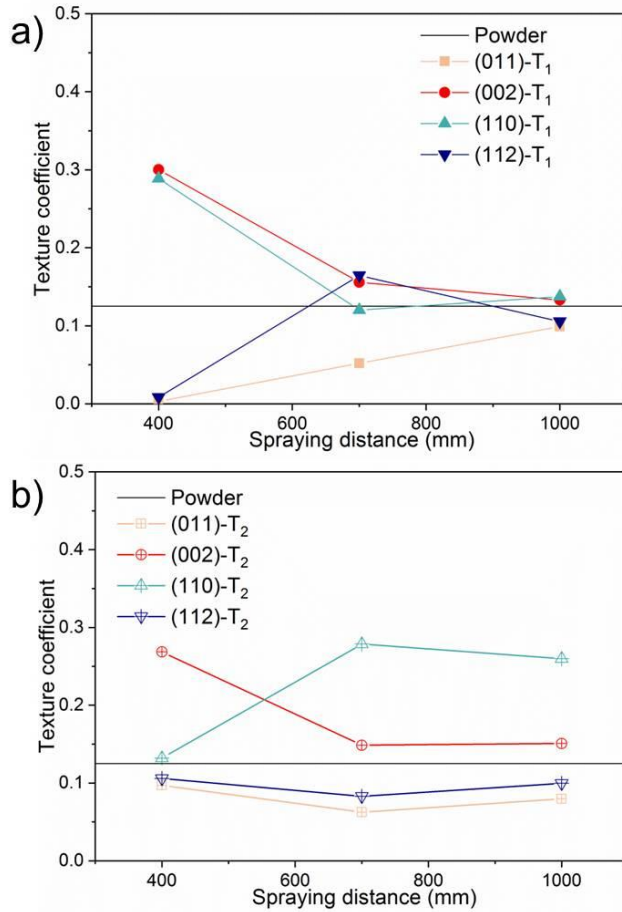


Fig. 5.17 Texture coefficients of coatings as a function of spray distances: a) coatings deposited in the center; b) coatings deposited at the edge of the plasma jet

The change of $TC(hkl)$ means that the preferred orientations change. In Fig. 5.17a, $TC(002)$ and $TC(110)$ have rather high values at a spray distance of 400 mm where the substrate temperature was the highest, which suggests that high T_s promote preferential growth. $TC(112)$ and $TC(002)$ show a slightly higher value at a spray distance of 700 mm compared with powder diffraction. Fig. 5.17b shows the TCs of coatings deposited at the edge of the plasma jet. Compared with the TCs in the center, the $TC(110)$ of coatings deposited at 1000 mm and 700 mm are higher than that of $TC(002)$, but they are inverse at 400 mm. As mentioned above, the deposition rate (concentration of deposits) at the edge is smaller than that in the center but comparable at different spray distances. This means that the crystal plane (002) can become preferred orientation when T_s is high and/or the deposition rate is low. Moreover, there is no obvious indication of preferred orientations in coating 1000-T₁, but preferred

orientation of $t(110)$ is found in coating 1000-T₂ even though the substrate temperature of coating 1000-T₁ was slightly higher than that of coating 1000-T₂. This means that a lower deposition rate favors orientated growth.

- **Crystal orientations and grain size distributions**

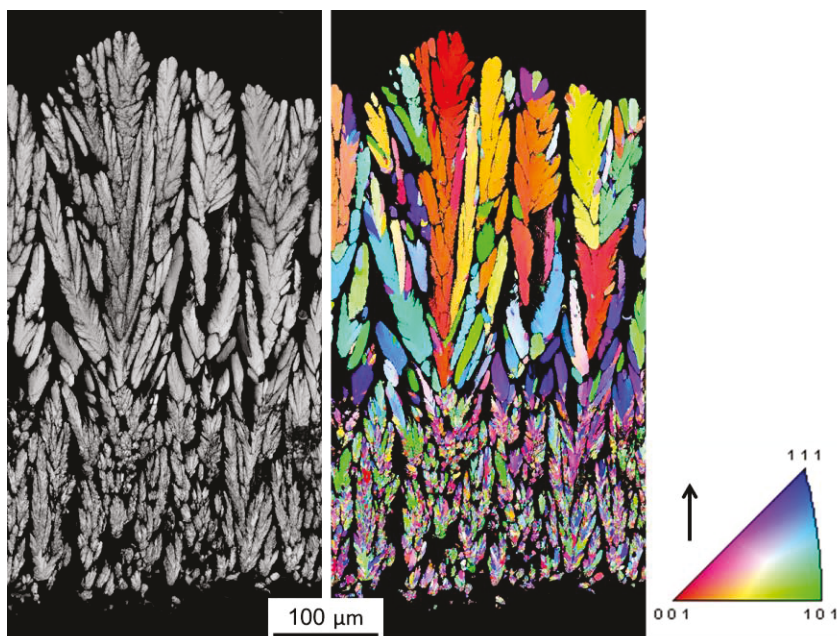


Fig. 5.18 EBSD image quality map (left) and orientation map (right) of the coating 1000-T₁

The EBSD measurements can provide efficient data of the crystallographic orientation of the grains, grain size distribution, and some other interesting information. Fig. 5.18 shows the image quality (IQ) map and the orientation map of the coating 1000-T₁. Due to the large thickness of this coating, a step size of 200 nm was used. The IQ map of this coating is good which means that good diffraction patterns were obtained with this measuring setting. Although the XRD analyses of coatings demonstrate the tetragonal lattice symmetry, the EBSD orientation determinations were indexed with reference file of cubic lattice symmetry, in which three different pole figures $\{001\}$, $\{011\}$, and $\{111\}$ were composed to observe the main crystalline directions. This phenomenon is sometimes termed as “the pseudo-symmetry problem.” That is, the patterns appear symmetric within the resolution of the imaging system, whereas the diffracting crystal is not truly symmetric [176]. Distinguishing the c -axis from a -axis on the Kikuchi pattern was difficult due to the near-unity of $c/\sqrt{2}a$ ratio [199]. In addition, the detected small amount of monoclinic phase in XRD could not be detected in EBSD phase

composition analysis. One reason could be that the monoclinic grains are in a nano-sized range smaller than the resolution of EBSD.

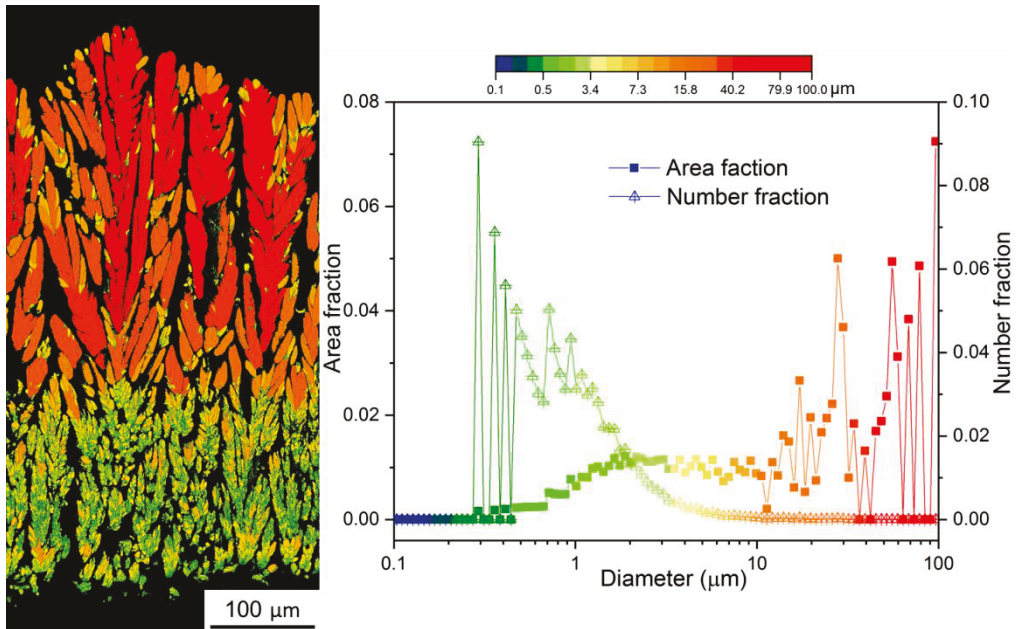


Fig. 5.19 Color-coded grain size map of the coating 1000-T₁ and diagrams of grain size distributions

According to the orientation map of the coating 1000-T₁, it is interesting to see that the coating growth starts from small and randomly orientated crystalline grains. With increasing coating thickness, the grains grow as large columns. A distinguishable column has uniform crystal orientation, but different columns have different orientations so that the whole coating appears as randomly orientated. The color-coded grain size map and the diagram (Fig. 5.19) illustrate that near the substrate the major grains are smaller than 1 μm coded with green color, along with some middle-sized columnar grains (approx. 3~10 μm) distributed among these small grains. The columnar grains in the upper part of the coating are in a large size range of 10~100 μm.

- **Non-line of sight deposition**

As mentioned previously, the interaction of particles and plasma gas makes non-line of sight deposition possible in PS-PVD. Fig. 5.20 gives the SEM image and XRD pattern of the coating (400-T_b) deposited on the back-side of the substrate in the test C-400 (see Table 5.4). Since only vapor phase can detour the substrate and reach the shadowed parts, this coating should be deposited from pure vapor. Coating 400-T_b composes of

many island-shaped deposits (see Fig. 5.20a). In every island, the crystals are pyramidal shape and made of very sharp faceted structure (see Fig. 5.20b). No nano particle was found on the surface. The average thickness is about 10 μm corresponding to a deposition rate of approx. 5 $\mu\text{m}/\text{min}$. XRD analysis of this thin coating testified that it is pure tetragonal phase; no monoclinic phase was detected. Comparing with the coatings deposited in the front side of the substrate, this non-line of sight coating (400-T_b) has the highest yttria content (7.46 YO_{1.5} (mol%) close to that in the powder feedstock), revealing a homogeneous deposition from pure vapor deposition. This result confirms that the pure vapor deposition forms only tetragonal phase as already suggested before. Also it further suggests that monoclinic phase in the coatings formed in front of substrate originates from the unevaporated powder particles. Besides, the estimated T_s on the back side for the coating 400-T_b was 1500 °C ($T_s/T_m > 0.59$). Normally, in this temperature range, surface diffusion is expected but the crystallographic structure of this thin coating is weakly textured showing no obvious preferred orientation even though the deposition rate is low. Moreover, one should note that the coating 400-T_b is too thin to be comparable to the coatings formed in front of the substrate. It can be regarded as the preliminary stage of coating growth just like the coating near to the substrate in the coating 1000-T₁, which also contains small and randomly orientated grains.

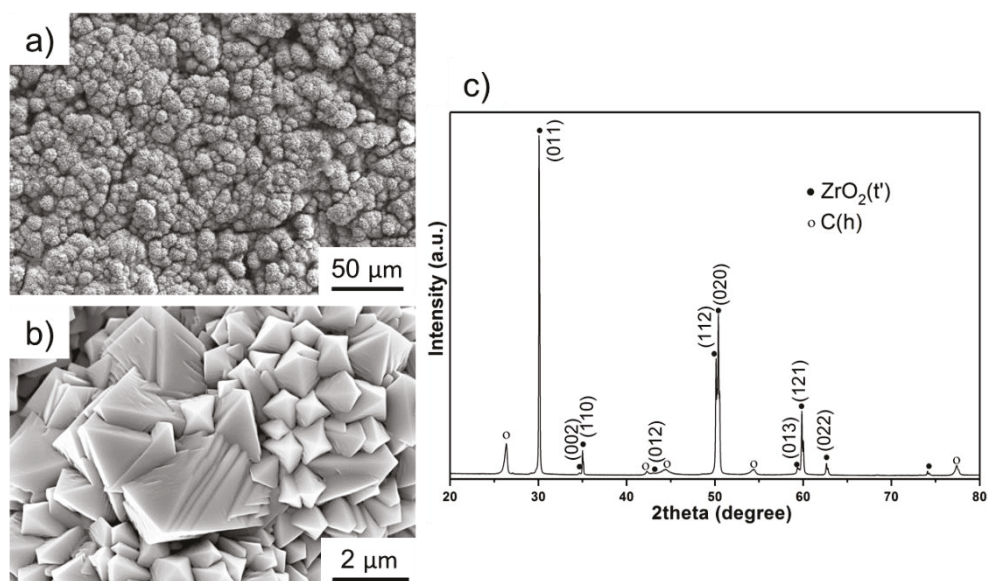


Fig. 5.20 a) and b) SEM (SE) images, and c) XRD pattern of the non-line of sight coating (400-T_b) formed at the backside of the substrate sprayed at 400 mm

5.2.2 Coatings deposited with torch swing

For the reason of investigation, the plasma torch and the substrate were stationary in the experiments described in section 5.2.1 and graphite was utilized as the substrate material in case of high T_s . However, in practical spraying, T_s has to be controlled by swinging the plasma torch with a certain velocity or by rotating the substrate to avoid overheating of the metallic substrate. In this section, the spraying parameter A-2 and parameter B in Table 3.5 were utilized for coating deposition on Inconel substrates at a spray distance of 1000 mm. So the preheating T_s is around 850~950 °C (measured by the pyrometer, it is about 1000 ~1100 °C if measured by a thermocouple).

- **Microstructures**

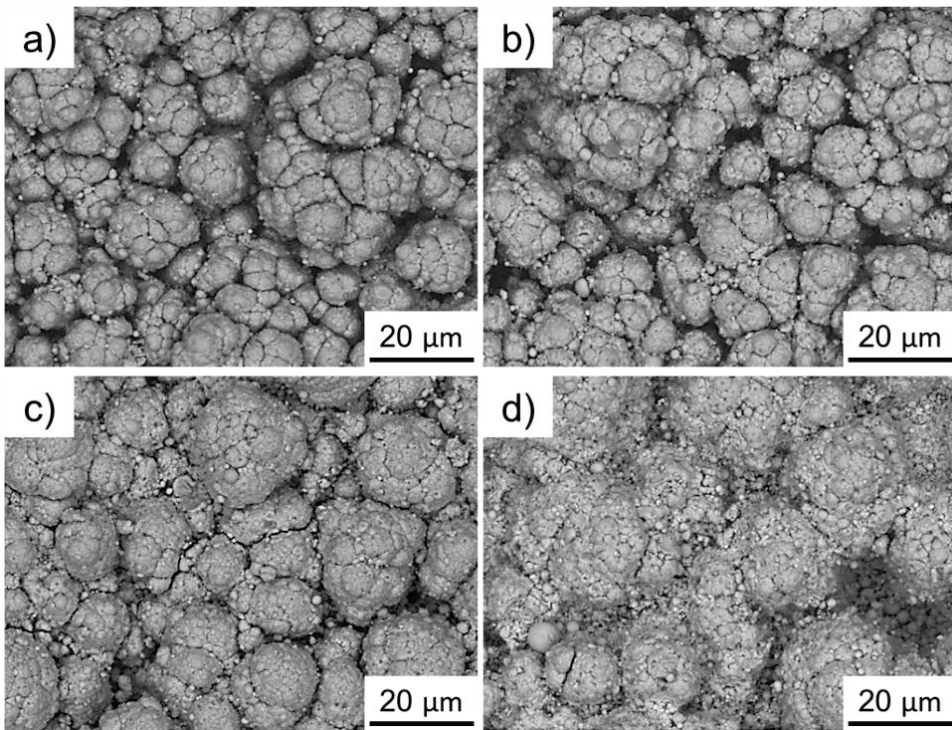


Fig. 5.21 SEM (BSE) images of surface morphologies for coatings deposited at different powder feeding rates with parameter A-2 (Ar/He jet): a) 6.9 g/min and b) 16.4 g/min; with parameter B (Ar/He/H₂ jet): c) 6.9 g/min and d) 16.4 g/min.

The surface morphologies of the coatings deposited with Ar/He jet (parameter A-2) are shown in Fig. 5.21a and b. The columns in the coatings have domed tops and some large round particles are incorporated in the gaps. Their surfaces look very similar although they are deposited at different PFRs. This is significantly different from the

coatings deposited without torch swing, in particular, the coating deposited at 6.9 g/min (see Fig. 5.4a and Fig. 5.15A1). To be stated again, the pronounced four-sided faceted structure was produced at a PFR of 6.9 g/min without torch swing. The differences caused by torch movement are the lower deposition rate, an interruption during coating growth, relatively low T_s and co-deposition of deposits from different regions of the plasma jet. However, as discussed before, a lower deposition rate is obviously not the reason for the absence of faceted structure. In addition, without torch swing, even the coatings deposited at the edge region of the plasma jet have also faceted structures (see Fig. 5.15A2). Therefore, the co-deposition of deposits from different regions of the plasma jet should not be a reason. So the possible influences of interruption and low T_s will be discussed in the following sections. Besides, the coating deposited with Ar/He/H₂ jet (parameter B) exhibit relatively narrow gaps and much more round particles in the column gaps, in particular, the coating shown in Fig. 5.21d deposited at high PFR. This could be caused by the lower heating condition of parameter B (H₂ as additional plasma gas) as discussed in chapter 4.

- **Crystallographic evaluations**

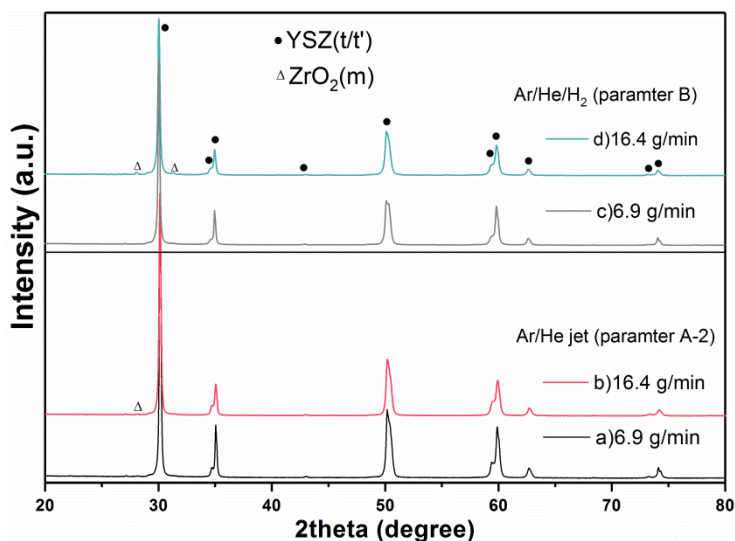


Fig. 5.22 XRD patterns of the coatings shown in Fig. 5.21

The XRD analyses reveal that the main phase of these coatings is the tetragonal phase without preferred orientation. This phase compositions of these coatings are also different with the coatings deposited without torch swing as approx. 40% mass fraction of m phase (see Table 5.2) was found in the coating deposited at PFR of 16.4 g/min. However, with torch swing, the XRD of this coating only shows less than 1% of m

phase. In general, a certain amount of yttria doping can stabilize tetragonal phase at room temperature. However, it is worth to note that tetragonal phase can be also stabilized even in pure zirconia if the crystallite size is in a nano scale. In the case of pure zirconia powder, crystallites below 10-18 nm tend to be tetragonal at room temperature [200]. In case of a low content of yttria, this critical crystallite size at room temperature can raise to 155 nm for 1.5 mol% YSZ. Therefore, nanocrystalline grains could also lead to tetragonal phase in the coatings. Even the coating deposited by parameter B at a PFR of 16.4 g/min shows only approx. 3% m phase.

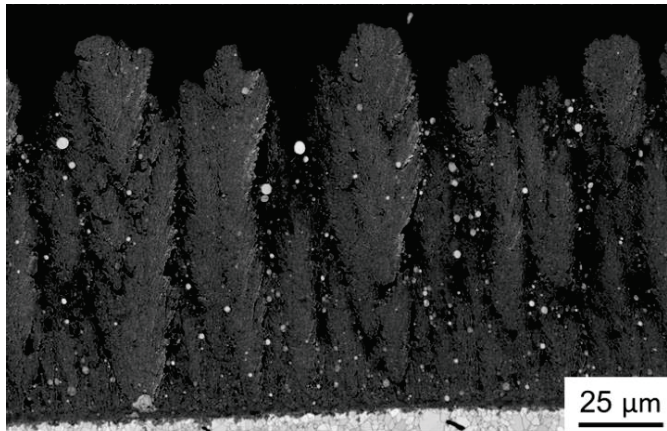


Fig. 5.23 EBSD image quality map of the cross-section for the coating shown in Fig. 5.21b

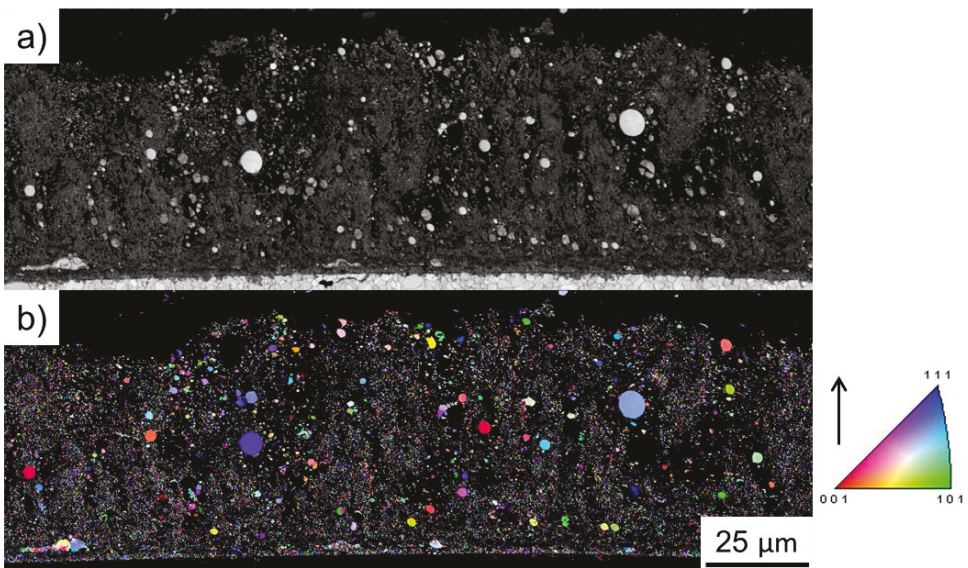


Fig. 5.24 a) EBSD image quality map and b) orientation map of the cross-section for coating shown in Fig. 5.21d

5.2 Deposition perpendicular to the axis of the plasma jet

A trial for EBSD investigation with a step size of 100 nm verified that the IQ (shown in Fig. 5.23) of the coating deposited by parameter A-2 at PFR of 16.4 g/min is very poor except for some spherical particles. The poor IQ is mainly caused by overlapping of Kikuchi patterns, meaning that the grain sizes are smaller than the excitation volume of the electron beam. In EBSD measurement, the excitation volume in the coating is roughly estimated around 50-100 nm along the tilt axis. Therefore, the grain size in this coating could be smaller than 100 nm, and thus it is meaningless to do any other EBSD analyses. Besides, those large spherical particles have relatively good image quality and the size of them is between 1 to 3.5 μm .

Fig. 5.24a gives the IQ map of the coating deposited with parameter B showing the same problem of a poor diffraction quality. A preliminary orientation map of this coating (Fig. 5.24b) indicates grains distributed randomly in the coating. There are quite a lot of "1-pixel-grains" in the orientation map, so the grain size would be determined by the thresholds setting for the grain size determination like min. number of pixels for a grain rather than an actual grain size. By image analysis, it is obtained that a lot of fine grains are in an approximate size range of 100~200 nm. Beyond this, some large spherical particles are in a size range of 1~6 μm . It is interesting to see that these large spherical particles can be indexed by cubic phase and are single crystal-like. This indicates that monoclinic phase in the coating is in fact not from these large particles. They might have been not evaporated by the plasma, but at least they were well heat-treated (melted or partially melted) so that they are not in the original m phase.

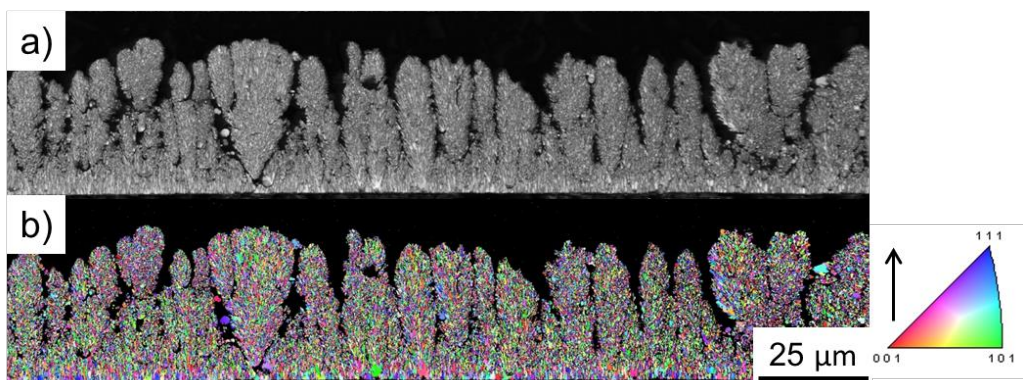


Fig. 5.25 a) EBSD image quality map and b) orientation map of the coating deposited with parameter A-1, but along with a powder feeding rate of 2.5 g/min (2x5%) and a lower torch swing speed of 10 mm/s.

The deposition rate of approx. $11 \mu\text{m}/\text{min}$ for parameter B is lower than that of $21 \mu\text{m}/\text{min}$ in parameter A-2. As discussed in section 4.4.2, the vapor density is likely low and this should be one of the reasons for this low deposition rate. In order to know the effect of lower deposition rate, a coating was produced with parameter A-2 (Table 3.5) in 10 min, but along with a lower torch swing speed of $10 \text{ mm}/\text{s}$ and a very low PFR of approx. $2.5 \text{ g}/\text{min}$ ($2 \times 5\%$). This leads to a very low deposition rate of approx. $3.3 \mu\text{m}/\text{min}$. XRD analyses determined a pure tetragonal phase of this coating (Fig. A3 in the appendix). The IQ map (Fig. 5.25) shows good diffraction quality and the orientation map reveals that this coating is randomly orientated. Besides, large spherical particles are rarely observed.

The grain size map (Fig. 5.26) shows that this coating has a rather homogeneous grain size distribution in a range of 150 nm to $2.5 \mu\text{m}$ and 90% of them smaller than 600 nm . Given the above, with torch swing, the coatings shown in Fig. 5.23, Fig. 5.24 and Fig. 5.25 have similar T_s of $\sim 1050 \text{ }^\circ\text{C}$, and a low PFR enables growth of large grains and vice versa. This is different from the coatings deposited without torch swing. In case of without torch swing, the deposition rates are rather high; however, the grains can grow to very large size. Therefore, either low T_s or interruption of torch swing can attribute to the small grain sizes in these coatings.

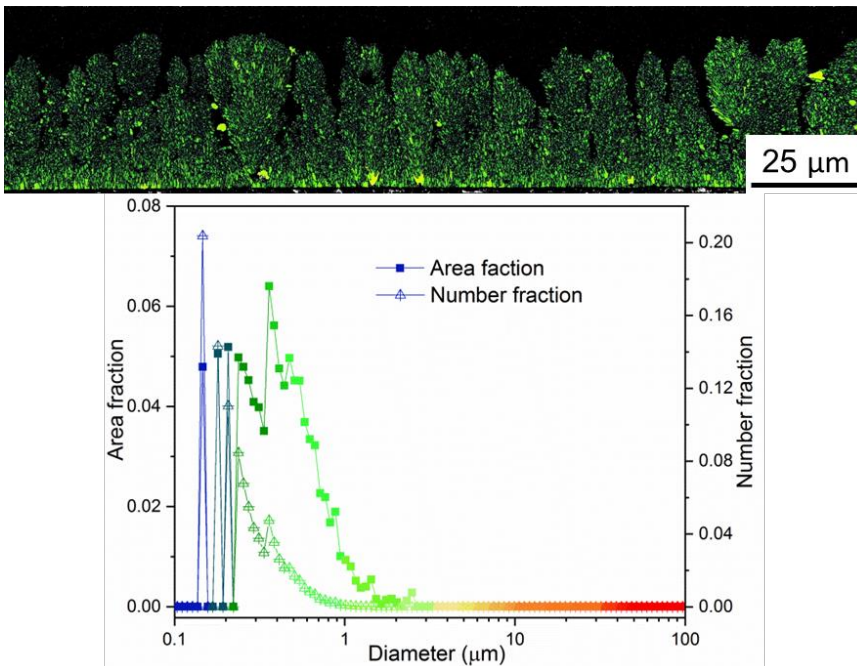


Fig. 5.26 Color-coded grain size map of the coating shown in Fig. 5.25 and diagrams of grain size distributions

5.3 Deposition parallel to the axis of the plasma jet

In general, the target surface of the substrate in thermal spraying is directly facing the plasma jet as described in section 5.2. The substrate would need rotation to obtain a homogeneous coating on different sides of the substrate. The non-line of sight characteristic of PS-PVD enables coating deposited not only on the front side but also on the shadowed parts without rotating the substrate. As presented in the previous section, the coating (400-T_b) was found on the backside of the substrate. In this section, it is to investigate the coating growth in the case that the axis of the plasma jet is parallel to the substrate as shown in Fig. 3.6b. The average VIA is defined as 90° from the substrate normal. The coating was deposited with parameter A-1 given in Table 3.5, and other parameters are listed in Table 5.6. Two similar spraying tests I and II were carried out at a low and a high PFR, respectively. The test R-I is a repeated test of the test I, the only difference from test I was a long preheating applied.

Table 5.6 Spraying parameters

Test	I	II	R-I
Spray distance (mm)	1000	1000	1000
Spray duration (min)	5	5	5
Powder feeding rate (g/min)	6.9	13.7	6.9
Preheating T_s (°C)	1050	1300	1300

5.3.1 Coatings deposited on different substrate locations

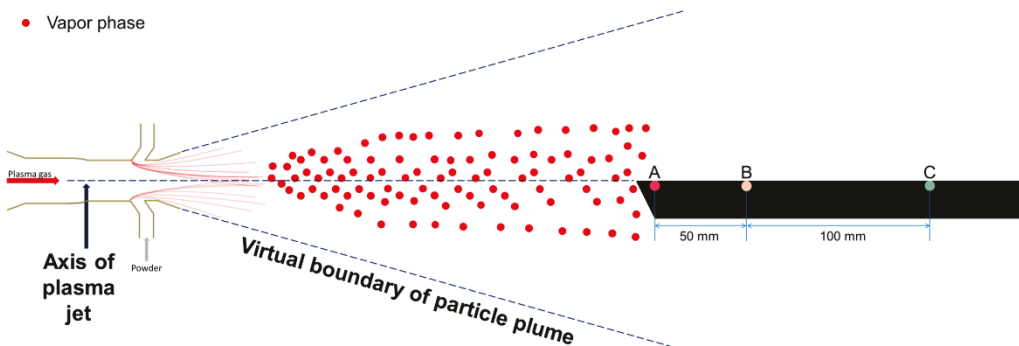


Fig. 5.27 Schematic drawing of the substrate position and the thermocouples (A, B and C)

As shown in Fig. 5.27, the substrate was placed in the center of plasma jet parallel to the axis of the plasma jet. In this section, results from the test I in Table 5.6 will be described. The substrate temperatures were monitored by type-K thermocouples at

three positions A, B and C, at which spray distances of 1010 mm, 1060 mm, and 1160 mm, respectively. Fig. 5.28 is the photograph of the as-sprayed sample. The black coating at the forefront of the sample has been demonstrated to be caused by the reduction of ZrO_2 . The sample was cut into 8 parts. Coatings deposited at positions A, B, and C were termed coating A, coating B, and coating C, and were investigated in depth.

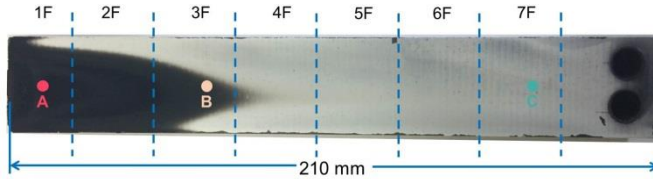


Fig. 5.28 Photo of the as-sprayed sample (top view); the dashed lines are the cutting positions for sample preparation.

- **Substrate temperatures**

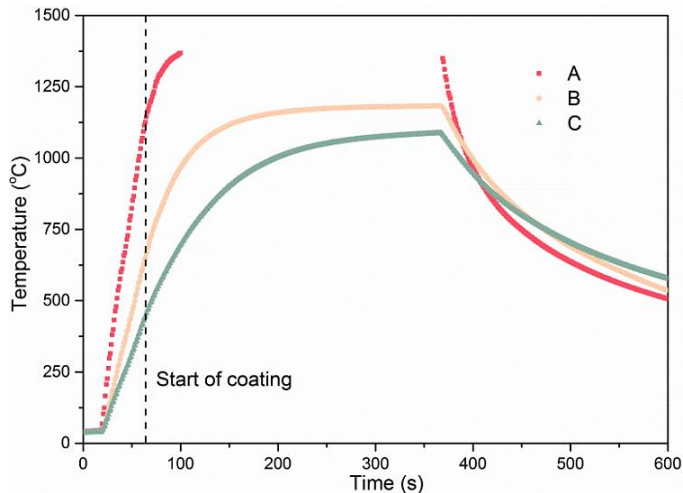


Fig. 5.29 Temperature developments during spraying process at positions A, B and C measured by thermocouples; the data loss of curve A is due to the limited measurement range of the type-K thermocouple.

The T_s profiles recorded at positions A, B and C are shown in Fig. 5.29. Along the spraying direction, T_s reduced. At position A, some data exceeding $1370\text{ }^\circ\text{C}$ was lost due to the limited measurement range of the type-K thermocouple, but the temperature estimated by a pyrometer shows that the temperature during coating was higher than $1500\text{ }^\circ\text{C}$ (1773 K). The preheating T_s at position A was about $1160\text{ }^\circ\text{C}$ ($T_s/T_m \geq 0.48$). It was considerably lower, $680\text{ }^\circ\text{C}$ ($T_s/T_m \geq 0.32$) at position B, and $470\text{ }^\circ\text{C}$ ($T_s/T_m \geq 0.25$) at position C, respectively. At the end of the coating process, T_s at position B and C became stable at $1183\text{ }^\circ\text{C}$ ($T_s/T_m \geq 0.48$) and $1087\text{ }^\circ\text{C}$ ($T_s/T_m \geq 0.45$), respectively.

- **Microstructures**

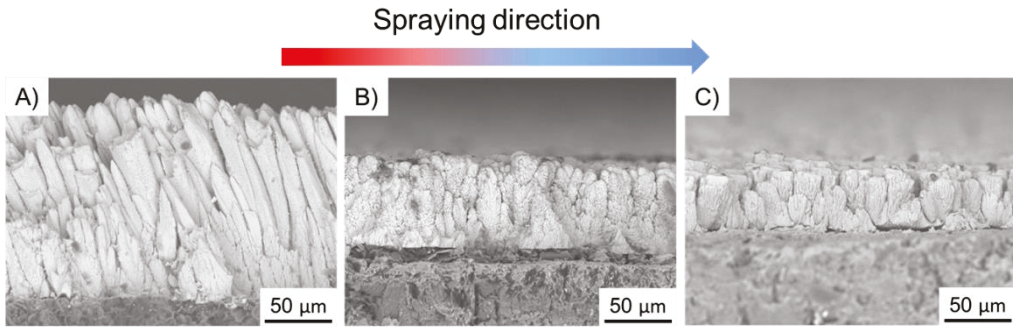


Fig. 5.30 Fracture morphologies (SEM (BSE) images) of coatings deposited at positions A, B and C

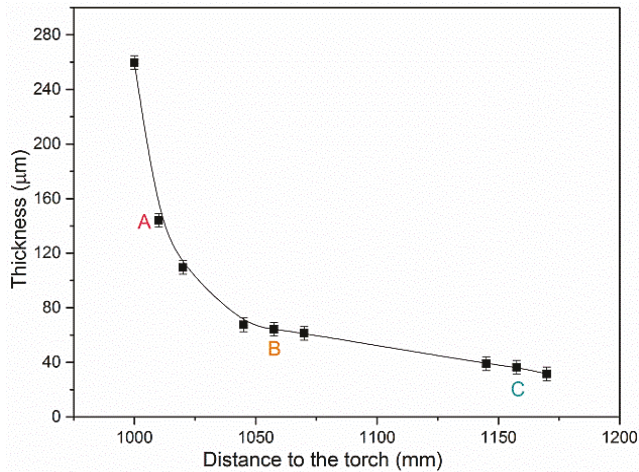


Fig. 5.31 Reducing coating thickness from the leading edge to the end of the substrate (the measured data points are connected with B-Splines as a guide for eyes)

Fig. 5.30 shows the fracture morphologies of the coatings A, B and C. The columns in the coating A are inclined to the direction of the plasma jet, but in the coating B and C, they are almost vertical to the substrate surface. The thickness of the coatings decreases from $\sim 143 \mu\text{m}$ at location A to $\sim 65 \mu\text{m}$ at location B and $\sim 37 \mu\text{m}$ at location C as illustrated in Fig. 5.31, corresponding to the deposition rates of $29 \mu\text{m}/\text{min}$, $13 \mu\text{m}/\text{min}$, and $7 \mu\text{m}/\text{min}$, respectively. Besides, the thickness at the leading edge of the substrate decreases drastically. This should be caused by a sharp decline of the vapor deposits concentration (will be further explained later). The highest growth rate of the coating at the leading edge (estimated based on the length of columns) is approx. $60 \mu\text{m}/\text{min}$ lower than $94 \mu\text{m}/\text{min}$ of the coating deposited on the substrate vertical to the axis of plasma jet (seen in Fig. 5.14A1). Looking closer on the coating A, its fracture

morphologies (Fig. 5.32) show that the inclination angles of columns diminish from the leading edge to the end of the substrate, and the observed maximum inclination angle is about 30° . In other words, the growth direction of columns changed gradually from inclined direction to vertical direction with increasing distance from the leading edge of the substrate.

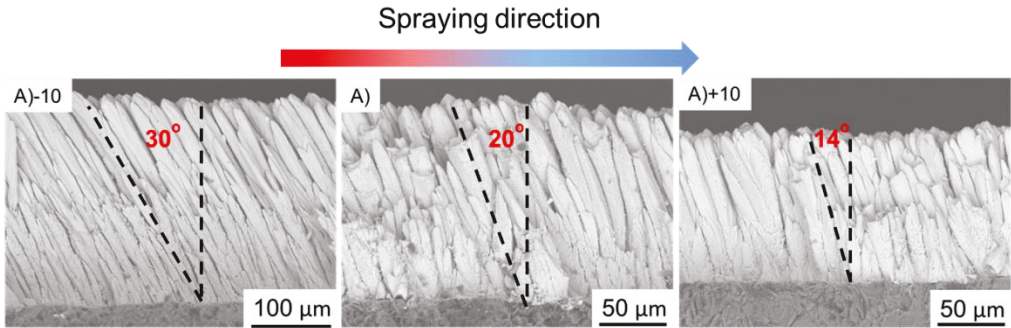


Fig. 5.32 Fracture morphologies (SEM (BSE) image) of the coating A at different locations along the spraying direction (A-10 means 10 mm ahead of position A, vice versa)

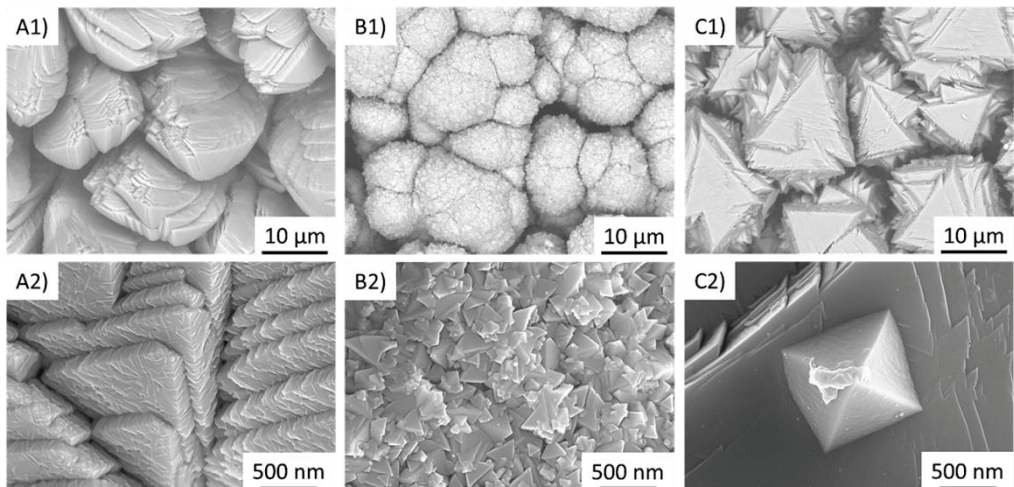


Fig. 5.33 Surface morphologies of the coatings deposited at positions A, B and C: A1 to C1 are back-scattered electron SEM images; A2 to C2 are secondary electron SEM images.

The surface morphologies of the coatings were found to be significantly different at positions A, B, and C. The columns in the coating A (Fig. 5.33A1) compose of abundant small facets (Fig. 5.33A2). This is the same with the coating (see Fig. 5.15A1) deposited on the substrate perpendicular to the plasma jet. It is also comparable to the “four-sided” EB-PVD (see Fig. 2.12a). Columns in the coating B (Fig. 5.33B1) have domed tops, each spherical lump consists of many nano-sized crystal grains (Fig. 5.33B2). This kind of cauliflower-like coating was also observed in the deposition

of YSZ by the thermal CVD process (see Fig. 2.33b) [143], which tends to be evolved when the substrate temperature is low or when the growth rate of the coating is high [144]. As mentioned in section 2.3.2, it was suggested that the nanostructure or cauliflower structure could be one of the microstructure criteria that distinguish between the atomic unit and the cluster unit deposition [143]. Because the evolution of the cauliflower structure is difficult to explain by the conventional atomic or molecular unit crystal growth as mentioned in section 2.3.2 [145].

Columns in the coating C have flat tops (Fig. 5.33C1) that look like stacked by many triangular lamellas. The similar microstructure was also formed in EB-PVD coating (see Fig. 2.12c) when the preheating substrate temperature was relatively low at 925 K (652 °C) to 1021 K (748 °C) [77]. The cross-sectional structure of the EB-PVD coating consists of a pile of pyramidal grains to produce a scale-like structure. They interpreted that the structure is likely to result from grain growth with periodic renucleation since the probability of nucleation increases as the substrate temperature decreases. Moreover, a few pyramidal grains (Fig. 5.33C2) on the surface of triangular lamellas can be found, which might be caused by the elevated temperature at the later period of the coating process.

- **Phase composition and texture**

XRD patterns of coatings deposited at different positions are shown in Fig. 5.34. Rietveld analyses in Table 5.7 reveal that the coatings are composed of pure tetragonal phase except for the coating A, a small amount of ZrC was formed due to high temperature. No monoclinic phase was detected in the coatings. Except for the peaks belonging to tetragonal ZrO₂ and ZrC, the possible cubic ZrO₂ peaks are also marked in Fig. 5.34. The calculated YO_{1.5} mol% in the tetragonal phase are all below that in the primary feedstock (about 7.6 mol%) even though the error is relatively large due to the broadening of the peaks.

Table 5.7 Rietveld analyses of coatings formed at different positions

Number	Lattice parameters		$c/a\sqrt{2}$	YO _{1.5} (mol%)	Preferred orientations
	a (Å)	c (Å)			
Coating A	3.608(4)	5.171(4)	1.0134 (±0.0019)	5.67 (±1.2)	(002) (110)
Coating B	3.610(3)	5.170(3)	1.0127 (±0.0015)	6.14 (±0.9)	Randomly orientated
Coating C	3.608(2)	5.172(2)	1.0136 (±0.0010)	5.55 (±0.6)	(011)

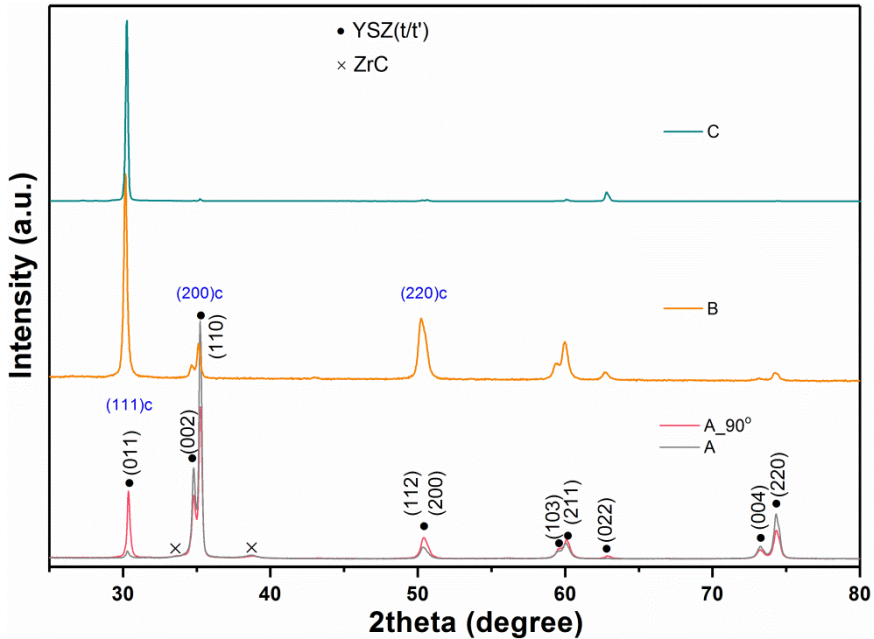


Fig. 5.34 XRD patterns of coatings A, B, and C (A_90° means that the substrate was rotated 90° in the substrate plane)

The diffraction patterns for the coating A and A_90° (the sample was rotated 90° in the substrate surface plane) have different peak intensities for some crystal planes (011), (002), and (110), which is caused by the oblique growth of the columns. In any case, the diffraction of the coating A is not powder diffraction like. The intensities of the (002) and (110) crystal planes are higher than that of (011), showing preferred orientations of (002) and (110). XRD pattern of the coating B gives a uniform distribution of peak intensities like powder diffraction pattern illuminating random orientation of crystals. Only the diffraction peak of the (011) plane and its next diffraction order of (022) in the coating C were detected evidently, which implies a preferred orientation along $\langle 011 \rangle$ direction.

Pole figures were prepared to determine the degree of crystal orientation as well as the in-plane orientation relationships between the columns. Because the (011) peaks in the standard XRD patterns of these three coatings are observed showing a high intensity, pole figure was first measured by focusing on the 2θ of the (011) peak of the coatings A, B, and C. Afterwards, pole figures of (002)_(110) peak and (200)_(112) peak were measured for the coating A and the coating C. Here, it has to be pointed out that the resolution of X-ray in pole figure measurement is not high enough to distinguish (002) and (110) peaks as well as (112) and (200) peaks because they are at quite similar 2θ positions in the standard XRD pattern.

5.3 Deposition parallel to the axis of the plasma jet

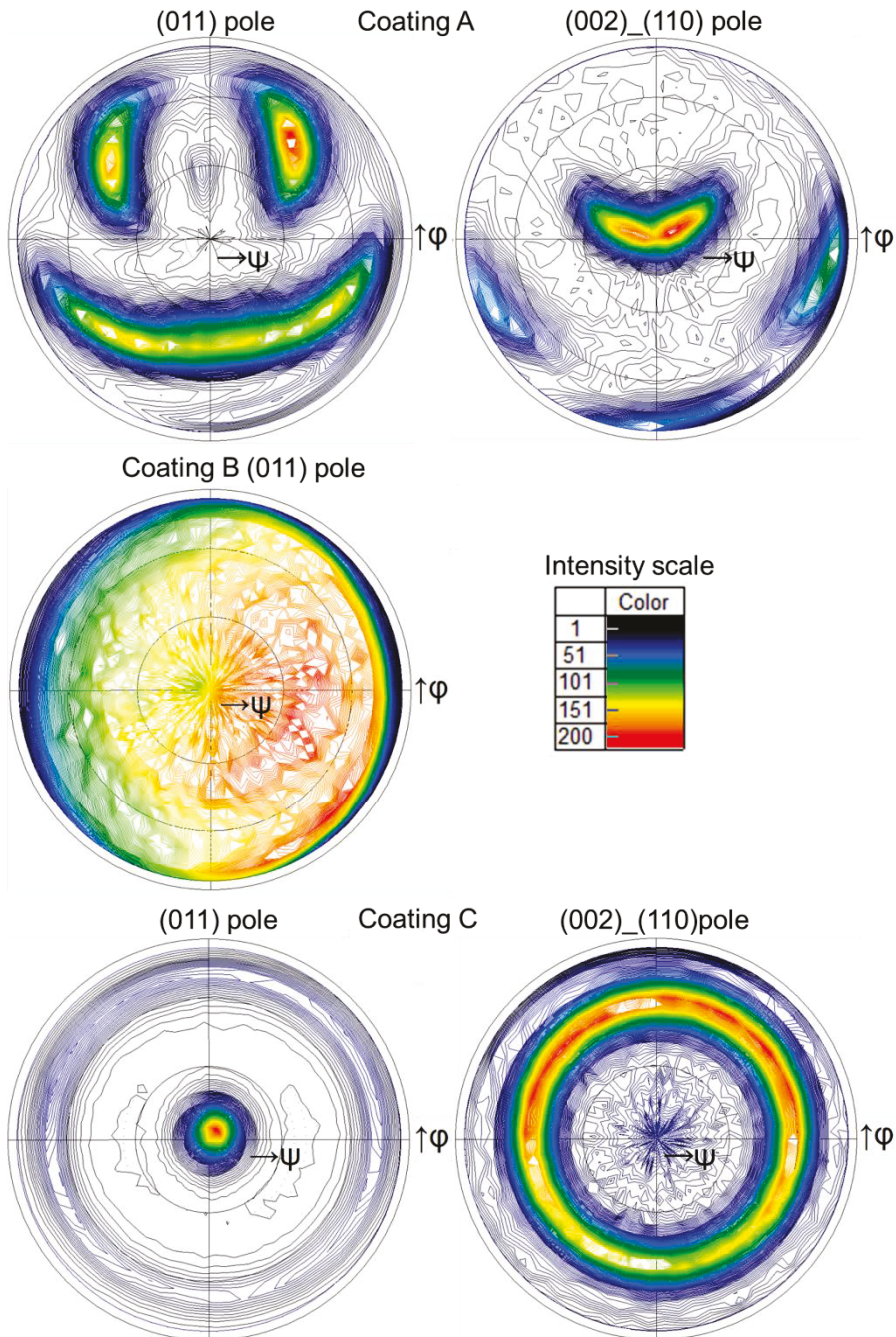


Fig. 5.35 Pole figures of coatings A, B and C (Pole figures were plotted with their left-right axis oriented parallel to the plasma jet axis.)

As shown in Fig. 5.35, the (011) pole figure of the coating A has no intensity in the center indicating that no crystal plane (011) is parallel to the substrate surface. Two

maxima in the pole figure indicate preferred in-plane orientation of (011). The strong intensity located near the center of the (002)₁₁₀ pole figure indicates a preferred orientation through the coating thickness direction (out-of-plane orientation). Therefore, the coating A has a so-called biaxial texture [113] (two-degree orientation described in ref. [118]) that have an in-plane and an out-of-plane orientation. But the maximum intensity has a slightly tilted angle ($\sim 5^\circ$) in the pole figure, which might be caused by the oblique angle ($\sim 20^\circ$) of the columns [201].

The (011) pole figure for the coating B shows a relatively homogeneous intensity distribution around the center of the pole figure, which means that the crystals in the coating B are totally randomly orientated. Considering its, every lump in the coating B consists of numerous nano-sized crystals as shown in Fig. 5.33B2. Individual nano crystal has its own orientation leading to the randomly orientated coating. Besides, the intensity distribution is not completely uniform. From the left to the right of the pole figure, the intensity rises gradually. Since the pole figure was plotted with its left-right axis oriented parallel to the plasma jet axis, it could also be caused by slightly tilted column growth direction.

The (011) pole figure of the coating C shows a strong intensity located at the center of pole figure, confirming a preferred $\langle 011 \rangle$ through column growth direction (out-of-plane orientation) and also indicating that the majority of the surface planes are parallel to the (011) plane. While the ring pattern of the (002)₁₁₀ pole figure means that no preferred in-plane crystal orientation developed in the coating C. This one out-of-plane orientation through the coating thickness direction is also termed fiber texture. Referring to the microstructure of the coating C (Fig. 5.33C1 and C2), it is also indicative that the layered lamellas are the crystal plane (011).

• Crystal orientations and grain size distributions

To get a better understanding about the transition of the crystallographic structure during coating growth, the cross-sections of the coatings were further investigated by EBSD, and results are given in Fig. 5.36. After placing the samples into the conductive resin, the mounting material cracked so that some discontinuities of the images appeared due to the dried polishing suspension covering the bottom part of the coatings, especially the coating A and the coating C. The left column of Fig. 5.36 (A1, B1, and C1) gives the IQ maps of the coatings A, B and C. It is obvious that, at the bottom of the coating A and C as well as in the middle region of the coating B, the black areas are

5.3 Deposition parallel to the axis of the plasma jet

corresponding to the areas where no diffraction patterns were obtained in the orientation maps (Fig. 5.36 A2, B2, and C2).

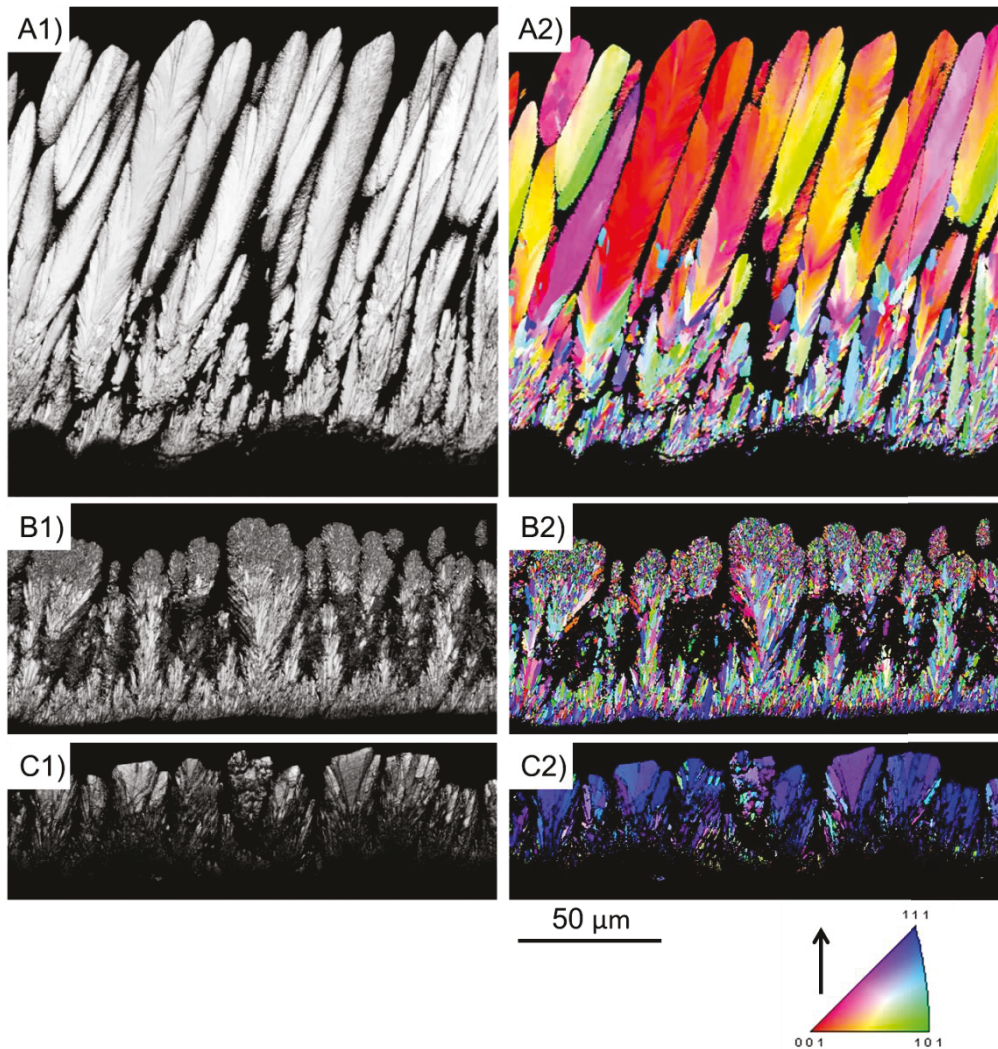


Fig. 5.36 EBSD images: quality maps (A1 to C1) and orientation maps (A2 to C2) of coatings A, B and C

According to the orientation map of the coating A, the coating growth starts from small and randomly orientated crystalline grains similar to the coating 1000-T₁. With increasing coating thickness, the more and more pronounced red color in the image illustrates that the top region of this coating has preferred orientation of c(001) (that is t(002) or t(110)) (The orientations are indexed with cubic lattice symmetry as well). The EBSD orientation map of the coating B in Fig. 5.36 also shows randomly

orientated crystals occurring near the substrate but blue color prevails. The difference to the coating A is that the top of the coating B contains many randomly orientated grains. In the coating B, it is not possible to define any preferred orientation. The random orientations of the grains are consistent with the XRD and pole figure analyses.

The orientation map of the coating C shows a few large and blue color-coded grains, which means that the crystal orientation is mainly along $c\langle 111 \rangle$ (that is $t\langle 011 \rangle$). Although the bottom part of EBSD images (Fig. 5.36C2) is almost dark, it is still possible to recognize slight red and green colors. The reproduced coating C (the sample for EBSD was well-prepared) (see Fig. 5.37) shows that a very thin layer near the substrate has very fine crystals being even smaller than 100 nm because they cannot be seen by EBSD. In addition, one can see a red colored crystal in Fig. 5.37 orientated along $c\langle 001 \rangle$ direction, which might be the orientation of the pyramidal crystal observed on top of the triangular lamellas in Fig. 5.33C2.

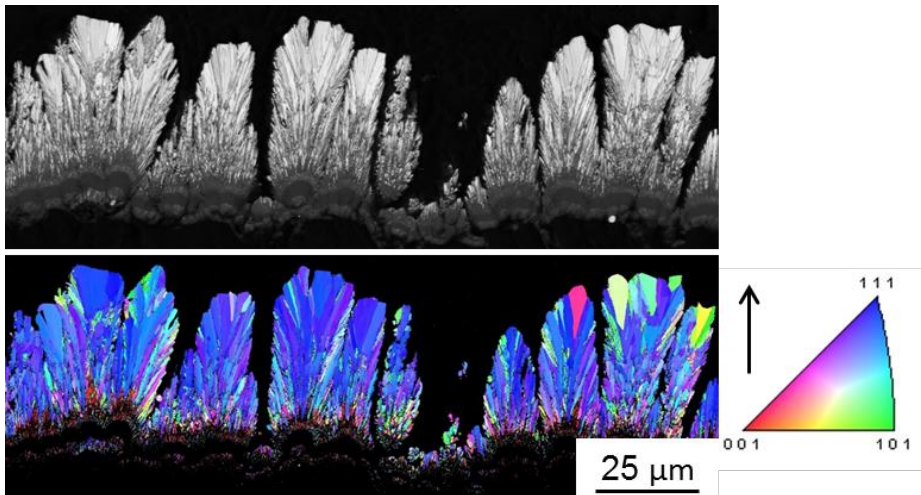


Fig. 5.37 IQ map and EBSD orientation map of a repeated coating C

The grain size distributions illustrate grains with a size of approx. 30 to 45 μm covering the largest area fraction on the top part of the coating A (see Fig. 5.38a). On the contrary, a large number of grains adjacent to the substrate have a size smaller than 250 nm. Such small grains are found in all coatings (see Fig. 5.38b). In the color-coded grain size map of the coating B, the area fraction of the grains shows a normal distribution centered at 1 μm due to large amount of fine grains in the top part of the coating B. In the coating C, the main area fraction of grains is distributed around 10 μm corresponding to the orange-colored grains. One could notice here that T_s (470~1087 $^\circ\text{C}$)

5.3 Deposition parallel to the axis of the plasma jet

of the coating C is comparable with 1000~1100 °C of coatings deposited with torch swing in section 5.2.2. However, the grain size of the coating C can be up to 14 μm. This comparison suggests that, instead of the low T_s , the small grain size of coatings deposited with torch swing might be mainly caused by the interruption of grain growth induced by torch swing.

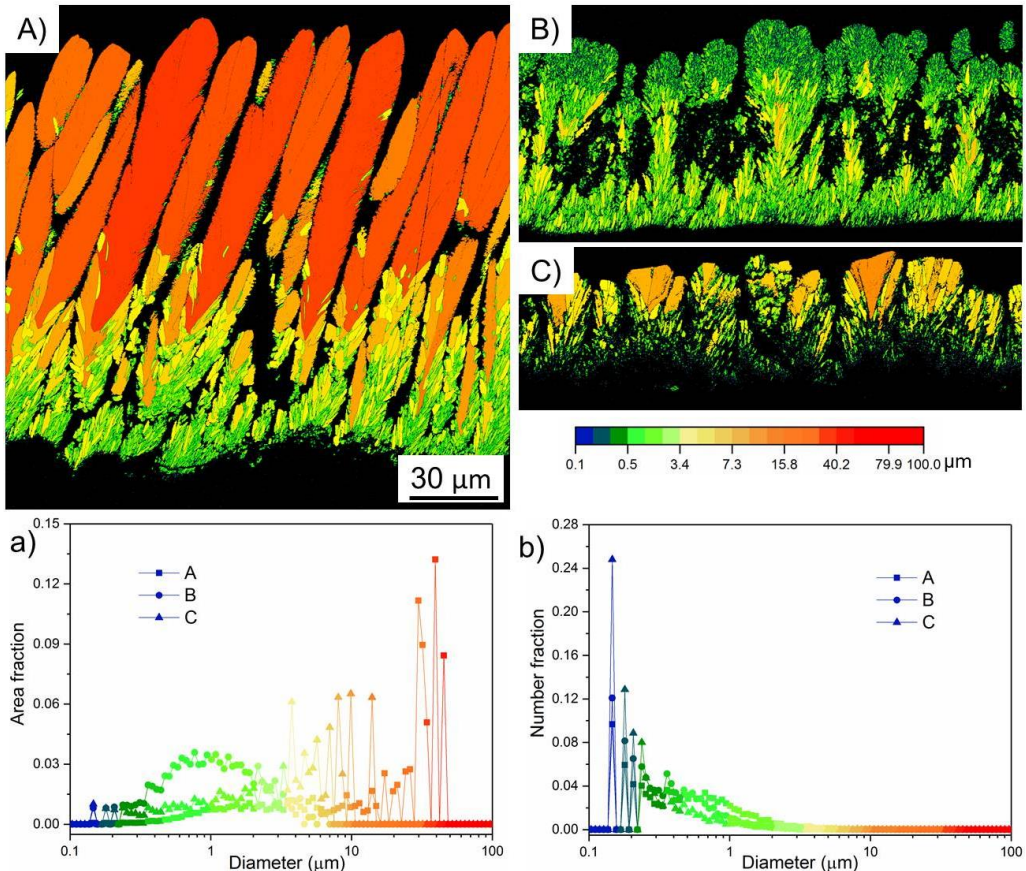


Fig. 5.38 Color-coded grain size maps of the coatings A, B and C. And their a) area fraction and b) number fraction of the grain size distributions

5.3.2 Coatings deposited at high powder feeding rate

In this section, results from the test II in Table 5.6 will be presented as a comparison with the test I in Table 5.6 (section 5.3.1) as well as the test C-20 in Table 5.1 (section 5.1.1). In the test II, a higher PFR of 13.7 g/min was used. Similar to the test I, the three different positions A, B, and C are investigated. And the coatings are termed as II-A, II-B, and II-C.

- **Microstructures**

Similar to the coating A in the test I, the columns in the coating II-A are inclined as shown in Fig. 5.39, whilst the columns in the other two coatings are almost vertical to the substrate. The thickness comparison between the two samples in test I and II in Fig. 5.40 indicates that the coatings in test II are thicker. The thickness of these two samples has the same degressively declining trend from the leading edge to the end of the substrate.

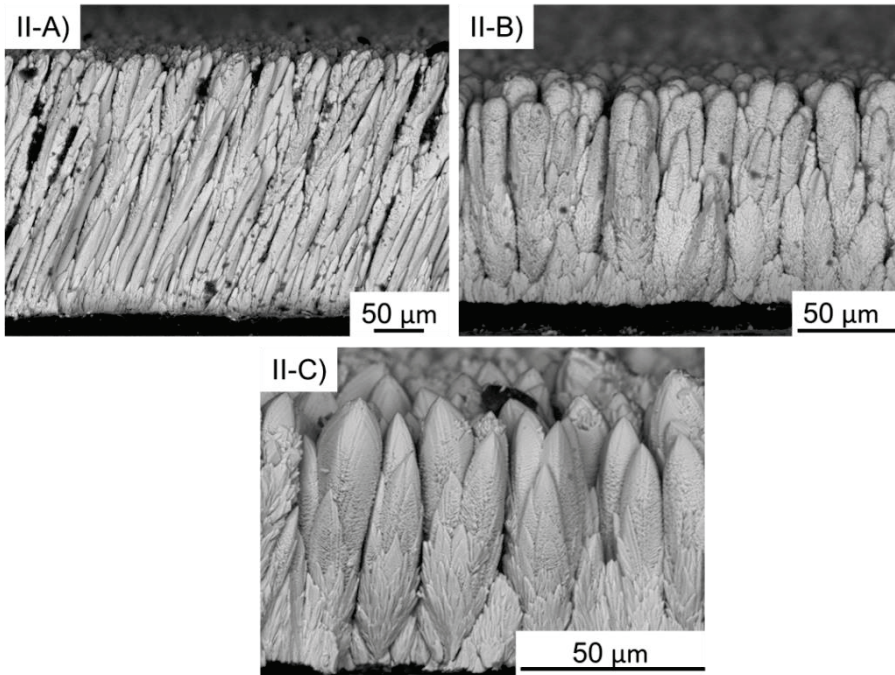


Fig. 5.39 Fracture morphologies (SEM (BSE) images) of coatings deposited at positions A, B and C

Fig. 5.41 shows the surface morphologies of the coatings formed at position A, B, and C, respectively. The tops of the columns in the coating II-A are also faceted similar to the coating A (see Fig. 5.33A1). The coating II-B shows domed tops, which are exactly like the coating B, each spherical lump consists of many nano sized crystal grains in the cauliflower structure. The coating II-C, however, is significantly different from the coating C (see Fig. 5.33C1). Instead of triangle lamellas, it has many columns with pyramidal tops, which are similar to the coating shown in Fig. 5.4a when the coating was deposited on a vertical substrate at a very low deposition rate of 3.9 g/min.

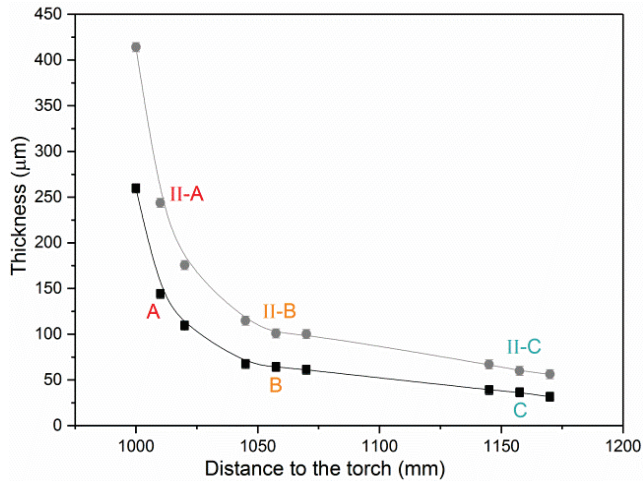


Fig. 5.40 Comparison of coating thickness from the leading edge to the end of the substrate between test I and test II (the measured data points are connected with B-Splines as a guide for eyes)

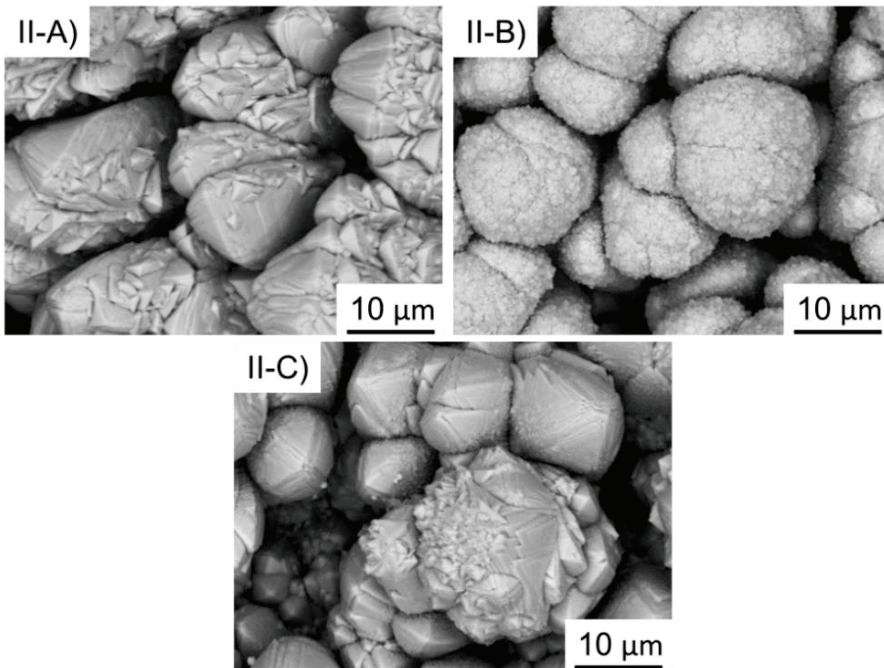


Fig. 5.41 Surface morphologies (SEM (BSE) images) of the coatings deposited at positions A, B and C in test II

- **Crystallographic evaluation**

The XRD analyses of the coatings II-A, II-B, and II-C reveal that the main phase is tetragonal phase and only small amount of ZrC exists in the coating II-A, which is

consistent with the coatings in test I. It is worth to note that the phase composition as well as the surface morphology of the coating II-A is different with the coating deposited at the same PFR but on a vertical substrate (see the XRD pattern (13.7 g/min) in Fig. 5.5). The latter one composes of $\sim 40\%$ m phase and does not show faceted structure. These results indicate that the flow condition over the substrate surface has influences not only on the microstructure but also on the phase composition. One possible reason is that, in case of substrate parallel to the axis of the plasma jet, those unevaporated feedstock particles might follow the gas stream flying away from the substrate so that only vaporized feedstock deposited on the substrate.

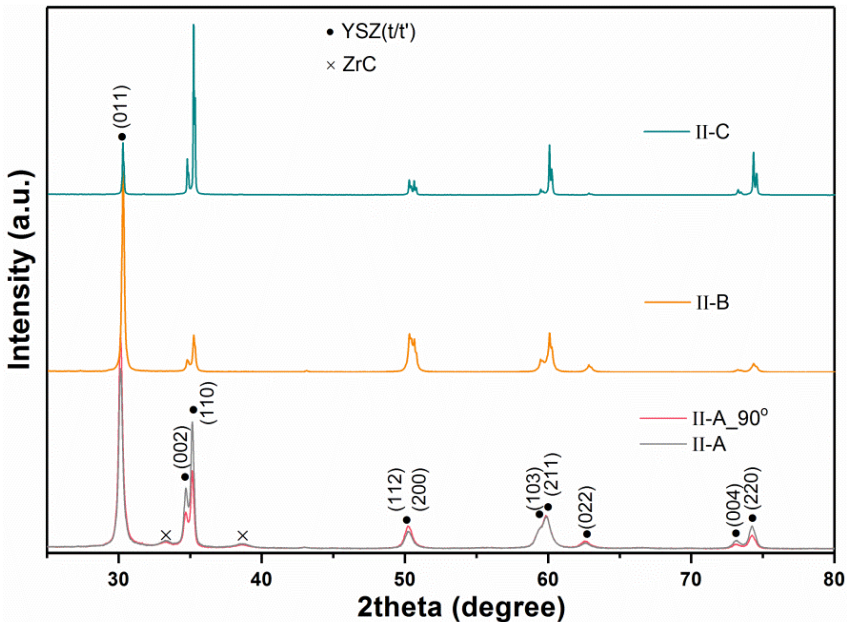


Fig. 5.42 XRD patterns of coatings II-A, II-B, and II-C (II-A_90° means the substrate was rotated 90° in the substrate plane)

Furthermore, the coatings also reveal different textures from the coatings in test I. In coating II-A, the preferred orientations $t(002)$ _ $t(110)$ is not that distinct as one can see the intensities of them are lower than that of the crystal plane $t(011)$. This might result from the high deposition rate. The oblique columns in coating II-A also cause the peak intensity variation when the substrate was rotated 90° in the surface plane. The cauliflower shaped coating II-B is randomly orientated. The coating II-C shows that the four-sided columns have pronounced preferred orientations of $t(002)$ _ $t(110)$, which is different from the coating C in test I. Possible reasons are the high T_s caused by a long preheating duration or a high PRF compared with the parameters in the test I.

5.4 Potential growth mechanisms

The EBSD results illustrate the variation of the crystal orientation and grain size during the whole coating growth process. According to the orientation map of a well-prepared coating formed at a position between A and B in test I illustrated in Fig. 5.43, the growth process of PS-PVD coating can be roughly divided into three stages.

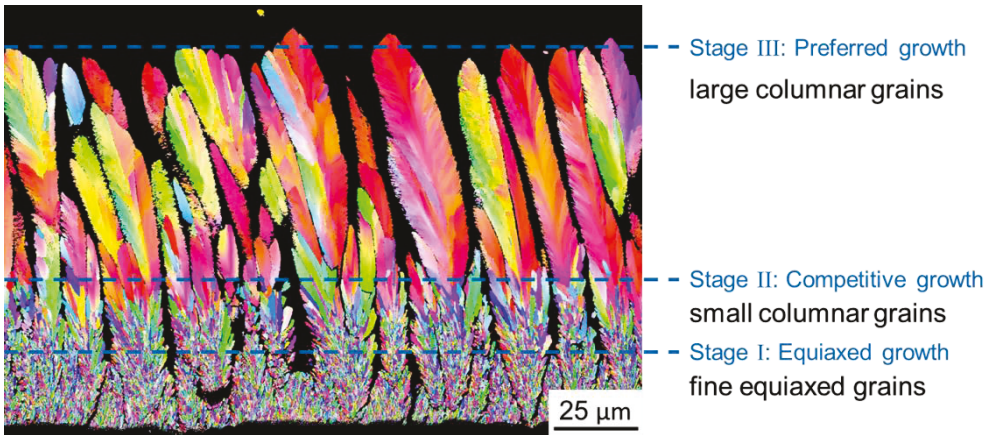


Fig. 5.43 Orientation map of a coating deposited in the test I at a position between A and B

- In stage I, no matter how the preheating conditions are, the coatings near to the substrate consist of many randomly orientated small grains. The grains tend to have equiaxed shape, not columnar shape.
- In stage II, the small grains grow into small elongated columnar grains. Owing to the increasing diameter, the grains grow competitively. They have no obvious preferred crystallographic orientation.
- In stage III, after some microns of growth, the number of columns decreases while their diameter increases and the coating starts to grow along favored orientations.

There is no well-defined boundary between these three stages. However, depending on the deposition conditions, these three stages can have different thicknesses and features. In the following three sections, atomic (or molecular) deposition will be discussed in section 5.4.1 and 5.4.2. In section 5.4.3, a concept of boundary-layer will be introduced to discuss the effects of the flow conditions in the boundary-layer on coating growth and the possibility of cluster deposition.

5.4.1 Equiaxed growth

As mentioned in section 2.1.3, previous research indicated that in EB-PVD the first thin layer (approximately 0.1 μm thick) adjacent to the substrate (so called equiaxed zone) consists of equiaxed grains of about 30 nm in diameter [80]. The thickness of this equiaxed layer was found to vary from sample to sample and sometimes no equiaxed zone was present at all. Immediately after the equiaxed zone, columns start to grow along $\langle 100 \rangle$ directions and the final symmetry appears within the first 2-5 μm [80]. Structure transition from equiaxed crystal to columnar crystal is very typical in metal casting. From the outer region to the inner region of a casted ingot, structures can be small equiaxed grains, columnar grains, and large equiaxed grains, respectively. Several theories were proposed to explain the formation of equiaxed crystals [202]. Wherein, the chill crystal theory proposed by Genders to explain the small equiaxed grains formed on the mould wall was well accepted although this theory cannot interpret all of the phenomena. Similar but not exactly the same, the formation of the equiaxed grains in PS-PVD can be basically explained by a chill mechanism. In the beginning of the deposition, the fast cooling of deposits on the substrate causes a large undercooling effect, thus intensive nucleation is expected. Deposition on amorphous or randomly textured polycrystalline substrates usually leads to island-by-island growth mode and the nucleation of islands with random orientation [109, 203]. In this work, neither the graphite nor the Inconel substrate is textured. Hence, this might be one reason for the formation of the randomly orientated equiaxed crystals in the beginning of coating deposition when the nucleation is dominated.

Subsequently, the latent heat of crystallization is released and may contribute to increasing of T_s . Besides, in PS-PVD, the plasma continues heating the substrate. Unfortunately, such constantly varying T_s can hardly be recorded locally by the existing measurement equipment. Notwithstanding, it can be understood that the undercooling is reduced with increasing the coating thickness. According to equations (2.2) and (2.3), the driving force of nucleation decreases with reducing undercooling or super-saturation. But the atomic diffusion gets faster with temperature increase according to equations (2.1). Consequently, nucleation would be inhibited and newly deposited atoms will predominantly join existing nucleation sites contributing to crystal growth. Fig. 5.44 shows EBSD measurements results of a sample produced in the test R-I in section 5.3.1. In this case, the coatings at same positions A, B, and C are termed as coating R-A, R-B, and R-C, respectively. The only difference between the test R-I and the test I (section 5.3.1) was a long preheating applied in the test R-I. The preheating T_s at position A measured by pyrometer was approx. 1300 $^{\circ}\text{C}$ (it is about

5.4 Potential growth mechanisms

1450 °C if measured by a thermocouple), higher than the preheating T_s of the coating A (1160 °C) in test I. It can be seen that the stage I of the coating R-A is thinner than that of the coating A. Large grains ($\sim 10 \mu\text{m}$) are formed close to the substrate. This indicates that high T_s inhibits nucleation and promotes crystal growth, thus reduces the thickness of the equiaxed growth stage.

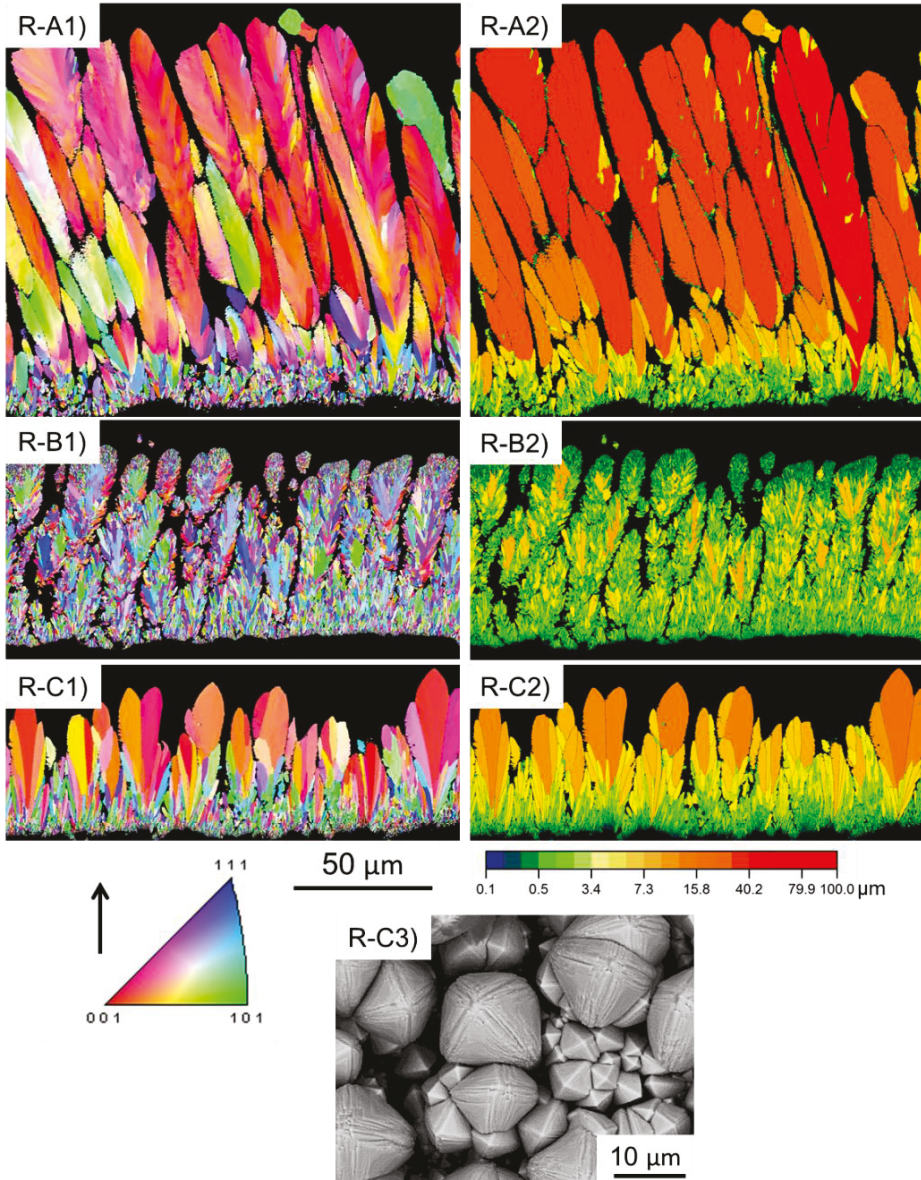


Fig. 5.44 EBSD orientation maps (R-A1 to R-C1) and color-coded grain size maps (R-A2 to R-C2) of coatings R-A, R-B and R-C; R-C3 is the SEM (BSE) image of a top view of the coating R-C.

Under the same temperature condition, a high super saturation induced by high deposition rate (massive transport of deposit species towards the substrate surface) can lead to a high nucleation rate. Compared with EB-PVD coatings, the stage I of PS-PVD coatings are much thicker and the grain size in it is much larger. One reason could be the high deposition rate in PS-PVD leading to a high super saturation ratio. On the other hand, this high deposition rate could reduce surface diffusion of vapor species as mentioned in section 2.3.1 that a diffusing species may be ceased by the next deposited species. If one compares the coating 1000-T₁ (section 5.2.1) and the coating A (section 5.3.1), in which the coating 1000-T₁ has higher deposition rate and a similar T_s with the coating A. Small equiaxed grains exist in a very large thickness range (according to Fig. 5.18 and Fig. 5.19) in the coating 1000-T₁. It seems that, except for the T_s , the thickness of the equiaxed growth stage has a positive relation to the deposition rate.

The above discussion of equiaxed growth is about the coatings deposited without torch swing. In section 5.2.2, some coatings were deposited with torch swing. The results showed that low T_s and interruption of the torch swing could be the two reasons for the small grain size. As mentioned before, the crystals can grow larger than 10 μm in the coating C at a T_s of 470 ~ 1087 °C comparable to T_s of deposition with torch swing (1000~1100 °C). Furthermore, the crystal size in the region close to the substrate is generally small, independent of T_s . These results indicate that the relatively low T_s during coating deposition with torch swing is not the only reason for the formation of small crystalline grains. Another reason could be that the crystal growth interrupted by torch swing and thus repeated nucleation takes place. This interruption might cause on one hand the latent heat of crystallization removed from the growing surface when the torch is moved away from the sample; on the other hand, cause change of flow conditions such as the incidence angle of the vapor species (this will be further discussed later). Due to this repeated process, the coatings deposited with torch swing are composed by many small equiaxed crystallites, and thus do not show any preferred growth orientation. The torch swing in PS-PVD might have a similar effect like the slow rotation of the substrate in EB-PVD. In ref. [82], the effect of substrate rotation on texture evolution in YSZ coatings fabricated by EB-PVD was investigated at a constant substrate temperature of 1200 K. It was found that a strong out-of-plane orientation along $\langle 111 \rangle$ was established after 12 s deposition on a stationary substrate. However, preferred orientation was not really distinct in the coating deposited with a low rotating speed (1 rpm) even after 300 s deposition. When the rotating speed was increased to 5 rpm, the orientation $\langle 111 \rangle$ disappeared after 36 s deposition [77]. Further increasing the speed to 10 rpm, the orientation changed to $\langle 200 \rangle$, and became evident only after 36 s deposition [82]. This indicates that stationary deposition or shortly interrupted

deposition (high rotating speed) favors textured crystal growth (growth of large grains), while long interruptions (low rotating speed) could cause a break off of any texture formation.

5.4.2 Preferential growth

In this stage, the dominant phenomenon is not nucleation but grain growth. As discussed in section 2.3.1, the final coating microstructure and its texture can be influenced by a number of deposition parameters and are determined by four regimes: shadowing, surface diffusion, bulk diffusion and recrystallization. One should notice that in PS-PVD most of the coatings are deposited at T_s higher than ~ 1000 °C, which means that T_s/T_m is approx. > 0.4 . According to the SZM proposed by Thornton [7], the deposition condition is already in zone 2 where the surface diffusion is sufficient to form highly faceted columnar grains. But, the deposition rates in PS-PVD are generally high, which might reduce the diffusion of the vapor species as mentioned before [113]. In addition, the observed microstructures of PS-PVD coatings indicate that they are deposited mainly in zone 1 and zone T as indicated in Fig. 2.35. Bulk diffusion and recrystallization are rarely seen in PS-PVD because they have higher energy barriers and generally take place at even high temperature. So, the preferential growth of PS-PVD coatings will be discussed based on shadowing and surface diffusion. Mahieu et al. [113] also divided the influence of deposition parameters into two main groups: diffusion and shadowing. Diffusion means the mobility of the deposit species at the growing surface, which leads to a reduction of porosity and smoothing of the surface. It could be influenced by T_s , deposition rate, impurities, and the materials system, etc. [204]. On the other hand, shadowing means the orientation distributions of the incoming material flux relative to the surface normal, which causes preferential growth direction and the formation of rough, porous, columnar microstructures [205]. It can be induced by surface roughness, the VIA, deposition geometries, and substrate rotation.

- **Surface diffusion**

As mentioned in section 2.3.1, the diffusion rate depends on diffusion barrier E_d and T but also on vapor species flux (deposition rate). Besides, diffusion is anisotropic in both diffusion rates and mechanisms at the various crystal orientations of a given material [112]. With increasing T_s (or diffusion ability (mobility)), atoms that were stable at lower temperatures can become active. The possible diffusion behaviors are:

- 1) At very low T_s , the deposited species have almost no mobility; they will stick at the same position where they arrive. Such kind of deposition will be only affected by shadowing [113, 119].
- 2) At higher T_s , the deposited species might be able to overcome the energy barrier for diffusion but their mobility is restricted to individual crystal planes. Due to such diffusion, the crystallites form facets. As mentioned in section 2.3.1, the mobility is higher on low-surface-energy planes so that the deposited species are much easier to be adsorbed on the high-surface-energy planes. So these high-surface-energy planes would have the kinetically highest growth rate [201]. Due to the anisotropy in growth rate, the crystal faceting occurs in such a way that the grains are terminated by the planes of lowest crystallographic growth rate as illustrated by Fig. 5.45.

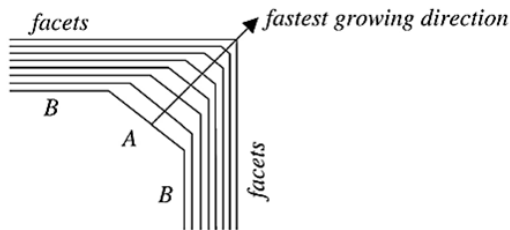


Fig. 5.45 Schematic drawing of the evolution to the kinetically determined growth shape in a two-dimensional representation. In this example, plane A has a larger crystallographic growth rate than plane B, and thus is extinguished during the growth process [113].

- 3) If T_s is high enough for sufficient diffusion but restricted to individual crystals (no diffusion from one grain to another), faceted columns can develop as well. Since no interdiffusion between grains takes place, the competition between grains is only due to shadowing. In other words, the tallest columns are able to grow over other short columns caused by anisotropic vapor species flux. Since this competition is due to shadowing, no preferential orientation would develop in this case.
- 4) Further increasing T_s , surface diffusion is not limited so that diffusion from one grain to another grain is possible. The grains will grow according to their kinetically determined crystal habit. In this case, the evolutionary selection mechanism proposed by Van der Drift [119] is involved due to the competition between the grains. The grains with the crystallographic fastest growing direction perpendicular to the substrate will overgrow all other grains and become the out-of-plane growth orientation as shown in Fig. 2.29. Van der Drift [119] proposed some fastest growth direction for different shaped crystals. In case of a tetragonal crystal ($c/a > \sqrt{2}$), it has $\langle 001 \rangle$ orientation nearly perpendicular to the substrate. In addition, the ref. [206] also proposed that the growth rate of a

crystallographic plane perpendicular to the substrate is influenced by binding probabilities of the vapor species on it. A higher binding probability will result in a higher condensation rate, and thus a higher perpendicular growth rate.

Notwithstanding, one should keep in mind that the diffusion can be ceased by subsequently arriving deposits in case of high deposition rates although deposited species could principally diffuse to find a stable site or crystal plane [113].

- **Shadowing**

Shadowing mainly results from the geometric interaction between the roughness of a growing surface and the VIA. In PS-PVD, there are likely two scales of shadowing.

- 1) One is the roughness of the growing surface, which is considered as macro-shadowing here. A high deposition rate could enhance this macro-shadowing because it increases surface asperity. Typical PS-PVD coatings have tapered columns with larger gaps between columns compared with EB-PVD coatings. This is most likely to be caused by the high deposition rate.
- 2) The second one is the interaction between particles and plasma gas, which enables non-line of sight deposition in PS-PVD. Such interaction could affect the VIA in a way as illustrated in Fig. 5.46, and it is considered as micro-shadowing in this work. In the case that the substrate is perpendicular to the axis of the plasma jet (Fig. 5.46a), the deposited species have a broad VIA distribution. In contrast, the case that the substrate is parallel to the axis of the plasma jet (Fig. 5.46b), the VIA distribution is narrow because that in such case only the atoms moving towards the substrate surface can deposit on the substrate while another portion of atoms will just flow past the substrate as shown in Fig. 5.46b.

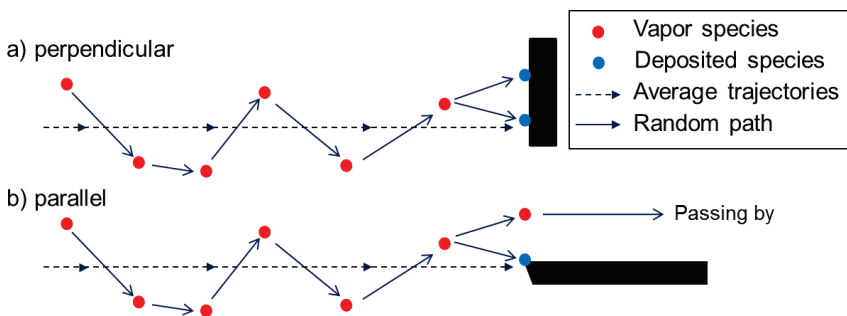


Fig. 5.46 Schematic illustration showing the microscopic trajectories of vapor atoms in the plasma jet with respect to different orientations of the substrates: a) perpendicular or b) parallel to the axis of the plasma jet

• Development of orientations

Since the coatings deposited with torch swing do not show any texture, here only the coatings deposited without torch swing will be discussed. Thus, the substrate temperature has higher value in the center of the plasma jet or at a short spraying distance.

1) In the case that the substrate was perpendicular to the axis of the plasma jet (spraying tests in section 5.2.1, PFR of 6.9 g/min), the observed preferred orientations of PS-PVD coatings in this work are shown in Fig. 5.47. In this diagram, the two coordinate axes are spraying distance and distance to the axis of the plasma torch, respectively. All of preferred orientations indicate out-of-plane orientations as they are evaluated by standard XRD patterns without tilting measurement. The shadowing in this case could mainly result from macro-shadowing. As shown in Fig. 5.46a, the interaction between the vapor deposits and the plasma gas can lead to a broader VIA distribution relative to the substrate normal.

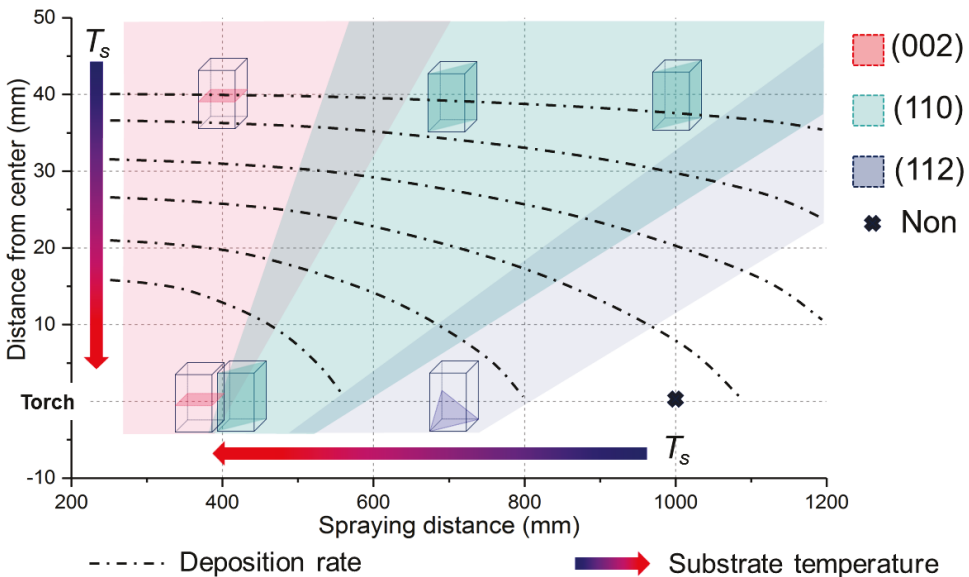


Fig. 5.47 Preferred growth orientations found in PS-PVD coatings deposited on substrates vertical to the axis of the plasma jet; the different colors illustrate the possibility of different out-of-plane orientations; the dashed lines indicate approx. deposition rate contours.

At 40 mm distance from the center of the plasma jet, the deposition rates were found to be relatively low at approx. 20~30 $\mu\text{m}/\text{min}$ (see Fig. 5.14). The preferred orientations changed from t(110) to t(002) as spray distance reduced (or T_s increased). As the

fore-mentioned evolutionary theory, the evolution of orientation from $t(110)$ to $t(002)$ with increasing T_s indicates that the crystallographic fastest growing direction perpendicular to the substrate changed from $t(110)$ to $t(002)$. Chen et al. compared that the surface energy ($\gamma(hkl)$) for the different crystallographic planes of tetragonal ZrO_2 and the results show $\gamma(002) > \gamma(010) > \gamma(011) > \gamma(110)$ [207]. As mentioned in section 2.3.1, the binding is stronger on facets of high-surface-energy. The reason for the evolution of fastest growth rate might be the increase of condensation rate on (002) crystal plane due to high binding energy at high temperature causing a fast perpendicular growth rate.

In the center of the plasma jet, the deposition rates were rather high. This reduces the effect of diffusion of deposited species in comparison with that at 40 mm distance from the center. Strong preferred orientations $t(002)_t(110)$ were found at a very short spraying distance of 400 mm where T_s was extremely high. However, in ref. [96], the tops of the coating deposited at 300 mm using a rather high PFR of 20 g/min are not faceted (Fig. 2.34a), and the coating is not preferentially orientated even though its T_s had the highest value. At 700 mm, the coating shows a slightly preferred orientation along $t(112)$. Obviously, T_s is not the only influence that can affect the preferred orientations of the coatings. As shown in Fig. 5.47, the high-surface-energy plane (002) was found in the coatings deposited at high temperature. In ref. [96], the coating (Fig. 2.34b) deposited at a spray distance of 800 mm (even lower temperature) along with a very low PFR of 2 g/min is faceted and shows a preferred orientation of (002). In other words, if the deposition rate is low, a high-surface-energy plane can be found at lower temperature, e.g. longer spraying distance, as indicated in Fig. 5.47.

- 2) When the substrate was parallel to the axis of the plasma jet (spraying tests in section 5.3), the micro-shadowing effect has to be considered as shown in Fig. 5.46b, in particular at the leading edge of the substrate where the columns are inclined towards the spraying direction.

In-plane orientation $t(011)$ and out-of-plane orientations $t(002)_t(110)$ were observed in the coating A. As mentioned in section 2.1.3, coexisting of in-plane orientations (220) and out-of-plane orientation (200) in EB-PVD coatings are normally found during high-speed rotation deposition [83]. This type of biaxial textured coatings was also reported for sputter deposited thin films on the substrates tilted with respect to the incoming material flux [113]. In ref. [113], a mechanism was proposed for the in-plane texture of a deposition carried out on a tilted substrate under the conditions that the deposited species have relatively high mobility so that the evolutionary selection mechanism drives the texture formation. In other words, the in-plane texture is also due

to an overgrowth mechanism in which the grains with the largest growth rate overgrow the other grains. The anisotropic in-plane growth rate is caused by:

- a) the directional diffusion of the vapor species because of the conservation of their momentum when impinging a tilted substrate; a perfect in-plane orientation can only be obtained when the deposited species was assumed to diffuse along one direction on the growing surface [206].
- b) the anisotropy of the capture length for diffusing vapor species is shown in Fig. 5.48 due to the growth of the grains according to their kinetically determined facets.

As shown in Fig. 5.48, when the deposition is carried out on a tilted substrate (the substrate was parallel to the axis of the plasma jet), the incoming vapor species are assumed to be diffusing along one direction on the growing surface. Then, the out-of-plane orientated grains might have anisotropic capture lengths for diffusing vapor species which leads to an anisotropic growth rate. The grains capturing more diffusing deposited species will have the largest growth rate and hence are able to overgrow other grains. The reason of the in-plane orientation $t(011)$ in the coating A might be that those out-of-plane orientated ($t<001>$ or $t<110>$) grains has the largest capture length along $<011>$ orientation.

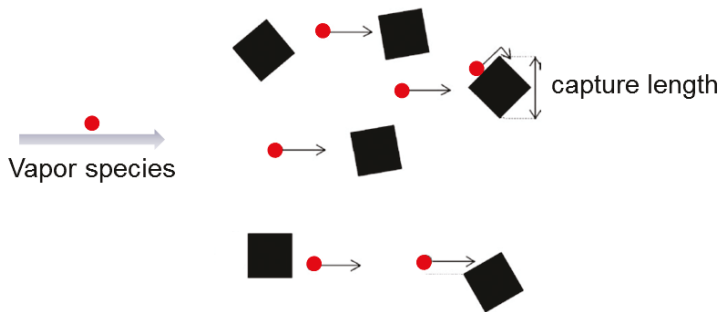


Fig. 5.48 Schematic drawing of plan view of square shaped $<001>$ out-of-plane oriented grains. The arrow indicates the orientation of the directional diffusion. Adapted from [113]

From the above discussed in-plane mechanism, a broad VIA distribution and the reduction of mobility (high deposition rate or low T_s) will hinder the formation of a biaxially aligned coating as the evolutionary mechanism cannot evolve. Compared with deposition conditions of the coating 1000-T₁, the coating A have a narrow VIA distribution, high T_s , and low deposition rate. All of these parameters contribute to the in-plane orientation in the coating A.

The column tops of the coating R-C as shown in Fig. 5.44R-C3 are well-developed four-sided, similar to the EB-PVD coating shown in Fig. 2.12a. According to the EBSD

orientation map (Fig. 5.44), such column has $\langle 001 \rangle$ column axis orientation in cubic lattice symmetry (that is out-of-plane orientations $t(002)_t(110)$, which is similar to the coating A as well as the coating R-A). This texture is common for EB-PVD coating and the tip of the columns is capped by four $\{111\}$ planes [83]. Since the value $c/a\sqrt{2}$ of the coatings is close to unity, the crystal axis $\langle 001 \rangle$ can be simply illustrated in Fig. 5.49. Consequently, in tetragonal lattice symmetry, the four-sided pyramidal top columns are also along $\langle 001 \rangle$ orientation capped by four $\{011\}$ planes.

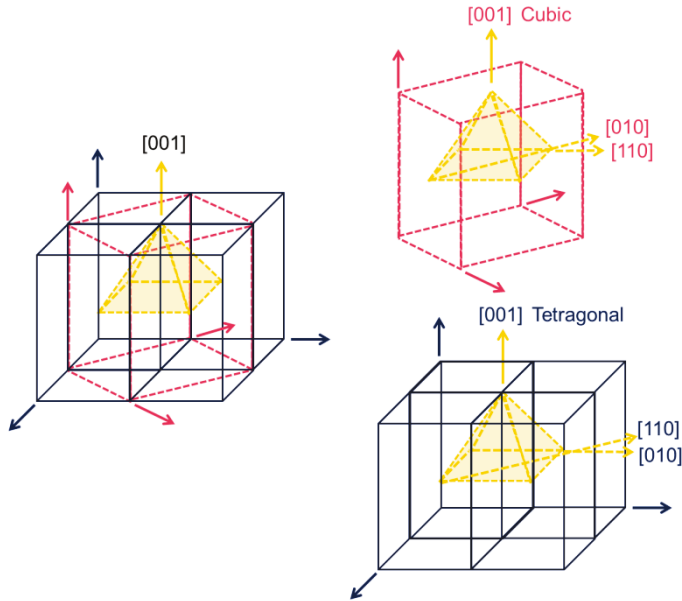


Fig. 5.49 Schematic drawing of the crystal orientation $\langle 001 \rangle$ in tetragonal lattice symmetry (blue) and cubic lattice symmetry (red); the arrows represent the crystal lattice coordinates. The four crystal planes (the yellow pyramidal shape) are four $\{111\}$ planes in cubic lattice symmetry, but four $\{011\}$ planes in tetragonal lattice symmetry.

In addition, the coating C exhibits only the out-of-plane orientation of $t(011)$. As observed in the coating C (Fig. 5.33C), small four-sided pyramidal crystals are formed on top of the coating C surface. This can be seen more clearly in a coating (Fig. 5.50) which was deposited at a longer spraying distance (~ 1180 mm) in the repeated test R-I. Its deposition T_s should be lower than that of the coating R-C (spraying distance of 1160 mm). The formation of out-of-plane orientation means the mobility of deposited species is sufficient for diffusion from grain to grain. The grain will grow according to their kinetically determined crystal habit. The change of orientation from $t(011)$ of the coating C to $t(002)_t(110)$ of the coating R-C was observed to be coincident with increasing T_s . In ref. [207], it shows that the surface energy $\gamma(002) > \gamma(011)$, so the

possible reason for such evolution might also be the enhanced condensation rate on (002) because of stronger binding at high temperature, causing a high growth rate perpendicular to the substrate surface. So the grains oriented with the fastest growing direction $\langle 001 \rangle$ perpendicular to the substrate can overgrow other oriented grains forming the out-of-plane orientation. This fast growth orientation is agree with that of tetragonal crystals ($c/a > \sqrt{2}$) proposed by Van der Drift [119] in case of infinite diffusion.

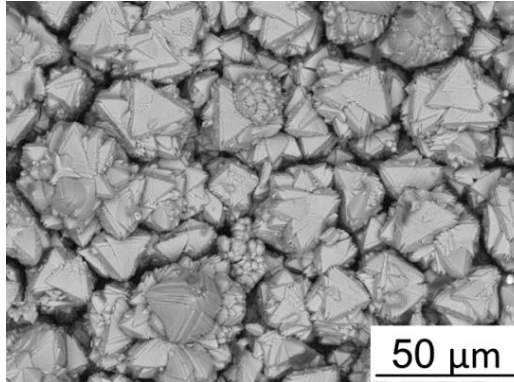


Fig. 5.50 SEM (BSE) image of top view of coating deposited at a spraying distance of ~ 1180 mm in a repeated sample (the test R-I)

To summarize, the preferential growth of PS-PVD coatings can be preliminarily understood by the influence of surface diffusion and shadowing. A high deposition rate in PS-PVD on one hand reduces the surface diffusion, on the other hand may lead to enhancement of the macro-shadowing effect due to increasing surface roughness. The out-of-plane orientation is explained by the evolutionary selection: the grains have the highest crystallographic growth rate perpendicular to the surface will overgrow other grains. It was argued that the highest growth rate of a crystal plane depends on the surface energy due to the anisotropic binding energies. In case that deposition was parallel to the plasma axis, there is a micro-shadowing effect due to interaction of vapor species and plasma gas. The in-plane orientation was explained based on a mechanism proposed in ref. [113]. The directional diffusion of vapor species is an assumption in this mechanism. So the grains orientated in a specific in-plane orientation which capture more vapor species will be able to overgrow the other grains, forming a in-plane preferential orientation.

5.4.3 Effects of the boundary-layer on growth

The coatings deposited at the wedged leading edge of the substrate in the test II are shown in Fig. 5.51. It is obvious that the coating is much thicker if the average VIA is 30° . The largest coating thickness is approx. $970\ \mu\text{m}$, which is about twice of that at an average VIA of 90° . In comparison with the deposition at the average VIA of 90° with the same spraying parameters (coating C-20), one can conclude that the smaller the average VIA, the higher the deposition rate is. In a previous work [96], it has been found that the relative orientation between plasma jet and the substrate has influence on the coating microstructure and the number of unevaporated particles in the coating. The fraction of particles in the coating can be decreased by reducing the congestion of plasma in front of the substrate because the particles can flow past the substrate more easily. The same phenomenon is also found in this work. The coatings deposited on the vertical substrate contain spherical particles while almost no spherical particles are incorporated in the coatings deposited on the parallel substrate. Recently, Harder et al. reported that the impingement angle had significant effects on the deposition mode, and microscopy of coatings indicated that there was a shift in the deposition mode at approximately VIA of 90° to PVD-like growth [208].

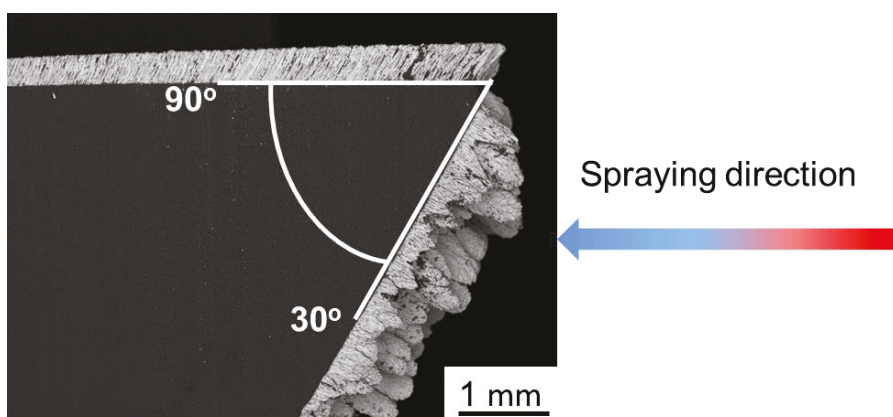


Fig. 5.51 SEM image (BSE) of the coating deposited at the leading edge in test II; average vapor incidence angles are as indicated.

Besides, the significant differences observed in coatings A, B and C is also an indication that the flow condition relative to the substrate can affect the coating's characteristics. For example, the cauliflower structure on top of the coating B, coating II-B and coating R-B containing fine crystals seems contradictory to the above analyses because it was formed where T_s was relatively high and could actually inhibit nucleation. However, the outcome is just the opposite. As mentioned in section 2.3.2,

this cauliflower structure could be an indication of cluster deposition. Cluster formation in PS-PVD is also possible as cluster formation was found in many CVD processes, in particular, PECVD where ion-induced nucleation would occur at a low nucleation barrier [133]. In the PS-PVD process, the working pressure 200 Pa is relatively higher compared to that of around 1 Pa in EB-PVD. Besides, parts of plasma gases are ionized (as discussed in chapter 4) as well as the ceramic feedstock (because singly ionized zirconium emission line Zr II, e.g. $\lambda=384.3$ nm, is discernible in the spectrum measured by OES) at high temperature, which might enable ion-induced nucleation.

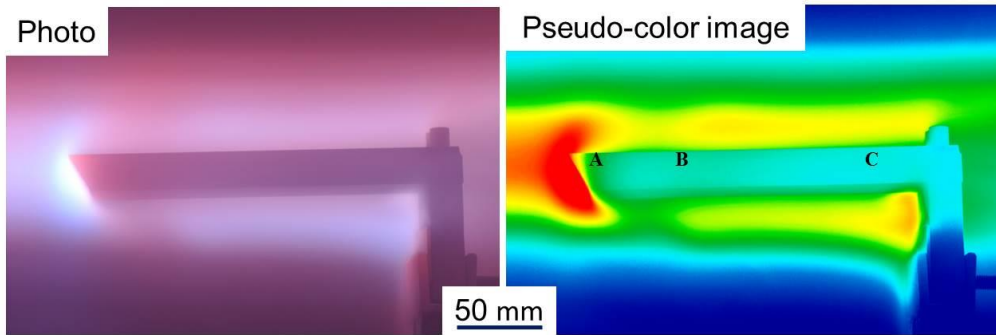


Fig. 5.52 Photo and transformed pseudo-color image of the sample during the coating process in the test I (described in section 5.3.1)

Fig. 5.52 shows the photo of a sample in test I during the coating process and its pseudo-color image. In this case, the bluish luminance is mainly caused by zirconium, and thus it represents the density of vapor deposits to some extent. Apparently, at VIA of 30° , the density of vapor deposits (as well as the pressure) is the highest case due to the stagnation of the plasma flow. This is obviously the reason of the thicker coating as shown in Fig. 5.51. At VIA of 90° , there is a zone with lower vapor density at the position between A and B. After that, the density of vapor deposits reduced gradually from B to C. It is probably the reason for the rapidly declining coating thickness from A to B and slower decrease from B to C as shown in Fig. 5.31. Under such condition, a boundary-layer is considered as in the case of a plasma jet flowing over a flat plate as illustrated in Fig. 5.53.

One can denote a boundary-layer by defining the boundary-layer thickness δ as the distance from the substrate to where the temperature (or velocity and concentration) equals to 99% of that of undisturbed plasma jet itself. The boundary-layer thickness grows from the leading edge of the substrate to the end. In order to determine whether the flow in the boundary-layer is laminar or turbulent, it is reasonable to assume that

5.4 Potential growth mechanisms

transition begins at a location x_c , which is determined by the critical Reynolds number, $Re(x_c)$. A representative value of

$$Re(x_c) = \frac{\rho u_\infty x_c}{\mu} = \frac{u_\infty x_c}{\nu} = 5 \times 10^5 \quad (5.2)$$

is often assumed for boundary-layer calculations [196], wherein, u_∞ is the velocity of the free flow; ρ is the density; μ is the dynamic viscosity; and ν is the kinematic viscosity of the fluid. Here, u_∞ is estimated approx. 1400 ms^{-1} based on ref. [96]; ν is estimated to be approx. $0.762 \text{ m}^2\text{s}^{-1}$ [209]. Then, x_c results to be approx. 272 m, which is longer than the substrate length (210 mm). In other words, the flow over the substrate is still in the laminar region.

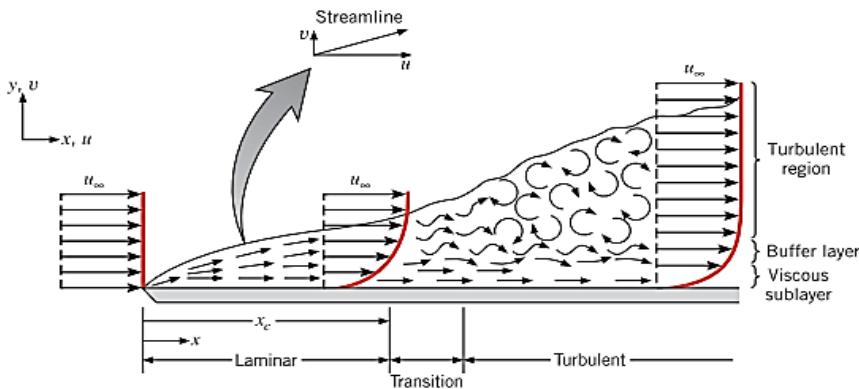


Fig. 5.53 The velocity boundary-layer on a flat plate (vertical thickness greatly exaggerated); adapted from [196]

A thermal boundary-layer is simply considered (as shown in Fig. 5.54) since the plasma jet and surface temperatures differ. Particles in contact with the substrate will be in thermal equilibrium with the substrate's surface temperature. In turn, these particles exchange energy with those in the adjoining fluid layer, and temperature gradients develop in the plasma jet. The thickness of the thermal boundary-layer δ_t is typically defined as the value of y for which the ratio $(T - T_s)/(T_\infty - T_s) = 0.99$ [196]. With increasing distance from the leading edge, the effects of heat transfer penetrate farther into the free stream and the thermal boundary-layer grows. The thickness of boundary-layer grows from leading edge to the end of the substrate, that is $\delta_A < \delta_B < \delta_C$. Before starting the coating process, the substrate temperatures at position A, B, and C increased with different heating rate, which can be seen from the slopes of the temperature curves in Fig. 5.29. The large heating rate means fast thermal exchange rate at position A while at position C the thermal exchange rate is low. In other words, the vapor species in the plasma flow have the largest temperature-gradient $(\partial T/\partial y)$ at the leading edge, and it decreases from position A to C. In addition, as noted above, the vapor concentration

probably decreases from A to C as well. Both the high cooling rate and the high vapor concentration promote super saturation ratio, and thus improve the possibility of cluster formation in the boundary-layer. Certainly, this possibility attenuates from A to C.

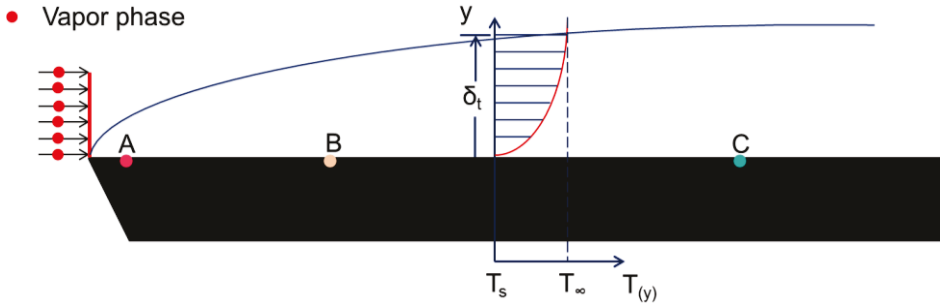


Fig. 5.54 Schematic thermal boundary-layer on the substrate surface in case the substrate parallel to the axis of the plasma jet

At spray distance of 1000 mm, the average plasma jet temperature was estimated above 4000 K (see section 4.4.1) while T_s is mainly below 1700 K depending on the spraying parameters. Assigning discrete temperatures and the chamber pressure [189, 190], the formation of cubic ZrO_2 was calculated by the CEA software to start at approx. 2700 K. Thus, it is possible that cluster formation already occurs in the boundary-layer. If it is like this, the coating microstructure and texture could be affected by the impact energy and size of these clusters. High energy cluster impacts may lead to denser coating morphologies and lower energy cluster could result in porous, granular coatings with equiaxed grain structures [139]. The mobility of the clusters strongly decreases as their size increases [128] and large clusters might favor retaining their own orientations. If there were cluster formation in the boundary-layer, the equiaxed grains can be easily interpreted by cluster deposition. In the beginning of the deposition, cluster formation can be intensive due to the large undercooling effect. With increasing T_s , the size of the clusters might gradually reduce and accordingly mobility increases. Consequently, the diffusion behavior can transform from slow-diffusion to fast-diffusion. Thus, the coating structure can transform from randomly orientated equiaxed crystals to orientated columnar crystals. Besides, with increasing temperature and coating thickness, also the surface roughness, the boundary-layer conditions can change and might shift away from the leading edge to the end of the substrate. Thus, the reason for the cauliflower structure of the coating B might be that the flow condition in the boundary-layer changed to a condition which is beneficial for formation of large clusters.

5.4 Potential growth mechanisms

When the plasma jet axis is vertical to the substrate, the boundary-layer could have a shape similar to the impingement of a gas jet on a surface in Fig. 5.55. The free jet here is the part of the plasma jet which is unaffected by the impingement surface. Within the stagnation or impingement zone, the plasma jet is influenced by the target surface. It is decelerated and accelerated in the normal (z) and transverse (r or x) directions, respectively [196]. The acceleration along x direction cannot continue due to the entrainment of ambient gas. So the accelerating flow in the impingement zone will transform into a decelerating wall jet. Here, the stagnation zone and wall jet zone can be considered as boundary-layer under such conditions. In both the stagnation and wall jet regions, heat transfer occurs due the high plasma jet temperature and low T_s . However, whether the transition of stagnation to wall jet occurs on the surface will depend not only on the size of the plasma jet but also on the geometry of the substrate.

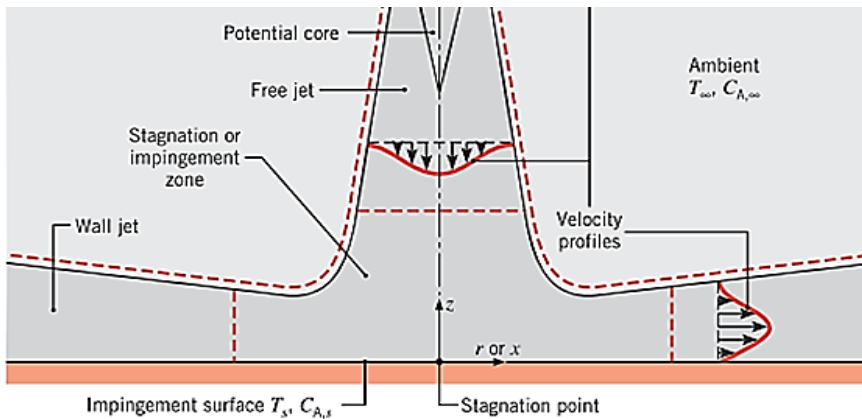


Fig. 5.55 Surface impingement of a single gas jet; Adapted from [196]

The remaining questionable phenomenon pointed in section 2.3.3 that columnar structured coating (Fig. 2.36a) and dense coating (Fig. 2.36b) were obtained in the center and 40 mm from the center of the plasma jet, respectively. It is also noteworthy that the deposition rate was approx. 700 $\mu\text{m}/\text{min}$ in the center, and reduced to 105 $\mu\text{m}/\text{min}$ at the edge [96]. Taking the extremely high T_s of ~ 2300 K into consideration, the diffusion should have been sufficient to form faceted crystals with preferential orientation. However, neither the columnar coating nor the dense coating has faceted crystals or preferred orientation [96]. These unexpected distinguish microstructures could be explained by cluster deposition. Large clusters formed in the boundary-layer could directly be congested on the center substrate producing columnar structure owing to macro-shadowing effect. Meanwhile, the smaller one could follow the gas stream (might be accelerated) to be deposited at the edge substrate forming a

dense coating (Here, either the large clusters or small clusters may not have sufficient diffusion to form faceted and orientated crystals).

5.5 Summary

In this chapter, the deposition mechanisms of columnar YSZ coating were discussed. The main conclusions can be drawn as follows:

- With increasing PFR, the efficiency of heat transfer from plasma to the powder declined gradually followed by a lower evaporation rate of the feedstock. PFR higher than 13.7 g/min can lead to deposition of nano particles. Excessive deposition of such nano particles can change the coating morphology, weaken the feather-like structure and reduce the porosity in the columns. The initial deposits from vapor phase are small faceted crystals.
- The agglomeration of feedstock M6700 by organic binder was found to be the most reasonable way for PS-PVD to achieve effective feedstock evaporation and thus vapor deposition.
- The coating growth process can be roughly divided into three stages: equiaxed growth, competitive growth, and preferential growth. Depending on the deposition conditions, these three stages have different thickness and features. In case of deposition with torch swing, the coatings have only small equiaxed crystallites which are randomly orientated.
- The potential growth mechanisms are discussed regarding to atomic (or molecular) deposition and the possibility of cluster deposition. The growth of equiaxed crystals was explained by high nucleation rate and repeated nucleation. The preferential growth can be preliminarily understood by the influence of surface diffusion and shadowing. Out-of-plane orientations along $t(011)$ or $t(002)_t(110)$ are interpreted by evolutionary selection. The in-plane orientation $t(011)$ was explained based on a mechanism assuming sufficient directional diffusion because this orientation was formed at high temperature and with a narrow VIA distribution by tilting the substrate.
- A concept of boundary-layer was introduced to illustrate the possibility of cluster deposition, and therefore to explain some specific coating microstructures, such as the cauliflower structure.

Chapter 6 Conclusions and Outlook

The deposition mechanisms of TBCs manufactured by PS-PVD were investigated in this thesis. The main results can be outlined into two parts: the first part focuses on the characterization of the plasma jets under PS-PVD conditions; the second part highlights the dependence of the microstructures and the crystallographic textures of the coatings on the processing conditions. Detailed conclusions and outlook are given as follows.

- **Plasma jet characterization**

Two different PS-PVD jets composed by Ar/He and Ar/He/H₂ were experimentally investigated. At spraying distance of 1000 mm, the integral intensities of emission lines of Ar, He, and H₂ along the line of sight were laterally measured by OES from the center to the fringe of the plasma jets. By introducing Abel inversion, the distributions of emission intensity as functions of the radial coordinates of the plasma jets were obtained. The reconstructed $\varepsilon(r)$ of Ar I was very low in the center of the plasma jet, which on one hand was due to the ionization of Ar; on the other hand this was probably caused by demixing that He prevails in the center of the plasma jet. The reconstructed $\varepsilon(r)$ distributions also enable calculations of the excitation temperature profiles applying Boltzmann plot method. From the center to the edge of the plasma jet, the local excitation temperature $T_{exc}(r)$ of Ar decreases gradually. However, apparently increasing temperatures at the outer fringe of the plasma jet were found if emission lines of He I were involved. It is suggested that, in the outer fringe region, the density of electrons is not sufficient to sustain LTE, in particular for He which is typically prone to strong deviations from LTE. A robust and simple method was proposed to estimate concentration profiles of atomic Ar/He in the plasma jet further verifying the low density of neutral Ar in the center of the plasma jet and possible demixing.

The reconstructed $\varepsilon(r)$ of the H₂ line (H β 486.1 nm) drops to 5% level of the maximum value at a rather large radius of approx. 160 mm, which clarifies the reason for the broader plasma jet appearance of Ar/He/H₂ jet in contrast to the Ar/He jet. The addition of H₂ into the plasma gas reduces the excitation temperature in the plasma jet, but leads to a relatively high substrate temperature (approx. 50 K higher than without H₂). This was found due to the dissociation of H₂, that the dissociation energy is consumed without contributing to an increase in the temperature. Also the dissociation of H₂

enhances the thermal conductivity of the plasma jet in the temperature range of 2000 K to 3000 K, which would be the reason for the higher substrate temperature.

Moreover, the average excitation temperature $T_{exc}^{(A)}$ was supposed to be representative of the average jet temperature when the feedstock powder was injected. The injection of powder feedstock into the plasma jet results in a decrease of the jet temperature, however, the overall average jet temperatures were still above 4000 K. Increasing the powder feeding rate from 13.7 g/min to 16.9 g/min, the average jet temperature did not drop further. In addition, the $\varepsilon(r)$ of Zr I line did not rise. These results indicate that the energy transfer between plasma and feedstock might reach a threshold, and using a high PFR would not enhance evaporation of feedstock. Furthermore, the overall emission intensity of the Zr I line was rather low in the Ar/He/H₂ plasma jet compared to the Ar/He case. This suggested a lower vapor concentration, which might be responsible for the low deposition rate if using Ar/He/H₂ as plasma gases.

This study on the characteristics of the plasma jets helps to understand the role of the plasma gas composition in the coating deposition. It also provides a way to further modify the spraying parameters, and accordingly to tailor the coating microstructures and properties. Beyond the scope of this work, some other properties are also interesting to be evaluated, such as the velocity and thermal transport coefficients of the plasma jet. The results in ref. [191] shows that the addition of H₂ in pure Ar plasma can increase the axial velocity of the plasma jet. Similarly, the addition of H₂ as secondary plasma gas could also increase the velocity and the impact energy of the vapor species, which might also contribute to the denser coating microstructure (Fig. 2.24b). Moreover, the departure from LTE found in this work should be investigated more in detail in the future. Finally, an intensity calibration of the OES device used in this work could allow absolute quantitative analyses of vapor concentration.

- **Deposition mechanisms of columnar structured YSZ coatings**

It was found that the efficiency of the heat transfer from plasma to the powder declined gradually with increasing PFR leading to a lower evaporation rate of the feedstock. PFR higher than 13.7 g/min can lead to an increasing deposition of nanoparticles. Excessive deposition of such nanoparticles can change the coating morphologies, weaken the feather-like structure and reduce the porosity in the columns. Therefore, a moderate PRF of 6.9 g/min was used to further investigate the vapor deposition in the remaining part of this work. The agglomeration of the primary particles by the organic binder in the feedstock powder was validated to be an effective way to achieve vapor

deposition in PS-PVD. Such binder enables on one hand, that the feedstock is not disintegrated in the feeding system; on the other hand, immediate fragmented in the nozzle.

Coatings deposited on substrates in different directions were characterized by means of microstructural and crystallographic analyses. A detailed insight of the growth process of PS-PVD coatings was gained by EBSD characterization on the crystal orientations and crystal size distributions. The coating growth process can be roughly divided into three stages: equiaxed growth, competitive growth, and preferential growth.

The equiaxed crystals were generally found to grow only at the beginning of coating growth if the torch was stationary. With torch swing, solely equiaxed crystals and very small columnar crystals (both smaller than 1 μm) were formed during the whole process. The formation of equiaxed crystals can be understood suggesting a high nucleation rate induced by a large undercooling effect. Initially, the equiaxed crystals are randomly orientated. With increasing the coating thickness (increasing T_s if the torch doesn't swing), the driving force of nucleation will decrease with reduced undercooling and the atomic diffusion gets faster. Consequently, nucleation is assumed to be inhibited and newly deposited atoms will predominantly join existing nucleation sites contributing to crystal growth. Therefore, the crystals transform from equiaxed to columnar shaped, and to preferential growth gradually. In contrast, the torch swing during coating process can cause relatively low T_s and an interruption of crystal growth, inducing repeated nucleation and continuous formation of equiaxed crystals.

The mechanisms of the preferential growth were preliminarily discussed based on the influence of diffusion and shadowing. The diffusion of deposited species on the growing surface is principally related to T_s and the deposition rate. Shadowing is mainly determined by vapor incidence angle and the deposition rate. High T_s can enhance the diffusion of the deposited species. Nevertheless, the diffusion can be ceased by subsequently arriving deposits in case of a high deposition rate although deposited species principally could diffuse to find a stable site or crystal plane. Moreover, a high deposition rate can cause a rough surface intensifying macro-shadowing effect. Large vapor incidence angles can magnify the micro-shadowing effect. Both of diffusion and shadowing contribute to the coatings' microstructures and textures. Then, the relatively high deposition rate should be a main reason for the rare preferential growth in the PS-PVD coatings compared with conventional PVD or CVD processes. Strong out-of-plane orientation was explained by a theory of evolutionary selection if diffusion for vapor species is sufficient from grains

to grains. In tetragonal zirconia, the surface energy of crystal planes are in an order of $(002) > (010) > (011) > (110)$. With increasing T_s , the evolution of the preferred out-of-plane orientation from $t(110)$ to $t(002)$ indicates that high T_s promotes orientation with high-surface-energy. This might be due to improved condensation rate on crystal plane (002) at high temperature. The observed typical pyramidal shaped column top in tetragonal zirconia is capped by four (011) crystal planes with a tip orientation along $\langle 001 \rangle$. In-plane orientation was only found in the case of deposition at the highest VIA (90°) and high T_s . This reveals that an in-plane evolutionary selection can be impelled by a micro-shadowing effect.

Finally, the flow conditions in the boundary-layer over the substrate surface can influence the coating growth. It is highly possible that clusters form in the boundary-layer due to enormous gradients of temperature, velocity, and vapor concentration. The cauliflower structures were interpreted by cluster deposition considering the changing of the flow conditions.

Although the understanding of the deposition mechanisms of columnar YSZ coatings has been improved with the findings in this work, further investigations to establish closer relationships among the processing conditions, coating properties, e.g. porosity, thermal conductivity, and the coating performance e.g. thermal cycling lifetime, are still required. The calculation of supersaturation and nucleation rate (vapor concentration) at different flow conditions could be also interesting to learn more about cluster formation. Furthermore, the velocity of the vapor particles and its impact on coating microstructures could lead to a deeper understanding of the deposition mechanisms in PS-PVD.

Reference

- [1] D. R. Clarke, M. Oechsner, N. P. Padture, Thermal-barrier coatings for more efficient gas-turbine engines. *MRS Bulletin* **37**, 891-898 (2012).
- [2] L. Chen, Yttria-stabilized zirconia thermal barrier coatings - a review. *Surface Review and Letters* **13**, 535-544 (2006).
- [3] K. von Niessen, M. Gindrat, A. Refke, Vapor phase deposition using plasma Spray-PVD. *Journal of thermal spray technology* **19**, 502-509 (2010).
- [4] S. Rezanka, G. Mauer, R. Vaßen, Improved thermal cycling durability of thermal barrier coatings manufactured by PS-PVD. *Journal of Thermal Spray Technology* **23**, 182-189 (2014).
- [5] S. Rezanka, D. E. Mack, G. Mauer, D. Sebold, O. Guillon, R. Vaßen, Investigation of the resistance of open-column-structured PS-PVD TBCs to erosive and high-temperature corrosive attack. *Surface and Coatings Technology* **324**, 222-235 (2017).
- [6] K. von Niessen, M. Gindrat, Plasma spray-PVD: a new thermal spray process to deposit out of the vapor phase. *Journal of Thermal Spray Technology* **20**, 736-743 (2011).
- [7] J. A. Thornton, The microstructure of sputter-deposited coatings. *Journal of Vacuum Science & Technology A* **4**, 3059-3065 (1986).
- [8] G. Mauer, A. Hospach, R. Vaßen, Process conditions and microstructures of ceramic coatings by gas phase deposition based on plasma spraying. *Surface and Coatings Technology* **220**, 219-224 (2013).
- [9] F. J. Brooks, GE gas turbine performance characteristics. (GE Power Systems, Schenectady, NY, 2000).
- [10] J. H. Perepezko, The hotter the engine, the better. *Science* **326**, 1068-1069 (2009).
- [11] S. Stecura, Two-layer thermal barrier coating for turbine airfoils-furnace and burner rig test results. (NASA Lewis Research Center, Cleveland, OH, United States, 1976).
- [12] C. H. Liebert, R. E. Jacobs, S. Stecura, C. R. Morse, Durability of zirconia thermal-barrier ceramic coatings on air-cooled turbine blades in cyclic jet engine operation. (NASA Lewis Research Center, Cleveland, OH, United States, 1976).
- [13] N. P. Padture, M. Gell, E. H. Jordan, Thermal barrier coatings for gas-turbine engine applications. *Science* **296**, 280-284 (2002).
- [14] D. Furrer, H. Fecht, Ni-based superalloys for turbine discs. *Journal of Metals* **51**, 14-17 (1999).
- [15] K.-M. Chang, M. Henry, M. Benz, Metallurgical control of fatigue crack propagation in superalloys. *Journal of Metals* **42**, 29-35 (1990).
- [16] T. M. Pollock, S. Tin, Nickel-based superalloys for advanced turbine engines: chemistry, microstructure and properties. *Journal of propulsion and power* **22**, 361-374 (2006).

- [17] M. Konter, M. Thumann, Materials and manufacturing of advanced industrial gas turbine components. *Journal of Materials Processing Technology* **117**, 386-390 (2001).
- [18] M. Gell, D. N. Duhal, D. K. Gupta, K. D. Sheffler, Advanced superalloy airfoils. *Journal of the Metals* **39**, 11-15 (1987).
- [19] P. Baldus, M. Jansen, D. Sporn, Ceramic fibers for matrix composites in high-temperature engine applications. *Science* **285**, 699-703 (1999).
- [20] K. K. Chawla, in *Composite Materials: Science and Engineering*. (Springer New York, New York, NY, 1998), pp. 212-251.
- [21] H. E. Eaton, G. D. Linsey, Accelerated oxidation of SiC CMC's by water vapor and protection via environmental barrier coating approach. *Journal of the European Ceramic Society* **22**, 2741-2747 (2002).
- [22] H. Ohnabe, S. Masaki, M. Onozuka, K. Miyahara, T. Sasa, Potential application of ceramic matrix composites to aero-engine components. *Composites Part A: Applied Science and Manufacturing* **30**, 489-496 (1999).
- [23] N. Eswara Prasad, A. Kumar, J. Subramanyam, in *Aerospace Materials and Material Technologies : Volume 1: Aerospace Materials*. N. E. Prasad, R. J. H. Wanhill, Eds. (Springer Singapore, Singapore, 2017), pp. 371-389.
- [24] R. Vaßen, M. O. Jarligo, T. Steinke, D. E. Mack, D. Stöver, Overview on advanced thermal barrier coatings. *Surface and Coatings Technology* **205**, 938-942 (2010).
- [25] Y. Zhang, W. Y. Lee, J. A. Haynes, I. G. Wright, K. M. Cooley, P. K. Liaw, Synthesis and cyclic oxidation behavior of a (Ni, Pt) Al coating on a desulfurized Ni-base superalloy. *Metallurgical and Materials Transactions A* **30**, 2679-2687 (1999).
- [26] A. Feuerstein, J. Knapp, T. Taylor, A. Ashary, A. Bolcavage, N. Hitchman, Technical and economical aspects of current thermal barrier coating systems for gas turbine engines by thermal spray and EB-PVD: a review. *Journal of Thermal Spray Technology* **17**, 199-213 (2008).
- [27] J. He, H. Guo, H. Peng, S. Gong, Microstructural, mechanical and oxidation features of NiCoCrAlY coating produced by plasma activated EB-PVD. *Applied Surface Science* **274**, 144-150 (2013).
- [28] W. R. Chen, X. Wu, B. R. Marple, D. R. Nagy, P. C. Patnaik, TGO growth behaviour in TBCs with APS and HVOF bond coats. *Surface and Coatings Technology* **202**, 2677-2683 (2008).
- [29] W. R. Chen, X. Wu, B. R. Marple, R. S. Lima, P. C. Patnaik, Pre-oxidation and TGO growth behaviour of an air-plasma-sprayed thermal barrier coating. *Surface and Coatings Technology* **202**, 3787-3796 (2008).
- [30] M. Matsumoto, T. Kato, K. Hayakawa, N. Yamaguchi, S. Kitaoka, H. Matsubara, The effect of pre-oxidation atmosphere on the durability of EB-PVD thermal barrier coatings with CoNiCrAlY bond coats. *Surface and Coatings Technology* **202**, 2743-2748 (2008).
- [31] W. Sloof, T. Nijdam, On the high-temperature oxidation of MCrAlY coatings. *International Journal of Materials Research* **100**, 1318-1330 (2009).

- [32] J. Smeggil, A. Shuskus, The oxidation behavior of CoCrAlY, CoCrAl and yttrium-implanted CoCrAl alloys compared and contrasted. *Surface and Coatings Technology* **32**, 57-68 (1987).
- [33] C. U. Hardwicke, Y.-C. Lau, Advances in thermal spray coatings for gas turbines and energy generation: a review. *Journal of Thermal Spray Technology* **22**, 564-576 (2013).
- [34] B. A. Pint, Optimization of reactive-element additions to improve oxidation performance of alumina-forming alloys. *Journal of the American Ceramic Society* **86**, 686-695 (2003).
- [35] J. Nicholls, Advances in coating design for high-performance gas turbines. *MRS bulletin* **28**, 659-670 (2003).
- [36] B. A. Pint, I. G. Wright, W. Y. Lee, Y. Zhang, K. Prübner, K. B. Alexander, Substrate and bond coat compositions: factors affecting alumina scale adhesion. *Materials Science and Engineering: A* **245**, 201-211 (1998).
- [37] R. C. Garvie, R. H. Hannink, R. T. Pascoe, Ceramic steel? *Nature* **258**, 703-704 (1975).
- [38] M. Peters, C. Leyens, U. Schulz, W. A. Kaysser, EB-PVD thermal barrier coatings for aeroengines and gas turbines. *Advanced Engineering Materials* **3**, 193-204 (2001).
- [39] T. E. Strangman, Thermal barrier coatings for turbine airfoils. *Thin Solid Films* **127**, 93-106 (1985).
- [40] R. A. Miller, Thermal barrier coatings for aircraft engines: history and directions. *Journal of Thermal Spray Technology* **6**, 35-42 (1997).
- [41] H. G. Scott, Phase relationships in the zirconia-yttria system. *Journal of Materials Science* **10**, 1527-1535 (1975).
- [42] J. W. Fergus, Electrolytes for solid oxide fuel cells. *Journal of Power Sources* **162**, 30-40 (2006).
- [43] R. Stevens, Zirconia and zirconia ceramics. (*Magnesium Elektron Limited*, Litho 2000, Twickenham, United Kingdom, 1986).
- [44] R. A. Miller, J. L. Smialek, R. G. Garlick, Phase stability in plasma-sprayed, partially stabilized zirconia-yttria. (NASA Lewis Research Center; Cleveland, OH, United States 1981).
- [45] G. Witz, V. Shklover, W. Steurer, S. Bachegowda, H. P. Bossmann, Phase evolution in yttria-stabilized zirconia thermal barrier coatings studied by rietveld refinement of X-ray powder diffraction patterns. *Journal of the American Ceramic Society* **90**, 2935-2940 (2007).
- [46] K. Muraleedharan, J. Subrahmanyam, S. B. Bhaduri, Identification of t' Phase in ZrO_2 -7.5 wt% Y_2O_3 Thermal-Barrier Coatings. *Journal of the American Ceramic Society* **71**, C-226-227 (1988).
- [47] J. Brandon, R. Taylor, Phase stability of zirconia-based thermal barrier coatings part I. Zirconia-yttria alloys. *Surface and Coatings Technology* **46**, 75-90 (1991).
- [48] C. Viazzi, J.-P. Bonino, F. Ansart, A. Barnabé, Structural study of metastable tetragonal YSZ powders produced via a sol-gel route. *Journal of Alloys and Compounds* **452**, 377-383 (2008).

- [49] K. H. Stern, Metallurgical and ceramic protective coatings. (*Springer Netherlands*, Chapman & Hall, 2-6 Boundary Row, London SE1 8HN, UK 1996).
- [50] D. Hasselman, L. F. Johnson, L. D. Bentsen, R. Syed, H. L. Lee, M. V. Swain, Thermal diffusivity and conductivity of dense polycrystalline ZrO₂ ceramics: a survey. *American Ceramic Society Bulletin* **66**, 799-806 (1987).
- [51] A. V. Virkar, Role of ferroelasticity in toughening of zirconia ceramics. *Key Engineering Materials* **153-154**, 183-210 (1998).
- [52] C. Mercer, J. Williams, D. Clarke, A. Evans, On a ferroelastic mechanism governing the toughness of metastable tetragonal-prime (t') yttria-stabilized zirconia. *Proceedings of the Royal Society of London A: Mathematical, Physical and Engineering Sciences* **463**, 1393-1408 (2007).
- [53] X. Q. Cao, R. Vaßen, D. Stöver, Ceramic materials for thermal barrier coatings. *Journal of the European Ceramic Society* **24**, 1-10 (2004).
- [54] D. Stöver, G. Pracht, H. Lehmann, M. Dietrich, J.-E. Döring, R. Vaßen, New material concepts for the next generation of plasma-sprayed thermal barrier coatings. *Journal of Thermal Spray Technology* **13**, 76-83 (2004).
- [55] R. Vaßen, F. Traeger, D. Stöver, New thermal barrier coatings based on pyrochlore/YSZ double-layer systems. *International Journal of Applied Ceramic Technology* **1**, 351-361 (2004).
- [56] E. Bakan, D. E. Mack, G. Mauer, R. Vaßen, Gadolinium zirconate/YSZ Thermal barrier coatings: plasma spraying, microstructure, and thermal cycling Behavior. *Journal of the American Ceramic Society* **97**, 4045-4051 (2014).
- [57] R. Vaßen, N. Czech, W. Mallener, W. Stamm, D. Stöver, Influence of impurity content and porosity of plasma-sprayed yttria-stabilized zirconia layers on the sintering behaviour. *Surface and Coatings Technology* **141**, 135-140 (2001).
- [58] P. Fauchais, M. Vardelle, A. Vardelle, Reliability of plasma-sprayed coatings: monitoring the plasma spray process and improving the quality of coatings. *Journal of Physics D: Applied Physics* **46**, 224016 (2013).
- [59] H. Herman, Plasma-sprayed coatings. *Scientific American* **259**, 112-117 (1988).
- [60] D. Thirumalaikumarasamy, K. Shanmugam, V. Balasubramanian, Influences of atmospheric plasma spraying parameters on the porosity level of alumina coating on AZ31B magnesium alloy using response surface methodology. *Progress in Natural Science: Materials International* **22**, 468-479 (2012).
- [61] H. B. Guo, R. Vaßen, D. Stöver, Atmospheric plasma sprayed thick thermal barrier coatings with high segmentation crack density. *Surface and Coatings Technology* **186**, 353-363 (2004).
- [62] H.-D. Steffens, Z. Babiak, M. Gramlich, Some aspects of thick thermal barrier coating lifetime prolongation. *Journal of Thermal Spray Technology* **8**, 517-522 (1999).
- [63] M. Karger, R. Vaßen, D. Stöver, Atmospheric plasma sprayed thermal barrier coatings with high segmentation crack densities: Spraying process, microstructure and thermal cycling behavior. *Surface and Coatings Technology* **206**, 16-23 (2011).

- [64] S. G. Terry, J. R. Litty, C. G. Levi, Evolution of porosity and texture in thermal barrier coatings grown by EB-PVD. *Elevated temperature coatings: science and technology III*, 13-25 (1999).
- [65] U. Schulz, S. Terry, C. Levi, Microstructure and texture of EB-PVD TBCs grown under different rotation modes. *Materials Science and Engineering: A* **360**, 319-329 (2003).
- [66] U. Schulz, B. Saruhan, K. Fritscher, C. Leyens, Review on advanced EB-PVD ceramic topcoats for TBC applications. *International journal of applied ceramic technology* **1**, 302-315 (2004).
- [67] K. An, K. S. Ravichandran, R. E. Dutton, S. Semiatin, Microstructure, texture, and thermal conductivity of single-layer and multilayer thermal barrier coatings of Y₂O₃-stabilized ZrO₂ and Al₂O₃ made by physical vapor deposition. *Journal of the American Ceramic Society* **82**, 399-406 (1999).
- [68] U. Schulz, K. Fritscher, H.-J. Rätzer-Scheibe, W. A. Kaysser, M. Peters, Thermocyclic behaviour of microstructurally modified EB-PVD thermal barrier coatings. *Materials science forum* **251-254**, 957-964 (1997).
- [69] J. Singh, D. E. Wolfe, Review Nano and macro-structured component fabrication by electron beam-physical vapor deposition (EB-PVD). *Journal of Materials Science* **40**, 1-26 (2005).
- [70] B.-K. Jang, H. Matsubara, Microstructure of nanoporous yttria-stabilized zirconia films fabricated by EB-PVD. *Journal of the European Ceramic Society* **26**, 1585-1590 (2006).
- [71] O. Unal, T. E. Mitchell, A. H. Heuer, Microstructures of Y₂O₃-stabilized ZrO₂ electron beam-physical vapor deposition coatings on Ni-base superalloys. *Journal of the American Ceramic Society* **77**, 984-992 (1994).
- [72] A. A. Kulkarni, H. Herman, J. Almer, U. Lienert, D. Haeffner, J. Ilavsky, S. Fang, P. Lawton, Depth-resolved porosity investigation of EB-PVD thermal barrier coatings using high-energy X-rays. *Journal of the American Ceramic Society* **87**, 268-274 (2004).
- [73] J. R. Nicholls, K. J. Lawson, A. Johnstone, D. S. Rickerby, Methods to reduce the thermal conductivity of EB-PVD TBCs. *Surface and Coatings Technology* **151-152**, 383-391 (2002).
- [74] B. Saruhan, P. Francois, K. Fritscher, U. Schulz, EB-PVD processing of pyrochlore-structured La₂Zr₂O₇-based TBCs. *Surface and Coatings technology* **182**, 175-183 (2004).
- [75] M. P. Borom, C. A. Johnson, L. A. Peluso, Role of environment deposits and operating surface temperature in spallation of air plasma sprayed thermal barrier coatings. *Surface and Coatings Technology* **86**, 116-126 (1996).
- [76] C. Mercer, S. Faulhaber, A. G. Evans, R. Darolia, A delamination mechanism for thermal barrier coatings subject to calcium–magnesium–alumino-silicate (CMAS) infiltration. *Acta Materialia* **53**, 1029-1039 (2005).
- [77] K. Wada, N. Yamaguchi, H. Matsubara, Crystallographic texture evolution in ZrO₂-Y₂O₃ layers produced by electron beam physical vapor deposition. *Surface and Coatings Technology* **184**, 55-62 (2004).

- [78] Y. H. Sohn, R. R. Biederman, R. D. Sisson, Microstructural development in physical vapour-deposited partially stabilized zirconia thermal barrier coatings. *Thin Solid Films* **250**, 1-7 (1994).
- [79] U. Schulz, H. Oettel, W. Bunk, Texture of EB-PVD thermal barrier coatings under variable deposition conditions. *Zeitschrift für Metallkunde* **87**, 488-492 (1996).
- [80] U. Schulz, M. Schmücker, Microstructure of ZrO₂ thermal barrier coatings applied by EB-PVD. *Materials Science and Engineering: A* **276**, 1-8 (2000).
- [81] P. Heydt, C. Luo, D. R. Clarke, Crystallographic texture and thermal conductivity of zirconia thermal barrier coatings deposited on different substrates. *Journal of the American Ceramic Society* **84**, 1539-1544 (2001).
- [82] K. Wada, N. Yamaguchi, H. Matsubara, Effect of substrate rotation on texture evolution in ZrO₂-4 mol.% Y₂O₃ layers fabricated by EB-PVD. *Surface and coatings technology* **191**, 367-374 (2005).
- [83] H. Zhao, F. Yu, T. D. Bennett, H. N. Wadley, Morphology and thermal conductivity of yttria-stabilized zirconia coatings. *Acta Materialia* **54**, 5195-5207 (2006).
- [84] H. Kassner, R. Siegert, D. Hathiramani, R. Vassen, D. Stöver, Application of suspension plasma spraying (SPS) for manufacture of ceramic coatings. *Journal of Thermal Spray Technology* **17**, 115-123 (2008).
- [85] R. Vaßen, H. Kaßner, G. Mauer, D. Stöver, Suspension plasma spraying: process characteristics and applications. *Journal of Thermal Spray Technology* **19**, 219-225 (2010).
- [86] A. Guignard, G. Mauer, R. Vaßen, D. Stöver, Deposition and characteristics of submicrometer-structured thermal barrier coatings by suspension plasma spraying. *Journal of Thermal Spray Technology* **21**, 416-424 (2012).
- [87] A. Ganvir, C. Kumara, M. Gupta, P. Nylen, Thermal conductivity in suspension sprayed thermal barrier coatings: Modeling and experiments. *Journal of Thermal Spray Technology* **26**, 71-82 (2017).
- [88] J. R. Vargas Garcia, T. Goto, Thermal barrier coatings produced by chemical vapor deposition. *Science and Technology of Advanced Materials* **4**, 397-402 (2003).
- [89] B. Préaucht, S. Drawin, Properties of PECVD-deposited thermal barrier coatings. *Surface and Coatings Technology* **142-144**, 835-842 (2001).
- [90] T. Goto, Thermal barrier coatings deposited by laser CVD. *Surface and Coatings Technology* **198**, 367-371 (2005).
- [91] T. Kimura, T. Goto, Rapid synthesis of yttria-stabilized zirconia films by laser chemical vapor deposition. *Materials Transactions* **44**, 421-424 (2003).
- [92] G. Mauer, A. Hospach, N. Zotov, R. Vaßen, Process development and coating characteristics of plasma spray-PVD. *Journal of Thermal Spray Technology* **22**, 83-89 (2013).
- [93] A. Hospach, G. Mauer, R. Vaßen, D. Stöver, Columnar-structured thermal barrier coatings (TBCs) by thin film low-pressure plasma spraying (LPPS-TF). *Journal of Thermal Spray Technology* **20**, 116-120 (2011).

- [94] K. von Niessen, M. Gindrat, A. Refke, Vapor Phase Deposition Using Plasma Spray-PVD (TM). *Journal of Thermal Spray Technology* **19**, 502-509 (2010).
- [95] G. Mauer, R. Vaßen, D. Stöver, Thin and dense ceramic coatings by plasma spraying at very low pressure. *Journal of Thermal Spray Technology* **19**, 495-501 (2010).
- [96] A. Hospach, Ph.D. Dissertation, Untersuchung zum Thin Film Low Pressure Plasma Spraying (LPPS-TF) Prozess, *Ruhr-Universität Bochum*, Forschungszentrum Jülich GmbH (2012).
- [97] G. Mauer, Plasma characteristics and plasma-feedstock interaction under PS-PVD process conditions. *Plasma Chemistry and Plasma Processing* **34**, 1171-1186 (2014).
- [98] X. Chen, P. He, Heat transfer from a rarefied plasma flow to a metallic or nonmetallic particle. *Plasma Chemistry and Plasma Processing* **6**, 313-333 (1986).
- [99] X. Chen, The drag force acting on a spherical non-evaporating or evaporating particle immersed into a rarefied plasma flow. *Journal of Physics D: Applied Physics* **29**, 995-1005 (1996).
- [100] J. L. Dorier, M. Gindrat, C. Hollenstein, M. Loch, A. Refke, A. Salito, G. Barbezat, Plasma jet properties in a new spraying process at low pressure for large area thin film deposition. *International Thermal Spray Conference*, Singapore, 2001.
- [101] M. Gindrat, R. Wäger, G. Mauer, W. He, Numerical modelling of a vacuum plasma spraying torch used for plasma spray physical vapor deposition. *Thermal Spray Bulletin* **9**, 148-156 (2017).
- [102] W. He, G. Mauer, M. Gindrat, R. Wäger, R. Vaßen, Investigations on the nature of ceramic deposits in plasma spray–physical vapor deposition. *Journal of Thermal Spray Technology* **26**, 83-92 (2017).
- [103] G. Mauer, R. Vaßen, Plasma spray-PVD: plasma characteristics and impact on coating properties. *Journal of Physics: Conference Series* **406**, 012005 (2012).
- [104] G. Mauer, M. O. Jarligo, S.Rezanka, A. Hospach, R. Vaßen, Novel opportunities for thermal spray by PS-PVD. *Surface & Coatings Technology* **268**, 52-57 (2015).
- [105] L. Gao, H. Guo, L. Wei, C. Li, H. Xu, Microstructure, thermal conductivity and thermal cycling behavior of thermal barrier coatings prepared by plasma spray physical vapor deposition. *Surface and Coatings Technology* **276**, 424-430 (2015).
- [106] J. A. Venables, G. D. T. Spiller, M. Hanbucken, Nucleation and growth of thin films. *Reports on Progress in Physics* **47**, 399 (1984).
- [107] N. Kaiser, Review of the fundamentals of thin-film growth. *Applied Optics* **41**, 3053-3060 (2002).
- [108] C. Ratsch, J. Venables, Nucleation theory and the early stages of thin film growth. *Journal of Vacuum Science & Technology A: Vacuum, Surfaces, and Films* **21**, S96-S109 (2003).
- [109] I. Petrov, P. Barna, L. Hultman, J. Greene, Microstructural evolution during film growth. *Journal of Vacuum Science & Technology A: Vacuum, Surfaces, and Films* **21**, S117-S128 (2003).

- [110] K. Oura, V. G. Lifshits, A. A. Saranin, A. V. Zotov, M. Katayama, in *Surface Science. (Springer-Verlag Berlin Heidelberg, Berlin, 2003)*, pp. 295-323.
- [111] S. Mahieu, Ph.D. Dissertation, Biaxial alignment in sputter deposited thin films, *Gent University*, (2006).
- [112] K. Oura, V. G. Lifshits, A. A. Saranin, A. V. Zotov, M. Katayama, in *Surface Science. (Springer-Verlag Berlin Heidelberg, Berlin, 2003)*, pp. 325-356.
- [113] S. Mahieu, P. Ghekiere, D. Depla, R. De Gryse, Biaxial alignment in sputter deposited thin films. *Thin Solid Films* **515**, 1229-1249 (2006).
- [114] Z. Zhang, M. G. Lagally, Atomistic processes in the early stages of thin-film growth. *Science* **276**, 377-383 (1997).
- [115] B. Movchan, A. Demchishin, Study of structure and properties of thick vacuum condensates of nickel, titanium, tungsten, aluminium oxide and zirconium dioxide. *Fiz. Metal. Metalloved* **28**, 653-660 (1969).
- [116] J. A. Thornton, Influence of apparatus geometry and deposition conditions on the structure and topography of thick sputtered coatings. *Journal of Vacuum Science & Technology* **11**, 666-670 (1974).
- [117] J. A. Thornton, High rate thick film growth. *Annual review of materials science* **7**, 239-260 (1977).
- [118] E. Bauer, Fiber texture. *The Ninth National Vacuum Symposium of the American Vacuum Society*, Statler Hilton Hotel, Los Angeles, California, 1962.
- [119] A. Van der Drift, Evolutionary selection, a principle governing growth orientation in vapour-deposited layers. *Philips Res. Rep* **22**, 267-288 (1967).
- [120] C. Wild, N. Herres, P. Koidl, Texture formation in polycrystalline diamond films. *Journal of applied physics* **68**, 973-978 (1990).
- [121] P. B. Barna, M. Adamik, in *Science and technology of thin films*. F. C. Maticcotta, G. Ottaviani, Eds. (*World Scientific Publishing Co. Pte. Ltd.*, Singapore, 1995), pp. 1-28.
- [122] I. Yamada, H. Usui, T. Takagi, Formation mechanism of large clusters from vaporized solid material. *Journal of physical chemistry* **91**, 2463-2468 (1987).
- [123] P. Jensen *et al.*, in *Nanoclusters and Nanocrystals*. H. S. Nalwa, Ed. (*American Scientific Publishers*, 2003) chap. 4.
- [124] O. F. Hagena, W. Obert, Cluster formation in expanding supersonic jets: effect of pressure, temperature, nozzle size, and test gas. *The Journal of Chemical Physics* **56**, 1793-1802 (1972).
- [125] H. Usui, M. Tanaka, I. Yamada, T. Takagi, Size estimation of vaporized-metal clusters by electron microscope. *Nuclear Instruments and Methods in Physics Research Section B: Beam Interactions with Materials and Atoms* **37**, 886-890 (1989).
- [126] G. Fuchs, M. Treilleux, F. S. Aires, B. Cabaud, P. Melinon, A. Hoareau, Cluster-beam deposition for high-quality thin films. *Physical Review A* **40**, 6128-6129 (1989).
- [127] G. Fuchs, P. Melinon, F. S. Aires, M. Treilleux, B. Cabaud, A. Hoareau, Cluster-beam deposition of thin metallic antimony films: Cluster-size and deposition-rate effects. *Physical Review B* **44**, 3926-3933 (1991).

- [128] P. Melinon, P. Jensen, J. X. Hu, A. Hoareau, B. Cabaud, M. Treilleux, D. Guillot, Comparison of molecular and cluster deposition: Evidence of different percolation processes. *Physical Review B* **44**, 12 562-512 564 (1991).
- [129] S.-C. Lee, B. Yu, D.-Y. Kim, N. M. Hwang, Effects of cluster size and substrate temperature on the homoepitaxial deposition of Au clusters. *Journal of crystal growth* **242**, 463-470 (2002).
- [130] H. Haberland, Z. Insepov, M. Moseler, Molecular-dynamics simulation of thin-film growth by energetic cluster impact. *Physical Review B* **51**, 11 061-011 067 (1995).
- [131] P. Han, T. Yoshida, Growth and transport of clusters in thermal plasma vapor deposition of silicon. *Journal of applied physics* **92**, 4772-4778 (2002).
- [132] T. Kim, S. Suh, S. Girshick, M. Zachariah, P. McMurry, R. Rassel, Z. Shen, S. Campbell, Particle formation during low-pressure chemical vapor deposition from silane and oxygen: Measurement, modeling, and film properties. *Journal of Vacuum Science & Technology A* **20**, 413-423 (2002).
- [133] P. Roca i Cabarocas, Plasma enhanced chemical vapor deposition of silicon thin films for large area electronics. *Current Opinion in Solid State and Materials Science* **6**, 439-444 (2002).
- [134] S. L. Girshick, C.-P. Chiu, Homogeneous nucleation of particles from the vapor phase in thermal plasma synthesis. *Plasma Chemistry and Plasma Processing* **9**, 355-369 (1989).
- [135] S. L. Girshick, Particle nucleation and growth in thermal plasmas. *Plasma Sources Science and Technology* **3**, 388-394 (1994).
- [136] X. Wang, J. Hafiz, R. Mukherjee, T. Renault, J. Heberlein, S. Girshick, P. McMurry, System for in situ characterization of nanoparticles synthesized in a thermal plasma process. *Plasma Chemistry and Plasma Processing* **25**, 439-453 (2005).
- [137] N. Rao, S. Girshick, J. Heberlein, P. McMurry, S. Jones, D. Hansen, B. Micheel, Nanoparticle formation using a plasma expansion process. *Plasma Chemistry and Plasma Processing* **15**, 581-606 (1995).
- [138] S. L. Girshick, S. J. Warthesen, Nanoparticles and plasmas. *Pure and applied chemistry* **78**, 1109-1116 (2006).
- [139] D. D. Hass, H. N. G. Wadley, Gas jet assisted vapor deposition of yttria stabilized zirconia. *Journal of Vacuum Science & Technology A: Vacuum, Surfaces, and Films* **27**, 404-414 (2009).
- [140] H. Nong-Moon, L. Dong-Kwon, Charged nanoparticles in thin film and nanostructure growth by chemical vapour deposition. *Journal of Physics D: Applied Physics* **43**, 483001 (2010).
- [141] N. M. Hwang, J. H. Hahn, D. Y. Yoon, Charged cluster model in the low pressure synthesis of diamond. *Journal of Crystal Growth* **162**, 55-68 (1996).
- [142] H. Fujita, Atom clusters-new applications of high-voltage electron microscopy "micro-laboratory" to materials science. *Ultramicroscopy* **39**, 369-381 (1991).
- [143] I.-D. Jeon, L. Gueroudji, D.-Y. Kim, N.-M. Hwang, Temperature dependence of the deposition behavior of yttria-stabilized zirconia CVD films: approach by

- charged cluster model. *Journal of the Korean Ceramic Society* **38**, 218-224 (2001).
- [144] I. D. Jeon, L. Gueroudji, N. M. Hwang, Deposition of Yttria stabilized zirconia by the thermal CVD process. *The Korean Journal of Ceramic* **5**, 131-136 (1999).
- [145] N. M. Hwang, Crystal growth by charged cluster focused on CVD diamond process. *Journal of Crystal Growth* **198/199**, 945-950 (1999).
- [146] L. Gao, L. Wei, H. Guo, S. Gong, H. Xu, Deposition mechanisms of yttria-stabilized zirconia coatings during plasma spray physical vapor deposition. *Ceramics International* **42**, 5530-5536 (2016).
- [147] X. Zhang, K. Zhou, C. Deng, M. Liu, Z. Deng, C. Deng, J. Song, Gas-deposition mechanisms of 7YSZ coating based on plasma spray-physical vapor deposition. *Journal of the European Ceramic Society* **36**, 697-703 (2016).
- [148] A. Hospach, G. Mauer, R. Vaßen, D. Stöver, Characteristics of ceramic coatings made by thin film low pressure plasma spraying (LPPS-TF). *Journal of Thermal Spray Technology* **21**, 435-440 (2012).
- [149] C. Li, H. Guo, L. Gao, L. Wei, S. Gong, H. Xu, Microstructures of yttria-stabilized zirconia coatings by plasma spray-physical vapor deposition. *Journal of Thermal Spray Technology* **24**, 534-541 (2015).
- [150] S. Rezanka, Ph.D. Dissertation, Abscheidung von Wärmedämmschichtsystemen mit dem Plasma Spray-Physical Vapor Deposition- (PS-PVD-) Prozess - Untersuchung des Prozesses und der hergestellten Schichten, *Ruhr-Universität Bochum*, Forschungszentrum Jülich GmbH (2015).
- [151] G. Mauer, J.-L. Marqués-López, R. Vaßen, D. Stöver, Detection of wear in one-cathode plasma torch electrodes and its impact on velocity and temperature of injected particles. *Journal of Thermal Spray Technology* **16**, 933-939 (2007).
- [152] G. Mauer, R. Vaßen, D. Stöver, Plasma and particle temperature measurements in thermal spray: approaches and applications. *Journal of Thermal Spray Technology* **20**, 391-406 (2011).
- [153] A. Kramida, Y. Ralchenko, J. Reader, a. N. A. Team, NIST Atomic Spectra Database (version 5.3), (2015) Available: <http://physics.nist.gov/asd> (Accessed date: 10 November 2015).
- [154] M. Calzada, M. Moisan, A. Gamero, A. Sola, Experimental investigation and characterization of the departure from local thermodynamic equilibrium along a surface-wave-sustained discharge at atmospheric pressure. *Journal of applied physics* **80**, 46-55 (1996).
- [155] J. A. M. van der Mullen, Excitation equilibria in plasmas; a classification. *Physics Reports* **191**, 109-220 (1990).
- [156] M. Quintero, A. Rodero, M. Garcia, A. Sola, Determination of the excitation temperature in a nonthermodynamic-equilibrium high-pressure He microwave plasma torch. *Applied spectroscopy* **51**, 778-784 (1997).
- [157] M. Mitchner, J. Charles H. Kruger, Partially ionized gases. Wiley series in plasma physics (*Wiley & Sons, Inc.*, New York, USA, 1973).
- [158] V. Rat, A. Murphy, J. Aubreton, M.-F. Elchinger, P. Fauchais, Treatment of non-equilibrium phenomena in thermal plasma flows. *Journal of Physics D: Applied Physics* **41**, 183001 (2008).

- [159] J. Jonkers, J. Van der Mullen, The excitation temperature in (He) plasmas. *Journal of Quantitative Spectroscopy and Radiative Transfer* **61**, 703-709 (1999).
- [160] N. H. Abel, Auflösung einer mechanischen aufgabe. *Journal für die reine und angewandte Mathematik* **1**, 153-157 (1826).
- [161] G. C.-Y. Chan, G. M. Hieftje, Estimation of confidence intervals for radial emissivity and optimization of data treatment techniques in Abel inversion. *Spectrochimica Acta Part B: Atomic Spectroscopy* **61**, 31-41 (2006).
- [162] G. Pretzler, A new method for numerical Abel-inversion. *Zeitschrift für Naturforschung. A, A Journal of physical sciences* **46**, 639-641 (1991).
- [163] G. Pretzler, H. Jäger, T. Neger, H. Philipp, J. Woisetschläger, Comparison of different methods of abel inversion using computer simulated and experimental side-on data. *Zeitschrift für Naturforschung A* **47**, 955-970 (1992).
- [164] C. Killer, Abel inversion algorithm (version 1.5), (2013) Available: <https://cn.mathworks.com/matlabcentral/fileexchange/43639-abel-inversion-algorithm> (Accessed date: 20 March 2016).
- [165] G. Eshel, G. J. Levy, U. Mingelgrin, M. J. Singer, Critical evaluation of the use of laser diffraction for particle-size distribution analysis. *Soil Science Society of America Journal* **68**, 736-743 (2004).
- [166] J. I. Eldridge, C. M. Spuckler, K. W. Street, J. R. Markham, in Proceedings of the 26th annual conference of composites, advanced ceramics, materials and structures: B H.-T. Lin, M. Singh, Eds. (*John Wiley & Sons, Inc.*, 2002) chap. 47, pp. 13-18.
- [167] G. Mauer, D. Sebold, R. Vaßen, D. Stöver, Characterization of plasma-sprayed yttria-stabilized zirconia coatings by cathodoluminescence. *Journal of Thermal Spray Technology* **18**, 572-577 (2009).
- [168] J. Czeknuszka, T. Page, Cathodoluminescence: a microstructural technique for exploring phase distributions and deformation structures in zirconia ceramics. *Journal of the American Ceramic Society* **68**, C-196-199 (1985).
- [169] W. H. Bragg, W. L. Bragg, The Reflection of X-rays by Crystals. *Proceedings of the Royal Society of London. Series A* **88**, 428-438 (1913).
- [170] H. M. Rietveld, A profile refinement method for nuclear and magnetic structures. *Journal of Applied Crystallography* **2**, 65-71 (1969).
- [171] J. Ilavsky, J. K. Stalick, Phase composition and its changes during annealing of plasma-sprayed YSZ. *Surface and Coatings Technology* **127**, 120-129 (2000).
- [172] O. Engler, V. Randle, Introduction to texture analysis: macrotexture, microtexture, and orientation mapping. (*CRC press, Taylor & Francis Group*, 2009).
- [173] S. Suwas, R. K. Ray, Crystallographic Texture of Materials. B. Derby, Ed., Engineering Materials and Processes (*Springer-Verlag London*, 2014), pp. 179-194.
- [174] T. Maitland, S. Sitzman, in Scanning microscopy for nanotechnology. W. Zhou, Z. L. Wang, Eds. (*Springer-Verlag New York*, 2007), pp. 41-75.
- [175] P. V. Hough, Method and means for recognizing complex patterns. *U. S. P. Office*, (1962).

- [176] S. I. Wright, M. M. Nowell, EBSD image quality mapping. *Microscopy and Microanalysis* **12**, 72-84 (2006).
- [177] P. Buchner, H. Schubert, J. Uhlenbusch, K. Willée, Modeling and spectroscopic investigations on the evaporation of zirconia in a thermal rf plasma. *Plasma chemistry and plasma processing* **19**, 341-362 (1999).
- [178] K. M. Green, M. C. Borrás, P. P. Woskov, G. J. Flores III, K. Hadidi, P. Thomas, Electronic excitation temperature profiles in an air microwave plasma torch. *Plasma Science, IEEE Transactions on* **29**, 399-406 (2001).
- [179] S. Semenov, B. Cetegen, Spectroscopic temperature measurements in direct current arc plasma jets used in thermal spray processing of materials. *Journal of thermal spray technology* **10**, 326-336 (2001).
- [180] B. Yotsombat, S. Davydov, P. Poolcharaunsin, T. Vilaithong, I. G. Brown, Optical emission spectra of a copper plasma produced by a metal vapour vacuum arc plasma source. *Journal of Physics D-Applied Physics* **34**, 1928-1932 (2001).
- [181] K. Jankowski, A. Jackowska, Spectroscopic diagnostics for evaluation of the analytical potential of Ar + He microwave-induced plasma with solution nebulization. *Journal of Analytical Atomic Spectrometry* **22**, 1076-1082 (2007).
- [182] A. Refke, M. Gindrat, S. M. AG, Process characterization of LPPS thin film processes with optical diagnostics. *Thermal Spray 2007: Global Coating Solutions*, Beijing, P. R. China, 2007.
- [183] N. Zotov, A. Hospach, G. Mauer, D. Sebold, R. Vaßen, Deposition of $\text{La}_{1-x}\text{Sr}_x\text{Fe}_{1-y}\text{Co}_y\text{O}_{3-\delta}$ coatings with different phase compositions and microstructures by low-pressure plasma spraying-thin film (LPPS-TF) processes. *Journal of Thermal Spray Technology* **21**, 441-447 (2012).
- [184] Q.-Y. Chen, X.-Z. Peng, G.-J. Yang, C.-X. Li, C.-J. Li, Characterization of plasma jet in plasma spray-physical vapor deposition of YSZ using a <80 kW shrouded torch based on optical emission Spectroscopy. *Journal of Thermal Spray Technology* **24**, 1038-1045 (2015).
- [185] S. Nakamura, Estimating measurement error values resulting from the peak position error, when using the Abel inversion and the numerical method in Ar inductively coupled plasma diagnostics. *Spectrochimica Acta Part B: Atomic Spectroscopy* **54**, 1899-1902 (1999).
- [186] A. Ramsey, M. Diesso, Abel inversions: Error propagation and inversion reliability. *Review of scientific instruments* **70**, 380-383 (1999).
- [187] H. Olsen, Thermal and electrical properties of an Ar plasma. *Physics of Fluids (1958-1988)* **2**, 614-623 (1959).
- [188] A. Murphy, Transport coefficients of hydrogen and Ar-hydrogen plasmas. *Plasma Chemistry and Plasma Processing* **20**, 279-297 (2000).
- [189] S. Gordon, B. J. McBride, Computer program for calculation of complex chemical equilibrium compositions and applications. I. Analysis. *NASA-Reference Publication, 1311*, (1994).
- [190] S. Gordon, B. J. McBride, Computer program for calculation of complex chemical equilibrium compositions and applications. II. User's manual and program description. *NASA-Reference Publication 1311* (National Aeronautics and Space Administration 1996).

- [191] A. Murphy, Demixing in free-burning arcs. *Physical Review E* **55**, 7473-7494 (1997).
- [192] A. Gleizes, Y. Cressault, Effect of metal vapours on the radiation properties of thermal plasmas. *Plasma Chemistry and Plasma Processing* **37**, 581-600 (2017).
- [193] A. Marotta, Determination of axial thermal plasma temperatures without Abel inversion. *Journal of Physics D: Applied Physics* **27**, 268-272 (1994).
- [194] A. F. Renteria, B. Saruhan, U. Schulz, H.-J. Raetzer-Scheibe, J. Haug, A. Wiedenmann, Effect of morphology on thermal conductivity of EB-PVD PYSZ TBCs. *Surface and Coatings Technology* **201**, 2611-2620 (2006).
- [195] Industry Updates. *Journal of Failure Analysis and Prevention* **11**, 401-408 (2011).
- [196] T. L. Bergman, F. P. Incropera, D. P. DeWitt, A. S. Lavine, Fundamentals of heat and mass transfer. (John Wiley & Sons, Inc., 2011).
- [197] G. M. Ingo, Origin of darkening in 8 wt% yttria-zirconia plasma-sprayed thermal barrier coatings. *Journal of the American Ceramic Society* **74**, 381-386 (1991).
- [198] R. Y. Korotkov, P. Ricou, A. J. E. Farran, Preferred orientations in polycrystalline SnO₂ films grown by atmospheric pressure chemical vapor deposition. *Thin Solid Films* **502**, 79-87 (2006).
- [199] J.-H. Pee, M. Tada, M. Hayakawa, Crystallographic study of the isothermal and athermal martensites of yttria-doped zirconia. *Materials Science and Engineering: A* **438**, 379-382 (2006).
- [200] T. Chraska, A. H. King, C. C. Berndt, On the size-dependent phase transformation in nanoparticulate zirconia. *Materials Science and Engineering: A* **286**, 169-178 (2000).
- [201] S. Sadeghi-Khosravieh, K. Robbie, Morphology and crystal texture in tilted columnar micro-structured titanium thin film coatings. *Thin Solid Films* **627**, 69-76 (2017).
- [202] J. Hutt, D. StJohn, The origins of the equiaxed zone-Review of theoretical and experimental work. *International Journal of Cast Metals Research* **11**, 13-22 (1998).
- [203] C. V. Thompson, R. Carel, Texture development in polycrystalline thin films. *Materials Science and Engineering: B* **32**, 211-219 (1995).
- [204] A. G. Dirks, H. J. Leamy, Columnar microstructure in vapor-deposited thin films. *Thin Solid Films* **47**, 219-233 (1977).
- [205] S. Mukherjee, D. Gall, Structure zone model for extreme shadowing conditions. *Thin Solid Films* **527**, 158-163 (2013).
- [206] S. Mahieu, G. De Winter, D. Depla, R. De Gryse, J. Denul, A model for the development of biaxial alignment in yttria stabilized zirconia layers, deposited by unbalanced magnetron sputtering. *Surface and Coatings Technology* **187**, 122-130 (2004).
- [207] C.-C. Chen, W.-Y. Cheng, S.-Y. Lu, Y.-F. Lin, Y.-J. Hsu, K.-S. Chang, C.-H. Kang, K.-L. Tung, Growth of zirconia and yttria-stabilized zirconia nanorod arrays assisted by phase transition. *CrystEngComm* **12**, 3664-3669 (2010).

- [208] B. J. Harder, D. Zhu, M. P. Schmitt, D. E. Wolfe, Microstructural effects and properties of non-line-of-sight coating processing via plasma spray-physical vapor deposition. *Journal of Thermal Spray Technology* **26**, 1052-1061 (2017).
- [209] G. Mauer, S. Rezanka, A. Hospach, R. Vaßen, The role of nucleation and growth in plasma spray-physical vapor deposition. *International Thermal Spray Conference and Exposition 2015 (ITSC 2015)*, Long Beach CA, USA, 2015.

Appendix

Table A1 Spraying parameters

Figure# or Test#	Protocol #	Plasma gases (slpm)			Spraying distance (mm)	Current (A)	Powder	Rotation speed of disc (2x)	Powder feeding rate (g/min)	Swivel angle (±°)	Swivel speed (mm/s)	Substrate	Size (mm ³)	Temperature (°C)	Duration (min.)
		Ar	He	H ₂											
Substrate perpendicular to the axis of the plasma jet															
Fig. 3.3a Fig. 5.11		35	60	0		2750									
Fig. 3.7	V-15- 110-O3	35	60	0	1000	2750	YSZ372M	10%		7	30	graphite	25x25x25		
Test A-5 Fig. 5.4a Fig. 5.6b	V-16- 157-O3	35	60	0	1000	2750	YSZ372M	5%	3.8	0	0	graphite	Ø30x11	1260	5
Test B-10 Fig. 5.4b Fig. 5.6b	V-16- 154-O3	35	60	0	1000	2750	YSZ372M	10%	6.9	0	0	graphite	Ø30x11	1350	5
Test C-20 Fig. 5.4c Fig. 5.6c	V-16- 155-O3	35	60	0	1000	2750	YSZ372M	20%	13.7	0	0	graphite	Ø30x11	1260	5
Test D-30 Fig. 5.4d Fig. 5.6d	V-16- 158-O3	35	60	0	1000	2750	YSZ372M	30%	16.4	0	0	graphite	Ø30x11	1260	5
Fig. 5.7a Fig. 5.8a Fig. 5.8c-f	V-14- 200-O3	35	60	0	1000	2750	YSZ372M	10%		7	15	IN738+BC	40x30x4	1000	
Fig. 5.8b	V-14- 202-O3	35	60	0	400	2750	YSZ372M	10%		7	15	IN738+BC	40x30x4	1100	

Appendix

Fig. 5.9a	V-15-070-O3	35	60	0	1000	2750	TZ-5Y-800	10%	7	0	0	graphite	150x40x20	1400	5
Fig. 5.9b/c Fig. 5.10	V-15-069-O3	35	60	0	400	2750	TZ-5Y-800	10%	7	0	0	graphite	150x40x20	1500	2
Test A-1000 Fig. 5.14 A1/A2 Fig. 5.15 A1/A2 Fig. 5.18 Fig. 5.19	V-15-061-O3	35	60	0	1000	2750	YSZ372M	10%	6.9	0	0	graphite	75x40x20	1350	5
Test B-700 Fig. 5.14 B1/B2 Fig. 5.15 B1/B2	V-15-061-O3	35	60	0	700	2750	YSZ372M	10%	6.9	0	0	graphite	75x40x20	1450	3
Test C-400 Fig. 5.14 C1/C2 Fig. 5.15 C1/C2 Fig. 5.20	V-15-068-O3	35	60	0	400	2750	YSZ372M	10%	6.9	0	0	graphite	150x40x20	1500	2
Fig. 5.21a	V-16-007-O3	35	60	0	1000	2600	YSZ372M	10%	6.9	7	30	IN738+BC	Ø30x3	1025	5
Fig. 5.21b	V-16-010-O3	35	60	0	1000	2600	YSZ372M	30%	16.4	7	30	IN738+BC	Ø30x3	1050	5
Fig. 5.21c	V-17-002-O3	35	60	10	1000	2200	YSZ372M	10%	6.9	7	30	IN738+BC	Ø30x3	890	5
Fig. 5.21d Fig. 5.24	V-16-184-O3	35	60	10	1000	2200	YSZ372M	30%	16.4	7	30	IN738+BC	Ø30x3	930	5
Fig. 5.23	V-17-008-O3	35	60	0	1000	2600	YSZ372M	30%	16.4	7	30	IN738+BC	Ø30x3	890	5
Fig. 5.25 Fig. 5.26	V-17-019-O3	35	60	0	1000	2600	YSZ372M	5%	3.8	7	10	IN738+BC	Ø30x3	920	10

Appendix

Substrate parallel to the axis of the plasma jet

Test I Fig. 5.28 Fig. 5.30 Fig. 5.32 Fig. 5.33 Fig. 5.36 Fig. 5.38 Fig. 5.43	V-15-071-O3	35	60	0	1000	2750	YSZ372M	10%	6.9	0	0	graphite	210x30x20	1400	5
Fig. 5.37	V-17-021-O3	35	60	0	1000	2750	YSZ372M	10%	6.9	0	0	graphite	210x30x20	1115	5
Test II Fig. 5.39 Fig. 5.41 Fig. 5.51	V-16-159-O3	35	60	0	1000	2750	YSZ372M	20%	13.7	0	0	graphite	210x30x20	1180	5
Test R-I Fig. 5.44 Fig. 5.50	V-16-182-O3	35	60	0	1000	2750	YSZ372M	10%	6.9	0	0	graphite	210x32x20	1320	5

Remarks:

- 1) Chamber pressure: 200 Pa
- 2) Carrier gas: Ar 2x16 slpm
- 3) Size of the powder hopper disc: 16x1.2 (mm) (powder hopper: V5 and V6)
- 4) O₂ led in during coating process: 4 slpm
- 5) The temperature in this table was measured by pyrometer during coating process.

Appendix

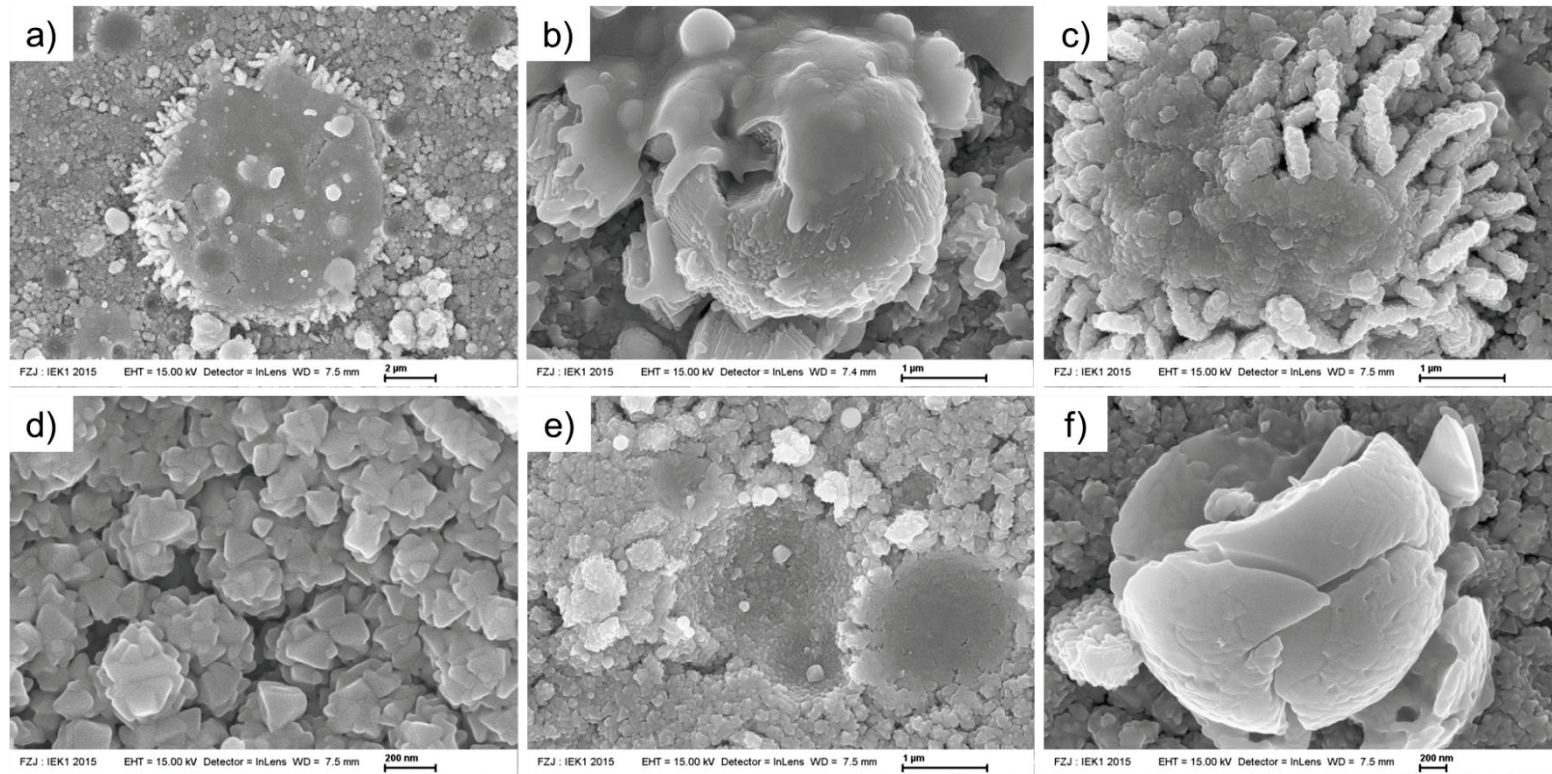


Fig. A1 Corresponding SEM (SE) images in Fig. 5.8

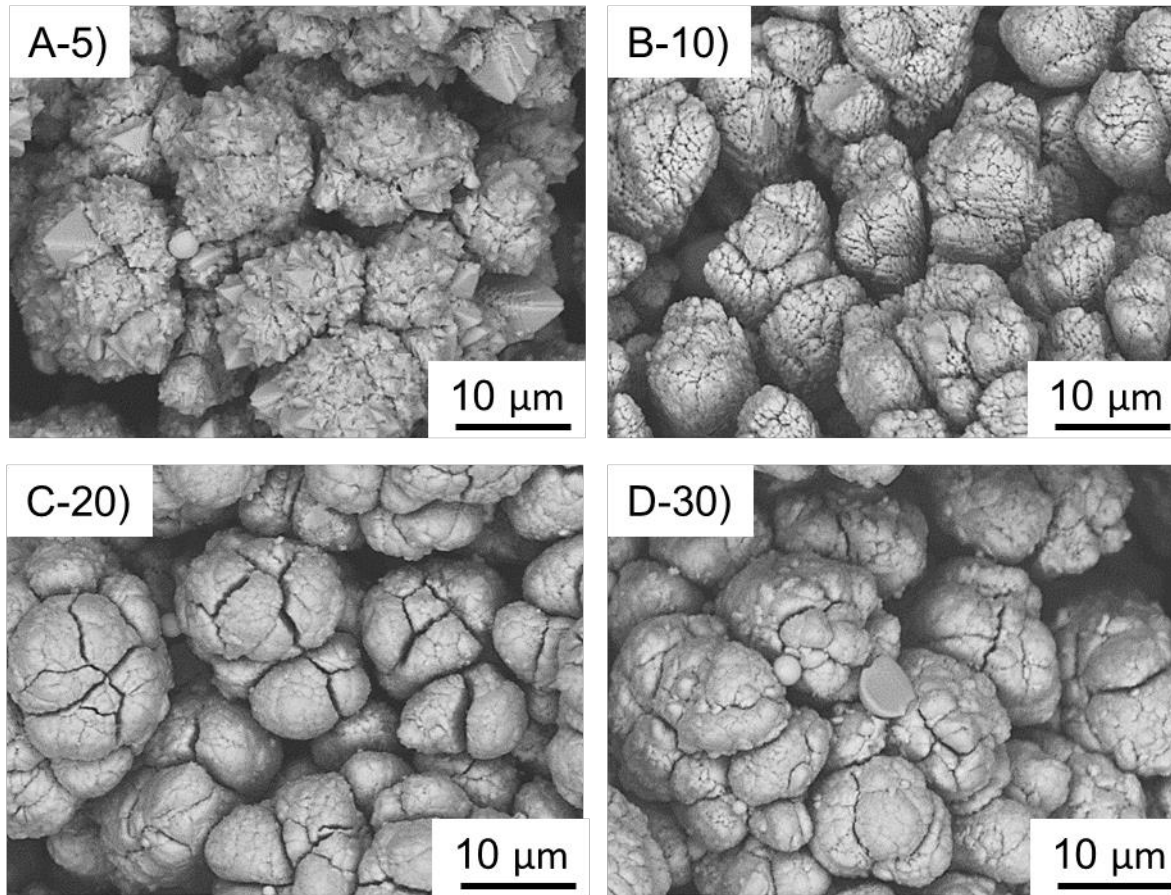


Fig. A2 Surface morphologies (SEM (BSE) images) of coatings deposited at powder feeding rates: A) 3.8 g/min, B) 6.9 g/min, C) 13.7 g/min and D) 16.4 g/min

Appendix

Table A2 Data of the crystal planes used for *TC* calculation

(hkl)	2theta(°)	Intensity (I ₀)	TC						
			Powder	400-T ₁	400-T ₂	700-T ₁	700-T ₂	1000-T ₁	1000-T ₂
(011)	30.270	459245.45	0.1250	0.0031	0.0969	0.0518	0.0625	0.0989	0.0797
(002)	34.812	38005.71	0.1250	0.3003	0.2686	0.1557	0.1486	0.1331	0.1507
(110)	35.255	67006.86	0.1250	0.2887	0.1319	0.1200	0.2787	0.1375	0.2598
(112)	50.376	175548.31	0.1250	0.0084	0.1058	0.1644	0.0829	0.1055	0.0996
(013)	59.610	65254.45	0.1250	0.0409	0.1123	0.1250	0.0717	0.1345	0.0804
(121)	60.205	126491.64	0.1250	0.0358	0.0639	0.0865	0.0903	0.1199	0.0873
(004)	73.466	11693.51	0.1250	0.1640	0.1448	0.1878	0.0941	0.1571	0.0983
(220)	74.539	25892.54	0.1250	0.1588	0.0759	0.1087	0.1713	0.1135	0.1441
		Average	0.1250	0.1250	0.1250	0.1250	0.1250	0.1250	0.1250
		Standard deviation (σ)	0.0000	0.1138	0.0597	0.0412	0.0680	0.0179	0.0570
		STDEV/Average	0.0000	0.9108	0.4777	0.3295	0.5442	0.1431	0.4562

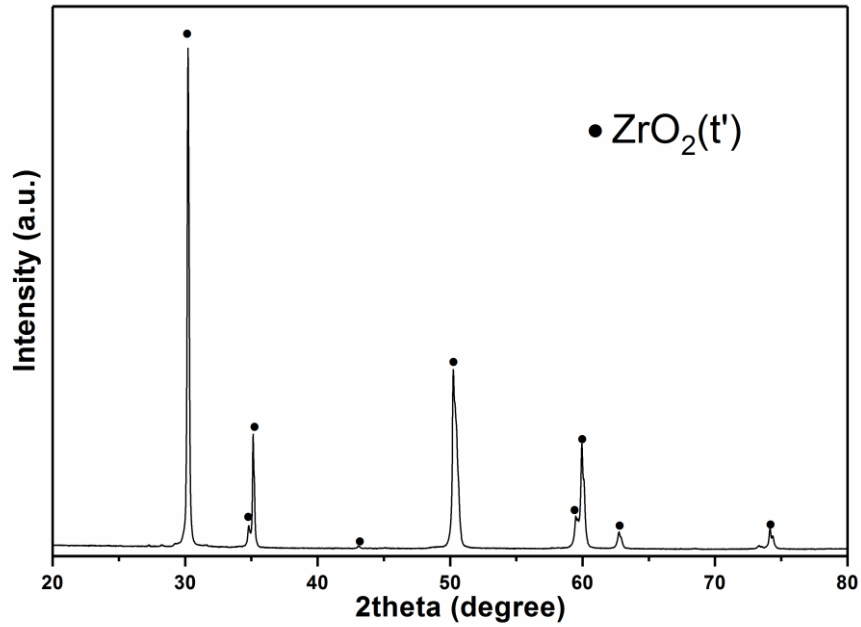


Fig. A3 XRD pattern of the coating shown in Fig. 5.25 deposited by the parameter A-2 (Table 3.5) at PFR of 2x5% (~ 2.5 g/min)

Academic Contributions during Ph.D. Research

- **Journal Articles**

- **W. He**, G. Mauer, M. Gindrat, R. Wäger, R. Vaßen, “Investigations on the Nature of Ceramic Deposits in Plasma Spray-Physical Vapor Deposition”, *Journal of Thermal Spray Technology* 26 (2017) 83-92 (invited article)
- **W. He**, G. Mauer, R. Vaßen, “Excitation Temperature and Constituent Concentration Profiles of the Plasma jet under Plasma Spray-PVD Conditions”, *Plasma Chemistry and Plasma Processing* 37 (2017) 1293-1311
- **W. He**, G. Mauer, O. Guillon, R. Vaßen, M. Gindrat, R. Wäger, “Investigations on the Nature of Ceramic Deposits in Plasma Spray-Physical Vapor Deposition”, *Thermal Spray Bulletin* 69 (2017) 70 -76
- M. Gindrat, R. Wäger, G. Mauer, **W. He**, “Numerical modelling of a Vacuum Plasma Spraying Torch used for Plasma Spray Physical Vapor Deposition”, *Thermal Spray Bulletin* 9 (2016) 148-156
- **W. He**, G. Mauer, A. Schwedt, O. Guillon, R. Vaßen, “Advanced Crystallographic Study of the Columnar Growth of YZS Coatings Produced by PS-PVD”, under review
- **W. He**, G. Mauer, O. Guillon, R. Vaßen, “Potential Growth Mechanisms of Columnar Ceramic Coating in PS-PVD”, in preparation
- **W. He**, G. Mauer, O. Guillon, R. Vaßen, “A review on development of thermal barrier coatings manufactured by plasma spray-physical vapor deposition”, in preparation

- **Conference Presentations**

- **W. He**, G. Mauer, R. Vaßen, “Potential growth mechanisms of columnar ceramic coating in plasma spray-physical vapor deposition”, International Thermal Spray Conference & Exhibition (ITSC2017), Düsseldorf, Germany, 7-9 June 2017
- **W. He**, G. Mauer, R. Vaßen, “Excitation temperature and concentration profiles of an Ar/He jet under Plasma Spray-PVD conditions”, The 14th High-Tech Plasma Processes Conference (HTPP 14), Universität der Bundeswehr München, Munich, Germany, 03-07 July 2016
- **W. He**, G. Mauer, O. Guillon, M. Gindrat, R. Wäger, R. Vaßen, “Investigations on the Nature of Ceramic Deposits in Plasma Spray-Physical Vapor Deposition”, International Thermal Spray Conference & Exhibition (ITSC2016), Shanghai, P.R. China, 10-12 May 2016 (One of the best paper awarded during the conference)

Acknowledgements

Time flies like an arrow, three years of my PhD study has come to the end. It has been a challenging life for me to pursue a PhD degree in Germany. Many people have made invaluable contributions, both directly and indirectly to my research in IEK-1. Also, I have received a number of selfless help in my life in this quiet and peaceful town “Jülich”. Without these contributions and help, it would not be possible to complete my PhD thesis successfully. I would like to express my gratitude sincerely to all those people. Thank you! Vielen Dank! 谢谢!

My deepest gratitude goes first to my distinguished supervisor, Prof. Dr. Robert Vaßen, for offering me this opportunity to complete my PhD thesis in IEK-1. Working in such great group is like standing on the shoulders of giants. Thanks for his profound knowledge in the subject of my PhD research, from which I have benefited a lot. Also, I always appreciate his sharp vision and insightful questions to prompt me to understand the nature of experimental phenomena.

I also owe my heartfelt thanks to my respectable scientific advisor Dr. Georg Mauer. I'm lucky to know him who becomes not only my scholarly mentor but also a good friend for me. His patient guidance, invaluable suggestions, and constant encouragement lead me in the right direction to the best science. I'm also grateful to him for sharing plenty of rest time to review and give feedback on every one of my work reports, papers as well as my thesis. I will keep in mind his encouraging saying that “Easy things everyone can do”.

My faithful appreciation also goes to my PhD examination committee, to Prof. Dr. Alfred Ludwig for evaluating my thesis and giving helpful comments to improve my thesis, to Prof. Dr. Viktor Scherer as the chairman of my PhD examination. I also want to thank Prof. Dr. Oliver Guillon for sharing time in my presentations and his guidance to be a good scientific worker.

Many sincere thanks should go to my colleagues who supported me a lot in my experimental work in IEK-1. I would like to thank Ralf Laufs, Karl-Heinz Rauwald, and Frank Kurze for their help in operating the PS-PVD facility and delicate work in the workshop. Cordial thanks go to Dr. Doris Sebold for her perfect work on the SEM investigation, to Dr. Yoo-Jung Sohn for the tireless help with XRD analyses and patient discussion, to Dr. Mark Kappertz for his careful guidance and support on metallographic sample preparation, to Volker Bader for his assistance in heat treatments, to Sigrid Schwartz-Lückge and Andrea Hilgers for their help in many particle size distribution tests, to Dr. Robert Mücke and Rainer Kriescher for their assist

Acknowledgements

in my computer related work, and to the workshop team. Special thanks to Dr. Alexander Schwedt and support from GFE RWTH Aachen for the EBSD investigation. Many sincere thanks should also go to colleagues who supported my daily work in Forschungszentrum Jülich, to Marianne Meyer, Hiltrud Moitroux, Vicky Tirtey, Stefan Weitz, and Sandra Schädel. Special thanks to Roswitha Gielen who helped me a lot when my wallet containing all my cards was robbed.

I would like to thank deeply all my Chinese colleagues who are so kind to me and helped me a lot during my life in Germany. My heartfelt thanks go to Dr. Yanli Zhang for being a very good friend since my first day in Germany, to Dr. Qianli Ma for his countless help and care, to Panpan Wang for being my nice roommate, to Dr. Ying Zou and Xiaoyan Yin for playing Pokémon together and making my lunch break much enjoyable, to Dapeng Zhou who has a sense of humor and added a lot of fun to us, to Yang Liu, Jun Zhang, Bowen Lu, Zhiyuan Wang, Tian Zhang, Wencai Leng, Dr. Hao Zheng, Lan Tu, Gang Yan and Dr. Chih-Long Tsai for being my lovely colleagues and friends and supporting me a lot. All the companionship alleviates my homesickness and makes me not alone.

Also, many thanks are given to my colleagues in the “WDS” group who created a harmony and motivated working environment. Special thanks to Dr. Diana Marcano who supported me a lot in the beginning of my work and always talks to me from time to time, to Dr. Stefan Rezanka who taught me many experimental tips, to Dr. Jan Bergholz for being a very nice talkative friend.

Last but not least, I would like to express my special thanks from the bottom of my heart to those most important people in my life even though I can only keep in touch with them by my mobile phone when I’m in Germany: to my beloved parents whose care and love motivate me to move on, to my dear old friends all over the world for lasting encouragement, to my dear Mr. Xinghua Liu for enduring a lot of my complaints and giving me a long-distance but truly intimate and heart-warming love.

With my very best wishes to all of you!

Band / Volume 384

IEK-3 Report 2017

Sektorkopplung –
Forschung für ein integriertes Energiesystem
(2017), 182 pp
ISBN: 978-3-95806-256-6

Band / Volume 385

Bestimmung der Wolframerosion mittels optischer Spektroskopie unter ITER-relevanten Plasmabedingungen

M. Laengner (2017), vi, 184, XI pp
ISBN: 978-3-95806-257-3

Band / Volume 386

IEK-3 Report 2017

Sector Coupling –
Research for an Integrated Energy System
(2017), 175 pp
ISBN: 978-3-95806-258-0

Band / Volume 387

Photochemistry of Highly Oxidized Multifunctional Organic Molecules: a Chamber Study

L. I. M. Pullinen (2017), II, 96, xviii pp
ISBN: 978-3-95806-260-3

Band / Volume 388

Poröse Transportschichten für die Polymerelektrolytmembran-Wasserelektrolyse

M. Höh (2017), VI, 186 pp
ISBN: 978-3-95806-262-7

Band / Volume 389

Modelling of High Temperature Polymer Electrolyte Fuel Cells

Q. Cao (2017), 173 pp
ISBN: 978-3-95806-263-4

Band / Volume 390

Potential use of nitrification inhibitors for mitigating N₂O emission from soils

D. Wu (2017), 206 pp
ISBN: 978-3-95806-264-1

Band / Volume 391

Mechanical Characterization of Solid Oxide Fuel Cells and Sealants

J. Wei (2017), II, 151 pp
ISBN: 978-3-95806-266-5

Band / Volume 392

Microcrystalline Silicon Carbide for Silicon Heterojunction Solar Cells

M. B. Pomaska (2017), 150 pp

ISBN: 978-3-95806-267-2

Band / Volume 393

Einfluss der Kristallisation auf das Fließverhalten oxidischer Schmelzen

S. Seebold (2017), 168 pp

ISBN: 978-3-95806-268-9

Band / Volume 394

Water vapour in the UTLS – Climatologies and Transport

P. R. Neis (2017), x, 124 pp

ISBN: 978-3-95806-269-6

Band / Volume 395

Neutronenaktivierungsanalyse mit gepulsten 14 MeV Neutronen zur Charakterisierung heterogener radioaktiver Abfälle

F. Mildenberger (2017), vi, 128 pp

ISBN: 978-3-95806-271-9

Band / Volume 396

Coupled biotic-abiotic mechanisms of nitrous oxide production in soils during nitrification involving the reactive intermediates hydroxylamine and nitrite

S. Liu (2017), xvii, 148 pp

ISBN: 978-3-95806-272-6

Band / Volume 397

Mixed-phase and ice cloud observations with NIXE-CAPS

A. Costa (2017), xviii, 117 pp

ISBN: 978-3-95806-273-3

Band / Volume 398

Deposition Mechanisms of Thermal Barrier Coatings (TBCs) Manufactured by Plasma Spray-Physical Vapor Deposition (PS-PVD)

W. He (2017), ix, 162 pp

ISBN: 978-3-95806-275-7

Weitere **Schriften des Verlags im Forschungszentrum Jülich** unter
<http://wwwzwb1.fz-juelich.de/verlagextern1/index.asp>

**Energie & Umwelt /
Energy & Environment
Band / Volume 398
ISBN 978-3-95806-275-7**

